NATHANN TEIXEIRA RODRIGUES

STUDY OF SOME LATTICE MODELS FOR POLYMERS AND FLUIDS

Thesis presented at Universidade Federal de Viçosa, as part of the requirements of the Graduate Program in Physics, to obtain the title *Doctor Scientiae*.

Advisor: Tiago José de Oliveira

VIÇOSA – MINAS GERAIS
2020

Ficha catalográfica elaborada pela Biblioteca Central da Universidade Federal de Viçosa - Campus Viçosa

T
R696s
2020

Rodrigues, Nathann Teixeira, 1991-
Study of some lattice models for polymers and fluids / Nathann Teixeira Rodrigues. – Viçosa, MG, 2020.
114 f. : il. (algumas color.) ; 29 cm.

Inclui apêndices.
Orientador: Tiago José de Oliveira.
Tese (doutorado) - Universidade Federal de Viçosa.
Referências bibliográficas: f.109-114.

1. Transformações de fase (Física estatística). 2. Fenômenos críticos. I. Universidade Federal de Viçosa. Departamento de Física. Programa de Pós-Graduação em Física. II. Título.

CDD 22. ed. 530.13

NATHANN TEIXEIRA RODRIGUES

STUDY OF SOME LATTICE MODELS FOR POLYMERS AND FLUIDS

Thesis presented at Universidade Federal de Viçosa, as part of the requirements of the Graduate Program in Physics, to obtain the title *Doctor Scientiae*

APPROVED: April 30, 2020.

Assent:

Nathann Teixeira Rodrigues
Author

Tiago José de Oliveira
Adviser

Acknowledgments

I would like to acknowledge first, my wife Juliana for all her support and always be on my side, my friends and family. To all my professors, in particular, Tiago for this ten-year journey until here and professor Thomas for all his advice in my short time in London. Lastly, I would like to acknowledge the financial support of the agencies, CNPq and FAPEMIG. Also, this study was financed in part by the Coordenação de Aperfeiçoamento de Pessoal de Nível Superior - Brasil (CAPES) - Finance Code 001.

Abstract

RODRIGUES, Nathann Teixeira, M.Sc., Universidade Federal de Viçosa, April, 2020. **Study of Some Lattice Models for Polymers and Fluids** Adviser: Tiago José de Oliveira.

Lattice models have been widely employed in the modeling of a sort of real systems, being especially important in study phase transitions and critical phenomena. In polymers, lattice models have helped to unveil the universal nature present in these systems, allowing a deep understanding of important phenomena such as protein folding and adsorption. When applied in the study of fluid systems, lattice models have been used to explore several properties as, e.g., fluid interfaces, phase transitions and multiphase flown. Here we investigate lattice models for both polymers and fluids. We explore two-dimensional lattice models for a single linear polymer chain near to a surface, with the polymer modeled through the path lattice model of interacting self-avoiding trails (ISATs). By using efficient Monte Carlo methods, we have characterized the thermodynamic behavior of adsorbing ISAT on the square and triangular lattices. In the former case, we have analyzed the universal nature of the adsorption transition for different boundary and solvent conditions. We have confirmed the universality hypothesis for the ordinary adsorption but, on the special point, a non-universal behavior has been found. On the triangular lattice, we have tackled the challenging problem of building up the three-dimensional phase diagram of the model, which is featured by several phases separated by a number of surfaces of phase transition and multicritical lines. In the part of fluids, we have investigated lattice gas models of hard-particles that excluded up to their k nearest-neighbor (kNN) in the square and cubic lattices with semi-analytic solutions on Husimi Lattices (HLs). By solving the models 1NN and 2NN on L-level HL built with squares we have characterized the critical parameters and, by using the coherent anomaly method (CAM), we have obtained the critical exponent β and γ. For both models, we have found critical parameters in good agreement with the more accurate estimates from Monte Carlo simulations. The values of the exponentes, however, are far from the expected values. On the cubic lattice, we have studied the binary 0NN-1NN, 0NN-2NN and 1NN-2NN and the ternary 0NN-1NN-2NN mixtures. By solving these mixtures on a HL built with cubes we have found a very rich thermodynamic behavior, with the presence of four stable phases, two fluid, and two solids, being separated by continuous and discontinuous phase transitions. We also have found critical, tricritical and triple points and even a density thermodynamic anomaly.

Keywords: Lattice models. Phase transitions. Critical phenomena. Self-avoiding trails. Lattice gas. Husimi lattice.

Resumo

RODRIGUES, Nathann Teixeira, M.Sc., Universidade Federal de Viçosa, abril de 2020. **Um Estudo de Modelos de Rede para Polímeros e Fluídos** Orientador: Tiago José de Oliveira.

Modelos de rede têm sido amplamente utilizados na modelagem de diversos tipos de sistemas reais, sendo de grande importância no estudo de transições de fase. Em polímeros, estes modelos foram essenciais no entendimento de propriedades universais, possibilitando um maior entendimento de importantes fenômenos, como o enovelamento e a adsorção de proteínas. Quando aplicados em sistemas fluidos, modelos de rede têm sido utilizados no estudo de diversas propriedades, e.g, interfaces de fluidos, transições de fases e fluxos de multifase. Nesta tese, investigamos modelos de rede para polímeros e fluídos. Exploramos redes bidimensionais para polímeros lineares próximos a uma superfície, com o polímero sendo aproximado pelo modelo de *interacting self-avoiding trails* (ISATs). Com a utilização de métodos de Monte Carlo, caracterizamos o comportamento termodinâmico de ISATs adsorventes nas redes quadrada e triangular. No primeiro caso, exploramos a natureza universal da transição de adsorção, considerando diferentes condições para a superfície e para o solvente. Confirmamos a hipótese de universalidade na adsorção ordinária, entretanto, no ponto especial, um comportamento não universal foi observado. Na rede triangular, estudamos o desafiador problema de analisar e construir o diagrama de fases tridimensional do modelo. Para os sistemas de fluidos, investigamos modelos de gases de redes compostos por partículas duras que excluem até o seu k-ésimo vizinho (k *nearest-neighbor* - kNN) nas redes quadrada e cúbica com soluções semi-analíticas em redes de Husimi (Husimi *lattices* - HLs). Resolvendo os modelos 1NN e 2NN em HL de nível L construídas com quadrados, caracterizamos os parâmetros críticos e, utilizando o método de anomalia coerente, tentamos obter os expoentes críticos β e γ. Em ambos os modelos, encontramos parâmetros em boa concordância com as estimativas mais precisas reportadas na literatura. Entretanto, não foi possível obter estimativas confiáveis para os expoentes críticos. Na rede cúbica, estudamos as misturas binárias 0NN-1NN, 0NN-2NN e 1NN-2NN e a ternária 0NN-1NN-2NN. Resolvendo estas misturas em uma HL construída com cubos, encontramos um comportamento termodinâmico bastante rico, com a presença de quatro fases estáveis, duas fluidas e duas sólidas, sendo separadas por transições de fases contínuas e descontínuas. Também encontramos pontos críticos, tricríticos e triplos e até mesmo uma anomalia termodinâmica.

Palavras-Chave: Modelos de rede. Transições de fase. Fenômenos críticos. *Self-avoiding trails*. Gás de rede. Redes de Husimi.

Contents

Chapter 1

Introduction

Soft condensed matter is a sub-field of condensed matter which deals with materials that presents distinguished, unique, properties that are not found in crystalline solids or simple liquids, i.e., materials like colloidal dispersions [1], crystal liquids [2], polymers [3], emulsions [4] and even biological materials [5]. The study of chemical and physical properties of those materials is of great importance in the advance of technological development and plays a central role in the understanding of biological systems, after all, we are mostly composed of soft matter.

The typical length scale of soft-matter systems, intermediary to the atomic and macroscopic scale, allows the use of coarse-grained models where not all atomic details need to be considered, highlighting universal properties. As an example, several properties of a polymer are not determined by the complicate chemical details of its components, but from the simple fact that the polymer is a long chain which does not cross itself. Although the scale of these structures is larger than the atomic scale, they are still small enough to be highly affected by thermal fluctuations and Brownian motion, allowing soft-matter systems able to move towards equilibrium. However, differently from the equilibrium states of usual solids and simple liquids, soft-matter systems are highly dependent on a subtle balance between energy and entropic leading to very rich phase behaviors, where complex structures are spontaneously formed.

The collective behavior is fundamental in the understanding of soft-matter properties. As they are composed of a large number of interacting atoms or molecules, the statistical mechanic theory gives the right tools to explore these systems. An important phenomenon occuring in almost all condensed matter materials is the phase transition. By changing the conditions of a given system as, e.g., its temperature, the quality of the solvent, the density of particles, the strength of an external field, etc. it can change dramatically its properties going through a phase transition. Phase transitions are daily-basis phenomena, in the simple act of boiling water to make a coffee we are changing the conditions, by increasing the temperature, allowing a phase change from liquid water to gas. Despite the simplicity needed to experiment a phase transition, the theoretical understanding of this phenomenon was only recently possible with the theory of critical phenomena [6]. Even with all development achieved in the last decades, the full understanding of phase properties and transitions is still a challenging problem, being exactly solved only for few simple models [67]. In most cases, we need to resort to numerical approaches allied with the critical phenomena and the statistical theory to investigate these phenomena.

Here, we are interested in the study of the thermodynamic behavior of polymers and fluids. Despite polymers being a soft-material system, fluids, on other hand, covers different areas with many systems fitting into it, with some being soft-matter materials.

So, it is important to remark that we will study a particular fluid system called hard-fluids and, despite they be used as a model for colloids [54], we will be interested in more general properties including the solid phase formed in these systems. With this in mind, our main goal is to explore the equilibrium properties of polymers and hard-fluids by characterizing the thermodynamic behavior for different lattice models. Through computational simulations, we will study path lattice models [98] for a single flexible homopolymer chain in the presence of an interacting surface in different solvent conditions. Using a semi-analytical approach with hierarchical lattices we will explore different lattice gas models for fluids, considering mixtures, binary and ternary, and also a problem with a single component fluid.

Polymer chains near surfaces consist in a very common system being present several materials with technological and biological importance [7]. An important phenomena in these materials is polymer adsorption [8]. When the polymer is close to a surface and there is a chemical affinity with the surface a phase transition where segments of the polymer adsorb on the surface can take place. When adsorbed polymers can change the surface properties making the adsorption transition an important process in, for example, the utilization of polymers and surfactants [9] and in the stabilization of colloids [10]. Then, in a more fundamental point-of-view, the study of global properties of polymers adsorption is crucial to understand the universal behavior present in such systems.

Another interesting system, studied here, is of fluid mixtures. In most of the cases, real systems are composed by more than one type of constituent and several properties depends of the interaction between them. As mentioned above, the terminology 'fluid' covers a broad range of different systems and so 'fluid mixtures'. As an example the polymer systems considered here, which consist of polymer + solvent + surface, can be seeing as a fluid mixture. So to be more precise, here we are interested in the study of mixtures of the fluids composed by hard-particles. In particular, we are interested in athermal hard-particles systems. In this condition the excluded volume of each particle plays a central role and all the process are driven by the entropy. Despite the simplicity, mixture of hard-particles can yields very complexes thermodynamic behaviors as, for example, the creation of depletion forces [75, 76] and thermodynamic anomalies [11], making the study of hard-particles mixtures important to help in the understanding of these complex phenomenon present in real systems.

Despite fluids and polymers being inside of the soft-matter theory, they are important enough to be treated separately. So, next, we will present separated introductions to the polymers and fluids problems considered here. The rest of the thesis is organized as follows. On Chap. 2 we present the works for lattice polymers, both works are already published [43, 44], and we choose to present as in the published version with a more detailed text about the computational methods being presented on the Appendix. A. On Chap. 3 we present the published versions [45, 46] of the three different binary mixtures considered here and also the published version of a ternary mixture lattice gas model [47]. The methods used for these three papers can be found in Appendix B. We also present in Chap. 4, in form of a preprint, an almost finished work of a single lattice gas on the square lattice using the high-order hierarchical lattice method described in the Appendix. B. On Chap. 5 we cover the ongoing work and on Chap. 6 we present our conclusions and further comments.

1.1 Polymers

A polymer is a long chain of bonded monomers, while the monomer are the basic structures that repeat along the chain. The chemistry and physics of polymers have

been widely developed in the past decades [3, 12] and a variety of applications has been discovered, from plastics to medicine. The polymer science can be divided into two main categories depending on the scale of interest. The first one is of strong magnification, and in this case, the local properties like the motion of a single monomer inside of the chain and their chemical details are relevant and atomistic models with effective interactions are usually employed [13]. On the other side, the weak magnification scale where the observable is of the size of the polymer chain and depends on global details like the concentration, temperature, and few interaction parameters.

As pointed out in the previous section, here we are interested in the global properties of a single linear polymer chain. Differently from the strong magnification scale, the monomer details are not relevant here and very simple coarse-grain models can be employed. More precisely, we are interested in coarse-grain models in which the length of the polymer chain is much bigger than the persistence length, l_p. If we take a close look into the chemical bonds of a polymer, the monomers connect with each other with a fixed angle α (see Fig. 1.1) leaving a rotation degree of freedom for the chemical bond. As the number of monomers increases the correlation between bond directions decreases and for lengths longer than l_p the bonds directions are basically uncorrelated. To eliminate the chemical details, our coarse-grain models must be on a scale such that a monomer is a structure of the size of l_p and the bond directions are random. Naturally, in this scale, the simplest model for a polymer is of a random-walk in a regular lattice.

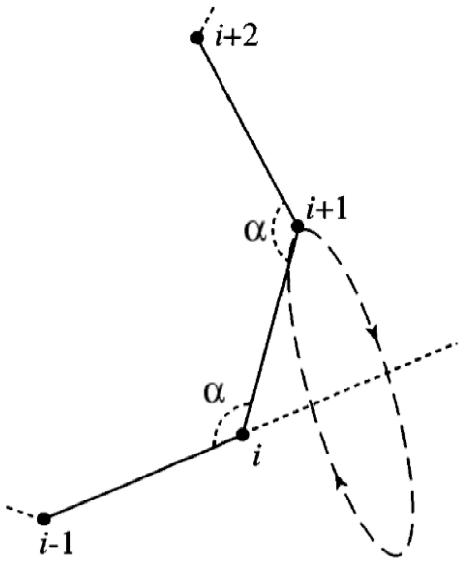

Figure 1.1: Figure from [21]. The set of monomers is presented by the points $i-1$, i and $i+1$ the bonds between monomers are presented by the lines that connect the points. The angle α is fixed allowing rotational freedom of the bonds.

A n-step random-walk on a regular lattice is a collection of vertices $(v_0, v_1, ..., v_n)$ where each pair of vertex v_{i-1}, v_i is connected by an edge of length a, where a is the lattice spacing. A polymer chain is represented by a random-walk by the identification of the vertices as monomers and the edges as the chemical bonds that connect them. In Fig. 1.2 an example of a random-walk with $n = 13$ steps on the square lattice is shown. It is important to note that as the "monomer" in our models is of the order of the persistence length, the situation of two monomers occupying the same vertex does not imply in real monomers occupying the same physical space. The random-walk model can have an infinite number of monomers at the same site.

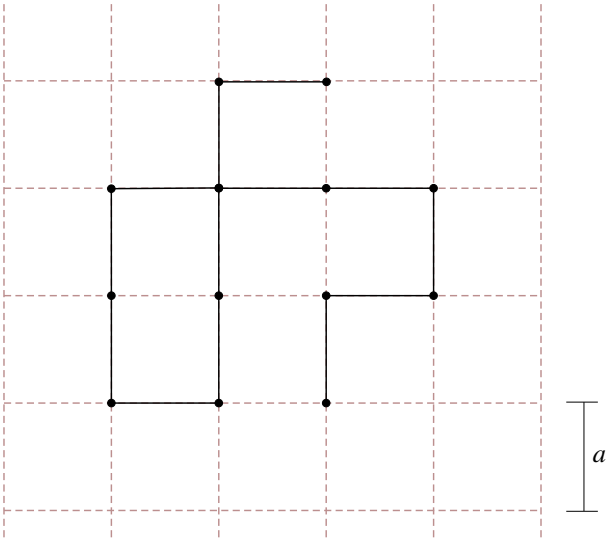

Figure 1.2: An example of a random-walk with $n = 13$ steps on the square lattice with spacing a. The black circles are the vertices of the walk (the monomers of the polymer) and the black lines connecting them the edges (bonds between monomers).

As there is no interaction between monomers, the random-walk is known as a model for an ideal polymer chain. Despite the absence of interactions being an unrealistic scenario, there are some cases where the polymer behaves as an ideal chain. Two important examples are the collapse transition and polymer melting in three dimensions [3]. Although the ideal chain regime being present at these examples, the random-walk model does not give the entire picture of these phenomena. For example, in the three-dimensions, a polymer in solution undergoes to collapse transition from a swollen-coil to a dense-globule configuration (see Fig. 1.5). The ideal chain describes only the polymer at the transition point and gives no clues on the thermodynamic behavior in the other phases. To do so we need to introduce interactions in the model.

Several types of complicated interactions can be present in a polymer [14]. Here, in our simplistic approach, we are interested in two global effects. First, a polymer is usually immersed in a solvent and, in a good solvent regime, the monomers in the chain tend to be surrounded by solvent molecules, creating an excluded volume to other monomers. Conversely, in a poor solvent regime, the monomers tend to be closer to each other, yielding a hydrophobic effect. All the details of these two effects are quite complicated and it is not our aim to explore them here. The simplest way to introduce these effects is by considering two very simple short-range interactions between monomers.

The clever way to introduce the excluded volume effect is by taking into account the solvent effect implicitly by imposing an occupation restriction in the random-walk model. If we impose that all vertices $(v_0, v_1, ..., v_n)$ that compose the n-step walk have to be unique, we obtain the famous model of a self-avoiding walk (SAW) model -see Fig .1.4 (a)-. This model was first introduced by Flory [12] as a model for polymers in a good solvent. As shown in Fig. 1.3 the excluded volume effect is indeed present, since for the same size, the SAW, Fig. 1.3 (b), is more stretched and along the chain the density of monomers is lower when compared with a random-walk, Fig. 1.3 (a).

The simple restriction in the occupancy of the sites in the lattice turns the SAW into a very challenging mathematical problem, with only a few rigorous results available [98]. As an example, in a d-dimensional hypercubic the most fundamental statistical quantity, the number of possible configuration, c_n, with n steps, is simply given by $(2d)^n$ for random-walks, where $2d$ is the number of nearest-neighbors of each vertex. For SAWs we only

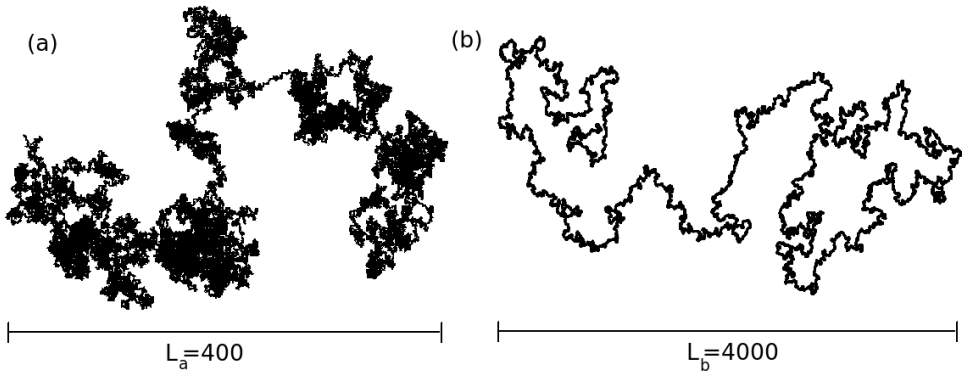

Figure 1.3: (a) A random-walk with 100000 steps on a square lattice, the walk has a short length, filling more the volume, due to the absence of the excluded volume effect. (b) A self-avoiding walk with 100000 steps on a square lattice, the configuration is more swollen than the random-walk, with a lower monomer density along the chain, as an effect of the excluded volume.

know, the asymptotic behavior (for $n \to \infty$) of c_n

$$c_n \sim \mu^n n^{\gamma-1}, \tag{1.1}$$

where μ is called the connectivity constant and, is also related to the lattice coordination. The exponent γ, know as the entropic exponent, depends on the dimension of the lattice and is assumed to be universal. For dimensions $d \geq 4$ the SAW behaves as an ideal chain and the exponent γ assume the classical value of $\gamma = 1$. Another important quantity in polymer physics is the end-to-end distance, R_n, which gives information about the conformation of the polymer chain. When modeling through lattice paths, as random-walks and SAWs, R_n can be calculated as follows

$$R_n = ||v_0 - v_n|| \tag{1.2}$$

where v_0 and v_n are, respectively, the initial vertex and the vertex at the nth step. As c_n, only the asymptotic behavior of the end-to-end distance is known for SAWs, the squared end-to-end distance behaves as

$$R_n^2 \sim n^{2\nu}, \tag{1.3}$$

where ν is know as the Flory (or metric) exponent and, like γ, is universal, depending only on the space dimension. For $d \geq 4$, ν assumes the ideal chain value of $\nu = 1/2$. For dimensions $d \leq 3$, the estimation of c_n and the calculation of μ, γ and ν are challenging problems and, in most of the cases, only numerical estimates are known [98].

A major leap forward in the understanding of the universal properties present in polymer physics was made by [15], who found a connection between the SAW model and the $O(N)$ model. In the limit of $N \to 0$ the magnetic susceptibility gives the grand-canonical partition function of SAWs. This connection shows that the SAW model is a critical phenomenon and Eqs. 1.1 and 1.3 can be understood as scaling laws with the exponents ν and γ being related to critical exponents of the $O(N)$ model in the limit of $N \to 0$. In two dimensions, the $O(N)$-model can be solved exactly by using a mapping in the Coulomb gas problem [16] and the exponents $\nu = 3/4$ and $\gamma = 43/32$ are found. In three dimensions, only approximated results are known, using the renormalization group theory for the Edwards polymer model [17] the values $\nu = 0.588(2)$ and $\gamma = 1.157(3)$ are obtained with the more precise values, $\nu = 0.587597(7)$ [18] and $\gamma = 1.15695300(95)$ [19], reported recently.

Once the SAW model is a critical phenomena the exponents ν and γ can be seeing as universal in the light of this theory. The universality means that the value of the exponent should depend on the space dimensionality and, in the case of short-range interactions, the symmetries of the order-parameter that describes the transition. Despite the symmetries of the order-parameter and the order-parameter by itself are unknown for the SAW problem, the universality hypothesis implies that the same set of exponents should be observed if we change details in the models. For instance, we can introduce the exclusion volume effect in a different manner: instead of restricting the vertex to be unique, we can require that all edges should be unique. In this case, we have the model of self-avoiding trails (SAT), or simply trails. In such model, as the occupancy restriction is in the edges, it is possible to exist more than one monomer per site (see Fig. 1.4 (b)). The maximum number of monomers per-site, however, is restricted by the lattice coordination. For a lattice with coordination q one site can has $q/2$ monomers-per site. As shown in the example of Fig. 1.4 (b), there are two forms for a site be visited twice at the square lattice: collisions and crossings. If we restrict even more the way the walk can be formed, by forbidding the occurrence of crossings, we obtain the vertex interacting self-avoiding walk (VISAW) model, see Fig. 1.4 (c), where a multiply visited site can happens only through collisions.

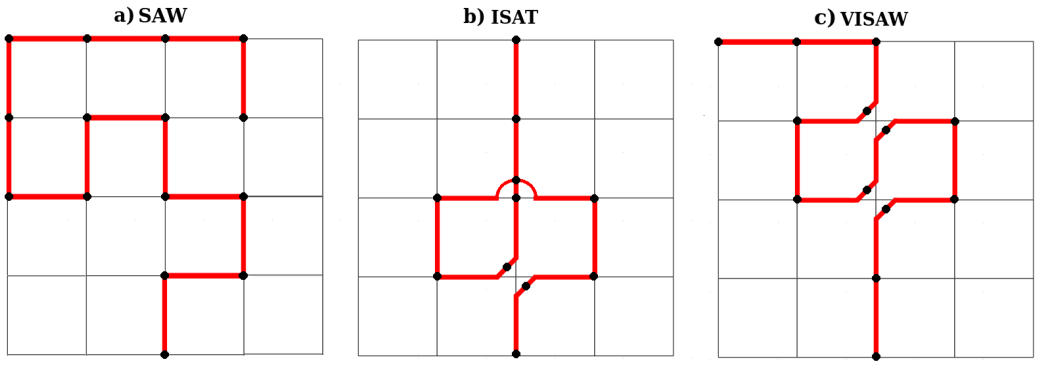

Figure 1.4: (a) A self-avoiding walk with $n = 14$ steps on the square lattice. (b) A self-avoiding trail with $n = 11$ steps on the square lattice. With a lattice of coordination $q = 4$ up to two monomers can be placed per vertex with intersections and collisions. (c) A vertex interacting self-avoiding walk (VISAW) with $n = 13$ steps, only collisions are allowed.

These models, SAW, SAT and VISAW, present three different ways for considering the excluded volume effect and all of them, as coarse-grained models, should capture the properties of a polymer chain dilute in a good solvent. Using any of those models the same values of exponents ν and γ are observed [20, 30, 31] showing the universal nature of them. However, the situation becomes more complicated when the hydrophobic effect is included.

1.1.1 The collapse transition

With only the excluded volume effect the models can simulate the good-solvent regime, to be able to study more complex phenomena, like the collapse transition, the hydrophobic effect have to be also considered. At high temperatures (or for a good solvent) the polymer chain is found on the coil phase, where the excluded volume effect dominate (see Fig. 1.5 (a)). Decreasing the temperature, or changing the condition of the solvent to a poor one, the hydrophobic effect starts to dominates and the chain collapses, forming a

dense configuration, the globule phase (see Fig. 1.5 (b)). This transition, frequently called coil-globule, occurs in a specific point called Θ point. At this point, in three dimensions, the excluded volume effect cancels the hydrophobic one and the polymer behaves as an ideal chain.

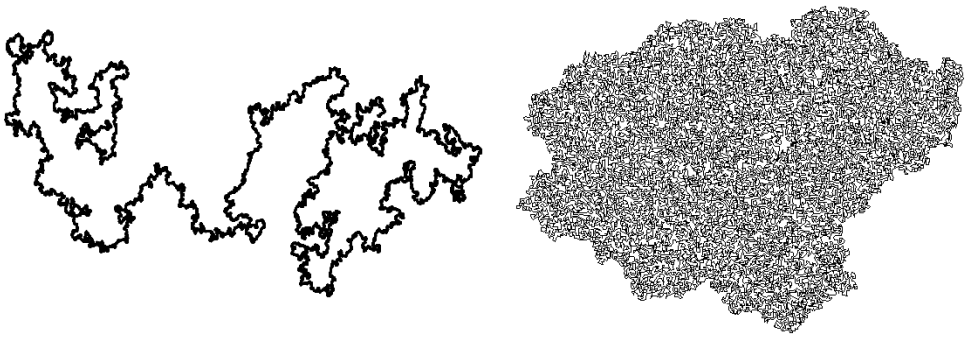

a) Good solvent regime and/or high T b) Good solvent regime and/or low T

Figure 1.5: (a) A representation of the coil phase using a SAW on the square lattice. (b) Globule phase on the square lattice for a interacting self-avoiding walk (ISAW) with $n = 100000$ steps

The hydrophobic effect can be introduced as an attractive interaction between monomers in the chain with an energy $-\epsilon < 0$ being assigned for each monomer contact. For the interacting SAW (ISAW) model, the canonical form to assign the energy is on the non-consecutive nearest-neighbors monomers of the walk. For the interacting SAT (ISAT) and the VISAW models, the monomer-monomer interaction is usually considered on multiply visited sites. In all cases, the same phases are observed at high or low temperatures. The equilibrium properties of polymers systems, and other systems in general, depend on a delicate balance between the internal energy and entropy. We can see this clearly for the collapse transition considering the free energy F given by

$$F = U - TS, \tag{1.4}$$

where U is the internal energy, S the entropy and T the temperature. The equilibrium state is achieved by minimizing F, then, at high temperatures, the term of entropy dominates over the energy and the chain tends to have few monomer-monomer contacts, giving rise to the coil phase. On another hand, at low temperatures, the energy term starts to be more important and the free energy is minimized by increasing the number of contacts between monomers. The higher number of contacts, either between nearest-neighbor monomers or those at multiply visited sites, form a dense configuration that mimics the hydrophobic effect regime, yielding the globule phase.

As in the coil phase, discussed above, the scaling relations with the exponents ν and γ characterize also the globule and the θ point. In the globule phase, the dense packing has the same dimension of the space and, by looking at the equation Eq. 1.3 as a mass-radius relation, we can identify the Flory exponent as $\nu = 1/d_f$, where d_f is the fractal dimension of the chain. Then in the globule phase one has $\nu = 1/d$. The γ exponent for the globule phase is more difficult to be determined. Due to the surface effect present in the globule phase, the Eq. 1.1 has to be changed and the exponent value is highly dependent on the geometry of dense configuration formed [22].

The characterization of the exponents at the Θ-point has been extensively studied [23–27]. Close to the Θ-point the squared end-to-end distance has the scaling behavior

$$R_n^2 = n^{2\nu_\Theta} f(\tau n^\phi), \tag{1.5}$$

where ν_Θ is the value of the Flory exponent at the transition point, τ is the reduced temperature given by $\tau = |T - T_\Theta|/T_\Theta$, ϕ is a universal exponent know as the crossover exponent and the scaling function $f(x)$ behave as [25–27]

$$f(x) \sim \begin{cases} x^{(2\nu_{SAW}-2\nu_\Theta)/\phi}, & \text{if} \quad x \to \infty, \\ const., & \text{if} \quad x = 0, \\ |x|^{(2/d-2\nu_\Theta)/\phi}, & \text{if} \quad x \to -\infty. \end{cases} \tag{1.6}$$

The collapse transition is then characterized by the exponents ν_Θ, γ_Θ and ϕ. As already mentioned, in three dimensions the polymer behaves like an ideal chain at the Θ-point. From the point-of-view of the critical phenomena theory the Θ-point is a tricritical transition point [28, 29], implying in an upper critical dimension $d = 3$ for it, so that the critical exponents assumes the mean-field (ideal chain) values, $\nu_\Theta = \phi = 1/2$ and $\gamma_\Theta = 1$, with logarithmic corrections to the scaling laws [29].

The nature of the collapse transition in two-dimensions is a question of a long debate on the literature [23, 30, 32, 33]. Duplantier and Saleur (DS), whom managed to exactly solve the collapse SAW model on a hexagonal lattice using a map with the percolation theory [23], obtaining the values $\nu_\Theta^{DS} = 4/7$, $\gamma_\Theta^{DS} = 8/7$ and $\phi^{DS} = 3/7$. Several subsequent works found values very similar to the ones of DS using Monte Carlo and other numerical methods in two dimensions (see [98] and references therein). A different set of values was found, however, by Blöte and Nienius (BN) [30,31] in the exact solution of the VISAW model on the square lattice, being $\nu_\Theta^{BN} = 23/42$, $\gamma_\Theta^{BN} = 53/46$ [31]. The situation becomes even worse when the crossings are allowed in the VISAW model, i.e. for the ISAT model. Differently from the VISAW, only numerical results are known for the ISAT. On the square lattice, some works claim to have observed the BN exponent for ν but with $\gamma_\Theta = 22/23$ [33] while others propose a different value for the Flory exponent [34]. Despite the DS values being more accepted as the exponents of the Θ class in two dimensions, the divergence observed in the VISAW and SAT models suggests that these models are in a different universality class at the Θ point in two dimensions.

Here we will explore the thermodynamic behavior of the ISAT model in two dimensions. As it is going to be shown in the next section, we studied the ISAT model on the square and on the triangular lattice considering not only the monomer-monomer interaction but also an interaction with a planar surface that introduces another phase transition in the system, the adsorption transition

1.1.2 The Adsorption Transition

When a polymer is near to an impenetrable surface and some form of attractive interaction (chemical affinity between monomers and the atoms or molecules of the surface) is present the monomers can bonded to the surface and an adsorption transition can takes place. At high temperatures, similar to the collapse transition, the entropic effect dominates and the chain tends to be away from the surface (see Fig. 1.6 (a)), decreasing the temperature the number of contacts with the surface starts to increase until the polymer chain being adsorbed at the surface (see Fig. 1.6 (b)).

The adsorption transition can be studied using the walk models (SAW, SAT or VISAW) by simply introducing an energy $-\epsilon_s$ to every site of the walk in contact with the surface. Usually, an infinite flat surface is considered containing the starting point of the walk. Differently from the collapse transition, a well-defined order parameter is known to characterize the adsorption transition. For $T > T_a$ the fraction of contacts with the surface vanishes in the thermodynamic limit (of infinite length chain) and for $T < T_a$ a non-null fraction of contacts is expected, then, the energy associated with the surface

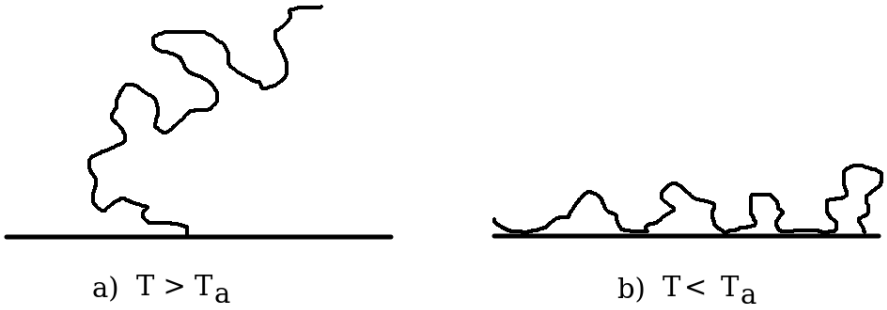

Figure 1.6: (a) Representation of non adsorbed polymer chain. (b) Adsorbed configuration, characterized by a large number of polymer-surface contacts.

contacts, u_n, is defined as the order parameter

$$u_n = \frac{< m_s >}{n}, \tag{1.7}$$

where $< m_s >$ is the average number of surface contacts for a walk with n steps. Close to the transition point, the order parameter is expected to behave as [35]

$$u_n \sim n^{\phi^{(a)}-1} g(\tau n^{1/\delta}), \tag{1.8}$$

where $\tau = |T_a - T|/T_a$ is the reduced temperature and $\phi^{(a)}$ and $1/\delta$ are the exponents that characterize the adsorption transition. These exponents are believed to assume the same value [35] and for $d \geq 4$ they have the mean-filed values $\phi^{(a)} = 1/\delta = 1/2$. Interestingly the mean-field values are also observed in two-dimensions [37], while in three-dimensions a value very close to 1/2 is observed, $\phi^{(a)} = 1/\delta = 0.484(3)$ [36].

The problem of adsorption transition becomes more interesting when, besides the monomer-surface, a monomer-monomer interaction is also considered. In this case, the monomer-monomer interaction induces a bulk coil-globule transition and a more complex thermodynamic behavior appears. For example, in three-dimensions, besides the coil, globule and adsorbed phase, an two-dimensional coil-globule transition can be induced while the polymer is adsorbed into the plane. Other phases can appear as the surface attached globule (SAG) [38] and adsorbed phases with a layering structure (for finite lengths) [39].

Recently, the universal nature of the exponents $\phi^{(a)}$ and $1/\delta$ has been questioned in the numerical study of the ISAW with surface interaction in the cubic lattice [40]. The authors have claimed that the adsorption exponents have a dependence on the strength of the bulk interaction (solvent condition) which is unexpected from the point-of-view of universality. They also found that the equality $\phi^{(a)} = 1/\delta$ may not hold when the solvent condition is modified. A series of subsequent works [35, 41, 42] were made exploring these points and in all universal nature of the exponents is observed. Motivated by this renewed interest in polymer adsorption we will explore the ISAT model with bulk and surface interactions in two-dimensional lattices.

In the first paper presented at the Chap. 2 we study the SAT model on the square lattice considering two forms of introducing the monomer-surface, one at each monomer in the surface and another for each bond at the surface. We also consider the case of an non-horizontal surface for the adsorption. Our main goal in the work is to verify if the universality hypothesis holds in this systems, by determining, in a very careful manner,

the adsorption exponents for different solvent conditions. To perform the simulation we have employed the flatPERM/PERM methods, which allowed us to the explore a large portion of the phase diagram and to sample very long chains. More details about them can be found in the Appendix A.

In the second paper presented in Chap. 2 we have extended our study of the ISAT model with bulk and surface interactions on the triangular lattice. In this case, the ISAT can have sites with up to three monomers, so that two distinct monomer-monomer interactions can be considered for doubly and triply visited sites. Along with the monomer-surface interaction, the model presents three interaction parameters, which lead to a 3D phase diagram. The challenging work of building this phase diagram was carried out using the flatPERM method.

1.2 Fluids

In fluid systems two types of interaction play a central role the van der Waals interaction and the Pauli principle. In a gas, the thermal energy makes the atoms or molecules move, almost, freely filling the entire available volume. When the temperature is decreased a condensation starts to happen and the gas turns into a liquid. This process lets evident that some form of attractive interaction between the gas constituents should be present, which becomes weaker as the separation between atoms (molecules) increases and stronger for short-range. This attractive part is mostly due to the van der Waals interaction which is a short-range interaction mostly part due to the electrical dipoles of the molecules [1].

Besides the attractive, some form of repulsive interaction should also exist to prevent the matter from collapsing, making the solid phase possible. The high comprehensibility of the liquids shows that this repulsive part must be strong and acting on a very close range between atoms. Such repulsive interaction is associated to the Pauli principle and so it is of quantum nature, preventing the overlapping of the electrical orbitals of atoms. The form of the potential for the Pauli principle is empirical and, usually, involves exponential functions of high powers of the inverse of the separation between atoms (molecules). A famous effective potential that captures the two types of interactions is the Lennard-Jones (LJ) potential, given by

$$V(r) = 4\epsilon \left[\left(\frac{\sigma}{r}\right)^{12} - \left(\frac{\sigma}{r}\right)^{6} \right], \tag{1.9}$$

where ϵ can be seen as the depth of the potential wall and σ as the finite distance at which the potential between particles is zero. The LJ potential has been widely used in both two- and three-dimensional fluids and it is often used in the study of gas-liquid-solid transitions for fluids in the continuum [48–51].

Another very famous way to approach the Pauli principle in fluid systems is by considering the models of hard-spheres [52, 53], an example is shown in Fig. 1.7. In this case, the potential is simply fixed to infinity when two molecules overlap ($r < 2R$) and null otherwise. Despite the hard-sphere model seems to lack a number of important features of real systems it present fluid-solid phase transition and is also suitable for modeling the low density regime of fluids. Real systems like some colloids are known to behave very close to hard-spheres [54] and this simple model can give useful insights to much more complex systems.

[1] Another type of attractive interactions as ionic interactions, covalent bonds, hydrogen bonds, metallic bonds, etc, can also be present depending on the type of fluid. Here, for the purpose of illustration, we will refer only to the van der Waals interaction.

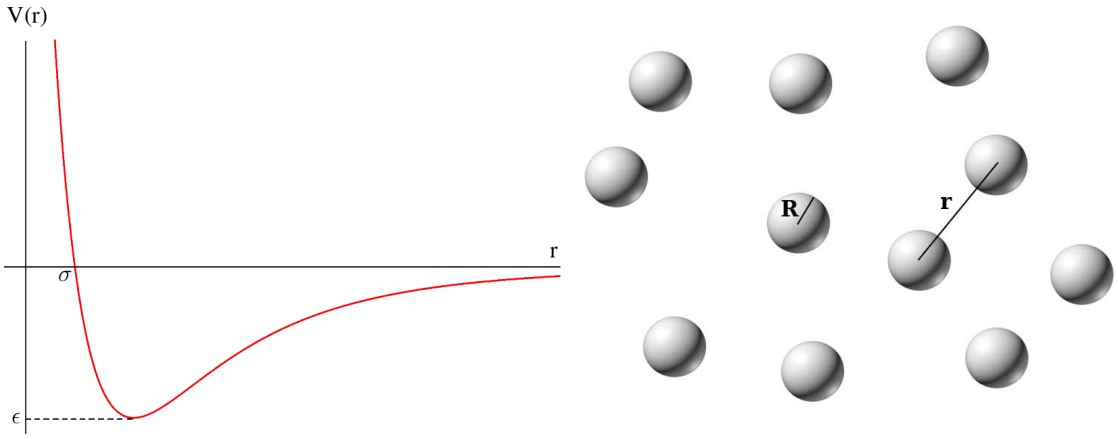

Figure 1.7: On the left, the curve of the LJ potential $V(r)$ where r is the distance between the molecules pairs. On the right, a representation of hard-spheres with R being the radius of each sphere and r denoting the separation between two spheres.

From the theoretical point of view, the hard-sphere model consists of a very useful approximation that allows some exact results. An important one is the analytic solution of the Ornstein-Zernike equation [58] with the Percus-Yevick (PY) approximation [55–57], which consists in an integral equation for the radial distribution function of a classical fluid. In three-dimensions, the PY equation is given by [56]

$$\tau(\vec{r}) = 1 - \rho \int \tau(\vec{r})(e^{-\beta V(\vec{r})} - 1)d\vec{r} + \rho \int \tau(\vec{r'})(e^{-\beta V(\vec{r'})} - 1)\tau(\vec{r} - \vec{r'})e^{-\beta V(\vec{r}-\vec{r'})}dr', \quad (1.10)$$

where $\beta = 1/k_bT$, ρ is the molecular density, $V(\vec{r})$ is the potential of interaction and $\tau(r)$ is related to the direct correlation function of Ornstein-Zerkine [58], $c(\vec{r})$, and the radial distribution $g(\vec{r})$ by

$$g(\vec{r}) = \tau(\vec{r})e^{-\beta V(\vec{r})} \text{ and } c(\vec{r}) = \tau(\vec{r})(e^{-\beta V(\vec{r})} - 1) \quad (1.11)$$

In three-dimensions, the PY equation of state predicts a first-order gas-liquid transition when potentials of the LJ type (with repulsive and attractive terms) are considered [59–63]. However, the original PY solution has some limitations. For high densities, the solution breaks down and no fluid-solid transition is predicted [64]. Another problem occurs in the case of hard-spheres without attractive interactions, in this case, the PY equation can be solved more easily and the equation of state follows

$$\frac{\beta P}{\rho} = \frac{1 + \eta + \eta^2}{(1 - \eta)^3}, \quad (1.12)$$

where $\eta = \pi R^3 \rho/6$ with R being the radius of the spheres. This equation of state does not predict any phase transition, however, hard-spheres systems are know to undergoes to a fluid-solid transition even with only the repulsive part of the potential [65].

The hard-sphere models present an interesting view for the role of the entropy [68]. Without any attractive interaction, the internal energy assumes a trivial form being dependent only on the temperature, as in an ideal gas. Then, all complexity that leads to phases transitions should be carried in the entropy. As the temperature is not relevant for the phase change these systems are often called athermal models. For the sake of simplicity, we can set the internal energy to zero and, by doing so, the free energy (Eq. 1.4) becomes simply $F = -TS$. Now, in order to minimize the free energy and to reach

the equilibrium, only one route is available: an increase in the entropy. The existence of the order-disorder transition in the athermal system implies that the system becomes more ordered by increasing the entropy, challenging our common notion about entropy. With a more careful look, however, it is easy to realize that, in fact, the ordered phase has an entropy larger than the disordered one. The entropy is dependent on the free volume of each molecule and in the ordered-solid phase the molecules are packed with high density, leaving, on average, more free space than in the disordered-fluid phase.

The entropy-driven process is one route to understand the self-assembly of complex structures in soft-condensate matter, making the study of athermal systems of great importance. Here, we will be interested in the study of athermal hard-sphere (or disks) models on regular lattices. Particularly, in the so-called kNN models, where the particles exclude up to their kth-nearest-neighbor of being occupied. The kNN models present interesting critical phenomena properties, for example, the nature of the phase transition depends on the geometry of the lattice considered. The particles assume different shapes in each geometry, changing how the translational symmetry is broken in the fluid-ordered transition. For example, in the 1NN model on the square lattice, the ordering can occur in two different ways, as shows Fig. 1.8, either in sub-lattices A or B being more occupied. A continuous fluid-solid transition is observed in this system with exponents of the 2D Ising universality class [2]. In opposition, the 1NN model on the triangular lattice, exactly solved by Baxter [66, 67], presents an ordering in one of three sub-lattices, A, B and C. As in the square lattice, a continuous order-disorder transition is observed, however, due to the different symmetry of the solid phase, the exponents are those of the 3-state Potts model. Several kNN models have already been studied [70] in the square lattice and, in most of the cases, the phase transition was properly characterized by a well-defined set of exponents. The case with most divergence is the 2NN model on the square lattice.

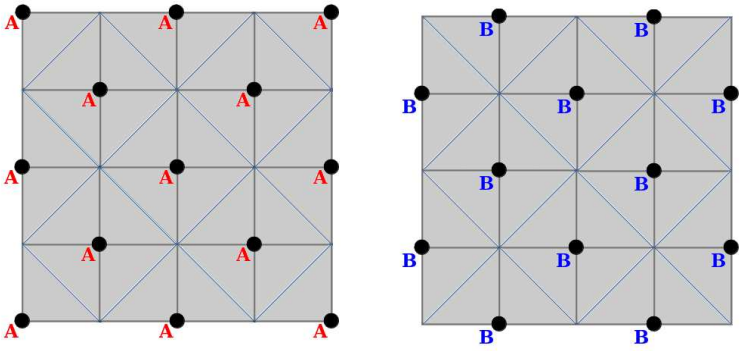

Figure 1.8: On the left the ground state of the 1NN lattice gas model with the sub-lattice A being populated. On the right the ground state with the sub-lattice B being the most populated for the 1NN lattice gas model.

The 2NN model on the square lattice presents an ordering in four sub-lattices, as shown in Fig. 1.9. Differently of the 1NN model, where one of the sub-latices is more occupied forming the solid phase, in the 2NN model the four sub-lattice structure allows the appearing of columnar phase, where the system become ordered along horizontal or vertical columns, with a freedom of sliding between columns (see Fig. 1.9. The presence of this columnar phase seems to make the characterization of the fluid-columnar transition more difficult. Some works report a critical fluid-columnar phase transition [70–72], while others claim a first-order [73] or even no phase transition [74]. Between the works who

[2] A detailed revision of this model is presented in Chap. 4.

claim a critical phase transition it is not clear what universality class the model 2NN belongs, some authors claim to be the 2D Ising class, while others claim to be the Ashkin-Teller, or Baxter model class [71, 72].

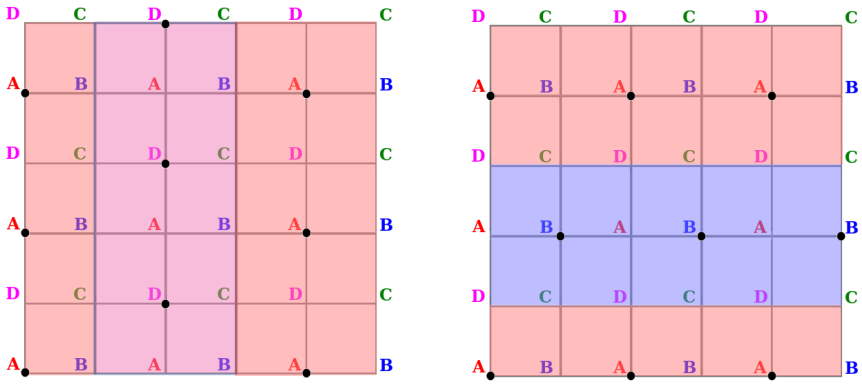

Figure 1.9: On the left the vertical columnar ordering in the sub-lattices A and D. On the right the horizontal columnar ordering in the sub-lattices A and B. Similar configurations can happens to B and C (vertical) and C and D (horizontal).

To shed some light on this debate in the Chap. 4 we study the 1NN and the 2NN model on the square lattice. To identify the order of the phase transition, if exist, and determine the exponents we tackle the problem by employing a semi-analytical solution of the model for Husimi lattices of high order [3]. When solving models in the Husimi lattice the correlation between sites is usually weaker than in the regular lattice due to the hierarchical nature of the lattice. In a Husimi lattice build with squares each generation has a single square, by increasing the number of squares in each generation, the level of the lattice, more correlation is introduced making a better approximation of the square lattice. However, at any level of the Husimi lattice the critical exponents are always the mean-field ones. To determine the non-classical exponents of the model, we use the coherent anomaly method [104] which gives a way of extracting the true exponents of the model from a succession of improved mean-field approximations. We have managed to found the critical parameters for the 1NN model with great accuracy differing less than 0.1% of the more precise values reported. For the 2NN we have found a critical fluid-columnar transition with critical parameters close of those previous reported [70, 71]. However, the application of the coherent anomaly method gives unreliable values for the 1NN and for the 2NN model.

Along with the pure lattice gas 2NN model we have also explored the problem of mixtures of kNN particles. When considering mixtures the thermodynamic behavior is much richer, and the entropy-driven process creates very interesting phenomena, an important one is the depletion force. Let's consider an athermal system composed by small particles and large ones, at the same volume fraction there will be more small particles than the large ones, then, the entropy is largely dominated by the small particles with large ones behaving to maximize the entropy of the small. In order to maximize the entropy, the small and large particles are driven to a configuration in which the excluded volume created by the large ones is the smallest possible. So, the configuration where the large particles are far apart is avoided and the equilibrium is reached by making the large particles closer to each other. Despite the only interaction being the hard-core repulsion,

[3] An more detailed explanation about the Husimi and the high-order Husimi lattice can be found in the Appendix. B.

the system behaves as if an attractive interaction, induced by the entropy, exists between the large particles. Such force is called the depletion force, which is of great importance in colloids, emulsions and in biological systems [75, 76].

Despite the clear importance in the study of mixtures, only a few works on the literature approached the problem of kNN mixtures with, as far as we know, only in two-dimensional lattices [11, 77–80]. The lack of studies of kNN mixtures on the cubic lattice motivated us to explore three different types of binary mixtures, 0NN-1NN, 0NN-2NN and 1NN-2NN. All mixtures are presented on Chap . 3. Initially we present the problem of the 0NN with 2NN particle followed by the problem of the binary mixtures 0NN-1NN and 1NN-2NN, both in the form of the published papers. For all three mixtures, we employed a mean-field approximation for the cubic lattice with a semi-analytical solution of the models in a Husimi lattice build with cubes (see Appendix. B. As mentioned above, despite the approximation with Husimi lattices be a mean-field one, due to the presence of weakened correlation, the approximation usually gives qualitatively correct results with even quantitative concordance in some cases [82]. The same method is also used to tackle the more physically challenging problem of a ternary mixture of 0NN-1NN-2NN particles. The ternary mixture problem is the last paper presented in Chap. 3.

Chapter 2

Adsorption and collapse of self-avoiding trails in two dimensions

In this chapter we present the results obtained for the self-avoiding trail model with bulk and surface interaction. We initiate presenting the published version [43] of the model on the square lattice where we explore the universality of the surface exponents. Next, we present the published version [44] of the trail model on the triangular lattice with the characterisation of the thermodynamic behavior by obtaining the 3D phase diagram of the model.

Editors' Suggestion

Adsorption of interacting self-avoiding trails in two dimensions

N. T. Rodrigues,[1,2,*] T. Prellberg,[2,†] and A. L. Owczarek[3,‡]

[1]*Departamento de Física, Universidade Federal de Viçosa, 36570-900 Viçosa, MG, Brazil*

[2]*School of Mathematical Sciences, Queen Mary University of London, Mile End Road, London E1 4NS, England, United Kingdom*

[3]*School of Mathematics and Statistics, University of Melbourne, Victoria 3010, Australia*

(Received 26 April 2019; published 15 August 2019)

We investigate the surface adsorption transition of interacting self-avoiding square lattice trails onto a straight boundary line. The character of this adsorption transition depends on the strength of the bulk interaction, which induces a collapse transition of the trails from a swollen to a collapsed phase, separated by a critical state. If the trail is in the critical state, the universality class of the adsorption transition changes; this is known as the special adsorption point. Using flatPERM, a stochastic growth Monte Carlo algorithm, we simulate the adsorption of self-avoiding interacting trails on the square lattice using three different boundary scenarios which differ with respect to the orientation of the boundary and the type of surface interaction. We confirm the expected phase diagram, showing swollen, collapsed, and adsorbed phases in all three scenarios, and confirm universality of the normal adsorption transition at low values of the bulk interaction strength. Intriguingly, we cannot confirm universality of the special adsorption transition. We find different values for the exponents; the most likely explanation is that this is due to the presence of strong corrections to scaling at this point.

DOI: 10.1103/PhysRevE.100.022121

I. INTRODUCTION

When a polymer in solution is in contact with an attractive surface, it adsorbs upon decreasing temperature [1–10]. In the presence of attractive bulk interactions, a polymer collapses from a swollen coil to a collapsed globule [11,12]. Additionally, a polymer can also undergo a collapse transition when adsorbed on a two-dimensional surface. To complicate matters, introduction of stiffness can give rise to a collapsed crystalline phase [13], giving rise to a complex phase diagram.

It hence is helpful to consider the simpler scenario of two-dimensional flexible interacting polymers adsorbing onto a line, where we find a two-dimensional phase diagram with three phases: swollen coil, collapsed globule, and adsorbed polymer [14]. The canonical lattice model for this is given by self-avoiding walks on the square lattice tethered to a point on the surface, with energetic contributions from the number of nonconsecutive nearest-neighbor sites of the walk (bulk interactions) and the number of sites of the walk in the surface (surface interactions). This model has been extensively studied previously, and theoretically predicted critical exponents have been confirmed numerically with high accuracy [15].

Recently, there has been renewed interest in the polymer adsorption transition. In [10,16], it was argued based on numerical simulations in three dimensions that the generally accepted scaling theory for polymer adsorption in terms of a single crossover exponent may break down in the presence of bulk interactions. Specifically, it was claimed that the exponent involved in the temperature scaling of the free energy around the adsorption critical point is distinct from the exponent describing the scaling of the order parameter at this critical point, and moreover that these two exponents are not universal with respect to varying the strength of the bulk interactions.

Thus, there was need to examine the adsorption transition more carefully in a variety of two- and three-dimensional models [17,18], in order to test both the universality assumption as well as the validity of the numerical methods used to estimate the scaling exponents. The main conclusion of that work was that existing methods for extracting critical exponents for the adsorption transition from numerical data do not seem to be able to capture the effect of finite-size corrections. Different methods produced different exponent estimates with statistical errors much smaller than the difference between the estimates, and there also was no clear indication as to which method was most reliable. It therefore seemed likely that any apparent nonuniversal behavior was due to the fact that the methods used could not account sufficiently well for systematic error.

One of the models studied in [17] was the model of self-avoiding trails (SATs) on the square and simple cubic lattice, weighted by the number of sites in the surface. Trails are lattice paths which may repeatedly visit sites but traverse bonds only once. If one associates a contact interaction to every multiply visited lattice site, then one can view self-avoiding walks as self-avoiding trails with infinite repulsion. It is known that self-avoiding trails and self-avoiding walks on the square lattice are in the same universality class, with subtle differences in the corrections to scaling [19]. Interacting self-avoiding trails on the square lattice undergo a collapse transition, which, however, is not in the same universality class as the collapse transition of interacting self-avoiding walks [20,21].

*nathan.rodrigues@ufv.br

†t.prellberg@qmul.ac.uk

‡owczarek@unimelb.edu.au

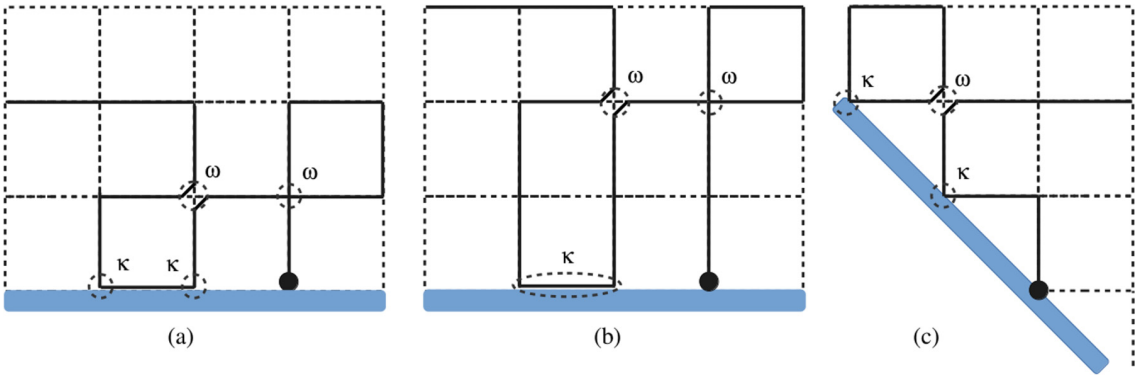

FIG. 1. Examples of trails for the three cases of surface interaction studied. The trail starts at the solid circle in the surface. Bulk and surface interactions are indicated by dashed circles and are denoted by ω and κ, respectively. Panel (a) shows monomer-surface interactions in a horizontal surface, panel (b) shows bond-surface interactions in a horizontal surface, and panel (c) shows monomer-surface interactions in a diagonal surface. Note that the starting point does not contribute for the surface energy.

In the current paper we extend previous studies by considering the adsorption transition for interacting self-avoiding trails on the square lattice. We analyze the adsorption transition in the presence of bulk interactions of varying strength. In addition to the normal adsorption transition from the swollen to the adsorbed phase, we also study the special surface transition occurring when collapsing polymers adsorb. The value of the bulk interaction at which interacting self-avoiding trails on the square lattice collapse is exactly known, as is the free energy at this point [20], which is a major advantage of studying this model in contrast to interacting self-avoiding walks, where only a numerical estimate of the collapse transition point is available.

The temperature of the adsorption transition is sensitive to the orientation of the boundary and type of boundary interaction, but the same universal critical exponents are expected. However, previous works [20,22] which have considered different surface interactions are in disagreement about the value of the exponents for the special transition. Alternatively to considering the number of sites of a trail in the surface [17], one can consider the number of bonds of a trail in the surface [22]. Also, while conventionally a horizontal surface is considered, for interacting self-avoiding trails at the collapse point it is advantageous to consider weighting the number of sites along a diagonal line, as in this case the value of the surface interaction at which collapsing trails adsorb is exactly known [20]. We hence investigate normal and special adsorption for all three scenarios: a horizontal boundary with either site or bond interactions, and a diagonal boundary with site interactions.

The paper is structured as follows. In Sec. II we define the lattice model we investigate, and introduce relevant thermodynamic quantities. In Sec. III we review scaling laws and critical exponents, and describe the methods by which we extract exponents from numerical data. In Sec. IV we describe the simulation methods used in this paper, and Sec. V describes our findings in detail.

II. THE MODEL

A SAT is a finite lattice path on a regular lattice in which every bond may only be traversed once. We identify the monomers of a polymer with the site visits of the path, and allow for more than one monomer on a site. In this paper we are interested in the adsorption and collapse transition in the SAT model on the square lattice. To achieve this we need to introduce two types of interaction: a bulk interaction ϵ_b between doubly visited sites (i.e., monomers on the same site), and a surface interaction ϵ_s for a monomer (or bond) lying in the surface, which we take to be the boundary of a half plane. We fix the boundary to contain the origin and consider trails starting at the origin, i.e., on the boundary.

We consider two ways to define the interaction between a trail and the surface, given by either the monomers or the bonds of the lattice path in the surface. We shall denote this the monomer-surface (MS) or bond-surface (BS) case. Examples of this are shown in Figs. 1(a) and 1(b), respectively, where the surface is aligned with one of the lattice directions. When the surface is not aligned, then bonds cannot lie in the surface, and it only makes sense to consider the monomer-surface case. An example of a diagonal surface (DS) oriented at 45° is shown in Fig. 1(c).

The canonical (fixed length) partition function for adsorbing and interacting trails is given by

$$Z_n(\kappa,\omega) = \sum_{m_s,m_b} C^{(n)}_{m_s,m_b} \kappa^{m_s} \omega^{m_b}, \tag{1}$$

where $\kappa = e^{\beta\epsilon_s}$, $\omega = e^{\beta\epsilon_b}$, and $C^{(n)}_{m_s,m_b}$ is the number of n-step lattice paths with m_s surface contacts and m_b doubly visited sites, and $\beta = 1/k_BT$ with T the temperature. The reduced finite-size free energy is

$$f_n(\kappa,\omega) = -\frac{1}{n}\log Z_n(\kappa,\omega), \tag{2}$$

which in the thermodynamic limit gives

$$f_\infty(\kappa,\omega) = \lim_{n\to\infty} f_n(\kappa,\omega). \tag{3}$$

Any general thermodynamic quantity Q gives rise to averages

$$\langle Q\rangle(\kappa,\omega) = \frac{1}{Z_n(\kappa,\omega)} \sum_{\psi_n} \kappa^{m_s(\psi_n)} \omega^{m_b(\psi_n)} Q(\psi_n), \tag{4}$$

where the sum ranges over all n-step lattice trails ψ_n. In particular, we are interested in the surface internal energy:

$$u_n(\kappa, \omega) = \frac{\langle m_s \rangle}{n}. \tag{5}$$

As this can be interpreted as the fraction of the trail that is adsorbed in the surface, it is an order parameter for the surface adsorption transition.

We also consider the components of the mean-squared end-to-end radius R_n^2 parallel and perpendicular to the surface. For a horizontal surface these are defined as

$$R^2_{\perp,n}(\kappa, \omega) = \langle x_n^2 \rangle, \tag{6}$$

$$R^2_{\parallel,n}(\kappa, \omega) = \langle y_n^2 \rangle, \tag{7}$$

with the end point of the trail being at (x_n, y_n), whereas for a diagonal surface they are defined as

$$R^2_{\perp,n}(\kappa, \omega) = \tfrac{1}{2}\langle (x_n + y_n)^2 \rangle, \tag{8}$$

$$R^2_{\parallel,n}(\kappa, \omega) = \tfrac{1}{2}\langle (x_n - y_n)^2 \rangle. \tag{9}$$

III. SCALING LAWS AND CRITICAL EXPONENTS

The surface internal energy u_n is the order parameter of the adsorption transition. For long lengths at the critical point u_n scales as $u_n \sim n^{\phi^{(a)}-1}$. For finite lengths, finite-size corrections need to be included:

$$u_n \sim n^{\phi^{(a)}-1} f_u^{(0)}(X)\big[1 + n^{-\Delta} f_u^{(1)}(X) + \cdots\big], \tag{10}$$

where $f_u^{(i)}$ are scaling functions of the variable $X = (T_a - T)n^{1/\delta}$ and Δ is the first correction term.

As a consequence, for a fixed value of X (i.e., near a critical transition), this induces a relationship between T and n and therefore we can infer a dependence of the finite-size transition temperature $T_a^{(n)}$ of the form

$$T_a^{(n)} \sim T_a + \text{const}\, n^{-1/\delta}, \tag{11}$$

and hence $1/\delta$ is identified as the crossover exponent for the adsorption transition. Both critical exponents $\phi^{(a)}$ and $1/\delta$ are believed to be universal and equal to each other [17]. For the normal surface transition in two dimensions it is expected that $\phi^{(a)} = 1/\delta = 1/2$.

In what follows, we need to modify our notion of temperature to take into account *only* the surface interactions, and not the bulk interactions. We accomplish this by formally introducing two temperature variables by writing $\kappa = e^{\beta\epsilon_s} = e^{1/T_s}$ and $\omega = e^{\beta\epsilon_b} = e^{1/T_b}$. For the adsorption transition, we fix T_b and in a slight abuse of notation identify T with T_s. We can then measure $1/\delta$ independently of $\phi^{(a)}$ by calculating the logarithmic derivative of u_n:

$$\Gamma_n = \frac{d \log u_n}{dT_s} = (\log \kappa)^2 \frac{\langle m_s^2 \rangle - \langle m_s \rangle^2}{\langle m_s \rangle}. \tag{12}$$

Γ_n is related to a second derivative of the free energy, therefore the peaks of Γ_n have the following scaling form:

$$\max \Gamma_n \sim n^{1/\delta} f_\Gamma^{(0)}(X)\big[1 + n^{-\Delta} f_\Gamma^{(1)}(X) + \cdots\big]. \tag{13}$$

Using the dependence of $\max \Gamma_n$ we can therefore determinate the adsorption transition temperature and the exponent $1/\delta$.

Another way to determine the adsorption point is using metric quantities. Using the scaling behavior of the parallel and the perpendicular components $R^2_{\perp/\parallel,n}$ with respect to the surface,

$$R^2_{\perp/\parallel,n} \sim n^{2\nu_{\perp/\parallel}}, \tag{14}$$

where $\nu_{\perp/\parallel}$ is the respective Flory exponent, we can calculate finite-size estimates of these exponents simply by using Eq. (14):

$$\nu_{\perp/\parallel,n} = \frac{1}{2\log 2} \log\left(\frac{R^2_{\perp/\parallel,n}}{R^2_{\perp/\parallel,n/2}}\right). \tag{15}$$

In the desorbed phase both components have the same value in the thermodynamic limit. For an adsorbed configuration the polymer becomes a quasi-one-dimensional system and $\nu_\perp \to 0$ while $\nu_\parallel \to 1$. For some intermediate temperature the components of ν cross, and using these crossing points we can locate the finite-size temperatures of adsorption $T_a^{(n)}$.

Similarly, we can use the asymptotic scaling of R_n^2 to determine and locate the collapse transition point as ω changes in the desorbed regime, i.e., for small values of κ. At high temperatures ν assumes the Flory value of $\nu = 3/4$ for the swollen phase, and for low temperatures the value of $\nu = 1/2$ for the collapsed phase. At the collapse point a transition occurs and the exponent ν assumes a different value. In the literature one can find $\nu = 12/23$ [21] and also $\nu = 1/2$ with the presence of logarithmic corrections [20] (this is different from interacting self-avoiding walks, where the value $\nu_\theta = 4/7$ is well established [23]). We can estimate the finite-size collapse temperature and the corresponding exponent ν by locating the crossing point in $\nu_n(\omega)$ curves for different lengths. Note that, while for the adsorption transition we considered the crossing of exponent estimates from two different components at the same length, here we consider the crossing of exponent estimates of different lengths.

While for the adsorption transition we use Γ_n to find the crossover exponent, in the collapse transition the quantity of interest is the bulk specific heat per monomer:

$$c_n(T_b) = \frac{(\log w)^2}{n}\big(\langle m_b^2 \rangle - \langle m_b \rangle^2\big). \tag{16}$$

Around the collapse temperature a tricritical crossover scaling form is expected. Assuming that in the thermodynamic limit the specific heat diverges as $c(T_b) \sim |T_b - T^{(c)}|^{-\alpha}$, and assuming that the tricritical scaling relation

$$2 - \alpha = \frac{1}{\phi^{(c)}} \tag{17}$$

holds, the finite-size specific heat $c_n(T_b)$ has the following scaling:

$$c_n(T_b) \sim n^{2\phi^{(c)}-1} f_c^{(0)}(Y)\big[1 + n^{-\Delta} f_c^{(1)}(Y) + \cdots\big], \tag{18}$$

where $Y = (T_b - T^{(c)})n^{\phi^{(c)}}$. The exponent $\phi^{(c)}$ is the crossover exponent for the collapse transition.

IV. NUMERICAL SIMULATIONS

We sample trail configurations using the flatPERM algorithm [24]. This method is an extension of the pruned-enriched Rosenbluth method (PERM) [25]. Both PERM and flatPERM are stochastic growth algorithms based on the Rosenbluth method; the addition of pruning and enrichment allows one to overcome attrition and to efficiently sample large configurations. PERM gives an estimate of the partition function Z_n for a specific temperature while flatPERM samples a flat histogram giving a good estimate of the density of states, i.e., the number of configurations $C^{(n)}_{m_s,m_b}$.

We perform simulations for three different scenarios, (a) a horizontal boundary with MS interactions, (b) a horizontal boundary with BS interactions, and (c) a DS with monomer-surface interactions. In all three scenarios we first run a two-parameter flatPERM simulation. In this case the algorithm samples a flat histogram in both m_s and m_b (as well as n up to a maximal length) and estimates the full density of states at these lengths, allowing us to construct a finite-size approximation to the phase diagram.

The two-parameter flatPERM simulation produces a two-dimensional density of states, and it is necessary to generate sufficiently many samples for each box of the histogram. Therefore this is only feasible for relatively short lengths. For all three scenarios we perform a two-parameter flatPERM simulation for trails with up to 128 steps with 10^{10} trails reaching the maximum length. From these simulations we can then determine the different phases and the approximate location of phase boundaries.

To determine more precisely the location of and the behavior around the phase boundaries we perform one-parameter flatPERM simulations for fixed values of ω or κ and generating a one-dimensional density of states for m_s or m_b, respectively. This allows for a more detailed analysis in specific regions of the phase diagram. As we only need to generate a one-dimensional density of states, we can perform simulations for longer lengths than for the two-parameter flatPERM simulations. We can generate trails with up to 1024 steps with 10^{10} trails reaching the maximum length for a wide range of ω and κ.

As we want to pay particular attention to the normal and the special surface transitions, we also perform PERM (i.e., zero-parameter flatPERM) simulations for all three scenarios, as this allows us to perform simulations for much larger lengths. We generate trails with length up to 10 240 steps with an average sample of 5×10^8 trails at maximum length for a set of fixed values of ω and κ. At these large lengths the finite-size corrections to scaling are significantly smaller than at shorter lengths, which allows for a more reliable estimate of the adsorption exponents for both ordinary and special surface transitions.

V. RESULTS

For all three scenarios we first generate a finite-size approximation to the phase diagram. Transition regions between different phases are characterized by large fluctuations in the number of bulk and surface interactions m_b and m_s. To identify the regions of maximal fluctuations, it is advantageous to consider the covariance matrix:

$$\begin{bmatrix} \langle m_s^2 \rangle - \langle m_s \rangle^2 & \langle m_s m_b \rangle - \langle m_s \rangle \langle m_b \rangle \\ \langle m_s m_b \rangle - \langle m_s \rangle \langle m_b \rangle & \langle m_b^2 \rangle - \langle m_b \rangle^2 \end{bmatrix}. \tag{19}$$

The covariance matrix is positive semidefinite and its leading eigenvalue is the greatest variance, with the corresponding eigenvector representing the linear combination (in this case of m_s and m_b) that gives rise to this variance. We produce finite-size fluctuation maps by plotting the logarithm of this eigenvalue as a function of ω and κ for trails with $n = 128$ steps.

In Fig. 2 the logarithm of the largest eigenvalue is shown in a density plot as a function of ω and κ. As expected, in each scenario we find three phases, which by considering averages of m_s and m_b we identify with the coil, collapsed, and adsorbed states of the trail.

Qualitatively, the phase diagrams in the three scenarios are similar, and we therefore only discuss the MS case in detail, which is shown in Fig. 2(a). For small values of ω and κ we find configurations dominated by a small number m_s of surface contacts and a small number m_b of double visited sites. We therefore conclude that this region can be identified with the swollen coil phase.

When increasing ω while keeping κ constant at a small value ($\kappa \lesssim 2$) the number of double visited sites increases through the region $2 < \omega < 5$ and gets saturated for large ω, where the trail configurations are dominated by a large number m_b of double visited sites, which is a characteristic of the collapsed phase in this model. We therefore conclude that there is a collapse transition, which for short trail lengths is smoothed out over a wide range.

For small values of κ, the average number m_s of surface contacts is small, and the trail remains desorbed, but for large values of κ we find an adsorbed phase characterized by trail configurations with a large number m_s of surface contacts. This phase exists for all values of ω, and we therefore have a transition between the desorbed and adsorbed regime. The transition between the desorbed phases and the adsorbed one can occur in three different ways.

For small values of ω there is a weak transition between the swollen coil and the adsorbed phase which is known as the "normal surface transition," and for large values of ω there is a strong transition between the collapsed and the adsorbed phase. For the latter transition we find a bimodal density of states which is indicative of a first-order transition. Between these two different transitions we expect to see another adsorption transition when increasing κ along the line of critical collapse. This transition is known as the "special surface transition." It occurs at a multicritical point at which three transition lines meet: the normal surface and the coil-collapsed and collapsed-adsorbed lines.

In order to estimate the location of the transitions and the associated critical exponents we simulate configurations of longer lengths by fixing either ω or κ, and use the following procedure for the analysis of the data. For the adsorption transition we choose a fixed value of ω and find the maximum point $(\kappa_n, \max \Gamma_n)$ as a function of n, shown as small circles in Fig. 3(a). We then use the asymptotic behavior of Eq. (13) to find the value of the exponent $1/\delta_n$. By extrapolating these

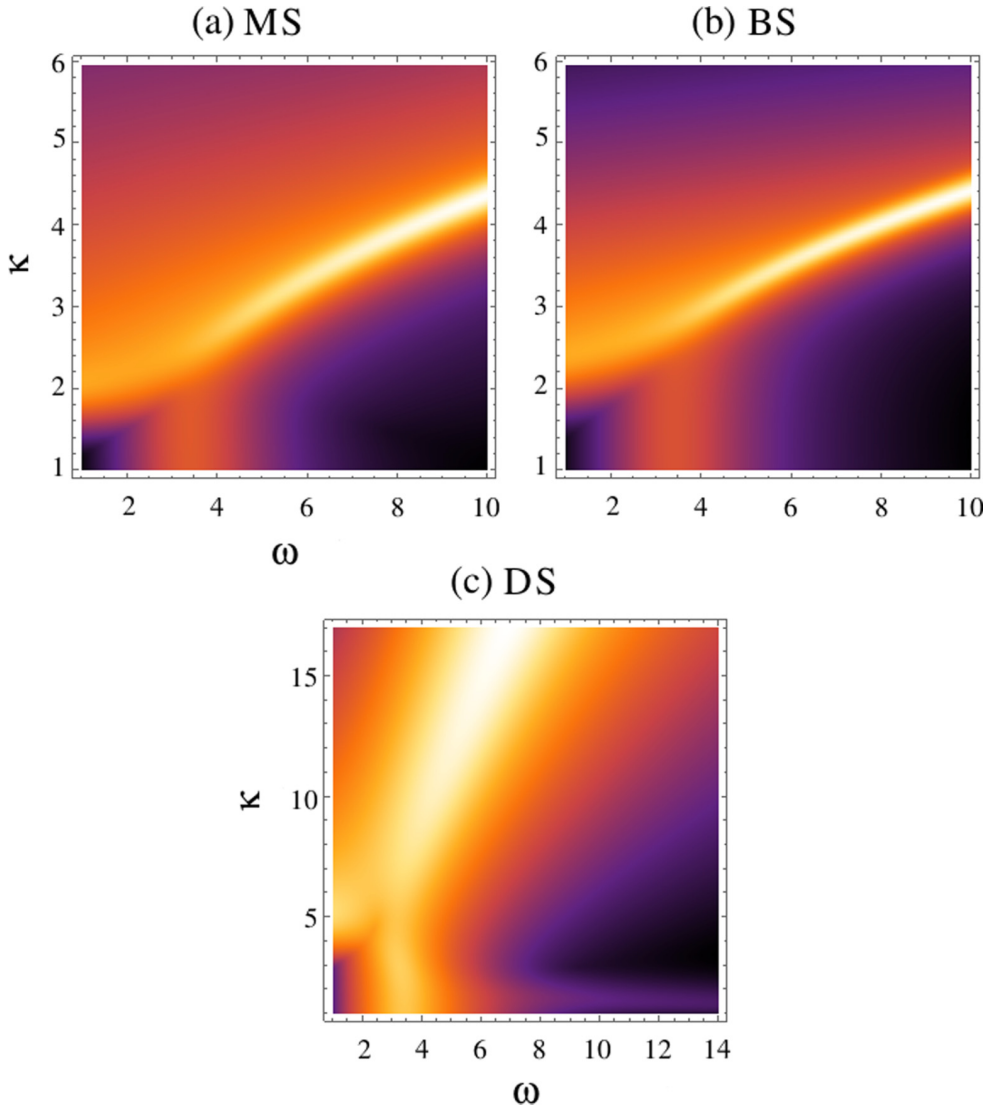

FIG. 2. Finite-size fluctuation map for 128-step trails for the three boundary cases MS, BS, and DS. Darker colors represent regions of small fluctuations, while brighter colors (yellow and orange) represent regions with strong fluctuations.

values to large n we then estimate the final value of $1/\delta$. As shown in [17,18], a good way to estimate the adsorption point is to find the crossing points of the parallel and the perpendicular length scale exponents $\nu_{\perp/\parallel,n}$ [Fig. 3(b)]. Finding these points and using the scaling of Eq. (11) and the value of $1/\delta$ previously estimated, we locate the transition point $(\omega^{(a)}, \kappa^{(a)})$. Knowing this adsorption point, we then calculate the average number of surface contacts $\langle m_s \rangle$ [Fig. 3(c)] at $(\omega^{(a)}, \kappa^{(a)})$ as a function of n. As expected, $\langle m_s \rangle$ grows linearly in the adsorbed regime and tends to a constant in the desorbed regime, while following a distinct power law growth with an exponent around 0.5 at the adsorption transition. Similarly to our method of estimating $1/\delta$ we use Eqs. (5) and (10) to find the finite-size values of $\phi_n^{(a)}$ and then we extrapolate these values to estimate the value of $\phi^{(a)}$.

To characterize the collapse transition for a fixed value of κ we first calculate the bulk specific heat per monomer [Eq. (16)] as a function of ω. By looking at the maxima [Fig. 3(d)] and using Eq. (18) we estimate the exponent $\phi^{(c)}$. To locate the collapse transition point we proceed similar to the adsorption transition, but we consider crossing points $(\omega_n^{(c)}, \nu_n^{(c)})$ of the graphs of ν_n as a function of ω for two lengths n and $n + \Delta n$. Using the value of $\phi^{(c)}$ we estimate $\omega^{(c)}$ by extrapolating from finite-size estimates $\omega_n^{(c)}$.

In the asymptotic estimation of the exponents above we assume that the finite-size estimate η_n of an exponent η asymptotically satisfies the ansatz:

$$\eta_n = \eta_\infty + \text{const}\, n^{-0.5} + \ldots . \tag{20}$$

In most cases, this ansatz appears to fit our data reasonably well, and changing the power in the correction-to-scaling term slightly does not seem to affect our results.

For the MS case we applied this procedure to the results of the one-parameter flatPERM simulation for trails with up to 1024 steps in the range of $1 \leqslant \kappa \lesssim 3.5$ and $1 \leqslant \omega \leqslant 5$. In Fig. 4 the phase diagram for the MS case is shown.

On the square lattice, the collapse transition for trails is expected to occur at $\omega^{(c)} = 3$ [20]. At this value, the

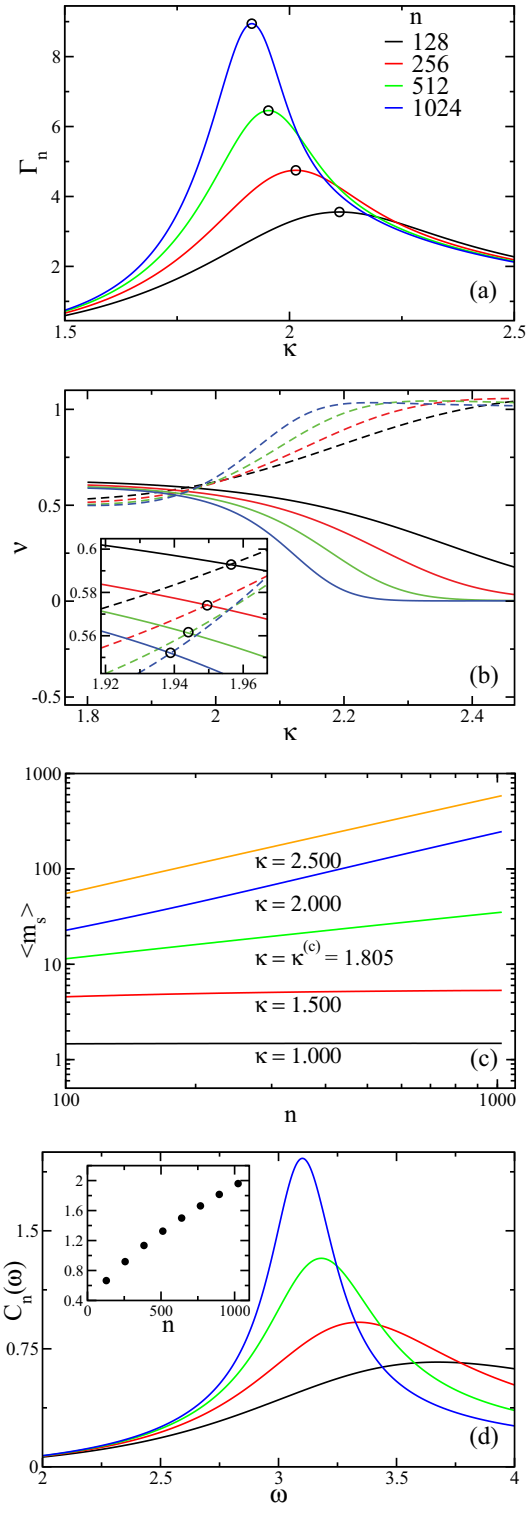

FIG. 3. (a) Graphs of Γ_n as a function of κ for $\omega = 2$. The black circles denote the maximum points $(\kappa_n, \max \Gamma_n)$ of the Γ_n curves. (b) Graphs of the length scale exponents $\nu_{\perp,n}$ (solid line) and $\nu_{\parallel,n}$ (dashed line) as a function of κ for $w = 3$. The inset shows the crossing points (black circles) of these exponents. (c) The average number of contacts $\langle m_s \rangle$ as a function of n for $\omega = 1$ for five different values of κ. (d) The bulk specific heat per monomer for $\kappa = 1$. The inset shows the location of the maximum values of the bulk specific heat as a function of the length n.

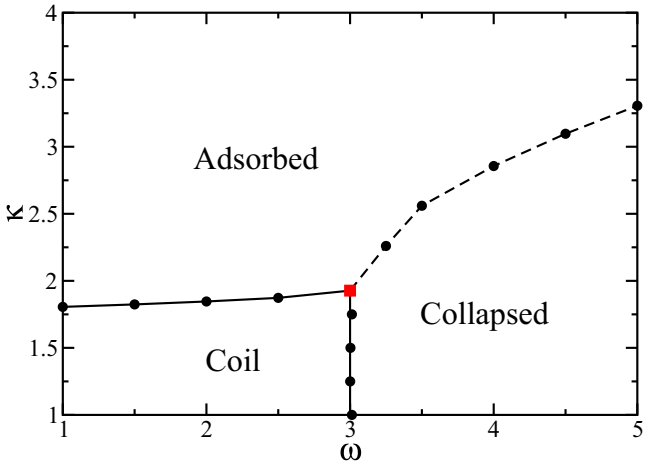

FIG. 4. The phase diagram for the MS case. The red square is the location of a multicritical point where the special surface transition occurs. The solid lines are critical transitions, i.e., the coil-collapsed transition and the normal surface transition. The dashed line is the coexistence line of the collapsed-adsorbed transition.

probabilities of a stochastic growth process are perfectly balanced by the Boltzmann weight $\omega^{(c)}$. This has also been confirmed numerically [21,22], where a value of 3.000(1) was found. The presence of a weakly interacting surface is not expected to have any effect on the location of this transition. This is because desorbed trails have $o(n)$ contacts with the surface, so that the free energy of desorbed trails is expected to be independent of the strength of the surface attraction. Upon increasing the strength of the surface interaction κ, the collapse transition remains therefore at $\omega^{(c)} = 3$ until a multicritical point is reached at $\kappa = \kappa^{(s)}$, where the special surface transition takes place. Our simulation of interacting trails in the presence of a noninteracting surface (i.e., $\kappa = 1$) gives a value of $\omega^{(c)} = 3.013(10)$ for the MS case, and values very close to 3 were also found for the BS and the DS cases. We further confirm that the location of the collapse transition does not change upon increasing κ, as shown in Fig. 4.

Together with estimating the location of the collapse transition, we also obtain estimates of the length-scale exponent $\nu^{(c)}$ at collapse, as well as the collapse crossover exponent $\phi^{(c)}$. On the line $\omega = \omega^{(c)}$ at the values of κ indicated in Fig. 4, we find $0.538 < \nu^{(c)} < 0.560$ and $\phi^{(c)}$ very close to 0.78. The values found for ν match well with finite-size estimates from the data presented in [20] at corresponding lengths when assuming simple power law scaling. They are not close to $\nu^{(c)} = 12/23$ reported in [21] or $\nu^{(c)} = 1/2$ found in [20], but rather indicative of strong finite-size corrections to scaling at the collapse transition. The value of the collapse crossover exponent $\phi^{(c)}$ is also not close to the expected $\phi^{(c)} \approx 0.88$ [20], but mirrors what was found for similar lengths in [26], again indicative of strong finite-size corrections.

We now turn to the discussion of the adsorption transition in the three regimes. For fixed $\omega > 3$, upon increasing κ we find a collapsed-adsorbed transition with a bimodal behavior in the density of states and an exponent α close to 1, which is a clear indication of a first-order transition. For $\omega \leqslant 3$ we observe a critical adsorption transition upon increasing κ. The

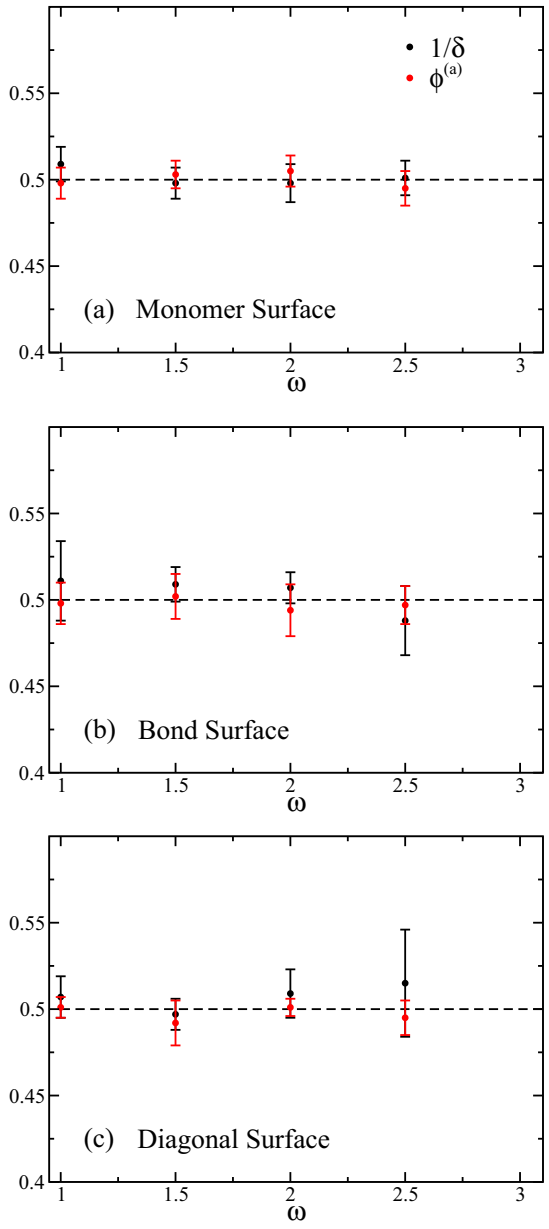

FIG. 5. Surface exponents as a function of the bulk interaction parameter ω for trails with up to 10 240 steps. The red circles are the values for the $\phi^{(a)}$ and the black circles are the values for $1/\delta$. The dashed line represents the expected value in two dimensions. (a) The MS case. (b) The BS case. (c) The DS boundary scenario.

value of κ at which adsorption occurs changes monotonically from 1.805(3) at $\omega = 1$ [17] to 1.924(2) at $\omega = 3$. For the normal surface transition ($\omega < 3$) the surface exponents $1/\delta$ and $\phi^{(a)}$ are expected to be equivalent and equal to $1/2$ in two dimensions. For the special surface transition at $\omega = 3$, however, a different value is expected. For the DS case, the value $\phi^{(s)} \approx 0.44$ was found previously in [20], and for the BS case values slightly lower were reported: $0.379 < \phi^{(s)} < 0.414$ [22].

By performing simulations with PERM for trails with up 10 240 steps we estimate the values of $1/\delta$ and $\phi^{(a)}$ for the normal and the special surface transition for all three boundary

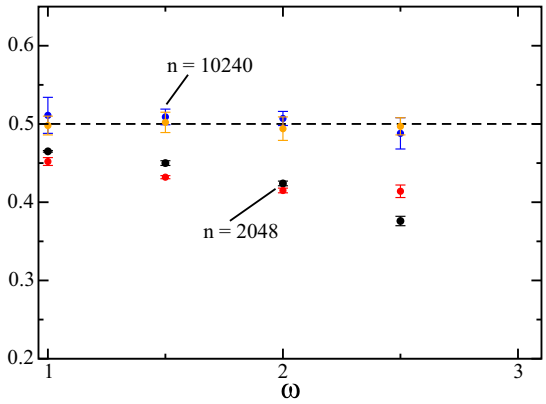

FIG. 6. Surface exponents $1/\delta$ and $\phi^{(a)}$ as a function of ω for the BS case for trails with 2048 and 10 240 steps. The black and red circles are the values of $1/\delta$ and $\phi^{(a)}$, respectively, for trails with 2048 steps (lower symbols), and the blue and orange circles are the values of $1/\delta$ and $\phi^{(a)}$, respectively, for trails with 10 240 steps (upper symbols).

scenarios. For the normal surface transition we investigate the four different values $\omega = 1.0$, 1.5, 2.0, and 2.5 in detail. In Fig. 5 our estimates of the surface exponents are shown as a function of ω. In all cases our estimates satisfy $1/\delta = \phi^{(a)}$ within error bars, and also agree with the expected value $\phi = 1/2$ in two dimensions. We conclude that the normal surface transition shows universal behavior as expected: the standard scaling hypothesis predicting $1/\delta = \phi^{(a)} = 1/2$ is correct in the presence of attractive bulk interactions and different surface boundary conditions.

At this point we note that we find strong corrections to scaling in the estimation of these exponents. Figure 6 shows surface exponent estimates obtained for trails with 2048 and 10 240 steps for the BS case. While the exponent estimates appear converged to the expected value of $1/2$ for the longer trails, there is a clear deviation for estimates from the shorter trails. Importantly, error bars at shorter lengths are misleading and would seem to support claims of nonuniversality. Similar deviations are evident for the other two cases.

In the remainder of this section we discuss the special surface transition in detail. As established above, the special transition occurs at $\omega = 3$ in all three scenarios, albeit at different values of $\kappa^{(s)}$. From an analysis of $R^2_{\perp/\parallel,n}$, we find $\kappa^{(s)}_{(\mathrm{MS})} = 1.924(2)$, $\kappa^{(s)}_{(\mathrm{BS})} = 2.442(4)$, and $\kappa^{(s)}_{(\mathrm{DS})} = 3.001(2)$. The latter value confirms the expected exact value $\kappa^{(s)}_{(\mathrm{DS})} = 3$; similar to the identification of $\omega^{(c)} = 3$, at this value the probabilities of a stochastic growth process are perfectly balanced by the Boltzmann weight $\kappa^{(s)}_{(\mathrm{DS})}$. There is no known exact value for the other two cases. The BS case has been investigated previously and a value $\kappa^{(s)}_{(\mathrm{BS})} = 2.45(5)$ was found [22]. We are not aware of any previous work regarding the value of $\kappa^{(s)}_{(\mathrm{MS})}$.

We note that our estimates satisfy $\kappa^{(s)}_{(\mathrm{MS})} < \kappa^{(s)}_{(\mathrm{BS})} < \kappa^{(s)}_{(\mathrm{DS})}$, which make sense heuristically due to the density of contacts in adsorbed configurations for each of the boundary scenarios.

While we have strong confirmation of universality for the normal adsorption transition, our findings do not support universality for the special transition. Intriguingly, we find

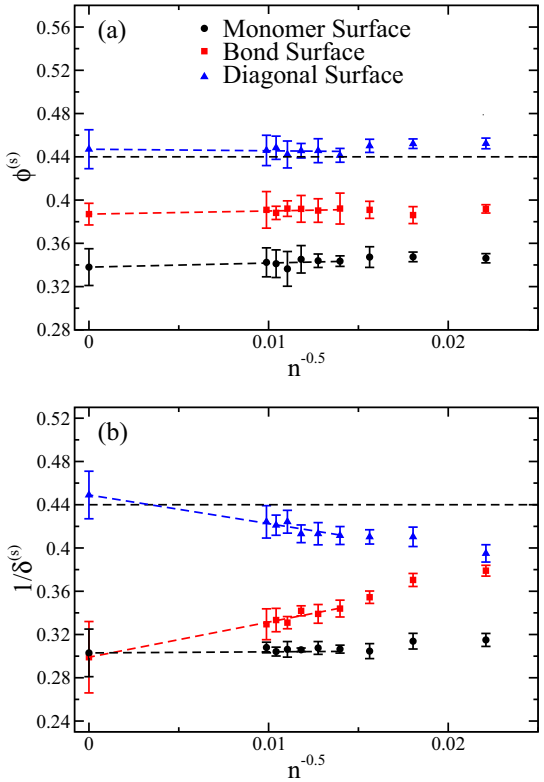

FIG. 7. (a) The surface exponent $\phi^{(s)}$ for different sizes as a function of $n^{-0.5}$ on the special surface point. Black circles are the values for the MS case, red squares are those for the BS case, and blue triangles are those for the DS case. The dashed black line is the expected value of 0.44. (b) Exponent $1/\delta^{(s)}$ as a function of $n^{-0.5}$ for the boundary scenarios.

different exponent values depending on the boundary studied. Figure 7 shows finite-size estimates of $\phi^{(s)}$ (panel a) and $1/\delta^{(s)}$ (panel b) for all three boundary scenarios. The estimates for $\phi^{(s)}$ seem to have no strong size dependence, and seem to converge to three distinct values in the thermodynamic limit. We estimate $\phi^{(s)}_{(\mathrm{MS})} = 0.338(17)$, $\phi^{(s)}_{(\mathrm{BS})} = 0.387(10)$, and $\phi^{(s)}_{(\mathrm{DS})} = 0.447(18)$, with the values for the DS and the BS cases being in a good agreement with those found in [20,22]. The estimates for $1/\delta^{(s)}$ show a stronger size dependence. We find $1/\delta^{(s)}_{(\mathrm{MS})} = 0.303(22)$, which is not too dissimilar from $\phi^{(s)}_{(\mathrm{MS})} = 0.338(17)$, and $1/\delta^{(s)}_{(\mathrm{DS})} = 0.449(22)$, which is in reasonable agreement with $\phi^{(s)}_{(\mathrm{DS})} = 0.447(18)$. We could thus be tempted to conclude that in both of these cases the equality $1/\delta^{(s)} = \phi^{(s)}$ holds, albeit with different exponent values. However, we also find $1/\delta^{(s)}_{(\mathrm{BS})} = 0.299(33)$, which does not support this equality. Our findings are summarized in Table I.

TABLE I. Values found for the surface exponents $1/\delta^{(s)}$ and $\phi^{(s)}$ for the boundary scenarios at the special surface transition point.

	Monomer surface	Bond surface	Diagonal surface
$\kappa^{(s)}$	1.924(2)	2.442(4)	3.001(2)
$\phi^{(s)}$	0.338(17)	0.387(10)	0.447(18)
$1/\delta^{(s)}$	0.303(22)	0.299(33)	0.449(22)

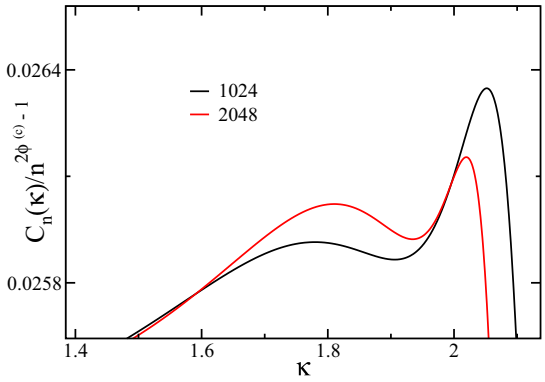

FIG. 8. Bulk specific heat per monomer normalized with $\phi \approx 0.78$ as a function of κ for $\omega = 3$ for the MS case. Two different sizes are shown, 1024 steps (black curve) and 2048 steps (lighter red curve).

These results do not support universality of the special surface exponents. Neither can we confirm $1/\delta^{(s)} = \phi^{(s)}$, nor does it seem that the exponent values are independent of the details of the boundary.

It is important to notice that the estimate of $\phi^{(s)}$ is highly dependent on the precise location of the adsorption point, but no such argument can be made for the method of estimating $1/\delta^{(s)}$. However, it is also important to highlight that the presence of strong finite-size corrections seriously affects exponent estimates for the ordinary surface transition, having recently led to claims of nonuniversality in the case of self-avoiding walks [10,16].

We also find evidence for strong finite-size corrections at the special point. When looking more closely at the line of critical collapse approaching the special adsorption transition, we find two peaks in the bulk specific heat near the special transition, as shown in Fig. 8 for the MS case. These two peaks were only found in the MS and the BS scenarios. This could be an indication of two neighboring phase transitions. These two peaks persist in the vicinity of $\omega = \omega^{(s)}$, however one of those peaks became weaker for longer lengths (2048), which indicates that instead of a second phase transition we are dealing with strong finite-size corrections. While we cannot see the weakening of one of those peaks (or merging of both peaks) near the special transition, we believe that this is likely to happen for longer trails. With trails with up to 10 240 steps it was not possible to resolve this question due to statistical errors of the simulations, and we suggest that simulations with even longer configurations have to be performed to understand the precise nature of these finite-size corrections and how they affect the estimates of the critical exponents.

VI. CONCLUSIONS

We performed simulations of the model of absorbing interacting self-avoiding trails on the square lattice using flatPERM, a uniform sampling stochastic growth algorithm. We used a two-parameter version of flatPERM to sample the density of states for trails with up 128 steps, and a one-parameter version of flatPERM to sample trails with up to 1024 steps, going up to 2048 steps for specifically chosen

values. We also performed PERM for trails with length up to 10 240 steps. Three different scenarios for the surface interaction were studied: MS interactions, BS interactions, and monomer interactions at a DS.

By analyzing the fluctuation map for these three scenarios we found similar phase diagrams with coil, collapsed, and adsorbed phases. In all three scenarios the coil-collapsed transition was found to occur at a constant line at $\omega = 3$. We also found evidence of a first-order transition between the collapsed phase and the adsorbed phase.

The main focus of this paper was the analysis of adsorption from the coil phase via the normal surface transition and of adsorption from the bulk-critical phase via the special surface transition.

We found for all three scenarios that the normal surface transition occurs along a critical line. The estimated values of the surface exponents $1/\delta$ and $\phi^{(a)}$ are both close to the expected value of $1/2$, showing that the normal surface transition is universal for trails and that the relation $\phi^{(a)} = 1/\delta$ holds for different solvent conditions and different types of boundary conditions. We point out that even for trails with 2048 steps strong finite-size corrections led to exponent estimates that indicated nonuniversality, and that we needed to simulate consider considerably longer trails to observe the actual exponent values.

These findings are relevant with regards to the recently claimed nonuniversality of the adsorption transition for polymers in the presence of bulk interactions [10,16]. This was based on simulations of relatively short self-avoiding walks of lengths up to 503 steps on the simple cubic lattice. A similar variability of exponent estimates was found for self-avoiding walks and trails in two and three dimensions for different lattices and varying interaction strengths [17,18]. In the latter works it was pointed out that different methods of analysis resulted in significantly different exponent estimates for configurations with steps up to length 1024, and that choosing any single method of estimation leads to exponent estimates with erroneously small error bars. The present paper indicates that increasing the size of the configurations by an order of magnitude is needed to go beyond finite-size correction terms which are seemingly not captured by any of the methods used in estimating the exponents.

When analyzing the special adsorption transition for $\omega = 3$, we found critical behavior in all three scenarios. One of the aims of the present paper was to investigate the discrepancy between the previously reported values of $\phi^{(s)}$ for the DS and BS cases. Our estimates, summarized in Table I, do not resolve this discrepancy. In addition, for the MS case we find yet another value of $\phi^{(s)}$. Moreover, our estimates of $1/\delta^{(s)}$ deviate from the respective values of $\phi^{(s)}$ with the exception of the DS case, where we find good agreement within error bars.

We would like to argue that the discrepancy between all of these estimates is likely due to very strong finite-size corrections to scaling around a higher-order critical point. Support for this comes from the observation that near this point we find two weak but clearly separated peaks in the bulk-specific heat, which seem to weaken and move closer to each other at longer lengths. This behavior is not captured by our scaling assumptions, and hence one needs to either amend these assumptions to capture this behavior or perform simulations at even longer lengths than 10 240 steps to get beyond these corrections to scaling.

We should like to point out the presence of confluent logarithms in some thermodynamic quantities at the trail collapse transition. For example, at the bulk collapse point (in the absence of a boundary) the partition function scales as $3^n/\log n$, the end-to-end distance grows as $n^{1/2}\log n$ [20], and the collapse crossover exponent is extremely difficult to determine, with the best estimate $\phi = 0.84(3)$ to date coming from simulations using trails with over 2×10^6 steps [27]. While we have no explicit evidence of logarithmic corrections for scaling at the special surface transition, they may well be present and introduce additional complications.

As the simulations in [20] have been performed for 10^6 steps at the exact value $\kappa^{(s)} = 3$, and as this is the only scenario for which in the present paper we find agreement between $\phi^{(s)}$ and $1/\delta^{(s)}$, we assert that most likely the special surface transition is universal and that the associated surface exponent equals $\phi^{(s)} = 1/\delta^{(s)} = 0.45(2)$. If there existed different sets of surface exponents for the special transition, then one would have to still identify a mechanism that would be capable of inducing this difference. We cannot discount this completely, as collapsing trails have a length scale exponent $\nu = 1/2(\log)$, and in a scaling limit the lattice structure near the boundary only becomes irrelevant if $\nu > 1/2$. One possible mechanism to cause a change, suggested to us by Tiago José de Oliveira, is that for the horizontal boundary long adsorbed segments of the trail in the surface suppress interactions in the layer above, which is not the case for the DS case. More work is needed to resolve this issue.

ACKNOWLEDGMENTS

N.T.R. thanks Queen Mary University London for hosting while this work was carried out, and gratefully acknowledges use of the university's High Performance Computing cluster. N.T.R. also acknowledges financial support from Coordenação de Aperfeicoamento de Pessoal de Nível Superior. Financial support from the Australian Research Council via its Discovery Projects scheme (Project No. DP160103562) is acknowledged by A.L.O. The authors are grateful to Tiago José de Oliveira for helpful comments and critical reading of the paper.

[1] E. Eisenriegler, K. Kremer, and K. Binder, J. Chem. Phys. **77**, 6296 (1982).
[2] K. De'Bell and T. Lookman, Rev. Mod. Phys. **65**, 87 (1993).
[3] T. Vrbová and S. G. Whittington, J. Phys. A **29**, 6253 (1996).
[4] T. Vrbová and S. G. Whittington, J. Phys. A **31**, 3989 (1998).
[5] T. Vrbová and K. Procházka, J. Phys. A **32**, 5469 (1999).
[6] P. Grassberger, J. Phys. A **38**, 323 (2005).

[7] A. L. Owczarek, A. Rechnitzer, J. Krawczyk, and T. Prellberg, J. Phys. A **40**, 13257 (2007).
[8] M.-B. Luo, J. Chem. Phys. **128**, 044912 (2008).
[9] L. I. Klushin, A. A. Polotsky, H.-P. Hsu, D. A. Markelov, K. Binder, and A. M. Skvortsov, Phys. Rev. E **87**, 022604 (2013).
[10] J. A. Plascak, P. H. L. Martins, and M. Bachmann, Phys. Rev. E **95**, 050501(R) (2017).
[11] P. Flory, *Principles of Polymer Chemistry* (Cornell University, Ithaca, 1953).
[12] P.-G. de Gennes, *Scaling Concepts in Polymer Physics* (Cornell University, Ithaca, 1979).
[13] U. Bastolla and P. Grassberger, J. Stat. Phys. **89**, 1061 (1997).
[14] A. R. Veal, J. M. Yeomans, and G. Jug, J. Phys. A **24**, 827 (1991).
[15] D. P. Foster, E. Orlandini, and M. C. Tesi, J. Phys. A **25**, L1211 (1992).
[16] P. H. L. Martins, J. A. Plascak, and M. Bachmann, J. Chem. Phys. **148**, 204901 (2018).
[17] C. J. Bradly, A. L. Owczarek, and T. Prellberg, Phys. Rev. E **97**, 022503 (2018).
[18] C. J. Bradly, A. L. Owczarek, and T. Prellberg, Phys. Rev. E **98**, 062141 (2018).
[19] I. Guim, H. W. J. Blöte, and T. W. Burkhardt, J. Phys. A. **30**, 413 (1997).
[20] A. L. Owczarek and T. Prellberg, J. Stat. Phys. **79**, 951 (1995).
[21] D. P. Foster, J. Phys. A **42**, 372002 (2009).
[22] D. P. Foster, J. Phys. A **43**, 335004 (2010).
[23] B. Duplantier and H. Saleur, Phys. Rev. Lett. **59**, 539 (1987).
[24] T. Prellberg and J. Krawczyk, Phys. Rev. Lett. **92**, 120602 (2004).
[25] P. Grassberger, Phys. Rev. E **56**, 3682 (1997).
[26] H. Meirovitch and H. A. Lim, Phys. Rev. Lett. **62**, 2640 (1989).
[27] A. L. Owczarek and T. Prellberg, Physica A (Amsterdam) **373**, 433 (2007).

Adsorption of two-dimensional polymers with two- and three-body self-interactions

Nathann T. Rodrigues [*] and Tiago J. Oliveira [†]
Departamento de Física, Universidade Federal de Viçosa, 36570-900, Viçosa, Minas Gerais, Brazil

Thomas Prellberg [‡]
School of Mathematical Sciences, Queen Mary University of London, Mile End Road, London, E1 4NS, United Kingdom

Aleksander L. Owczarek [§]
School of Mathematics and Statistics, University of Melbourne, Victoria 3010, Australia

(Received 3 November 2019; published 27 December 2019)

Using extensive Monte Carlo simulations, we investigate the surface adsorption of self-avoiding trails on the triangular lattice with two- and three-body on-site monomer-monomer interactions. In the parameter space of two-body, three-body, and surface interaction strengths, the phase diagram displays four phases: swollen (coil), globule, crystal, and adsorbed. For small values of the surface interaction, we confirm the presence of swollen, globule, and crystal bulk phases. For sufficiently large values of the surface interaction, the system is in an adsorbed state, and the adsorption transition can be continuous or discontinuous, depending on the bulk phase. As such, the phase diagram contains a rich phase structure with transition surfaces that meet in multicritical lines joining in a single special multicritical point. The adsorbed phase displays two distinct regions with different characteristics, dominated by either single- or double-layer adsorbed ground states. Interestingly, we find that there is no finite-temperature phase transition between these two regions though rather a smooth crossover.

DOI: 10.1103/PhysRevE.100.062504

I. INTRODUCTION

Understanding the behavior of self-interacting single polymer chains in a solvent is of fundamental interest from both the theoretical and experimental point of view [1,2]. In general, one can find a rich phase structure. In a good solvent, a polymer exists in a swollen globule state, whereas in a bad solvent the polymer collapses into a partially dense amorphous globule or presents in a fully dense crystal-like structure.

The study of a variety of lattice models of polymers has played a fundamental role in elucidating these phases and phase transitions between them. For example, the coil-globule transition between a swollen coil and a collapsed globule at the so-called θ point has been analyzed in both two and three dimensions [3–5], with theoretically predicted critical exponents [6–8] associated with the transition confirmed by simulations and experiment.

More generally, interacting self-avoiding walks and trails with competing two-body and three-body interactions give rise to phase diagrams, which, in addition to the swollen phase, show both collapsed globule and dense crystal-like phases, with all three phases meeting at a multicritical point [9–11]. A schematic phase diagram is shown in Fig. 1.

Adsorption of a polymer chain onto a surface is another fundamental problem in polymer physics [12–20]. If a polymer is tethered with one end to a sticky surface, then increasing the strength of the surface attraction induces an adsorption transition from a desorbed bulk state to an adsorbed state in which the polymer is bound to the surface. If the polymer is in a swollen bulk phase, then one speaks of a "normal" surface transition, whereas if the polymer in bulk is in the critical θ-state, one speaks of a "special" surface transition, each of which is associated with its own set of critical surface exponents [21]. If the polymer adsorbs from a collapsed coil, one finds a surface-attached globule (which is absent in two-dimensional models, in which the adsorbing surface is modeled by a line).

Recently, there has been renewed interest in the polymer adsorption transition due to the fact that numerical studies pointed at possible nonuniversal behavior of the normal adsorption transition [22–25]. Of interest here is the fact that these works show that the determination of these exponents is rather subtle due to the presence of strong finite-size effects, despite the fact that the phases themselves could be identified in a robust manner.

In this paper, we consider the adsorption transition of a polymer chain with both two-body and three-body interactions. The lattice model considered here is one of self-avoiding trails with on-site interactions on the triangular lattice, which has been studied previously [9]. We now study this model in a half-plane with the trails restricted to start at the origin, and adsorption mediated by on-site attractive interactions at vertices in the boundary line. In addition to the three

[*] nathan.rodrigues@ufv.br
[†] tiago@ufv.br
[‡] t.prellberg@qmul.ac.uk
[§] owczarek@unimelb.edu.au

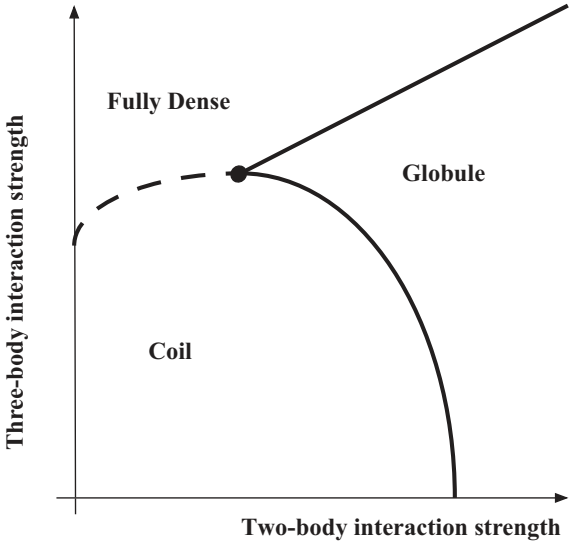

FIG. 1. Schematic phase diagram for a single polymer chain in a solvent with two-body and three-body interactions, showing the presence of coil, globule, and fully dense phases. The coil-globule transition is critical, whereas the coil-dense transition is first-order. In two dimensions, the globule-dense transition is expected to be continuous.

bulk phases, we find an adsorbed phase. All phases meet each other pairwise at transition surfaces, which meet each other in multicritical lines joining in a single special multicritical point. The analysis is made somewhat more difficult by the fact that the adsorbed phase shows two distinct regions with different characteristics, dominated by either single or double layer adsorbed ground states.

We point out that an analogous scenario has been analyzed using the bond-fluctuation model, which can be seen as a self-avoiding lattice path model in which step lengths different from unity are allowed [26], with a certain set of short-range interactions added. The interplay of interaction and adsorption in such a model has been studied in two [27] and three [28] dimensions.

This paper is organized as follows. In Sec. II we define the model and the quantities used to investigate its thermodynamics properties. Some details on the Monte Carlo methods and simulations are given in Sec. III. Sections IV and V present results, respectively, for the boundary planes and for slices of the three-dimensional parameter space. A summary of the full phase diagram is presented in Sec. VI.

II. MODEL AND QUANTITIES OF INTEREST

A self-avoiding trail (SAT) is defined as a path on a regular lattice, composed of a finite collection of adjacent vertices on the sites of the lattice that are linked by steps along the edges of the lattice, with the restriction that all edges have to be unique. We identify the vertices of this path as monomers and the edges as a sequence of bonds connecting such monomers, in a way that no closed loop is formed. Thereby, the polymer excluded volume interaction is introduced in this model by the restriction of one bond per edge, while more than one monomer can be placed at the same site. In a lattice of coordination number q, the maximal number of monomers at one site is $\lfloor q/2 \rfloor$.

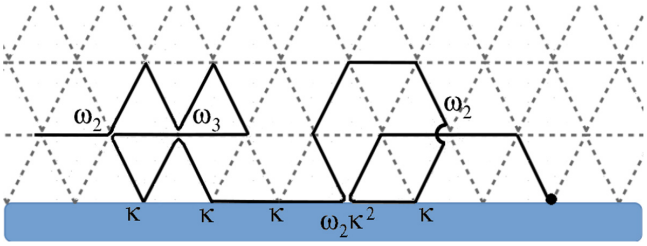

FIG. 2. Illustration of a self-avoiding trail with $n = 22$ steps on the triangular lattice. The solid black circle denotes the origin where the trail is tethered. The Boltzmann weights associated with different site configurations are also indicated.

Here we are interested in investigating transitions among bulk and adsorbed phases of polymers modeled as self-attracting SATs defined on the half-plane consisting of a triangular lattice limited by a horizontal surface (see Fig. 2). As the triangular lattice has coordination number $q = 6$, bulk sites can be visited by up to three monomers. The coordination number of sites on the surface is 4, so surface sites can have at most two monomers. Self-attraction is included in the SATs by associating energies $-\epsilon_2 \leqslant 0$ to doubly visited (regardless they are in surface or bulk) and $-\epsilon_3 \leqslant 0$ to triply visited sites. Moreover, a polymer-surface interaction is introduced by assigning an energy $-\epsilon_s \leqslant 0$ to each monomer lying on the surface. A configuration for this system is illustrated in Fig. 2. The trail is tethered to the origin, which is located on the surface.

To write down the partition function of the system, we associate Boltzmann weights $\omega_2 = e^{\beta\epsilon_2}$ and $\omega_3 = e^{\beta\epsilon_3}$ to each doubly and triply visited site, respectively, and $\kappa = e^{\beta\epsilon_s}$ to each monomer on the surface, with $\beta = 1/(k_B T)$, where k_B is the Boltzmann constant and T the temperature. The partition function is then given by

$$Z_n(\omega_2, \omega_3, \kappa) = \sum_{m_2,m_3,m_s} C^{(n)}_{\{m_2,m_3,m_s\}} \omega_2^{m_2} \omega_3^{m_3} \kappa^{m_s}, \qquad (1)$$

where $C^{(n)}_{\{m_2,m_3,m_s\}}$ is the number of n-step lattice trails with m_2 (m_3) doubly (triply) visited sites and m_s monomers on the surface. The expected value of any thermodynamic quantity Q is then defined by the average

$$\langle Q \rangle(\omega_2, \omega_3, \kappa) = \frac{1}{Z_n} \sum_{\psi_n} \omega_2^{m_2(\psi_n)} \omega_3^{m_3(\psi_n)} \kappa^{m_s(\psi_n)} Q(\psi_n), \qquad (2)$$

where the sum runs over all n-step trails ψ_n. We are particularly interested in the energy contribution per step $e_j^{(n)}$ for doubly, triply, and surface contacts:

$$e_j^{(n)} = \frac{\langle m_j \rangle}{n} = \frac{1}{nZ_n} \sum_{m_2,m_3,m_s} m_j C^{(n)}_{\{m_2,m_3,m_s\}} \omega_2^{m_2} \omega_3^{m_3} \kappa^{m_s}, \qquad (3)$$

where $j = 2, 3, s$.

A key quantity to identify possible phase transitions is the fluctuation $c_j^{(n)}$ of these energy contributions:

$$c_j^{(n)}(\omega_2, \omega_3, \kappa) = \frac{\langle m_j^2 \rangle - \langle m_j \rangle^2}{n}. \tag{4}$$

Close to a continuous bulk transition the fluctuations $c_2^{(n)}$ and $c_3^{(n)}$ of doubly and triply visited sites, respectively, are expected to follow the scaling law

$$c_i^{(n)} \sim n^{2\phi_b - 1} h(\tau n^{\phi_b}), \tag{5}$$

where ϕ_b is the crossover exponent related to bulk transitions, $\tau \equiv T - T_c$ is the temperature relative to the bulk transition temperature T_c, and $h(\cdot)$ is a scaling function. Scaling around the bulk transition is discussed in [2], see also [3,29]. Further analysis can be found in [30].

The scaling theory around the adsorption transition was developed in [31]. For an adsorption transition, the internal surface energy $e_s^{(n)}$ is the order parameter. Close to the adsorption point the surface energy is expected to behave as

$$e_s^{(n)} \sim n^{\phi_s - 1} f(\tau n^{1/\delta}), \tag{6}$$

where $\tau \equiv T - T_a$ is the temperature relative to the adsorption temperature T_a, ϕ_s is a critical exponent, $1/\delta$ is the crossover exponent associated with the adsorption transition, and $f(\cdot)$ is a scaling function.

To analyze the phase transitions, we need to introduce several quantities. The exponent $1/\delta$ can be obtained from the quantity

$$\Gamma_n = \frac{\langle m_s^2 \rangle - \langle m_s \rangle^2}{\langle m_s \rangle}, \tag{7}$$

whose maximum in curves of Γ_n as function of T behaves as

$$\Gamma_{n,\max} \sim n^{1/\delta}. \tag{8}$$

Although we will not be concerned with a careful study of critical exponents here, in some cases estimates for such exponents are very important to locate the transition points. In particular, the crossover exponents ϕ_b and $1/\delta$ are crucial if we want to determine $T_{x,\infty}$ from finite-size estimates $T_{x,n}$, for $x = c$ or a, since

$$T_{x,n} \simeq T_{x,\infty} + n^{-\psi}, \tag{9}$$

where ψ is equal to ϕ_b (when $x = c$) or $1/\delta$ (when $x = a$).

Some metric quantities, such as the mean squared end-to-end distance, R_n^2, are also important in the study of both bulk and surface transitions. For our simulations we created a triangular lattice by augmenting a square lattice with diagonals, and a simple linear transform implies that the parallel and perpendicular components of R_n^2 with respect to the surface are given by

$$R_{\perp,n}^2(\omega_2, \omega_3, \kappa) = \tfrac{3}{4}\langle y_n^2 \rangle, \tag{10}$$

$$R_{\parallel,n}^2(\omega_2, \omega_3, \kappa) = \langle x_n^2 \rangle + \tfrac{1}{4}\langle y_n^2 \rangle + \langle x_n y_n \rangle. \tag{11}$$

Close to the adsorption such quantities are expected to follow

$$R_{\perp/\parallel,n}^2 \sim n^{2\nu_{\perp/\parallel}} g(\tau n^{1/\delta}), \tag{12}$$

where $g(\cdot)$ is a scaling function and $\nu_{\perp/\parallel}$ are the Flory exponents. Clearly the scaling of $R_n^2 = R_{\perp,n}^2 + R_{\parallel,n}^2$ is dominated by the scaling of the larger quantity on the right-hand side, and thus has an associated Flory exponent $\nu = \max(\nu_\perp, \nu_\parallel)$. In nonadsorbed (bulk) phases, such exponents are equal (i.e., $\nu_\parallel = \nu_\perp$) in the thermodynamic limit, but in finite systems one finds effective exponent estimates $\nu_{\perp/\parallel,n}$ for which $\nu_{\parallel,n} < \nu_{\perp,n}$. In adsorbed phases, on the other hand, the trails behave as quasi-one-dimensional walks, so that $\nu_{\parallel,n} \to 1$ and $\nu_{\perp,n} \to 0$. Therefore, in finite trails these exponents cross at some temperature $T_{a,n}$, located in between the nonadsorbed and adsorbed phases. These crossing temperatures can thus be used as a finite-size estimate of the adsorption transition temperature.

We can also use the exponent ν to locate bulk transitions such as the coil-globule transition. In two dimensions, in the coil phase ν assumes the value of 3/4 [32], while in the globule phase a value $\nu = 1/2$ [32] is expected. For finite systems, however, we have that $\nu_{\text{coil},n} \to 3/4$ from below and $\nu_{\text{globule},n} \to 1/2$ from above as the length n increases, so that curves of ν_n against T for different values of n cross at some intermediate temperature, which can be taken as an estimate of $T_{c,n}$. At criticality, we expect to find $\nu = 4/7$ [7]. In a similar fashion, we can locate the collapse transition by using the scaling of the partition function

$$Z_n \sim \mu^n n^{\gamma - 1}, \tag{13}$$

where μ is the connective constant and γ the entropic exponent. Similarly to ν, curves of $\gamma \times T$ for different lengths n should cross each other in between the coil and globule phases, giving also estimates of $T_{c,n}$.

III. NUMERICAL SIMULATIONS

To build up the full phase diagram of the model for a broad range of parameters, we sample SATs with the flatPERM algorithm [33]. Similarly to the pruned-enriched Rosenbluth method (PERM) [34], flatPERM is an improvement of the classical Rosenbluth algorithm. In both flatPERM and PERM, a SAT is stochastically grown with pruning and enrichment strategies intended to prevent its attrition and the appearance of rare configurations with small or extremely large statistical weights. In the flatPERM, the pruning and enrichment processes are implemented independently of the thermodynamic parameters of the system, so that the method gives us an estimate of the density of states $C_{\{m_2,m_3,m_s\}}^{(n)}$. PERM, on the other hand, gives us an estimate of the partition function Z_n for a given set of parameters.

The dimensionality of the density of states (i.e., the number of energy parameters in the model, which is three here) is the main factor limiting the trails' sizes studied with flatPERM. For instance, by not fixing any of the model parameters (ω_2, ω_3, and κ), in principle we can numerically obtain the full density of states and from this the entire thermodynamic behavior of the model. It turns out, however, that with this three-parameter approach we are not able to obtain accurate estimates of $C_{\{m_2,m_3,m_s\}}^{(n)}$ for lengths larger than $n \approx 64$ steps in a reasonable amount of time. We can overcome this limitation by fixing one of the parameters and running a two-parameter flatPERM simulation for several slices of the full parameter space. In the following, we will use this strategy to build up the finite-size phase diagram of the model for trails with up

to $n = 128$ steps. To extrapolate from these relatively short finite-size results to the phase diagram in the thermodynamic limit, we perform one-parameter flatPERM simulations (by keeping two parameters fixed) for lengths up to $n = 1024$ for values of particular interest. We also ran PERM simulations for $n \leqslant 4096$ with all parameters fixed. In all cases, results from averages of at least of 10^9 trails are presented.

IV. RESULTS FOR THE BOUNDARY PLANES

As implicit in the model definition above, we are interested here in investigating only the most physically interesting situation where all interactions are attractive. This means that we will explore the three-parameter space $(\omega_2, \omega_3, \kappa)$ where the three Boltzmann weights are larger than or equal 1. To begin, it is interesting to analyze the three planes forming the boundary of such a space. Namely, the planes $(\omega_2, \omega_3, 1)$, $(1, \omega_3, \kappa)$, and $(\omega_2, 1, \kappa)$. These planes correspond to the absence of surface, two-body, and three-body interactions, respectively.

A. Plane $(\omega_2, \omega_3, 1)$

First we investigate the case where the surface is inert, that is, it does not interact with the polymer. This should be directly comparable to the bulk case previously studied without a surface [9]. To determine the thermodynamic behavior of this plane, we analyze the density of states $\sum_{m_s} C_{\{m_2,m_3,m_s\}}$ obtained from a two-parameter flatPERM simulation at $\kappa = 1$ for $n = 128$. We calculate the covariance matrix

$$\begin{bmatrix} \langle m_2^2 \rangle - \langle m_2 \rangle^2 & \langle m_2 m_3 \rangle - \langle m_2 \rangle \langle m_3 \rangle \\ \langle m_3 m_2 \rangle - \langle m_3 \rangle \langle m_2 \rangle & \langle m_3^2 \rangle - \langle m_3 \rangle^2 \end{bmatrix}, \tag{14}$$

whose maximum eigenvalue λ is a measure of the fluctuations, which can be plotted against ω_2 and ω_3 as a density plot. In general, local maxima in such fluctuation maps indicate the possible existence of phase boundaries there, so that we can associate lines of suitably defined maxima with pseudo-transition lines, for the finite system. Then, by considering other quantities such as the distributions of monomer contacts, we can identify the phases present in each region of the fluctuation map, and also whether the pseudotransition lines can be associated with discontinuous or continuous phase transitions. This method allows us to build a "finite-size phase diagram," which, in most cases, captures the main features of the actual phase diagram in the thermodynamic limit. We caution that this method does not necessarily pick up higher-order phase transitions and would also identify smooth crossovers as transitions. Hence scaling in length needs to be performed to conclusively identify the presence of phase transitions.

The fluctuation map along with approximate transition lines (i.e., the finite-size phase diagram) for the plane $(\omega_2, \omega_3, 1)$ is shown in Fig. 3. Distributions of doubly and triply visited sites [not shown] reveal, for small values of ω_2 and ω_3, the presence of configurations typically dominated by a high number of singly visited sites, characteristic of the swollen coil phase. In the region of small ω_3 and large ω_2, we find configurations with a large number of doubly visited sites, which may be identified as the trails' collapsed globule phase.

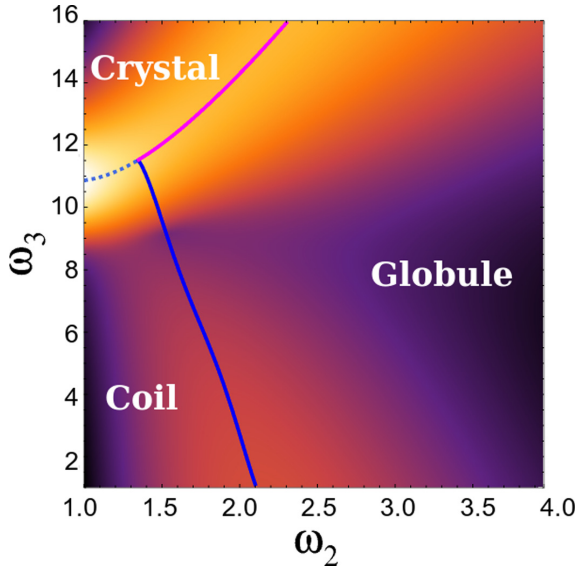

FIG. 3. Fluctuation map for the plane $(\omega_2, \omega_3, 1)$. The lighter (darker) colors indicate regions of larger (smaller) fluctuations. The lower (higher) solid lines are approximations for the continuous coil-globule and crystal-globule transition lines, while the dashed line is the discontinuous coil-crystal transition line.

Conversely, for small ω_2 and large ω_3 the trails are dominated by triply visited sites. In this region the configurations are maximally dense, so that we will refer to this phase as a crystal phase [9]. (More correctly, one should think of this phase as crystal-like, as it has a nonvanishing entropy.)

Along the line of maximal fluctuation separating the coil-globule and globule-crystal phases the distributions have a single peak, indicating the existence of continuous transitions there. Between the coil and crystal phases, on the other hand, the distributions of triply visited sites are double-peaked, suggesting that the coil-crystal transition is discontinuous. It is important to remark that it is difficult to accurately determine the transition lines when the regions of maximal fluctuation separating different phases become close to each other. For instance, in Fig. 3, we can identify only a region where the coil-crystal line change to a globule-crystal one and due to the proximity of this region with the coil-globule line, it is reasonable to infer that exists a multicritical point there, where the three lines meets. As prefigured above, such phase behavior is very similar to the one reported in [9], for the case where the surface is absent, where indeed such lines meet at a multicritical point. This is quite expected since the presence of an inert surface should not change the thermodynamic behavior of such systems.

To verify the reliability of these results for small trails (with $n = 128$ steps), we perform a finite-size analysis considering trails with lengths up to $n = 1024$. The bulk transitions are investigated, in most cases, through the fluctuations c_j in the number of doubly ($j = 2$) and triply ($j = 3$) visited sites. As an example, curves of c_3 versus ω_3 are depicted in Fig. 4(a), for $\omega_2 = 1$ and different lengths. From the maximum in such curves, $c_{3,\max}^{(n)}$, and the scaling behavior from Eq. (5), we estimate the crossover exponent ϕ_b, which is slightly larger than 1 in this case, consistently with the strong increase

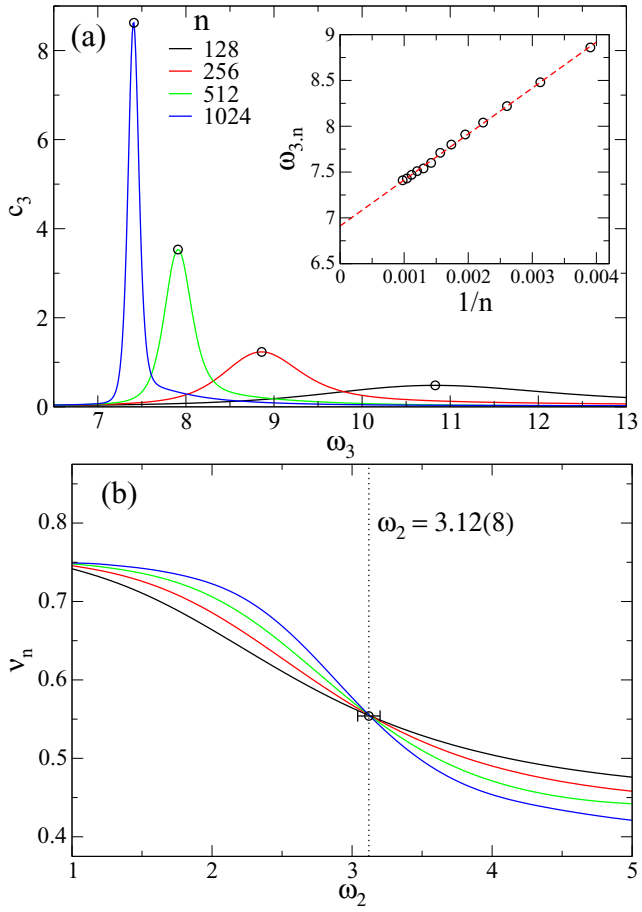

FIG. 4. (a) Fluctuation in the number of triply visited sites c_3 versus ω_3, for $\omega_2 = \kappa = 1$ and different lengths. The open black circles indicate the maximum of each curve. In the insert the values of $\omega_{3,n}$ at the maxima are plotted against $1/n$. The dashed line is a linear fit used in the extrapolation. (b) Effective exponents ν_n as function of ω_2, for $\omega_3 = \kappa = 1$ and several lengths. The dashed vertical line indicates the asymptotic value estimated from the crossing points.

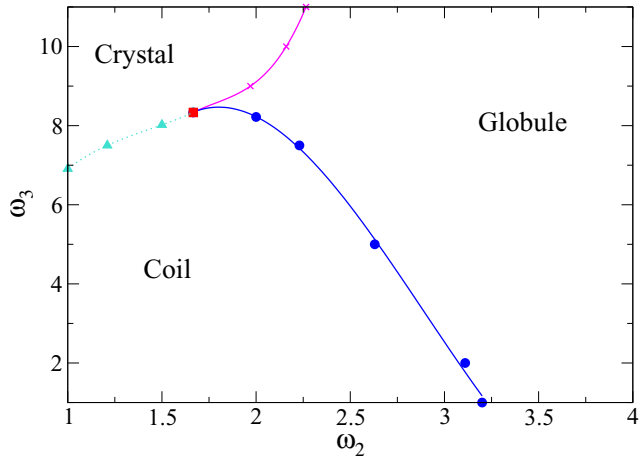

FIG. 5. Phase diagram for the plane $(\omega_2, \omega_3, 1)$. The blue circles indicate the continuous coil-globule transition, the magenta stars the continuous globule-crystal transition, and the cyan triangles the discontinuous coil-crystal transition. The red square is a multicritical point. In all cases the lines are interpolations.

of fluctuations observed in Fig. 4(a). Then we identify the values of ω_3 at each maximum as the finite-size transition parameter and by assuming that they follow Eq. (9), with the ϕ_b just estimated, we extrapolate such values to obtain the transition point in the thermodynamic limit [see the insertion in Fig. 4(a)]. For $\omega_2 = 1$, this yields $\omega_3 = 6.91(5)$, which is on the locus of the coil-crystal transition. Similar to the findings for $n = 128$ around the transition point the distribution of the number of triply visited sites still exhibits a bimodal behavior for the long trails, which together with the large ϕ_b exponent indicates that such transition is most likely discontinuous.

By increasing ω_2 one still finds a very similar behavior until $\omega_2 \lesssim \frac{5}{3}$, confirming the existence of a line of discontinuous coil-crystal transition in the phase diagram (see Fig. 5). Exactly at $\omega_2 = \frac{5}{3}$, we observe a continuous transition at $\omega_3 = 8.37(4)$. All these results are consistent with those reported by Doukas *et al.* [9], where a discontinuous coil-crystal transition ending at a multicritical point located at $(\omega_2, \omega_3) = (\frac{5}{3}, \frac{25}{3})$ was found.

From Fig. 3 and also from the results in Doukas *et al.* [9], we expect to find a coil-globule transition for (relatively) small ω_3. Following a procedure similar to the one above for the coil-crystal transition, the exponent ϕ_b was estimated from the scaling behavior of $c^{(n)}_{2,\max}$. For example, for $\omega_3 = 1$, one obtains $\phi_b = 0.53(4)$, which is a bit larger than the value for the θ class in two dimensions: $\phi_{b,\theta} = 3/7$ [7]. However, as extensively reported elsewhere [35–37], estimates of ϕ_b from the bulk fluctuations are usually hampered by strong finite-size effects. For instance, by extrapolating the finite-size transition points, $\omega_{2,n}$, obtained from the maximum of $c^{(n)}_2$ curves for $\omega_3 = 1$ using $\phi_{b,\theta}$, as done in Doukas *et al.* [9], we find $\omega_2 \approx 2.6$ in agreement with the value found in [9]. However, curves of $\omega_{2,n}$ versus $n^{-\phi_b}$ do not display a good linear behavior neither for $\phi_b = \phi_{b,\theta}$ nor for $\phi_b = 0.53$, indicating that such estimate of ω_2 is not so reliable. Other evidence of this is the fact that if one uses the maximum in the fluctuations in the number of trimers, instead of dimers [that is, $c^{(n)}_3$ rather than $c^{(n)}_2$] to determine $\omega_{2,n}$, an extrapolated value $\omega_2 \gtrsim 3$ is obtained (for $\omega_3 = 1$).

To obtain a more accurate estimate of the location of the coil-globule transition, we study the crossing of curves of effective exponents ν_n and γ_n versus the appropriate parameter. Fig. 4(b) shows an example of this for $\omega_3 = 1$, where one sees that curves for a broad range of lengths cross each other in a narrow interval of ω_2, demonstrating that finite-size effects are very small in this measure. In fact, by using the crossing points for pairs of successive lengths as estimates of $\omega_{2,n}$, one observes only a mild dependence with n. Extrapolating such values using Eq. (9), with the exponent $\phi_{b,\theta}$, we obtain $\omega_2 = 3.12(8)$. A very similar value is obtained from an analysis of the crossing points of effective entropic γ exponents, where finite-size corrections are also weak. The same scenario discussed here for $\omega_3 = 1$ is found for larger values of ω_3, along the entire coil-globule transition line. Since the results coming from the effective exponents are more accurate than those for $c^{(n)}_2$ and somewhat agree with those from $c^{(n)}_3$, we use them

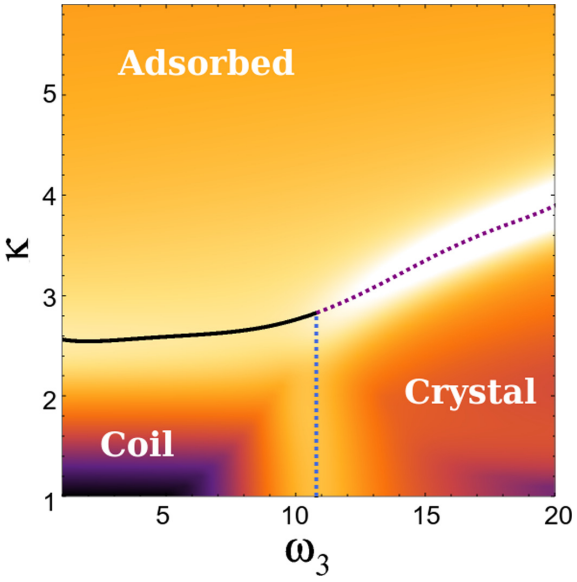

FIG. 6. Fluctuation map for the plane $(1, \omega_3, \kappa)$. The lighter (darker) colors indicate regions of larger (smaller) fluctuations. The solid (black) line is the continuous coil-adsorbed line, while the slanted (indigo) and vertical (blue) dashed lines are the discontinuous crystal-adsorbed and coil-crystal transition lines, respectively.

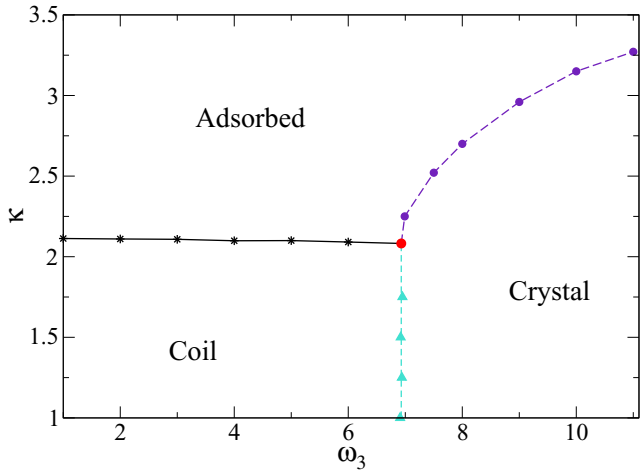

FIG. 7. Phase diagram for the plane $(1, \omega_3, \kappa)$. The cyan triangles indicate the discontinuous coil-crystal transition, the indigo circles the discontinuous crystal-adsorbed transition, and the black stars the continuous coil-adsorbed transition. The red circle represents the critical-end-point. All lines are guide-to-eye.

to determine the correct coil-globule transition line, which is shown in Fig. 5. We notice that the location of this line differs considerably from the one reported in Doukas *et al.* [9]. Regardless of the numerical difference, both line estimates end at the same multicritical point, limiting similar regions of the phase diagram. Moreover, our analysis of exponents confirms the claim in [9] that this is a tricritical θ line, since the values of ν and γ at the crossing points are found to be reasonably close to the θ exponents.

Finally, for large values of ω_3 we find a continuous crystal-globule transition line [see Fig. 5], which was determined following the same procedure employed above using the maxima of fluctuations. We notice that, similarly to the coil-crystal transition, here results from $c_2^{(n)}$ and $c_3^{(n)}$ are consistent. However, once again the locus of our transition line is shifted from that reported in [9], resulting from differing finite-size analyses. Importantly, similar to the phase diagram from [9] our line seems to start at the multicritical point and extends to large values of ω, as also suggested by the fluctuation map for $n = 128$. Actually, despite their quantitative differences, the entire "finite-size diagram" from the fluctuation map in Fig. 3 is consistent with the phase diagram given here in Fig. 5.

B. Plane $(1, \omega_3, \kappa)$

Now we investigate the case where the two-body monomer-monomer interaction is absent, so that $\omega_2 = 1$. Similar to the plane $(\omega_2, \omega_3, 1)$, we will start analyzing the properties of the fluctuation map and the respective finite-size phase diagram, for $n = 128$. This is shown in Fig. 6, where one clearly sees three regions separated by stripes of large fluctuations. The distributions of number of monomers reveal that such regions are associated with the phases: coil (for small κ and ω_3), crystal (for small κ and large ω_3), and adsorbed (for large κ). This last one is characterized by a high number of contacts with surface. An analysis of the modality of the distribution for the number of trimers points out that the coil-crystal and crystal-adsorbed phases are separated by discontinuous transitions, while a continuous transition line seems to exist between coil and adsorbed phases. As it is well known [14], when the strength of the polymer-surface interaction is not so large, the bulk transitions should not be affected by such interaction. This means that the discontinuous coil-crystal transition is expected to happen at a straight line parallel to the κ axis in the (κ, ω_3) space. This important observation facilitates the determination of the phase boundaries in the finite-size diagram. The maxima of fluctuations in Fig. 6 suggest that the three transition lines meet at single point, which turns out to be a critical end point (CEP).

Let us now explore the phase behavior in the thermodynamic limit. To determine and confirm the existence of the (bulk) coil-crystal transition line, we follow the same procedures described in the previous subsection. This yields an approximately vertical (κ-independent) line in the phase diagram, located at $\omega_3 \approx 6.93$ (see Fig. 7). This coil-crystal coexistence line ends at $\kappa \approx 2.08$, above which it gives place to a crystal-adsorbed discontinuous transition. The crystal-adsorbed coexistence line, which was determined in the same way of the coil-crystal one, increases monotonically with ω_3, as seen in Fig. 7.

To analyze the (presumed continuous) coil-adsorbed transition, one starts calculating Γ_n [Eq. (7)] and using the maxima in their curves to estimate the crossover exponent $1/\delta$ from the scaling relation 8. We always find $1/\delta \approx 1/2$ along this line, in agreement with the expected value for the adsorption transition in two dimensions [38]. Then, we use the position of the maxima of Γ_n as the finite-size transition estimate κ_n and extrapolate them according to Eq. (9) with $1/\delta = 1/2$. An

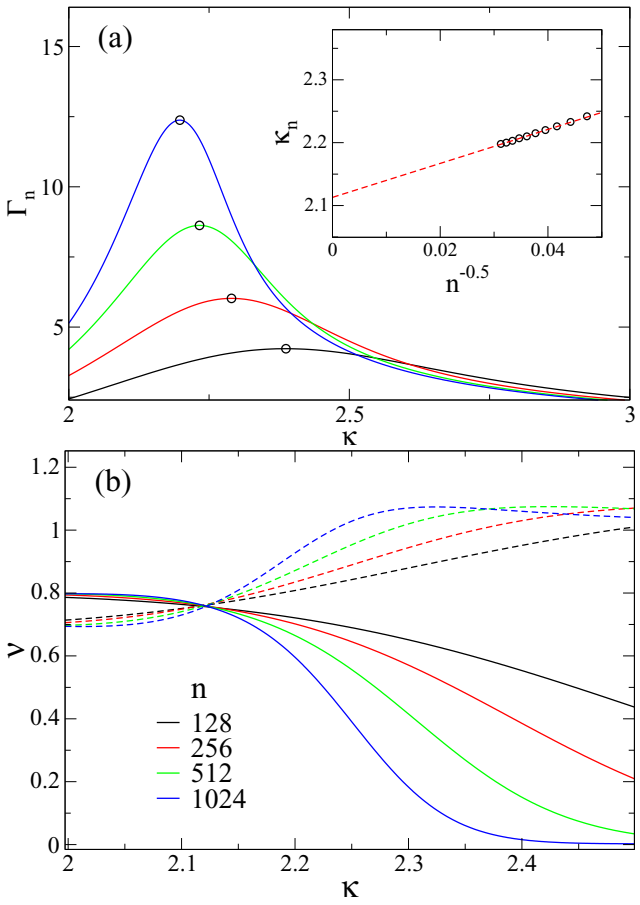

FIG. 8. (a) Γ_n for different lengths as function of κ, for $\omega_2 = \omega_3 = 1$. The circles indicate the maximum in each curve. The insertion shows the values of κ_n at the maxima against $n^{-1/2}$. The dashed line is a linear fit used in extrapolation. (b) Effective Flory exponents $\nu_{\parallel,n}$ (dashed lines) and $\nu_{\perp,n}$ (solid lines) versus of κ, for $\omega_2 = 1$ and $\omega_3 = 2$ and several lengths.

example of this is shown in Fig. 8(a), for $\omega_3 = \omega_2 = 1$, for which one obtains $\kappa = 2.113(5)$.

The other accurate way of locating the adsorption transition is through the crossing of the Flory exponents $\nu_\parallel$ and $\nu_\perp$ [24]. Figure 8(b) presents an example for $\omega_3 = 2$. The crossing points for different lengths serve also as good estimates of κ_n and their extrapolation [with Eq. (9) and $1/\delta = 1/2$] yields an estimate for the thermodynamic value for the adsorption point. Though this method returns results similar to those from fluctuations, it has weaker finite-size effects, being so more reliable to determine the adsorption transition line. Such a line is also depicted in the phase diagram shown in Fig. 7, where one sees that it ends at the point where the coexistence lines meet, confirming the existence of a CEP in the diagram at $(\omega_3, \kappa) \approx (6.93, 2.08)$, as suggested by the finite-size fluctuation map.

C. Plane $(\omega_2, 1, \kappa)$

Next we discuss the case where trimers at a given site do not interact, so $\omega_3 = 1$. The fluctuation map and the finite-size

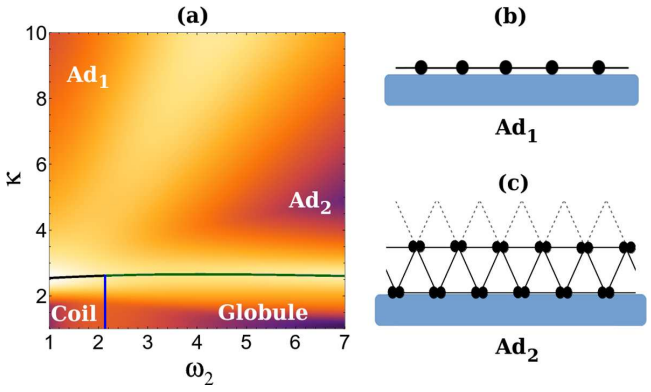

FIG. 9. (a) Fluctuation map for the plane $(\omega_2, 1, \kappa)$. The vertical blue line indicates the coil-globule transition. The approximately horizontal line to the left (right) of the coil globule transition is the black (green) line being the coil-adsorbed (globule-adsorbed) transition line. The transitions in all these lines seem to be continuous. While the adsorbed phase is a single phase (there are no finite temperature phase transitions) it has two regions where the ground state differs. Illustrations of the two different ground state configurations are shown in (b) for the Ad_1 region and (c) Ad_2 region.

transition lines are displayed in Fig. 9(a). Using the same methodology previously discussed, we find for small values of κ indications of a continuous coil-globule transition. For large values of κ one has signatures of two adsorbed regions. The ordinary adsorbed region (characterized, in the ground state, by a single line of monomers lying on the surface [see Fig. 9(b)]) is found for small ω_2. For large ω_2, on the other hand, we observe an adsorbed region which, in the ground state, is featured by a bilayer of doubly visited sites, as illustrated in Fig. 9(c). Hereafter, we will refer to these monolayer and bilayer regions as Ad_1 and Ad_2 regions, respectively. Importantly below our analysis indicates that there are no finite-temperature transitions between them, so they are *not* thermodynamically stably different phases.

Our finite-size analysis indicates that both bulk (coil and globule) phases adsorb through a continuous transition. While the globule adsorbs to the Ad_2 region, the coil phase adsorbs to either an Ad_1 or Ad_2 region, depending on the value of ω_2. The globule adsorption to the Ad_2 region can be understood, from an energetic "cost" point of view since both feature a relatively large proportion of doubly visited sites. By locating the phase boundaries in the finite-size phase diagram, we found indications of a possible multicritical point located where all the three continuous lines, coil-globule, coil-adsorbed, and globule-adsorbed meet.

In the fluctuation map, we see a clear region with large fluctuation between the regions Ad_1 and Ad_2, suggesting the possible existence of an Ad_1-Ad_2 transition. As already remarked, however, from the finite behavior alone we cannot determine whether this is a phase transition or simply a smooth crossover. To check this, we performed PERM calculations for trails with up to $n = 4096$ steps, for several values of κ and $\omega_2 = 2.4$. We chose this value of ω_2 since here the coil adsorbs to an Ad_2 region at the transition. Moreover, for very large values of κ the adsorbed phase becomes Ad_1.

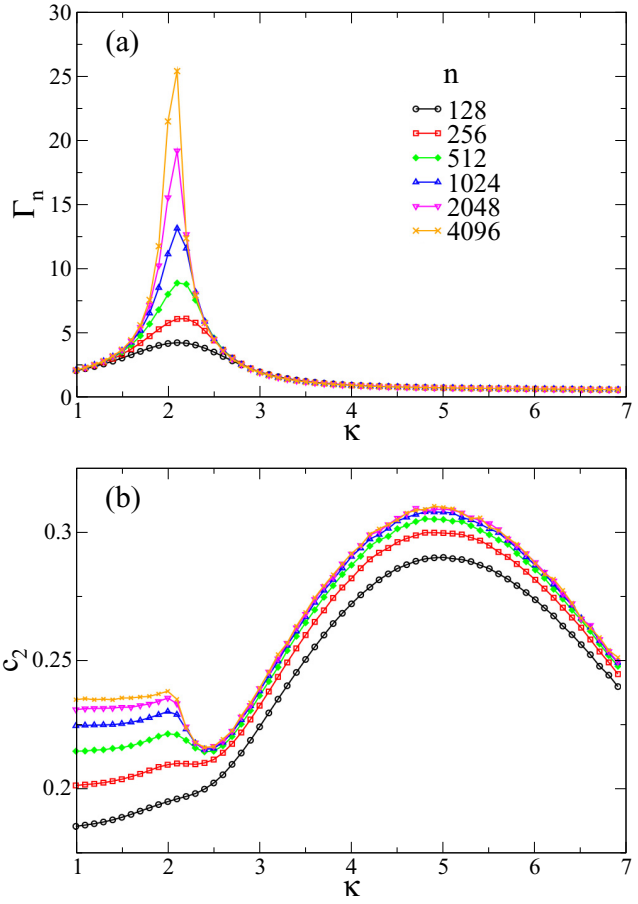

FIG. 10. (a) Γ_n as function of κ for $\omega_3 = 1, \omega_2 = 2.4$, and several lengths. (b) Fluctuation in the number of doubly visited sites $c_2^{(n)}$ versus κ for the same parameters as in (a).

Figures 10(a) and 10(b) present Γ_n and $c_2^{(n)}$, respectively, from such simulations, verifying this scenario. There is a single peak in Γ_n around $\kappa \approx 2$, where the coil-adsorbed transition is expected. There is no indication of an Ad_1-Ad_2 transition, but rather evidence for a smooth crossover.

From a physical point of view, one can understand the two regions simply as two one-dimensional layers, and short-range interactions in one-dimensional systems are not able to induce any finite-temperature phase transition, so that there can only be a smooth crossover between these regions.

Therefore, by using the same methods employed in previous subsections, we obtain the phase diagram depicted in Fig. 11. Once again, it is consistent with our findings from the fluctuation map, with continuous coil-globule, coil-adsorbed, and globule-adsorbed transition lines. Similarly to the coil-crystal transition found in the plane $(1, \omega_3, \kappa)$, an approximately vertical (κ-independent) straight line is found separating the coil and the globule phases, as expected. This line, located at $\omega_2 \approx 3.2$, starts at $\kappa = 1$ and ends at a multicritical point located at $\kappa = 1.96(2)$, where it meets the coil-adsorbed and globule-adsorbed lines. It is interesting to note in Fig. 11 that the globule-adsorbed line appears for lower values of κ than those at the crystal-adsorbed line (see Fig. 7). This shows that trails in the globule phase adsorb easier than those in the

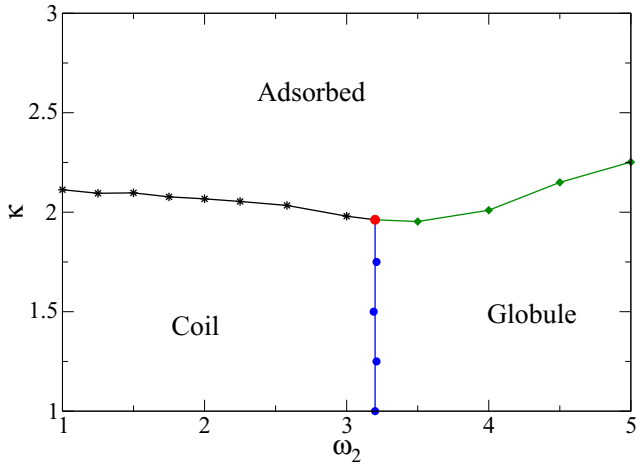

FIG. 11. Phase diagram for the plane $(\omega_2, 1, \kappa)$. The black stars indicate the continuous coil-adsorbed transition, the blue circles the θ-like coil-globule transition, and the green diamonds the continuous globule-adsorbed transition. The multicritical point is denoted by the red circle. All lines are guide-to-eye.

crystal phase. One way to understand this is that due to the presence of the Ad_2 region in the plane $(\omega_2, 1, \kappa)$ the globule phase adsorbs to a state in which the trails can retain their large number of doubly visited sites.

V. THREE-PARAMETER MODEL

To get some insight on the phase behavior in the full three-parameter space, it is instructive to begin by synthesizing the information from the three boundary planes discussed in the previous section. By simply putting these together one finds a picture as depicted in Fig. 12, which indicates the regions where each of the four thermodynamic phases (coil, globule,

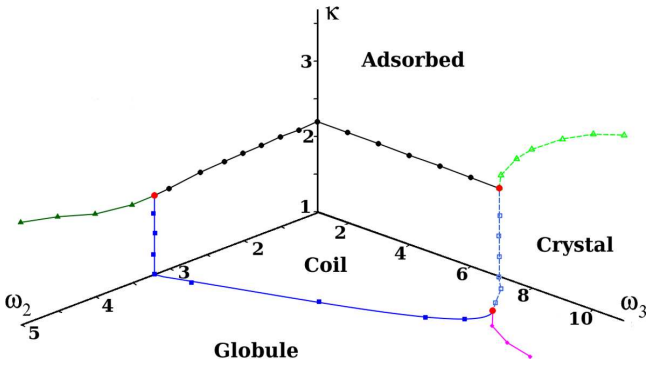

FIG. 12. Summary of the phases diagrams for the three boundary planes of three parameter space plotted together. The blue squares are the coil-globule transition lines estimated here. The open cyan squares are the points of discontinuous coil-crystal transitions, while the open green triangles the discontinuous crystal-adsorbed transition. The black circles denote the continuous coil-adsorbed transitions and the dark-green triangles the critical globule-adsorbed transition. The magenta diamonds indicates the continuous globule-crystal transition. The red filled circles represent the CEP and the two multicritical points.

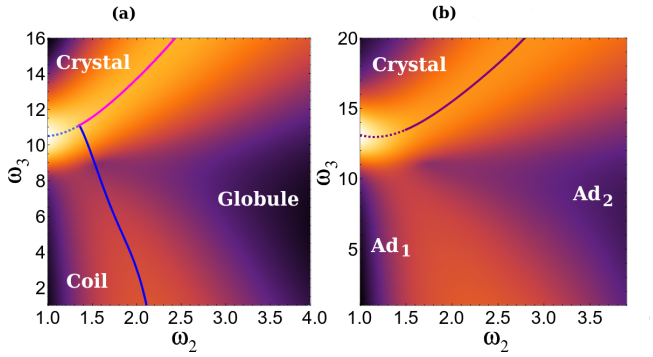

FIG. 13. Fluctuation maps in spaces $(\omega_2, \omega_3, 2)$ and $(\omega_2, \omega_3, 3)$ in (a) and (b), respectively, with transition lines indicated. In both panels solid and dashed lines indicate the presence of unimodal and bimodal energy distributions near the transition, respectively.

crystal, and the adsorbed) found above appears in the full phase space and how they are separated. Of course one is assuming no new phases appear. So for instance, the continuous coil-adsorbed transition lines in the planes $(\kappa, \omega_2, 1)$ and $(\kappa, 1, \omega_3)$ strongly suggest that a critical surface exists separating these phases. Similarly, the tricritical coil-globule lines in the planes $(\kappa, \omega_2, 1)$ and $(\omega_2, \omega_3, 1)$ indicate that such phases are separated by a tricritical (possibly θ) surface. Moreover, the discontinuous transition lines between the coil and crystal phases [in the planes $(\kappa, 1, \omega_3)$ and $(\omega_2, \omega_3, 1)$] provide strong evidence on the existence of a coil-crystal coexistence surface.

As remarked above the full three-parameter flatPERM simulations could only be undertaken for length less than $n \approx 64$ to a reasonable degree of convergence. As such we investigated the full phase diagram based on the finite-size behavior of two-parameter slices of the three-parameter space, for $n = 128$. We remark that even such two-parameter flatPERM approach has demanded extensive simulations. As already shown in the previous section, these finite-size phase diagrams (built up from the fluctuation maps) capture the correct thermodynamic properties of the system, though quantitatively incorrect in most cases. Indeed we found no evidence of new phases, beyond the four ones already discussed. Moreover, since there is only a crossover between the adsorbed Ad_1 rich and Ad_2 rich regions, no transition line separating them will be shown, even if we indicate their locations in the figures.

A. κ slices

Let us start analyzing slices for κ fixed. We recall that for $\kappa = 1$ [i.e., the plane $(\omega_2, \omega_3, 1)$ considered in Sec. IV A] the three bulk phases (coil, globule, and crystal) are present in the system, as shows Figs. 3, 5, and 12. Since, for small values of κ, the bulk transitions are not expected to be affected by the presence of an interacting surface, the same diagram of $\kappa = 1$ is expected in this region. In fact, as demonstrated in Fig. 13(a), the finite-size phase diagram for $\kappa = 2$ is practically identical to the one for $\kappa = 1$ shown in Fig. 3. This strongly indicates that the transition lines between the three bulk phases give rise to three surfaces: a tricritical coil-globule, a critical crystal-globule, and a coexistence coil-crystal, consistently with the predictions above based on Fig. 12. Moreover, the multicritical point found in the case $\kappa = 1$ gives rise to a multicritical line, where the three surfaces above meet. Since this line is related to bulk phases only, we will refer to it as the bulk multicritical line (BML). Note that these bulk transition surfaces, as well as the BML are all expected to be κ-independent, i.e., perpendicular to the (ω_2, ω_3) plane. This is indeed confirmed by the quantitative agreement between the finite-size transition lines in Figs. 3 and 13(a) for $\kappa = 1$ and 2, respectively, as well as for intermediate κ slices (not shown).

All these bulk transition surfaces (and the BML, as well) are expected to end when they meet the adsorption transition surfaces. Figures 7, 11, and 12 indicate that the coil-adsorbed and the globule-adsorbed critical surfaces in the thermodynamic limit change mildly with ω_2 and ω_3, being located close to $\kappa = 2$. The same thing happens in the diagrams for $n = 128$, as seen in Figs. 6 and 9(a), where such surfaces are in the region $2 \lesssim \kappa \lesssim 3$. Therefore, it is hard to observe these adsorption surfaces in planes of fixed κ. Anyhow, as shown in Fig. 13(b), for the $\kappa = 3$ slice, the only bulk phase appearing in this diagram is the crystal one, confirming that we are above the coil-adsorbed and globule-adsorbed surfaces. Interestingly, in the region for small ω_2 (where the coil phase was observed for smaller κ) one finds the adsorbed phase is Ad_1 rich, while for large values of ω_2 the adsorbed phase is Ad_2 rich.

At finite length $n = 128$, as shown in the diagram for $\kappa = 3$ [Fig. 13(b)], the crystal-adsorbed transition is still found to be discontinuous for small ω_2, as evidenced by a bimodal energy distribution. As discussed above, there is only one adsorbed phase, so that one would expect this transition to remain discontinuous for all values of ω_2. Unfortunately, we are unable to detect a bimodal distribution for large ω_2 but believe that this is simply a finite size effect.

B. ω_2 slices

Now we investigate planes for ω_2 fixed. As already demonstrated in Sec. IV B, for $\omega_2 = 1$ three phases are present in the diagram: adsorbed, coil, and crystal (see Fig. 6, for $n = 128$). Figure 14(a) displays the behavior for $\omega_2 = 1.5$, which is the same for $\omega_2 = 1$, confirming the existence of a continuous coil-adsorbed transition surface, as well as of discontinuous coil-crystal and crystal-adsorbed ones. Moreover, since the former critical surface seems to end at its junction with the latter two coexistence ones, they shall form a line of critical-end-points (a CEP line) there.

The slice $\omega_2 = 2$ is shown in Fig. 14(b), where a different thermodynamic behavior is observed. According to Figs. 3 and 13, in such plane, with κ small, one should observe transitions from coil to globule and then from globule to crystal by increasing ω_3. It turns out, however, that the fluctuation map displayed in Fig. 14(b) fails in capturing the coil-globule transition, although for very small ω_3 the trails have the characteristics of the coil phase. This caveat is certainly due to the short lengths considered. For large values of κ, the expected adsorbed phase is observed.

We note that for the crystal-adsorbed transition at $\omega_2 = 2.0$ we were unable to detect a bimodal distribution. While

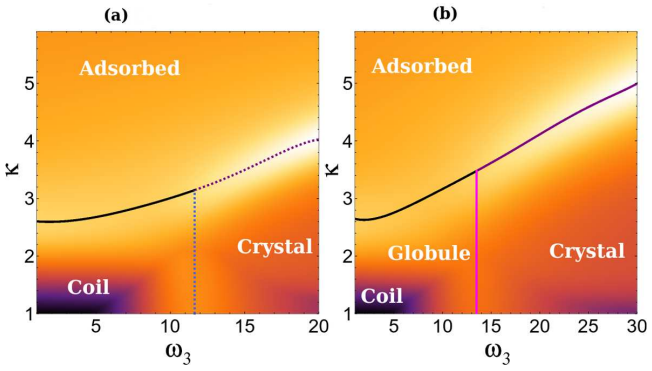

FIG. 14. Fluctuation maps in spaces $(1.5, \omega_3, \kappa)$ and $(2.0, \omega_3, \kappa)$ in (a) and (b), respectively, with transition lines indicated. In all panels solid and dashed lines indicate the presence of unimodal and bimodal energy distributions near the transition, respectively.

consistent with the numerical evidence in the κ slices we reiterate that we expect this to be a finite-size effect.

For fixed ω_2, the globule-crystal transition line meets the adsorbed phase at a dense-adsorbed multicritical point, which in the full phase diagram extends to a dense-adsorbed multicritical (DAM) line. Such a line seems also to join the CEP and the BML lines at a special multicritical point.

C. ω_3 slices

We now present the results for planes with ω_3 fixed. Fig. 15(a) presents the diagram for the $\omega_3 = 8$ slice, which is qualitatively identical to the one for $\omega_3 = 1$, see Fig. 9(a); slices for intermediate values of ω_3 (not shown) display the same behavior. This gives additional confirmation of the existence of a tricritical coil-globule and of critical coil-adsorbed and globule-adsorbed surfaces. These three surfaces meet, yielding a third multicritical line in the three-parameter space, which we will refer to as the collapsed-adsorbed multicritical (CAM) line. We expect that this CAM line also ends at the special multicritical point where the DAM, CEP, and BML lines meet.

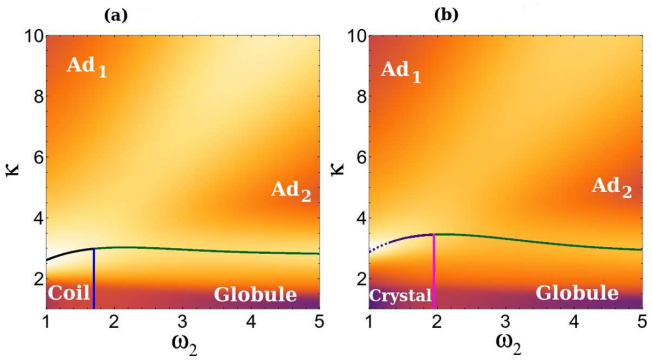

FIG. 15. Fluctuation maps in spaces $(\omega_2, 8, \kappa)$ and $(\omega_2, 12, \kappa)$ in (a) and (b), respectively, with transition lines indicated. In both panels solid and dashed lines indicate the presence of unimodal and bimodal energy distributions near the transition, respectively.

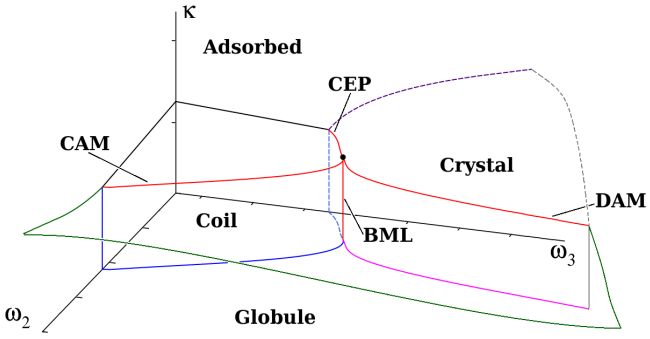

FIG. 16. Qualitative representation of the full phase diagram, presenting the four phases found (regarding the regions Ad_1 and Ad_2 simply as the adsorbed phase), the critical-end-point (CEP) line, as well as the bulk (BML), collapsed-adsorbed (CAM), and dense-adsorbed (DAM) multicritical lines. The special multicritical point is denoted by a circle.

As expected from Figs. 3, 6, and 12, for large values of ω_3 the crystal phase appears in place of the coil phase for small values of ω_2 and κ. For $\omega_3 = 12$, this is demonstrated in Fig. 15(b). We are unable to detect a bimodal energy distribution along the whole crystal-adsorbed transition line, but attribute this to finite-size effects as discussed above.

VI. SUMMARY: FULL PHASE DIAGRAM

Our simulation results for self-attracting self-avoiding trails living on the triangular lattice and attractively interacting with a surface reveals a very rich thermodynamic behavior, with three bulk phases (coil, globule, and crystal) and an adsorbed phase with two regions related to different ground states (the ordinary monolayer Ad_1 rich region and a bilayer Ad_2 rich region). The coil phase exists in a bounded part of the full phase diagram where the three Boltzmann weights ω_2, ω_3, and κ are small. The crystal phase appears in the region where κ and ω_2 are relatively small, but ω_3 is large. Similarly, the globule phase exists for small κ and large ω_2. Finally, the adsorbed phase appear in the region of large κ. These features are summarized in the sketch of the full phase diagram depicted in Fig. 16, where no distinction is made between both adsorbed regions since we determined that there is only a smooth crossover between them.

Three bulk transition surfaces are present in the system, for small κ: the continuous coil-globule (possibly in θ class [9]) and globule-crystal surfaces and a discontinuous coil-crystal surface. These three surfaces meet at the multicritical BML line, which seems to end close to $\kappa = 2$. We remark that the coordinates of such line in the plane (ω_2, ω_3) with $\kappa = 1$, i.e., in the absence of the surface interaction, is exactly known to be $(\omega_2, \omega_3) = (\frac{5}{3}, \frac{25}{3})$ [9]. Hence, by assuming that the bulk transitions are not affected by the surface interaction when κ is small, the BML line should end at a special multicritical point located at $(\omega_2 = \frac{5}{3}, \omega_3 = \frac{25}{3}, \kappa \approx 2)$.

Beyond the three bulk surfaces, there are also several adsorption transition surfaces in the full phase diagram, which separate the bulk phases from the adsorbed ones. The coil-adsorbed and the globule-adsorbed are continuous, and they

meet the tricritical coil-globule surface at the multicritical CAM line. Part of the critical coil-adsorbed surface ends at the coexistence surfaces separating the crystal phase from the coil and adsorbed ones, so that a CEP line exists there. Moreover, the globule-crystal, globule-adsorbed, and crystal-adsorbed surfaces meet at another multicritical DAM line. Therefore, there are three multicritical (BML, CAM, and DAM), and a CEP line in the phase diagram. Our results for finite trails indicate that all these lines meet at the special multicritical point discussed above.

ACKNOWLEDGMENTS

T.J.O. and N.T.R. acknowledge support of the Brazilian agencies CNPq, CAPES, and FAPEMIG, and the use of the computing cluster of Universidade Federal de Viçosa. N.T.R. thanks Queen Mary University London for hosting while this work was begun, and gratefully acknowledges use of the university's HPC cluster. Financial support from the Australian Research Council via its Discovery Projects scheme (DP160103562) is acknowledged by A.L.O.

[1] J. des Cloizeaux and G. Jannink, *Polymers in Solution: Their Modelling and Structure* (Clarendon, Oxford, 1990).
[2] P.-G. De Gennes, *Scaling Concepts in Polymer Physics* (Cornell University Press, Ithaca, NY, 1979).
[3] P.-G. De Gennes, J. Physique Lett. **36**, 55 (1975).
[4] M. Stephen, Phys. Lett. A **53**, 363 (1975).
[5] B. Duplantier, J. Phys. France **43**, 991 (1982).
[6] B. Duplantier, Europhys. Lett. **1**, 491 (1986).
[7] B. Duplantier and H. Saleur, Phys. Rev. Lett. **59**, 539 (1987).
[8] B. Duplantier, J. Chem. Phys. **86**, 4233 (1987).
[9] J. Doukas, A. L. Owczarek, and T. Prellberg, Phys. Rev. E **82**, 031103 (2010).
[10] A. Bedini, A. L. Owczarek, and T. Prellberg, Phys. Rev. E **86**, 011123 (2012).
[11] A. Bedini, A. L. Owczarek, and T. Prellberg, J. Phys. A: Math. Theor. **49**, 214001 (2016).
[12] E. Eisenriegler, K. Kremer, and K. Binder, J. Chem. Phys. **77**, 6296 (1982).
[13] K. De'Bell and T. Lookman, Rev. Mod. Phys. **65**, 87 (1993).
[14] T. Vrbová and S. G. Whittington, J. Phys. A: Math. Gen. **29**, 6253 (1996).
[15] T. Vrbová and S. G. Whittington, J. Phys. A: Math. Gen. **31**, 3989 (1998).
[16] T. Vrbová and K. Procházka, J. Phys. A: Math. Gen. **32**, 5469 (1999).
[17] P. Grassberger, J. Phys. A: Math. Gen. **38**, 323 (2005).
[18] A. L. Owczarek, A. Rechnitzer, J. Krawczyk, and T. Prellberg, J. Phys. A: Math. Theor. **40**, 13257 (2007).
[19] M.-B. Luo, J. Chem. Phys. **128**, 044912 (2008).
[20] L. I. Klushin, A. A. Polotsky, H.-P. Hsu, D. A. Markelov, K. Binder, and A. M. Skvortsov, Phys. Rev. E **87**, 022604 (2013).
[21] N. T. Rodrigues, T. Prellberg, and A. L. Owczarek, Phys. Rev. E **100**, 022121 (2019).
[22] J. A. Plascak, P. H. L. Martins, and M. Bachmann, Phys. Rev. E **95**, 050501(R) (2017).
[23] P. H. L. Martins, J. A. Plascak, and M. Bachmann, J. Chem. Phys. **148**, 204901 (2018).
[24] C. J. Bradly, A. L. Owczarek, and T. Prellberg, Phys. Rev. E **97**, 022503 (2018).
[25] C. J. Bradly, A. L. Owczarek, and T. Prellberg, Phys. Rev. E **98**, 062141 (2018).
[26] I. Carmesin and K. Kremer, Macromolecules **21**, 2819 (1988).
[27] Ch. Sandhya, K. H. Bindu, K. P. N. Murthy, and V. S. S. Sastry, AIP Conf. Proc. **1349**, 117 (2011).
[28] J. Luettmer-Strathmann, F. Rampf, W. Paul, and K. Binder, J. Chem. Phys. **128**, 064903 (2008).
[29] M. A. Moore, J. Phys. A: Math. Gen. **10**, 305 (1977).
[30] R. Brak, A. L. Owczarek, and T. Prellberg, J. Phys. A: Math. Gen. **26**, 4565 (1993).
[31] P.-G. De Gennes, J. Phys. France **37**, 1445 (1976).
[32] P. J. Flory, *Principles of Polymer Chemistry* (Cornell University Press, Ithaca, NY, 1971).
[33] T. Prellberg and J. Krawczyk, Phys. Rev. Lett. **92**, 120602 (2004).
[34] P. Grassberger, Phys. Rev. E **56**, 3682 (1997).
[35] J. H. Lee, S.-Y. Kim, and J. Lee, J. Chem. Phys. **135**, 204102 (2011).
[36] I. Chang and H. Meirovitch, Phys. Rev. E **48**, 3656 (1993).
[37] H. Meirovitch and H. A. Lim, J. Chem. Phys. **91**, 2544 (1989).
[38] T. W. Burkhardt, E. Eisenriegler, and I. Guim, Nuc. Phys. B **316**, 559 (1989).

Chapter 3

Mixtures of hard-spheres on the cubic lattice

This chapter is dedicated to the presentation of the works done about mixtures of lattice gases on the cubic lattice. We initiate the chapter by presenting the published version [45] of the binary mixture composed by 0NN and 2NN particles followed by the published version [46] of the mixtures 0NN-1NN and 1NN-2NN. Lastly, the published version of the ternary mixture 0NN-1NN-2NN is presented [47].

The Journal of Chemical Physics ARTICLE scitation.org/journal/jcp

Three stable phases and thermodynamic anomaly in a binary mixture of hard particles

Cite as: J. Chem. Phys. 151, 024504 (2019); doi: 10.1063/1.5109896
Submitted: 13 May 2019 • Accepted: 24 June 2019 •
Published Online: 11 July 2019

Nathann T. Rodrigues[a] and Tiago J. Oliveira[b]

AFFILIATIONS

Departamento de Física, Universidade Federal de Viçosa, 36570-900 Viçosa, MG, Brazil

[a]Electronic mail: nathan.rodrigues@ufv.br
[b]Electronic mail: tiago@ufv.br

ABSTRACT

While the realistic modeling of the thermodynamic behavior of fluids usually demands elaborated atomistic models, much has been learned from simplified ones. Here, we investigate a model where pointlike particles (with activity z_0) are mixed with molecules that exclude their first and second neighbors (i.e., cubes of lateral size $\lambda = \sqrt{3}a$, with activity z_2), both placed on the sites of a simple cubic lattice with parameter a. Only hard-core interactions exist among the particles so that the model is athermal. Despite its simplicity, the grand-canonical solution of this model on a Husimi lattice built with cubes revels a fluid-fluid demixing, yielding a phase diagram with two fluid phases (one of them dominated by small particles—$F0$) and a solidlike phase coexisting at a triple-point. Moreover, the fluid-fluid coexistence line ends at a critical point. An anomaly in the total density (ρ_T) of particles is also found, which is hallmarked by minima in the isobaric curves of ρ_T vs z_0 (or z_2). Interestingly, the line of minimum density crosses the phase diagram starting inside the region where both fluid phases are stable, passing through the $F0$ one and ending deep inside its metastable region, in a point where the spinodals of both fluid phases cross each other.

I. INTRODUCTION

Lattice gas (LG) models have a long history in the atomistic modeling of fluids, among a wide variety of other systems.[1] In general, two key ingredients are expected to be necessary to reproduce the gas-solid-liquid phase behavior of simple fluids: repulsive excluded volume interactions, which can naturally be imposed by the particle size and lattice structure in LG systems, and short-range attractive interactions. The first one alone, even in the simplest hard-core (athermal) case, is capable of yielding entropy-driven fluid-solid transitions, provided that the range of exclusion (associated with the lateral particle size λ and its placement on the lattice) is larger than the lattice spacing a. The ordering transition in these hard-LGs is usually studied considering molecules which exclude up to their kth nearest-neighbors (NN)—the so-called kNN models. These are discrete versions of hard disks and hard spheres in two- and three-dimensions, respectively, which have been numerically investigated for a broad range of k's on the square (see Refs. 2 and 3 and references therein) and simple cubic lattices.[4] The 1NN case on the triangular lattice is the famous hard hexagon model exactly solved by Baxter.[5,6] Entropy-driven transitions in hard-LGs with particles of several other shapes have also been considered, such as triangles,[7] dimers,[8] rectangles,[9] rods,[10] Y-shaped,[11] and cubes.[12]

In mixtures of hard particles, the situation becomes much more interesting, once demixing transitions may also take place in the system. For instance, in binary nonadditive mixtures of hard particles—whose minimum distance σ_{ij} between particles i and j follows $\sigma_{AB} > (\sigma_{AA} + \sigma_{BB})/2$—a demixing is expected since the space is filled more effectively by the pure phases than by the mixture. Fluid-fluid demixing has indeed been observed in different theoretical[13–16] and numerical approaches[17–21] for binary nonadditive mixtures of isotropic hard particles. Mixtures of molecules with anisotropic shapes are also known to undergo such transition.[22–28] For additive mixtures—where $\sigma_{AB} = (\sigma_{AA} + \sigma_{BB})/2$—the situation is more controversial; while the possibility of fluid-fluid phase separation has been raised in some analytical studies of hard-spheres, provided that the particle's sizes are dissimilar enough,[29,30] it seems that the demixing is usually preempted by a fluid-solid or solid-solid coexistence (see, e.g., Refs. 31 and 32 for a detailed discussion and references).

Once *k*NN systems can display fluid-solid transitions and since binary mixtures of them are nonadditive, we are immediately led to inquire whether such mixtures display fluid-fluid demixing, yielding phase diagrams with three stable phases. This important point was first addressed by Frenkel and Louis,[20] investigating a mixture of hard hexagons (1NN) with point particles (0NN) on the triangular lattice, but no fluid-fluid transition was found. Subsequently, Van Duijneveldt and Lekkerkerker[33,34] claimed to have found three stable (gas-liquid-solid) phases for this system. However, their results were contested by Verberkmoes and Nienhuis (VN) in Ref. 35, where strong numerical evidence was presented that such mixture has in fact only the fluid and solid phases reminiscent from the simple hard hexagon model. The mixture of point particles with 1NN ones has been also studied by different methods on the square lattice.[36–38] The phase diagram of this system presents again only a fluid and a solid phase, which are separated by a critical and a coexistence line meeting at a tricritical point. The same properties were also found in an exact (mean-field) solution of this model on the Bethe lattice.[39] It is noteworthy that the same scenario was suggested for the hard hexagons with point particles by VN.[35] In three dimensions, as far as we know, there exists no study of mixtures of *k*NN molecules. Therefore, it seems that the existence of three stable ("gas-liquid-solid") phases arising in LG systems consisting of binary mixtures of *k*NN particles is still an open issue.

Here, we investigate the (nonadditive) mixture of 0NN with 2NN molecules placed on the simple cubic lattice and demonstrate that beyond the solid phase, two stable fluid phases are also present in the phase diagram. Actually, we present a mean-field approximation for the model on the cubic lattice, consisting of its semi-analytical grand-canonical solution on a Husimi lattice—the core of a Cayley tree—built with cubes [see Fig. 1(a)]. As an aside, we remark that this kind of solution on hierarchical lattices advances over other typical mean-field treatments because some correlations

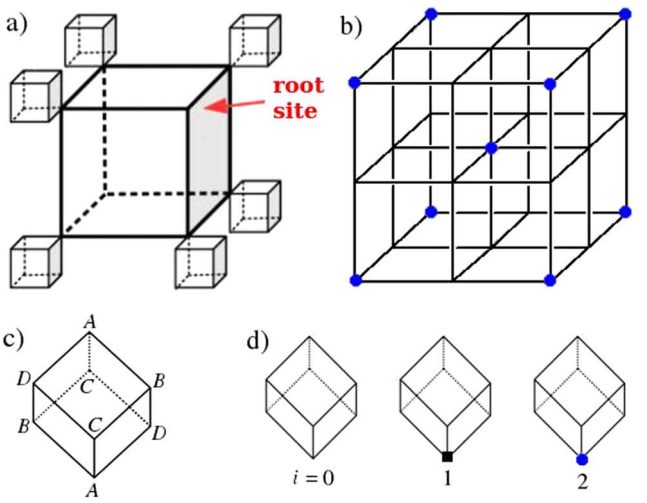

FIG. 1. (a) Illustration of part of a Husimi lattice built with cubes. (b) The ground state of the solid phase (the limit $z_2 \to \infty$, with $z_0 = 0$) in the cubic lattice. (c) Definition of sublattices in an elementary cube. (d) Possible states of the root site, where 0NN and 2NN particles are indicated by a square and a circle, respectively.

are still present in the system.[40] For this reason, they not only usually provide the qualitatively correct thermodynamic behavior for the analyzed models (as is the case, for instance, in the 0NN-1NN mixture on the square and Bethe lattices[38,39]), but for some LG models, they yield even some quantitative agreement with results from Monte Carlo simulations on regular lattices.[41,42] In some LG systems (e.g., with nematic order), however, more elaborated lattices may be need.[43] In our present study, beyond the fluid and solid phases expected for the simple 2NN model,[4] a second disordered (fluidlike) phase is also stable for large activity of 0NN particles, which is featured by a dominance of such particles. A rich phase diagram is obtained, with this 0NN fluid (*F*0) phase coexisting with the regular fluid (*RF*) and solid (*S*) ones at a triple point (TP), where the *RF*-*S*, *RF*-*F*0, and *F*0-*S* coexistence lines meet. The fluid-fluid coexistence line ends at a critical point (CP). A density anomaly, characterized by minima in the isobaric density curves, is observed in this system, indicating that it can be very useful as a starting point for understanding the behavior of more complex fluids.

The rest of the paper is organized as follows. In Sec. II, we define the model and solve it on the Husimi lattice in terms of recursion relations (RRs). The thermodynamic properties of the model are presented in Sec. III. Our final discussions and conclusions are summarized in Sec. IV. The calculation of the free energy is devised in the Appendix.

II. MODEL DEFINITION AND SOLUTION IN TERMS OF RECURSION RELATIONS

We consider a lattice gas with a binary mixture of hard particles placed on (and centered at) the vertices of a cubic lattice. Assuming that the lattice spacing is a, the small particles (0NN) are cubes of lateral size $\lambda = a$, with faces parallel to the lattice, so that they occupy a single lattice site and do not exclude their neighbors. On the other hand, the large particles (2NN) are cubes of lateral size $\lambda = \sqrt{3}a$ slanted in a way that they exclude their first and second nearest neighbors. Activities z_0 and z_2 are associated with 0NN and 2NN particles, respectively. Thereby, for $z_0 = 0$, one recovers the simple 2NN model, which have already been investigated through Monte Carlo simulations on the cubic lattice and displays a discontinuous fluid-solid transition.[4] Moreover, in the limit $z_0 \to \infty$, with z_2 finite, all sites are occupied with 0NN particles, leading to the densities $\rho_0 = 1$ and $\rho_2 = 0$ for the densities of small and large particles, respectively. In the opposite limit ($z_2 \to \infty$, with z_0 finite), however, only 1/4 of the lattice sites can be occupied by the large particles so that $\rho_2 = 1/4$ and $\rho_0 = 0$. In this case, one has the ground state of the solid phase, which is featured by a sublattice ordering, as shows Fig. 1(b). Namely, dividing the lattice into four sublattices (A, B, C, and D), composed by the two diametrically opposite sites in each elementary lattice cube [see Fig. 1(c)], the solid phase is hallmarked by a symmetry breaking, such that one of these sublattices is more populated than the others.

In order to solve this model on a Husimi lattice built with cubes, we define partial partition functions (ppfs) according to the state of the root site of an elementary cube. As shows Fig. 1(d), for each sublattice, there are three possible states: the root site can be empty ($i = 0$), occupied by a 0NN ($i = 1$) or a 2NN particle ($i = 2$). Since there are four sublattices, one has a total of 12 possible states for the

root site. For sake of simplicity, for a while, let us consider that it is in sublattice A. Note that by attaching seven cubes to the vertices of another cube, with exception of the root site, we obtain a subtree with 1 generation. Then, by attaching the root sites of seven of these subtrees to the vertices of another new cube, a 2-generation subtree is built. Proceeding in this way, we can obtain a $(M+1)$-generation subtree from seven ones with M generations. Now, by taking into account the allowed configurations of the model in the new cube, we can determine all the possible ways of attaching seven subtrees to it, keeping its root site in state A_i. This give us the ppf A_i' in generation $M+1$ as a function of the ppfs A_j, B_j, C_j, and D_j (with $j = 0$, 1 and 2) in generation M. This simple procedure allows us to construct a set of recursion relations for the ppfs of the model, which for sublattice A reads

$$\begin{aligned} A_0' = {} & z_2A_2B_0^2C_0^2D_0^2 + A_0\{2z_0z_2B_1B_2C_0^2D_0^2 + z_2^2B_2^2C_0^2D_0^2 + z_0^2B_1^2(C_0+z_0C_1)^2(D_0+z_0D_1)^2 + 2B_0[z_2B_2C_0^2D_0^2 + z_0B_1(C_0+z_0C_1)^2(D_0+z_0D_1)^2] \\ & + B_0^2[2z_0z_2C_1C_2D_0^2 + z_2^2C_2^2D_0^2 + z_0^2C_1^2(D_0+z_0D_1)^2 + 2C_0(z_2C_2D_0^2 + z_0C_1(D_0+z_0D_1)^2) + C_0^2(D_0+z_0D_1+z_2D_2)^2]\} \\ & + z_0A_1(B_0+z_0B_1)^2(C_0+z_0C_1)^2(D_0+z_0D_1)^2, \end{aligned} \tag{1a}$$

$$A_1' = (A_0+z_0A_1)(B_0+z_0B_1)^2(C_0+z_0C_1)^2(D_0+z_0D_1)^2 + z_2A_2B_0^2C_0^2D_0^2, \tag{1b}$$

$$A_2' = (A_0+z_0A_1+z_2A_2)B_0^2C_0^2D_0^2. \tag{1c}$$

The ppfs for the other sublattices can be obtained from these ones by cyclic permutations of the letters ($A \to B$, $B \to C$, $C \to D$, and $D \to A$). Clearly, these recursion relations (RRs) shall diverge if they are iterated too many times, what corresponds to the building up of infinite subtrees, which is the desired thermodynamic limit. Thereby, we analyze ratios of them, defined as $R_1^{(A)} = A_1\ A_0$ and $R_2^{(A)} = A_2\ A_0$ for sublattice A, which remains finite in the thermodynamic limit. For the other sublattices, the definition is the same, with A replaced by B, C, or D. Therefore, from the 12 RRs for the ppfs, we obtain eight RRs for these ratios.

The real and positive solutions (fixed points) of these RRs correspond to the thermodynamic phases of the model on the Husimi lattice. To determine the stability limits of each phase, we calculate the Jacobian matrix, whose 64 entries are given by the derivatives $\partial R_i'^{(K)}\ \partial R_j^{(W)}$, with $i, j = 1, 2$ and $K, W = A, B, C, D$, calculated in a given fixed point. In regions of the parameter space (z_0, z_2) where the largest eigenvalue (Λ) of this matrix is smaller than one $(\Lambda < 1)$, the fixed point is stable, as well as the corresponding thermodynamic phase. The condition $\Lambda = 1$ defines the stability limits.

The partition function (Y) can be obtained, similarly to the ppfs, by considering the operation of attaching the root sites of eight subtrees to the eight vertices of a central cube. It can be written in a compact form, e.g., as

$$Y = A_0A_0' + z_0A_1A_1' + z_2A_2A_2' = (A_0B_0C_0D_0)^2y. \tag{2}$$

Using Eq. (1) to write the expanded expression for Y, the densities of small and large particles at the central cube, in sublattice K, are given, respectively, by

$$\rho_0^{(K)} = \frac{R_1^{(K)}}{8Y}\frac{\partial Y}{\partial R_1^{(K)}} \quad \text{and} \quad \rho_2^{(K)} = \frac{R_2^{(K)}}{8Y}\frac{\partial Y}{\partial R_2^{(K)}}. \tag{3}$$

Thence, $\rho_j = \rho_j^{(A)} + \rho_j^{(B)} + \rho_j^{(C)} + \rho_j^{(D)}$ gives us the total density of small $(j = 0)$ and large $(j = 2)$ particles at the central cube.

Following the ansatz proposed by Gujrati[40] and discussed in detail in the Appendix, the bulk free energy per site of each phase of the model can be calculated from

$$\phi_b = -\frac{1}{8}\ln\left[\frac{\left(R_0^{(A)}R_0^{(B)}R_0^{(C)}R_0^{(D)}\right)^2}{y^6}\right], \tag{4}$$

where $R_0^{(A)} \equiv A_0'\ \left(A_0B_0^2C_0^2D_0^2\right)$ and the others are obtained from cyclic permutations of the labels (A, B, C, and D). In regions where two or more phases are stable, the points (or lines) where the free energies of these phases are equal define the coexistence loci. We notice also that since each lattice site occupies a volume $v_0 = a^3$, the pressure in our grand-canonical formalism is given by $P = -\phi_b/a^3$.

III. THERMODYNAMIC BEHAVIOR OF THE MODEL

A. 2NN model

Let us start discussing the simple 2NN model. Since $z_0 = 0$ in this case, one has $R_1^{(A)} = R_1^{(B)} = R_1^{(C)} = R_1^{(D)} = 0$ and the recursion relations (RRs) considerably simplify. Even then we are not able to calculate simple analytical expressions for their fixed points, and so we numerically estimate them by iterating the RRs. For small values of z_2, one finds a homogeneous solution $R_2^{(A)} = R_2^{(B)} = R_2^{(C)} = R_2^{(D)}$, which corresponds to a disordered fluid (F) phase where all sublattices are equally populated. This phase is stable for $z_2 \leqslant 15.1364$. For large z_2, on the other hand, we find four equivalent fixed points featured by a symmetry breaking, such that one of the four sublattices dominates. For example, if A is the dominant sublattice, one has $R_2^{(A)} \gg R_2^{(B)} = R_2^{(C)} = R_2^{(D)}$. This corresponds to the ordered solid (S) phase, which is stable for $z_2 \geqslant 5.0620$.

Therefore, both phases coexist in the region $5.0620 \leqslant z_2 \leqslant 15.1364$, and hence, the fluid-solid transition is discontinuous. The free energy of both phases are equal $[\phi_b^{(F)} = \phi_b^{(S)}]$ at $z_2 = 5.7932$,

which defines the transition point. The particle densities at this point for the fluid and solid phases are given, respectively, by $\rho_2^{(F)} = 0.1551$ and $\rho_2^{(S)} = 0.2025$, confirming the discontinuous nature of the transition. This result is consistent with Monte Carlo simulations of this model on the cubic lattice, where a first-order transition was also found.[4] In this case, notwithstanding, the transition point is located at $z_2 \approx 1.70$,[45] which is considerably smaller than our value. In agreement with this, the densities at coexistence $\rho^{(F)} \approx 0.10$ and $\rho^{(S)} \approx 0.13$ estimated in Ref. 4 are also smaller than the ones found here. We remark that while mean-field approximations usually predict smaller critical points for continuous transitions than their correct values, this is not necessarily a rule in discontinuous transitions. In our specific case, the treelike structure of the Husimi lattice turns the ordering of 2NN particles more difficult than on the cubic lattice, demanding thus higher densities (and so a large z_2).

B. 0NN-2NN model

Now, we turn to the analysis of the properties of the full model, with two kinds of particles. For small $z_0 > 0$, one still find the fluid and solid (S) phases reminiscent from the 2NN model, but now $R_1^{(K)} \neq 0$, for $K = A, B, C$, and D. The fluid phase is still homogeneous so that $R_i^{(A)} = R_i^{(B)} = R_i^{(C)} = R_i^{(D)} \equiv R_i$, while in the solid phase, there still exists a symmetry breaking and one of the sublattices dominates (e.g., $R_i^{(A)} \approx 1$ and $R_i^{(B)} = R_i^{(C)} = R_i^{(D)} \approx 0$, for $i = 1, 2$). Beyond these expected phases, a remarkable result found here is the existence of a second homogeneous fluid phase, which is stable in the system for large values of z_0. In such phase, one also has $R_i^{(A)} = R_i^{(B)} = R_i^{(C)} = R_i^{(D)} \equiv R_i$, but with $R_1 \approx 1$ and $R_2 \approx 0$. Namely, this phase is featured by a dominance of the RRs associated with small particles, and so, hereafter we will refer to it as the 0NN fluid ($F0$) phase. By contrast, in the regular fluid (RF) phase, the values of R_1 and R_2 depend more on the activities (z_0 and z_2).

Figure 2(a) presents the stability limits (the spinodals) of these phases in the (z_0, z_2) space. We find that the S phase is stable for any value of z_0 provided that z_2 is large enough. Conversely, the $F0$ phase is stable for any value of z_2 for large z_0's. The RF phase, on the other hand, is stable only in a limited region of the parameter space where z_0 and z_2 are both not too large. Interestingly, the spinodals of the RF and $F0$ phases meet each other and end at the point $(z_{0,c}, z_{2,c}) = (0.6297, 5.4243)$, which turns out to be a critical point (CP). Hence, in the region below this point (for $z_2 < z_{2,c}$), we have a single fluid since we cannot distinguish between the RF and $F0$ phases.

With exception to the CP and some points where they cross each other, the spinodals do not coincide elsewhere. This implies that there are no continuous transition lines in the phase diagram of the model, and only discontinuous transitions separate the phases.

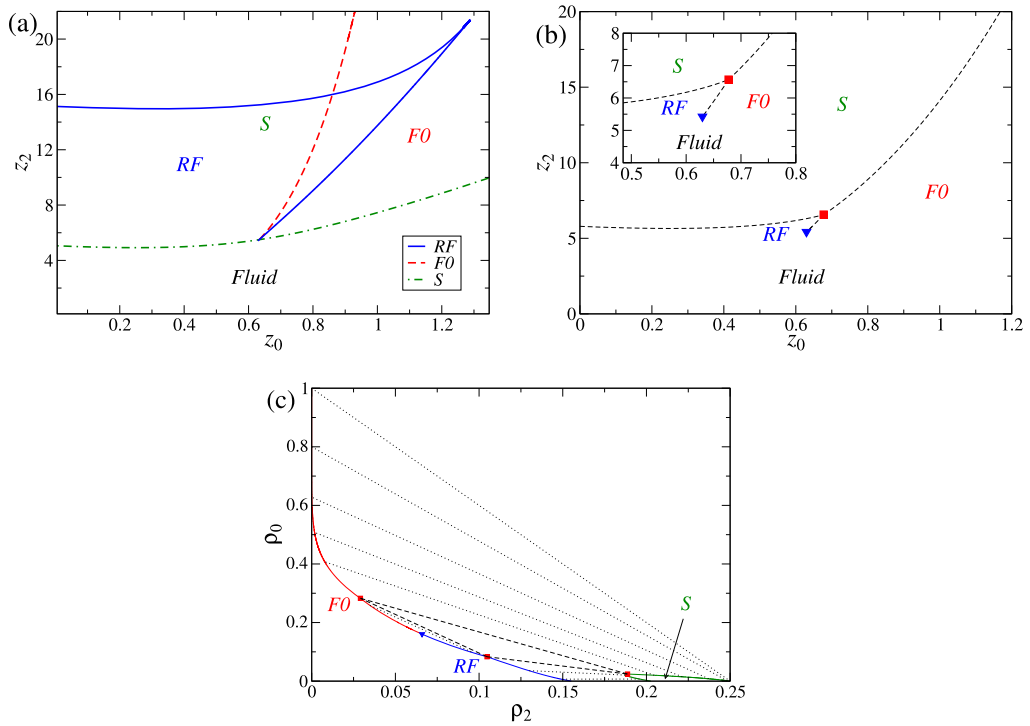

FIG. 2. (a) Stability limits of the regular fluid (RF), 0NN fluid ($F0$), and solid (S) phases. For small z_2, the RF and $F0$ phases become indistinguishable in a single *fluid*. (b) Phase diagram in space (z_0, z_2). The dashed lines are the coexistence loci, while the square (red) and triangle (blue) symbols are the triple and critical points, respectively. The inset highlights the region around these points. (c) Phase diagram in density (ρ_2, ρ_0) space. The solid, dashed, and dotted lines are the coexistence loci, the triple point, and tie lines, respectively.

Indeed, we have found three coexistence lines: *RF*-*S*, *RF*-*F*0, and *F*0-*S*, which meet at a triple point (TP) located at $(z_{0,TP}, z_{2,TP}) = (0.6774, 6.5671)$. See Fig. 2(b). The *RF*-*S* transition line starts at $z_0 = 0$ (and $z_2 = 5.7932$ as discussed in Subsection III A) and ends at the TP. It is interesting to notice that initially this line decreases with z_0, having an initial slope $(dz_2\ dz_0)|_{z_0\to 0} = -1$. Then, it passes through a minimum—located at $z_0 = 0.2523$ and $z_2 = 5.6522$—after which it increases toward the TP. A very similar behavior has been found for the fluid-solid transition in the mixture of 0NN and 1NN particles on the square lattice and approximations to it, although in this case, such transition is continuous for small z_0.[37–39] Anyhow, in all cases, the initial decreasing in the transition lines is certainly a consequence of the effectively attractive depletion interaction among the large particles induced by the smaller ones.

The *RF*-*F*0 coexistence line extends from the CP to the TP, giving rise to a fluid-fluid demixing transition. The *F*0-*S* transition line starts at the TP and extends to $z_0, z_2 \to \infty$, being associated with a fluid-solid demixing. For large values of z_0 and z_2, the fixed point of the *S* phase tends to, e.g., $R_1^{(A)} = R_2^{(A)} = 1$ and $R_1^{(K)} = R_2^{(K)} = 0$ for $K = B$, C, and D, whilst for the *F*0 phase, one has $R_1^{(K)} = 1$ and $R_2^{(K)} = 0$ for $K = A$, B, C, and D. Inserting such limiting values into the (expanded) expression for the free energy, it is easy to demonstrate that the *F*0-*S* coexistence line is given by

$$z_2 = 3z_0 + 6z_0^2 + 4z_0^3 + z_0^4, \tag{5}$$

for large values of z_0 and z_2. Hence, in the limit $z_0 \to \infty$, we have $z_2 \approx z_0^4$ at the coexistence. This is indeed expected since a 2NN particle effectively occupies a volume of four 0NN ones.

To better understand the differences among the three phases, especially between the two fluid ones, let us take a closer look at the particle densities. The phase diagram in (ρ_2, ρ_0) space is presented in Fig. 2(c), where one sees that the *F*0 phase is featured by large ρ_0 and small ρ_2, the opposite occurring in the *S* phase, while in the *RF* phase both densities assume intermediate values interpolating between the ones for the other two phases. Figures 3(a)–3(c) display the densities ρ_0 and ρ_2 as functions of z_2 for three values of z_0, chosen such that the three coexistence lines are crossed. The first point to notice is that the *S* phase is indeed always featured by $\rho_2^{(S)} \gg \rho_0^{(S)}$, as expected, while an opposite behavior is observed in the *F*0 one, namely, $\rho_0^{(F0)} \gg \rho_2^{(F0)}$. This confirms that this phase is indeed dominated by 0NN particles, as already anticipated by the fixed point symmetry. In the *RF* phase, on the other hand, the densities strongly depend on the activities. Anyhow, in general, one has that $\rho_2^{(RF)} > \rho_0^{(RF)}$ and $\rho_2^{(RF)} < \rho_0^{(RF)}$ at the *RF*-*S* and *RF*-*F*0 coexistence, respectively. This is also evidenced in the diagrams $z_0/(1 + z_0) \times \rho_0$ and $z_0/(1 + z_0) \times \rho_2$, depicted in Figs. 4(a)–4(b), where the densities at the coexistence lines are shown. Once we know the exact asymptotic form of the coexistence line [Eq. (5)] and the fixed points there for large z_0, the densities of small and large particles can be

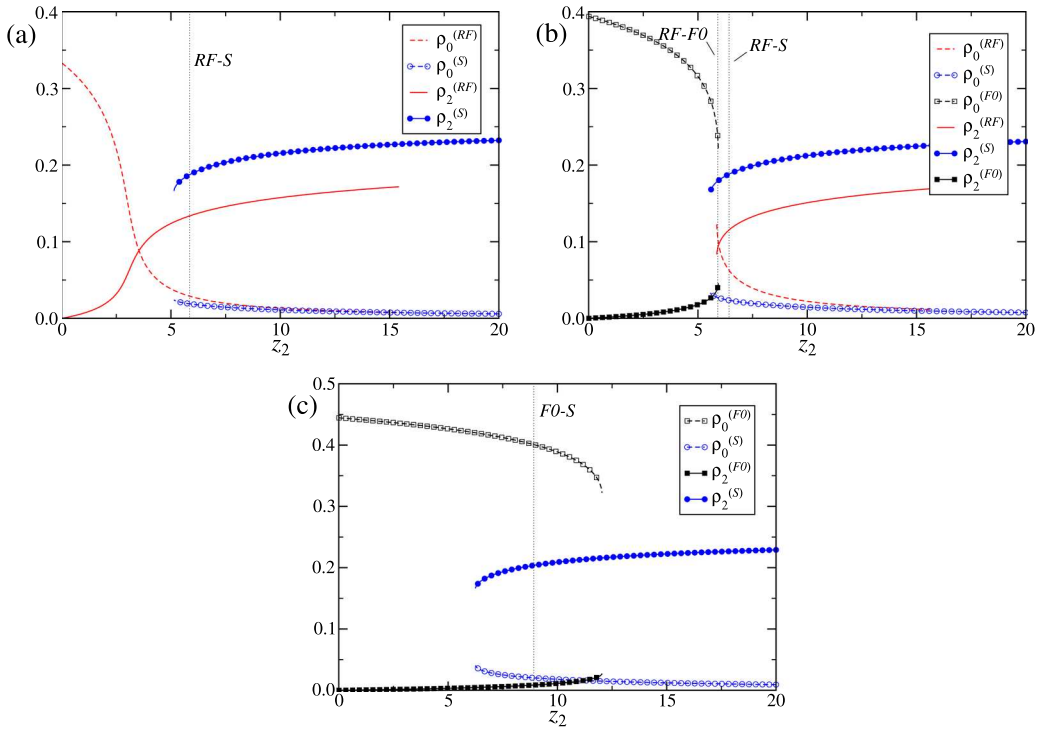

FIG. 3. Densities of small (ρ_0) and large (ρ_2) molecules as a function of z_2 for (a) $z_0 = 0.5$, (b) $z_0 = 0.65$, and (c) $z_0 = 0.8$. The vertical lines are located at the transition points between the phases indicated in each case.

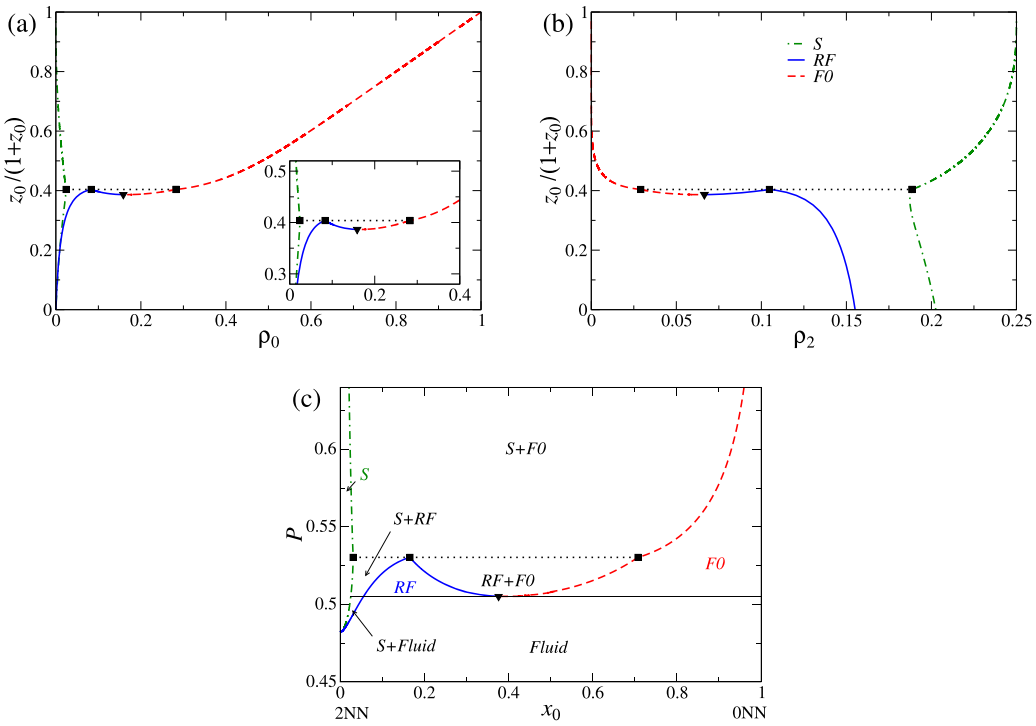

FIG. 4. Phase diagrams in the variable $z_0/(1 + z_0)$ as a function of the densities (a) ρ_0 and (b) ρ_2; and (c) in the pressure (P) vs molar fraction of 0NN particles (x_0) plane. The thicker lines are the displayed quantities at coexistence, with exception of the horizontal dotted lines, which indicate the triple point, where the three squares are connected. The critical point is represented by the triangle and the thin horizontal solid line in (c) separates the regions above and below it. The insertion in (a) highlights the region around these points.

obtained in such limit. This gives $\rho_0^{(F0)} \approx 1 - \frac{1}{z_0}$ and $\rho_2^{(F0)} \approx \frac{1}{z_0^2}$ in the $F0$ phase and $\rho_0^{(S)} \approx \frac{1}{4z_0^3}$ and $\rho_2^{(S)} \approx \frac{1}{4} - \frac{1}{4z_0^3}$ in the S one, in fully agreement with the behaviors presented in Figs. 4(a)–4(b). Particularly, this explains the asymptotic linear variation observed in $\rho_0^{(F0)}$ in Fig. 4(a). We remark that we have refrained from referring to the RF and $F0$ phases as gas and liquid, respectively, because the total density of particles ($\rho_T = \rho_0 + 4\rho_2$) at coexistence can be larger in the RF phase. For instance, for $z_0 = 0.65$, whose densities are displayed in Fig. 3(b), one finds $\rho_T^{(RF)} \approx 0.47$ and $\rho_T^{(F0)} \approx 0.40$ at the coexistence point.

Figure 4(c) shows the phase diagram in the pressure-composition (P, x_0) plane, where the molar fraction of 0NN particles was defined as $x_0 = \rho_0/\rho_T$. In such diagram, which is qualitatively similar to the $z_0/(1 + z_0) \times \rho_0$ shown in Fig. 4(a), a detailed description of the several coexistence regions is presented. Although this is not clear in the scale of Fig. 4(c), which highlights the region around the critical and triple points, the (dashed-dotted) line for the

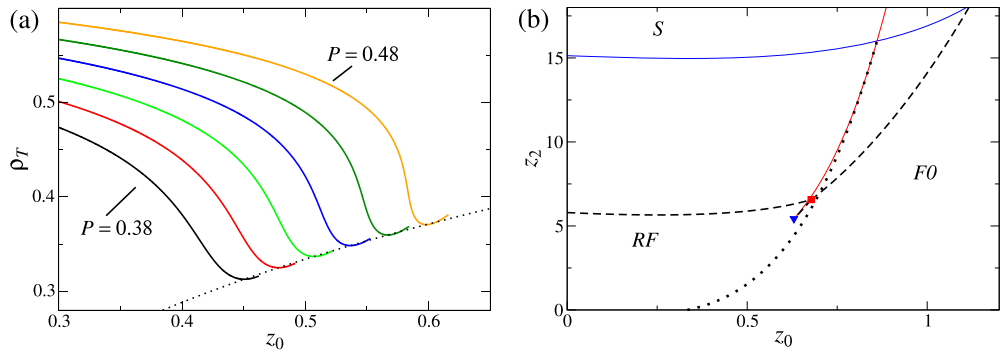

FIG. 5. (a) Isobaric curves of the total density of particles ρ_T vs z_0 for pressures in the interval [0.38, 0.48]. The dotted line indicates the line of minimum density (LMD). In (b), such curve is plotted along with the (z_0, z_2)-phase diagram and some spinodals.

S phase and the (dashed) one for the $F0$ phase increase indefinitely as $x_0 \to 0$ and $x_0 \to 1$, respectively. In fact, in such limits, which correspond to z_0, $z_2 \to \infty$ along the coexistence line, it is simple to shown [from the asymptotic behaviors discussed around Eq. (5)] that $P^{(S)} \sim \ln[1 + z_0 + z_2] \sim \ln z_0^4$ and $P^{(F0)} \sim \ln[1 + z_0] \sim \ln z_0$. So, from the asymptotic behavior of the densities just discussed above, we readily obtain $P^{(S)} \sim -\ln x_0$, as $x_0 \to 0$, and $P^{(F0)} \sim -\ln[1 - x_0]$, for $x_0 \to 1$.

Interestingly, the total density of particles for the fluid phases, calculated along isobaric curves, display a thermodynamic anomaly characterized by minima in $\rho_T \times z_0$ curves, as shows Fig. 5(a). A similar anomalous behavior is also found in $\rho_T \times z_2$ curves. The coordinates (z_0, z_2) of such minima for different pressures give rise to a monotonic increasing line of minimum density (LMD), which starts below the CP, at $z_0 \approx 0.333$ when $z_2 \to 0$, enters the region where the $F0$ phase is stable, crosses the $F0$-S coexistence line, continues within the metastable $F0$ phase, and finally ends at a point where the RF and $F0$ spinodals cross each other [see Fig. 5(b)]. This point is located deep inside the region where the solid phase is more stable so that one may say that the LMD extends to a region where the fluids are super-cooled. We recall that a similar LMD was found in the 0NN-1NN mixture on the square lattice, where it also starts inside the fluid phase but ends at the tricritical point present in such model, without passing through metastable regions.[38]

IV. FINAL DISCUSSIONS AND CONCLUSIONS

In summary, we have demonstrated that the athermal binary mixture of 2NN molecules (excluding up to their second-nearest neighbor sites) with 0NN ones (which only exclude the site they are sited on) display a stable fluid-fluid demixing, yielding a very rich thermodynamic behavior with three stable phases in the diagram. The regular fluid (RF) and solid (S) phases are quite expected since they are already present in the pure 2NN model. On the other hand, the existence of a second fluid phase ($F0$) featured by a dominance of 0NN particles, although it is somewhat expected because of the nonadditivity of the mixture, turns out to be a very interesting result, in face of its absence in other mixtures of kNN particles. We remark that other phases, such as columnar and smectic (observed in some studies of hard cubes with faces parallel to the cubic lattice[12,32]) are absent in our approach. This is consistent with numerical simulations of the pure 2NN model on the cubic lattice, where only a fluid and a solid phase were found.[4] The fluid-fluid demixing observed here, but inexistent in the 0NN-1NN mixtures analyzed (on planar lattices) so far, indicate that, in the last case, the particle's sizes are not so dissimilar to make this transition stable. Following this thought, our results suggest that 0NN-kNN mixtures, with $k \geq 2$, shall present two stable fluid phases. Moreover, kNN-k'NN with $k' \geqslant k + 2$ can be the condition for fluid-fluid demixing. These points are very important to be analyzed in future works. We anticipate that unfortunately the Husimi lattice built with elementary cubes does not capture the symmetries of the solid phases of kNN particles for $k > 2$ so that other methods shall be employed to investigate mixtures with larger k's. Particularly important might be Monte Carlo simulations for kNN mixtures on the cubic lattice, even to confirm the fluid-fluid demixing observed here, where the differences in particle densities in both fluid phases [as demonstrated in Fig. 3(b)] might be very important to distinguish them and to determine the possible transition lines.

Finally, we notice that the thermodynamic anomalies observed, e.g., in water and other polymorphic fluids usually require a complex modeling to be reproduced.[44] Our system, similarly to the 0NN-1NN mixture on other lattices,[38,39] demonstrates that a density anomaly can arise in such very simplified models for fluids. Although minima in the isobaric curves of the total density are observed here, whereas in water, for example, there exist maxima, this indicates that athermal binary mixtures might be useful as a starting building block for the modeling of complex fluids.

ACKNOWLEDGMENTS

This work was partially supported by CNPq, CAPES, and FAPEMIG (Brazilian agencies).

APPENDIX: FREE ENERGY IN A HUSIMI LATTICE BUILT WITH CUBES

A M-generation Cayley tree built with cubes has $N_s = 8 \times 7^M$ sites at the surface and $N_b = 4[7^M - 1]/3$ ones in the bulk. Hence, in contrast to regular lattices, the tree is dominated by surface sites in the thermodynamic limit ($M \to \infty$). Thereby, in order to calculate the free energy in the bulk of such Cayley tree (i.e., in the Husimi lattice), we have to discount the surface contribution. Once the free energy of a M-generation tree is $\Phi_M = \tilde{\Phi}_M \; k_B T = -\ln Y_M$, following Ref. 40, if we assume that ϕ_b and ϕ_s denote the free energy per site of bulk and surface sites, respectively, then, we may also write $\Phi_M = N_b\phi_b + N_s\phi_s$. From here, it is a simple matter to see that

$$\phi_b = \frac{1}{8}(\Phi_{M+1} - 7\Phi_M) = -\frac{1}{8}\ln\left[\frac{Y_{M+1}}{Y_M^7}\right]. \tag{A1}$$

From Eq. (2), we have $Y_M = \left[A_0^{(M)}B_0^{(M)}C_0^{(M)}D_0^{(M)}\right]^2 y$, while Eq. (1a) demonstrates that $A_0^{(M+1)} = A_0^{(M)}(B_0^{(M)}C_0^{(M)}D_0^{(M)})^2R_0^{(A)}$ and similar relations can be obtained for the other sublattices by cyclic permutations of their labels. Substituting these expressions into the rhs of Eq. (A1), we arrive at Eq. (4). We note that y and $R_0^{(K)}$, for $K = A, \ldots, D$, do depend only on the ratios and, so, are independent of M in the thermodynamic limit.

REFERENCES

[1] B. Simon, *The Statistical Mechanics of Lattice Gases* (Princeton University Press, New Jersey, 1993).
[2] H. C. Marques Fernandes, J. J. Arenzon, and Y. Levin, J. Chem. Phys. **126**, 114508 (2007).
[3] T. Nath and R. Rajesh, Phys. Rev. E **90**, 012120 (2014).
[4] A. Z. Panagiotopoulos, J. Chem. Phys. **123**, 104504 (2005).
[5] R. J. Baxter, J. Phys. A: Math. Gen. **13**, L61 (1980).
[6] R. J. Baxter, *Exactly Solved Models in Statistical Mechanics* (Academic Press, London, 1989).
[7] A. Verberkmoes and B. Nienhuis, Phys. Rev. Lett. **83**, 3986 (1999).
[8] P. Kasteleyn, Physica **27**, 1209 (1961); H. N. V. Temperley and M. E. Fisher, Philos. Mag. **6**, 1061 (1961); D. A. Huse, W. Krauth, R. Moessner, and S. L. Sondhi, Phys. Rev. Lett. **91**, 167004 (2003); R. Dickman, J. Chem. Phys. **136**, 174105 (2012).
[9] J. Kundu and R. Rajesh, Phys. Rev. E **89**, 052124 (2014); **91**, 012105 (2015); T. Nath, J. Kundu, and R. Rajesh, J. Stat. Phys. **160**, 1173 (2015); P. Gurin,

S. Varga, M. González-Pinto, Y. Martínez-Ratón, and E. Velasco, J. Chem. Phys. **146**, 134503 (2017).
[10]A. Ghosh and D. Dhar, Europhys. Lett. **78**, 20003 (2007); J. Kundu, R. Rajesh, D. Dhar, and J. F. Stilck, Phys. Rev. E **87**, 032103 (2013); A. Gschwind, M. Klopotek, Y. Ai, and M. Oettel, *ibid.* **96**, 012104 (2017); N. Vigneshwar, D. Dhar, and R. Rajesh, J. Stat. Mech. **2017**, 113304.
[11]D. Mandal, T. Nath, and R. Rajesh, Phys. Rev. E **97**, 032131 (2018).
[12]N. Vigneshwar, D. Mandal, K. Damle, D. Dhar, and R. Rajesh, Phys. Rev. E **99**, 052129 (2019).
[13]B. Widom and J. S. Rowlinson, J. Chem. Phys. **52**, 1670 (1970).
[14]T. W. Melnyk and B. L. Sawford, Mol. Phys. **29**, 891 (1975).
[15]A. A. Louis, R. Finken, and J. P. Hansen, Phys. Rev. E **61**, R1028 (2000).
[16]A. Santos, M. López de Haro, and S. B. Yuste, J. Chem. Phys. **132**, 204506 (2010).
[17]M. Dijkstra, Phys. Rev. E **58**, 7523 (1998).
[18]M. Schmidt, J. Phys.: Condens. Matter **16**, L351 (2004).
[19]J. M. Brader and R. L. C. Vink, J. Phys.: Condens. Matter **19**, 036101 (2007).
[20]D. Frenkel and A. A. Louis, Phys. Rev. Lett. **68**, 3363 (1992).
[21]R. Dickman and G. Stell, J. Chem. Phys. **102**, 8674 (1995).
[22]R. van Roij, B. Mulder, and M. Dijkstra, Physica A **261**, 374 (1998).
[23]H. H. Wensink, G. J. Vroege, and H. N. W. Lekkerkerker, J. Chem. Phys. **115**, 7319 (2001).
[24]S. Dubois and A. Perera, J. Chem. Phys. **116**, 6354 (2002).
[25]S. Varga, A. Galindo, and G. Jackson, J. Chem. Phys. **117**, 7207 (2002).
[26]M. Schmidt and A. R. Denton, Phys. Rev. E **65**, 021508 (2002).
[27]Y. Martínez-Ratón, E. Velasco, and L. Mederos, Phys. Rev. E **72**, 031703 (2005).
[28]D. de las Heras, Y. Martínez-Ratón, and E. Velasco, Phys. Rev. E **76**, 031704 (2007).
[29]T. Biben and J. P. Hansen, Phys. Rev. Lett. **66**, 2215 (1991).
[30]H. N. W. Lekkerkeker and A. Stroobants, Physica A **195**, 387 (1993).
[31]L. Lafuente and J. A. Cuesta, Phys. Rev. Lett. **89**, 145701 (2002).
[32]L. Lafuente and J. A. Cuesta, J. Chem. Phys. **119**, 10832 (2003).
[33]J. S. van Duijneveldt and H. N. W. Lekkerkeker, Phys. Rev. Lett. **71**, 4264 (1993).
[34]J. S. van Duijneveldt and H. N. W. Lekkerkeker, J. Stat. Phys. **77**, 103 (1995).
[35]A. Verberkmoes and B. Nienhuis, Phys. Rev. E **60**, 2501 (1999).
[36]D. Poland, J. Chem. Phys. **80**, 2767 (1984).
[37]D.-J. Liu and J. W. Evans, J. Chem. Phys. **114**, 10977 (2001).
[38]T. J. Oliveira and J. F. Stilck, Phys. Rev. E **92**, 032101 (2015).
[39]T. J. Oliveira and J. F. Stilck, J. Chem. Phys. **135**, 184502 (2011).
[40]P. D. Gujrati, Phys. Rev. Lett. **74**, 809 (1995).
[41]C. Buzano, E. De Stefanis, and M. Pretti, J. Chem. Phys. **129**, 024506 (2008).
[42]T. J. Oliveira, J. F. Stilck, and M. A. A. Barbosa, Phys. Rev. E **82**, 051131 (2010).
[43]D. Dhar, R. Rajesh, and J. Stilck, Phys. Rev. E **84**, 011140 (2011).
[44]*Liquid Polymorphism*, Advances in Chemical Physics Vol. 152, edited by H. E. Stanley (Wiley, 2013).
[45]Note that the chemical potential at coexistence ($\beta\mu = 2.18 \pm 0.01$) reported in Ref. 4 is related with the activity through $z_2 = e^{\beta\mu}/\sigma^3$, where $\sigma = \lambda\ \ a = \sqrt{3}$ for the 2NN particles.

Thermodynamic behavior of binary mixtures of hard spheres: Semianalytical solutions on a Husimi lattice built with cubes

Nathann T. Rodrigues [*] and Tiago J. Oliveira [†]
Departamento de Física, Universidade Federal de Viçosa, 36570-900 Viçosa, MG, Brazil

(Received 9 July 2019; published 9 September 2019)

We study binary mixtures of hard particles, which exclude up to their kth nearest neighbors (kNN) on the simple cubic lattice and have activities z_k. In the first model analyzed, point particles (0NN) are mixed with 1NN ones. The grand-canonical solution of this model on a Husimi lattice built with cubes unveils a phase diagram with a fluid and a solid phase separated by a continuous and a discontinuous transition line which meet at a tricritical point. A density anomaly, characterized by minima in isobaric curves of the total density of particles against z_0 (or z_1), is also observed in this system. Overall, this scenario is identical to the one previously found for this model when defined on the square lattice. The second model investigated consists of the mixture of 1NN particles with 2NN ones. In this case, a very rich phase behavior is found in its Husimi lattice solution, with two solid phases—one associated with the ordering of 1NN particles ($S1$) and the other with the ordering of 2NN ones ($S2$)—beyond the fluid (F) phase. While the transitions between F-$S2$ and $S1$-$S2$ phases are always discontinuous, the F-$S1$ transition is continuous (discontinuous) for small (large) z_2. The critical and coexistence F-$S1$ lines meet at a tricritical point. Moreover, the coexistence F-$S1$, F-$S2$, and $S1$-$S2$ lines meet at a triple point. Density anomalies are absent in this case.

DOI: 10.1103/PhysRevE.100.032112

I. INTRODUCTION

Hard spheres (and hard disks in two dimensions) interacting only through an infinite hard-core potential form the simplest interacting models for a classical fluid. Such athermal models have received a lot of attention in the last decades, because they allow us to investigate only the entropic effect on the thermodynamics of fluids and for their appealing role in the modeling of granular systems [1]. In the monodisperse case, a first-order fluid-solid transition has been observed in numerical simulations of hard spheres [2–4]. For binary mixtures of particles with dissimilar sizes, several solid phases may arise [see, e.g., Ref. [5] and references therein]. Moreover, beyond the freezing transition, the existence of solid-solid and fluid-fluid demixing transitions are also expected. For nonadditive mixtures of hard particles a demixing is expected because particles fill the space more effectively when separated into pure phases [6–9]. Numerical simulations of binary nonadditive mixtures of hard spheres have indeed confirmed this [8,10]. In the case of additive mixtures the scenario is a bit more controversial, with the possibility of fluid-fluid phase separation being demonstrated in some recent analytical treatments, provided that the particle's sizes are dissimilar enough [11,12], in contrast with elder analytical approaches ruling out the demixing [13]. However, in general, fluid-solid or solid-solid coexistence can preempt the fluid-fluid transition [see, e.g., Refs. [14,15] and references therein].

When defined on a lattice, the hard spheres (and disks) are approximated by kNN particles, i.e., particles which forbid up to their kth nearest neighbor (NN) sites of being occupied. The 0NN case consists of point particles which do not interact and, so, do not undergo any transition. However, pure kNN models with $k \geqslant 1$ are known to present fluid-solid transitions. For instance, the 1NN case on the triangular lattice is the famous hard-hexagon model exactly solved by Baxter [16,17], whose continuous fluid-solid transition belongs to a universality class different from the Ising one found for this model on the square lattice [18]. In the cubic lattice, 3D Ising exponents have been found for the 1NN model [19,20]. While recent works indicate that the transition in the 2NN model on the square lattice is continuous, its universality class is still a subject of debate (see, e.g., Refs. [21,22] and references therein). On the cubic lattice, a discontinuous fluid-solid transition has been found for this model both on numerical simulations [23] and mean-field approximations [24]. For larger k's, discussions on the behavior can be found in Refs. [22,25] for the square and [23] for the cubic lattice.

As an aside, let us notice that entropy-driven transitions have been also investigated for other particle shapes, such as cubes [26], dimers [27], rectangles [28], rods [29], triangles [30], Y-shaped [31], etc., on different lattices. Some binary mixtures of hard lattice gases with isotropic [10,32–37] and anisotropic particles [38–45] have been also analyzed, which in several cases exhibit fluid-fluid or solid-solid demixing transitions.

Curiously, however, mixtures of kNN particles are far less explored. For instance, the 0NN-1NN case has been investigated on the square lattice by means of series expansions [46] and transfer matrix calculations [47,48]. These later studies revealed a grand-canonical phase diagram featured by a fluid and a solid phase separated by a continuous and a discontinuous transition line, which meet at a tricritical point.

[*] nathan.rodrigues@ufv.br
[†] tiago@ufv.br

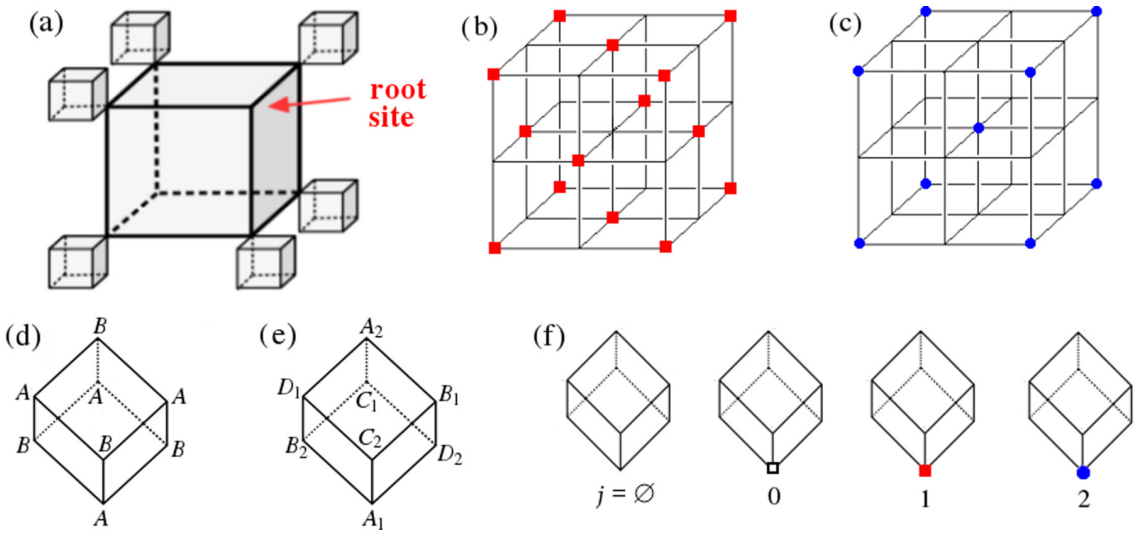

FIG. 1. (a) Illustration of part of a Husimi lattice built with cubes. The ground states of the solid $S1$ (b) and $S2$ (c) phases on the cubic lattice. Definitions of sublattices in an elementary cube used to solve the 0NN-1NN (d) and 1NN-2NN (e) mixtures. (f) Possible states of the root site, where 0NN, 1NN and 2NN particles are indicated by an open square, a full square and a circle, respectively.

The same scenario was found in a mean-field solution of this model on the Bethe lattice [49]. Interestingly, such model display a thermodynamic anomaly characterized by minima in isobaric curves of the total density of particles [48,49]. On the triangular lattice, some authors [50,51] claimed to have numerically found a fluid-fluid transition, yielding three stable (gas-liquid-solid) phases for the 0NN-1NN mixture. However, evidence against the fluid-fluid demixing have been presented in other works [34,52]. Particularly, in Ref. [52] strong numerical evidence for a phase diagram similar to the one just discussed for the square lattice was presented.

On the cubic lattice, for the best of our knowledge, only the 0NN-2NN mixture has been considered up to now, via a semianalytical (mean-field) solution of the model on a Husimi lattice built with cubes [24]. Interestingly, a stable fluid-fluid transition was found in this system, so that three stable phases are present in its grand-canonical phase diagram: two fluids (being one regular and other featured by a dominance of point particles) and a solid phase. These phases are separated by first-order transition lines which meet at a triple point, while the fluid-fluid coexistence line ends at a critical point. A density anomaly similar to the one found on the square lattice 0NN-1NN model is also present in this system. In face of the scarcity of binary systems presenting fluid-fluid transitions, it turns out very important to extend the existing studies for other mixtures of kNN particles, in order to determine the conditions (e.g., the difference in particle size) necessary for its onset. Moreover, binary mixtures of hard particles are certainly more appealing for the modeling of real fluids or granular matter than the monocomponent case—for instance, binary mixtures of colloidal hard-spheres have been widely studied [53]—which also justify further investigations of these systems.

Here, we address this by analyzing the mixtures of 0NN-1NN and 1NN-2NN particles defined on the simple cubic lattice. From semianalytical grand-canonical solutions of these models on Husimi lattices built with cubes [see Fig. 1(a)], we demonstrate that no fluid-fluid demixing occurs in such mixtures, in contrast with the 0NN-2NN one [24]. In fact, the thermodynamic behavior of the 0NN-1NN model is qualitatively the same described above for its counterpart on the square lattice. For the 1NN-2NN mixture, a solid-solid demixing is found, between the ordered phases characteristic of the 1NN and 2NN particles, while a single fluid phase is present in the system. These three phases give rise to a very rich phase diagram, with continuous and discontinuous transitions lines, a tricritical and a triple point.

The rest of the paper is organized as follows. In Sec. II we define the models and devise their solutions on the Husimi lattice built with cubes. The thermodynamic properties of the 0NN-1NN and 1NN-2NN mixtures are presented in Secs. III and IV, respectively. In Sec. V our final discussions and conclusions are summarized. Some details on the model solutions are presented in the Appendix.

II. MODELS AND THEIR SOLUTION ON A HUSIMI LATTICE BUILT WITH CUBES

We consider lattice gases consisting of binary mixtures of hard particles placed on (and centered at) the vertices of a cubic lattice. Assuming that the lattice spacing is a, the small particles (0NN) are cubes of lateral size $\lambda = a$, which occupy a single lattice site and do not exclude their neighbors. However, the larger 1NN (2NN) particles are cubes of lateral size $\lambda = \sqrt{2}a$ ($\lambda = \sqrt{3}a$) placed on the lattice in a way that they exclude their first (first and second) nearest neighbors. An activity z_k is associated with each kNN particle. The mixture 0NN-2NN ($z_1 = 0$ case) was already investigated by us in Ref. [24], so here we will focus on the cases $z_2 = 0$ and $z_0 = 0$, corresponding, respectively, to the mixtures 0NN-1NN and 1NN-2NN.

Let us remark that while the pure 0NN system ($z_1 = z_2 = 0$) can be trivially solved and does not display any transition, the pure 1NN ($z_0 = z_2 = 0$) and 2NN ($z_0 = z_1 = 0$) models

on the cubic lattice are known to undergo a continuous and a discontinuous transition, respectively, from disordered fluid phases to ordered solid ones [23]. As illustrated in Figs. 1(b) and 1(c), both solid phases are characterized by a sublattice ordering. In the 1NN solid ($S1$) phase one of two sublattices is preferentially occupied and in the ground state (the full occupancy limit) the density per site of 1NN particles is $\rho_1 = 1/2$. In the 2NN solid ($S2$) phase one of four sublattices is more occupied and the maximum density of 2NN particles is $\rho_2 = 1/4$. Therefore, to investigate the 0NN-1NN mixture one has to divide the lattice into two sublattices (A and B), as shows Fig. 1(d). For the 1NN-2NN system, eight sublattices [as defined in Fig. 1(e)] are need in order to capture the symmetries of both $S1$ and $S2$ phases.

Following our previous study of the 0NN-2NN mixture [24], instead of investigating the models on the simple cubic lattice, we will solve them on a Husimi lattice built with cubes [see Fig. 1(a)]. Let us note that the solution of a given model in the core of a Cayley tree of coordination q usually corresponds to the (mean-field) Bethe approximation for this model on a regular lattice with the same coordination, and for this reason this is known as the *Bethe lattice* [17]. Once the Cayley tree (and so the Bethe lattice) has no loops, an improved approximation can be obtained by building such tree with polygons or polyhedrons. The core of this cactus is the *Husimi lattice* [54]. We remark that solutions on these lattices usually provide the qualitatively correct thermodynamic behavior of the investigated models, as is indeed the case for the 0NN-1NN mixture on the square [47,48] and Bethe lattices [49]. Moreover, for certain lattice gases even a quantitative agreement with Monte Carlo simulation results on regular lattices have been observed [55,56].

To solve the kNN mixtures on Husimi lattices, we proceed as usual by defining partial partition functions (ppf's) according to the state of the root site of an elementary cube. As shows Fig. 1(f), in general, for each sublattice the root site can be empty ($j = \varnothing$), occupied by a 0NN ($j = 0$), a 1NN ($j = 1$), or a 2NN particle ($j = 2$). In the 0NN-1NN model only $j = \varnothing$, 0, and 1 are allowed and since there are two sublattices one has a total of six possible states for the root site (and, so, six ppf's). The situation worsen in the 1NN-2NN mixture, where $j = \varnothing$, 1 and 2 are allowed and there are eight sublattices, totaling 24 states.

Let us now consider the operation of attaching seven cubes to the vertices of another cube, with exception of the root site. This give us a 1-generation subtree. Repeating this process by attaching the root sites of seven subtrees to the vertices of another new cube, we can build a $(M+1)$-generation subtree from seven M-generation ones. So, if we keep the root site of the new cube in a given state s and sublattice g, and sum over all the possible ways of attaching the seven M-generation subtrees to it, then we obtain the ppf g'_s in generation $(M+1)$ as a function of the ppf's g_j in generation M, with $s, j = \varnothing, 0, 1$ and $g = a, b$ in the 0NN-1NN case and $s, j = \varnothing, 1, 2$ and $g = a_1, a_2, \ldots, d_1, d_2$ in the 1NN-2NN model. Therefore, we obtain six (twenty-four) recursion relations (RRs) for the ppf's of the 0NN-1NN (1NN-2NN) mixture. These RRs are presented in the Appendix. Since they diverge in the thermodynamic limit ($M \to \infty$), we will work with ratios of them. From the RRs for the ppf's, we may define 4 (16) RRs for the ratios in the 0NN-1NN (1NN-2NN) model, whose definitions are also presented in the Appendix. The stable (real and positive) fixed points of these last RRs gives us the stable thermodynamic phases of the models. To determine the stability limits of a given phase, we calculate the Jacobian matrix at the related fixed point. Wherever the largest eigenvalue (Λ) of this matrix is smaller than 1, the fixed point is stable, as well as the corresponding thermodynamic phase. The condition $\Lambda = 1$ defines the stability limits.

The partition function (Y) of the models can be obtained, similarly to the ppf's, by attaching the root sites of eight subtrees to the eight vertices of a central cube. For the 0NN-1NN mixture, it can be written in a compact form, e.g., as

$$Y = a_\varnothing a'_\varnothing + z_0 a_0 a'_0 + z_1 a_1 a'_1 = (a_\varnothing b_\varnothing)^4 y, \tag{1}$$

where y depends only on the activities and ratios $A_j = a_j/a_\varnothing$ and $B_j = b_i/b_\varnothing$, with $j = 0, 1$ (see the Appendix) and, so, it attains a constant value in the thermodynamic limit. Using Eqs. (A1) in the Appendix to write down the expanded expression for y, the densities of small and large particles at the central cube, in sublattice A, are given, respectively, by

$$\rho_0^{(A)} = \frac{A_0}{8Y}\frac{\partial Y}{\partial A_0} \quad \text{and} \quad \rho_1^{(A)} = \frac{A_1}{8Y}\frac{\partial Y}{\partial A_1}. \tag{2}$$

By replacing A to B one obtains the densities in sublattice B. Thence, $\rho_j = \rho_j^{(A)} + \rho_j^{(B)}$ gives the total density of small ($j = 0$) and large ($j = 1$) particles at the central cube in the 0NN-1NN mixture. We can obtain Y and the densities in a similar fashion for the 1NN-2NN system, as devised in the Appendix.

The bulk free energy (per site) of each phase of the models can be calculated following the ansatz proposed by Gujrati [57], and discussed in detail for Husimi lattices built with cubes in Ref. [24]. For the 0NN-1NN model it reads

$$\phi_b = -\frac{1}{8}\ln\left[\frac{(A_\varnothing B_\varnothing)^4}{y^6}\right], \tag{3}$$

where $A_\varnothing = a'_\varnothing/a_\varnothing^3 b_\varnothing^4$ and $B_\varnothing = b'_\varnothing/a_\varnothing^4 b_\varnothing^3$. The equivalent expression for the 1NN-2NN mixture is presented in the Appendix. In general, in regions of the parameter space where two or more phases are stable, the equality of their free energies will define the points, lines, or surfaces of coexistence (where the first-order transitions take place). Since each lattice site occupies a volume $v_0 = a^3$, the pressure (in our grand canonical formalism) is given by $P = -\phi/a^3$.

III. THERMODYNAMIC BEHAVIOR OF THE 0NN-1NN MIXTURE

Before discussing the 0NN-1NN system, it is interesting to analyze the pure 1NN lattice gas. Once $z_0 = 0$ in this case, one has $A_0 = A_1 = A$ and $B_0 = B_1 = B$, so that only two recursion relations (RRs, A and B) have to be analyzed (see the Appendix). For small activity ($z_1 \leqslant 0.8298$) only a homogeneous, disordered fluid phase with $A = B$ is stable, while for large activity ($z_1 \geqslant 0.8298$) there are two equivalent fixed points, where $A = R > B = r$ or $A = r < B = R$. These last ones correspond to the two possible states of the ordered solid ($S1$) phase. Since the stability limits of both fluid and $S1$ phases coincide at $z_{1,c} = 0.8298$ this is a critical point and there is a continuous fluid-solid transition in this model. This

is consistent with several numerical studies of the 1NN model on the cubic lattice, where a critical point located at $z_1 \approx 1.05$ has been found [19,20,23], which is a bit larger than the value from our mean-field approximation, as expected. In agreement with this, the critical density in the cubic lattice is given by $\rho_{1,c} \approx 0.21$ [23,58], while here one finds a slightly smaller value $\rho_{1,c} = 0.1762$.

By including the 0NN particles in the system, we observe that $A_0 \neq A_1$ and $B_0 \neq B_1$, so that now we have to deal with four RRs for the ratios. In the fluid phase $A_j = B_j$, while in the solid phase $A_j > B_j$ when sublattice A is the one more populated, for $j = 0, 1$. For small activity (and so density) of point particles, one still find a continuous fluid-solid transition, which becomes discontinuous for large z_0. Namely, for small z_0 the stability limits of the fluid and solid phases are coincident, giving rise to a critical line, but for $z_0 > z_{0,\mathrm{TC}} = 0.5958$ (and $z_1 > z_{1,\mathrm{TC}} = 1.1277$) they become different, yielding a coexistence region [see Fig. 2(a)]. From the equality of the free energies of both phases, one finds a first-order transition line which starts at $(z_{0,\mathrm{TC}}, z_{1,\mathrm{TC}})$ and extends to $z_0, z_1 \to \infty$. In such limit, the fixed point of the $S1$ phase is given, e.g, by $A_0 = A_1 = 1$ and $B_0 = B_1 = 0$, while the F phase is characterized by $A_0 = B_0 = 1$ and $A_1 = B_1 = 0$. By calculating the free energy with these limiting values, we find that the F-$S1$ coexistence line is given by

$$z_1 \simeq z_0^2 + z_0, \tag{4}$$

for large z_0 and z_1. Therefore, for $z_0 \to \infty$ we have $z_1 \approx z_0^2$, which is consistent with the fact that effectively one 1NN particle occupies the volume of two 0NN ones.

The critical line starts at $(z_0, z_1) = (0, 0.8298)$ and tangentially meet the coexistence line at $(z_{0,\mathrm{TC}}, z_{1,\mathrm{TC}})$, demonstrating that this is a tricritical point. In contrast with the coexistence line, which is a monotonic increasing function of z_0 [in (z_0, z_1) space], the critical line initially decreases with z_0, having a slope $dz_1/dz_0|_{z_0 \to 0} = -1$. Then, it passes through a minimum at $(z_0, z_1) = (0.1974, 0.7284)$ and finally increases towards the tricritical point. See Fig. 2(a). Such initial decreasing of the critical line shows that a small density of small particles facilitates the ordering of the large ones, which is certainly due to an effective attractive depletion interaction among the 1NN particles. We remark that a very similar behavior have been found for small z_0's in the solution of the 0NN-2NN mixture on a Husimi lattice built with cubes [24], although in such case the fluid-solid transition is discontinuous. Moreover, in studies of the 0NN-1NN model on the square [47,48] and Bethe lattice [49] a minimum in the critical fluid-solid transition line has also been found. Actually, the full phase diagram for the 0NN-1NN mixture on these lattices is qualitatively identical to the one found here, with a continuous and a discontinuous transition line meeting at a tricritical point [47–49].

This is true also for the diagram in density space, as displayed in Fig. 2(b), where the critical line starts at $(\rho_0, \rho_1) = (0, 0.1762)$ and ends at the tricritical point, which is located at $(\rho_{0,\mathrm{TC}}, \rho_{1,\mathrm{TC}}) = (0.2190, 0.0761)$. There, one can see that in general the solid phase is featured by a small density of 0NN particles ($\rho_0 \leqslant \rho_{0,\mathrm{TC}}$), whereas the opposite happens in the fluid phase (where $\rho_1 \leqslant 0.1762$). For large z_0 (and z_1), using the asymptotic behaviors discussed above for the RRs and coexistence line, it is straightforward to demonstrate that $\rho_0^{(S1)} \approx \frac{1}{2z_0}$ and $\rho_1^{(S1)} \approx \frac{1}{2} - \frac{1}{2z_0}$ in the solid phase, while $\rho_0^{(F)} \approx 1 - \frac{1}{z_0}$ and $\rho_1^{(F)} \approx \frac{1}{z_0^5}$ in the fluid one. Thereby, as $z_0 \to \infty$ one obtains the expected densities in the full

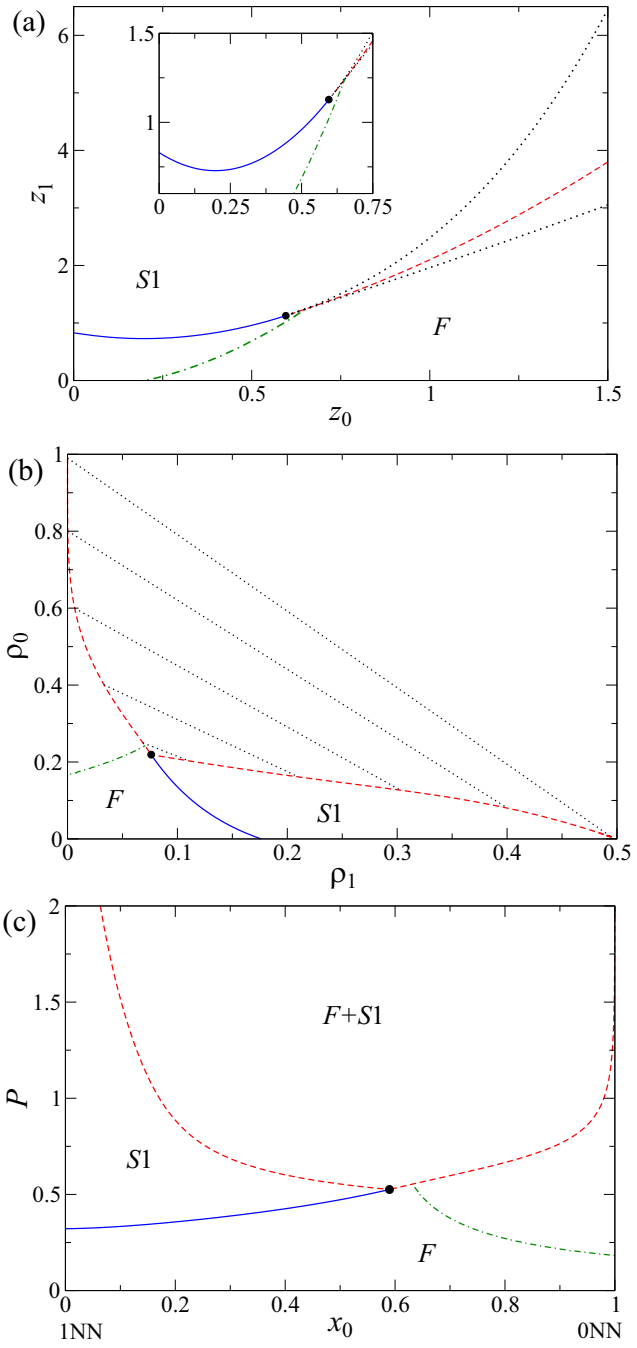

FIG. 2. Phase diagrams for the 0NN-1NN mixture in (a) activities (z_1, z_0), (b) densities (ρ_0, ρ_1), and (c) pressure-composition (P, x_0) spaces. In all panels, the solid (blue) and dashed (red) lines indicated the continuous and discontinuous transitions loci, respectively. The dash-dotted (green) lines are the LMDs. The tricritical point (TC) is indicated by the circle. The dotted lines in (a) are the spinodals, while in (b) they are tie lines. The inset in (a) highlights the region around the minimum in the critical line and the TC point.

occupancy limit: $\rho_0^{(S1)} \to 0$ and $\rho_1^{(S1)} \to 1/2$, and $\rho_0^{(F)} \to 1$ and $\rho_1^{(F)} \to 0$, as indeed observed in Fig. 2(b).

The fluid-solid demixing transition is also clearly observed in the pressure (P) versus composition (x_0) phase diagram displayed in Fig. 2(c). Here, the molar fraction of 0NN particles was defined as $x_0 = \rho_0/\rho_T$, where $\rho_T = \rho_0 + 2\rho_1$ is the total density of particles. In this phase diagram one sees that for small pressures ($P < 0.3219$) only the fluid phase is stable, regardless the composition x_0. For larger P, up to the tricritical point, which is located at $(x_{0,\mathrm{TC}}, P_{\mathrm{TC}}) = (0.5898, 0.5258)$, there is a continuous F-$S1$ transition line. For $P > P_{\mathrm{TC}}$ a coexistence region is observed. We notice that in the limit of large P (corresponding to large z_0 and z_1) the molar fraction in the fluid and solid phase tend to $x_0 = 1$ and $x_0 = 0$, respectively. In this limit, it is simple to demonstrate that P diverge as $P^{(F)} \sim -\ln(1 - x_0)$ and $P^{(S1)} \sim -\ln(x_0)$.

Finally, let us notice that, similarly to what happens in the 0NN-1NN mixture on the square lattice, a density anomaly is also observed in our cubic approximation, which is characterized by minima in the isobaric curves of the total density of particles ρ_T against z_0 (or z_1). A behavior analogous to the ones displayed, e.g., in Figs. 5(a) and 6 from Refs. [24] and [48], respectively. The (z_0, z_1) coordinates of these minima gives rise to a line of minimum density (LMD), which is also shown in the phase diagram of Fig. 2(a). Such line starts inside the fluid phase at $z_0 \approx 0.2$ as $z_1 \to 0$, which is a result consistent with the one analytically predicted in the solution of the model on the Bethe lattice [49], where the LMD was found to start at $z_0 = 1/(q-1)$, with q being the lattice coordination ($q = 6$, here). Then, the LMD crosses the stable and metastable fluid regions, ending at the spinodal of this phase. The LMD in other thermodynamic variables are also depicted in the Figs. 2(b) and 2(c), where the same behavior is observed, as expected. We remark that such behavior is somewhat different from that found on the square lattice, where the LMD seems to end at the tricritical point [48,49]. However, it is similar to the LMD found for the 0NN-2NN mixture on the Husimi lattice built with cubes, which also ends inside the region where the fluid is metastable [24], indicating that this can be a general feature of the LMDs of such mixtures in the cubic lattice. Regardless the location of their end points, in all these systems the LMDs divide the fluid phase in two regions: a regular one, for small z_0, ρ_0 and x_0, where $\partial\rho_T/\partial z_0 < 0$, as expected; and the anomalous region, for large z_0, ρ_0, and x_0, where $\partial\rho_T/\partial z_0 > 0$.

IV. THERMODYNAMIC BEHAVIOR OF THE 1NN-2NN MIXTURE

Now, we investigate the 1NN-2NN model. Let us start noticing that three stable phases are found in this system: (i) the isotropic, disordered fluid (F) phase, for which the RRs (at the fixed point) have the form $A_{i,j} = B_{i,j} = C_{i,j} = D_{i,j}$ for $i = 1, 2$ and $j = 1, 2$; (ii) the solid ($S1$) phase, associated with the ordering of 1NN particles, whose fixed point is featured by, e.g., $A_{1,j} = B_{1,j} = C_{1,j} = D_{1,j} > A_{2,j} = B_{2,j} = C_{2,j} = D_{2,j}$, for $j = 1, 2$, when the sublattices indexed by 1 [see Fig. 1(e)] are the more populated ones; and (iii) the solid ($S2$) phase, associated with the ordering of 2NN particles,

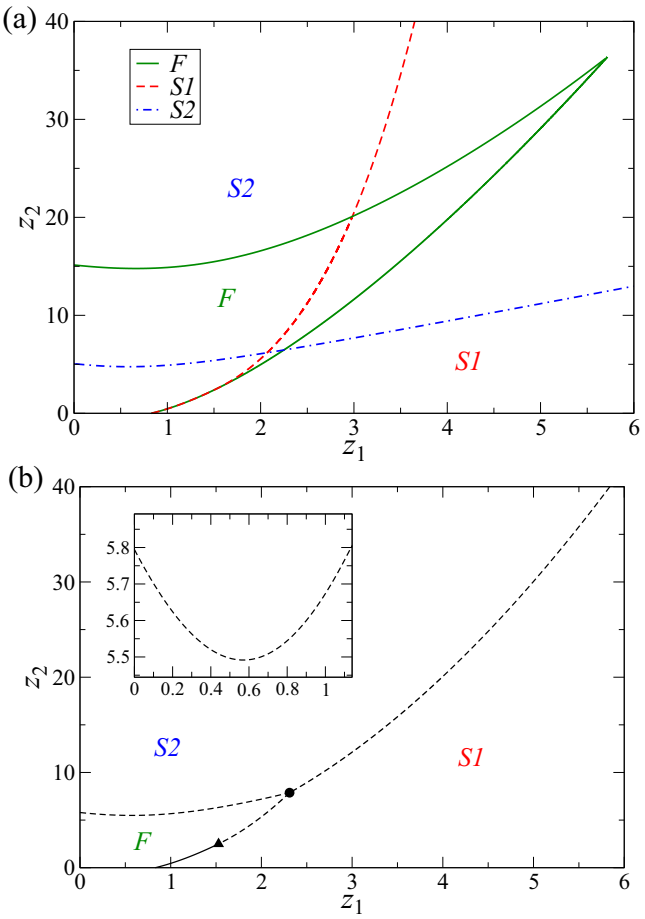

FIG. 3. (a) Stability limits of the three stable (fluid, $S1$ and $S2$) phases found in the 1NN-2NN mixture. (b) Phase diagram of this model in variables z_1, z_2. In (b), the solid and dashed lines represent continuous and discontinuous transitions, respectively. The triple point is indicated by a circle and the tricritical point by a triangle. The inset highlights the region around the minimum in the F-$S2$ coexistence line.

where we find, e.g., $A_{i,j} > B_{i,j} = C_{i,j} = D_{i,j}$, for $i = 1, 2$ and $j = 1, 2$, when the sublattices labeled by A are the ones more occupied. Although the notations are different, the fixed points' symmetries for the fluid and $S1$ phases are the same from the previous section. Since for the pure 1NN model ($z_2 = 0$) a continuous fluid-solid (F-$S1$) transition is found (as discussed above), we might expect to find a continuous F-$S1$ transition line for small z_2. However, for the pure 2NN model ($z_1 = 0$) a discontinuous fluid-solid (F-$S2$) transition takes place, as observed by Panagiotopoulos [23] in Monte Carlo simulations on the cubic lattice and by us in the cubic Husimi lattice approximation [24]. Therefore, for small z_1 a first order F-$S2$ transition line is expected. Such behaviors are indeed found here for the 1NN-2NN mixture, as confirmed in Fig. 3. There, the stability limits of the three stable phases are shown in panel (a), where one sees that for small z_2 the spinodals of the fluid and $S1$ phases indeed coincide, up to $(z_{1,\mathrm{TC}}, z_{2,\mathrm{TC}}) = (1.5273, 2.5016)$, after which they become different, giving rise to a coexistence region between these phases. The spinodal of the $S2$ phase, however, never

coincides with the ones for the fluid and $S1$ phases, with exception of few points where they cross each other, indicating that such phases are always separated by first order transition lines.

In fact, from the equality of the bulk free energies, three coexistence (F-$S1$, F-$S2$ and $S1$-$S2$) lines are obtained, all of them meeting at a triple point, located at $(z_{1,\mathrm{TP}}, z_{2,\mathrm{TP}}) = (2.3102, 7.8746)$. See Fig. 3(b). The F-$S1$ coexistence line tangentially meet the F-$S1$ critical line at $(z_{1,\mathrm{TC}}, z_{2,\mathrm{TC}})$, showing that this is a tricritical point. The F-$S2$ coexistence line starts at $z_1 = 0$ (and $z_2 = 5.7932$) and ends at the triple point. In between, however, it presents a minimum located at $(z_1, z_2) = (0.5702, 5.4907)$, as shows the insertion in Fig. 3(b). Therefore, initially this line decreases, indicating that a small fraction of 1NN particles facilitates the ordering of the larger 2NN ones. This is similar to the effect of the 0NN particles on the ordering of 1NN ones discussed in the previous section or in Refs. [48,49] for the square lattice, as well as on the ordering of 2NN particles, as demonstrated in Ref. [24] for the 0NN-2NN mixture. Interestingly, in all these systems the initial slope of the decreasing critical or coexistence lines is $dz_k/dz_0|_{z_0\to 0} = -1$ (with $k = 1, 2$), and here one also finds $dz_2/dz_1|_{z_1\to 0} = -1$.

The $S1$-$S2$ coexistence line starts at the triple point and extends to $z_1, z_2 \to \infty$. In such limit, one finds that all RRs vanish in $S1$ phase, with exception, e.g., of $A_{1,1} = B_{1,1} = C_{1,1} = D_{1,1} = 1$, while in the $S2$ phase one has, e.g., $A_{i,j} = 1$ and $B_{i,j} = C_{i,j} = D_{i,j} = 0$, for $i = 1, 2$ and $j = 1, 2$. Inserting these limiting values in the free energies, we find the $S1$-$S2$ coexistence line as

$$z_2 \simeq z_1^2 + z_1, \tag{5}$$

for large z_1. So, for $z_1 \to \infty$ one obtains $z_2 \approx z_1^2$, which is again consistent with the fact that effectively two 1NN particles occupy the same volume of a 2NN one.

To let clear the differences among the three phases, specially between the two solid ones, it is worthy analyzing in detail the particle densities. Figures 4(a)–4(c) display the densities ρ_1 and ρ_2 as functions of z_2 for three values of z_1, chosen such that all transition lines are crossed, where the continuous and discontinuous nature of the transitions are confirmed. As expected, for all phases and parameters ρ_1 decreases, while ρ_2 increases, with z_2. The $S1$ ($S2$) phase is always featured by a large density of 1NN (2NN) particles and a small density of 2NN (1NN) ones. In the fluid phase, however, the densities are more sensitive to the activities. For instance, at the F-$S2$ coexistence we find $\rho_1^{(F)} < \rho_2^{(F)}$ for $z_1 = 1$, but $\rho_1^{(F)} > \rho_2^{(F)}$ for $z_1 = 2$ [see Figs. 4(a) and 4(b)]. These density behaviors are also confirmed in the phase diagram in the (ρ_1, ρ_2) space, which is depicted in Fig. 5(a). In such diagram, the tricritical point is located at $(\rho_{1,\mathrm{TC}}, \rho_{2,\mathrm{TC}}) = (0.1463, 0.0435)$, while at the triple point one has $(\rho_1^{(F)}, \rho_2^{(F)}) = (0.1126, 0.0823)$, $(\rho_1^{(S1)}, \rho_2^{(S1)}) = (0.3000, 0.0115)$ and $(\rho_1^{(S2)}, \rho_2^{(S2)}) = (0.0550, 0.1679)$. The F-$S1$ critical line starts at $(\rho_1, \rho_2) = (0.1762, 0)$ and ends at the tricritical point. From the asymptotic behaviors discussed above for the RRs and the $S1$-$S2$ coexistence line in the limit of large z_1, it is easy to show that $\rho_1^{(S1)} \approx \frac{1}{2} - \frac{1}{2z_1}$ and $\rho_2^{(S1)} \approx \frac{1}{2z_1^4}$, while $\rho_1^{(S2)} \approx \frac{1}{4z_1}$ and $\rho_2^{(S2)} \approx \frac{1}{4} - \frac{1}{4z_1}$. Hence, for $z_1 \to \infty$ we obtain $\rho_1^{(S1)} \to 1/2$ and $\rho_2^{(S1)} \to 0$, and $\rho_1^{(S2)} \to 0$ and $\rho_2^{(S2)} \to 1/4$, as expected and confirmed in Fig. 5(a).

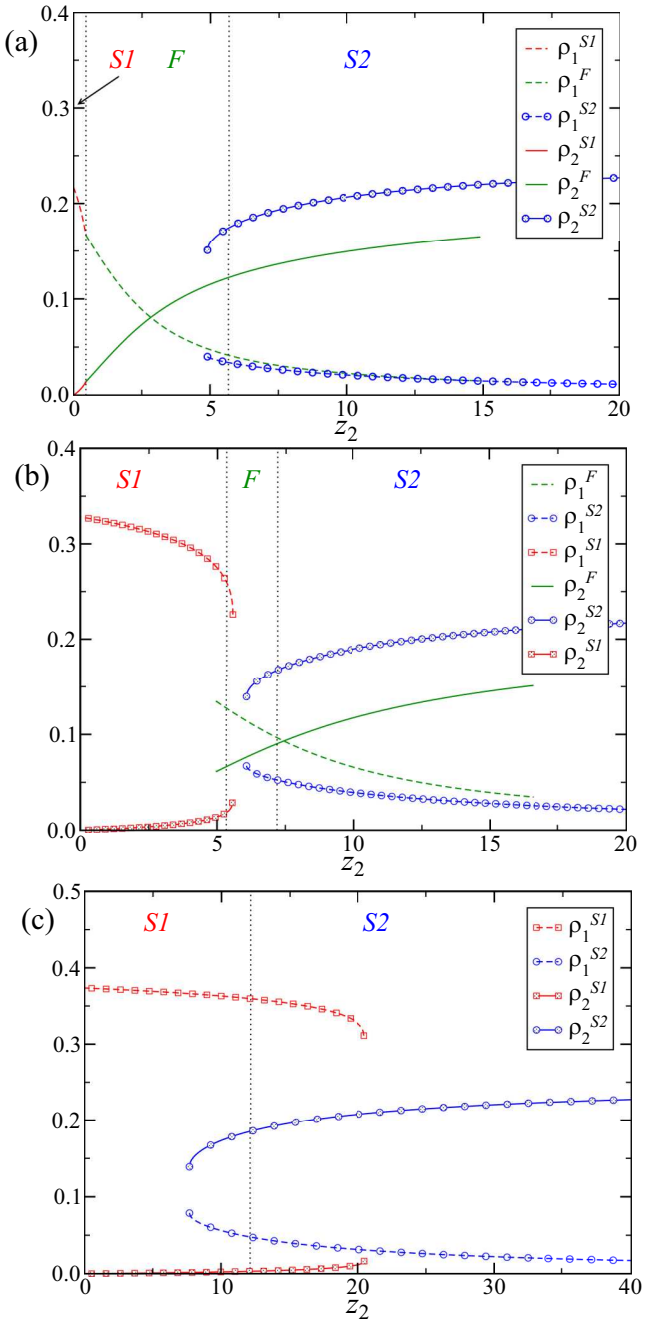

FIG. 4. (a) Densities of small ρ_1 and large ρ_2 particles in the indicated phases, for the 1NN-2NN mixture, as functions of z_2 for (a) $z_1 = 1$, (b) $z_1 = 2$, and (c) $z_1 = 3$. The vertical lines are the transition loci between the indicated phases.

Figure 5(b) shows the phase diagram in pressure-composition (P, x_1) plane, where the molar fraction of 1NN particles was defined as $x_1 = 2\rho_1/\rho_T$, with $\rho_T = 2\rho_1 + 4\rho_2$ being the total density of particles in this model. For small pressures, specifically for $P < 0.3219$, only the fluid phase is stable, but above this point the $S1$ phase becomes also

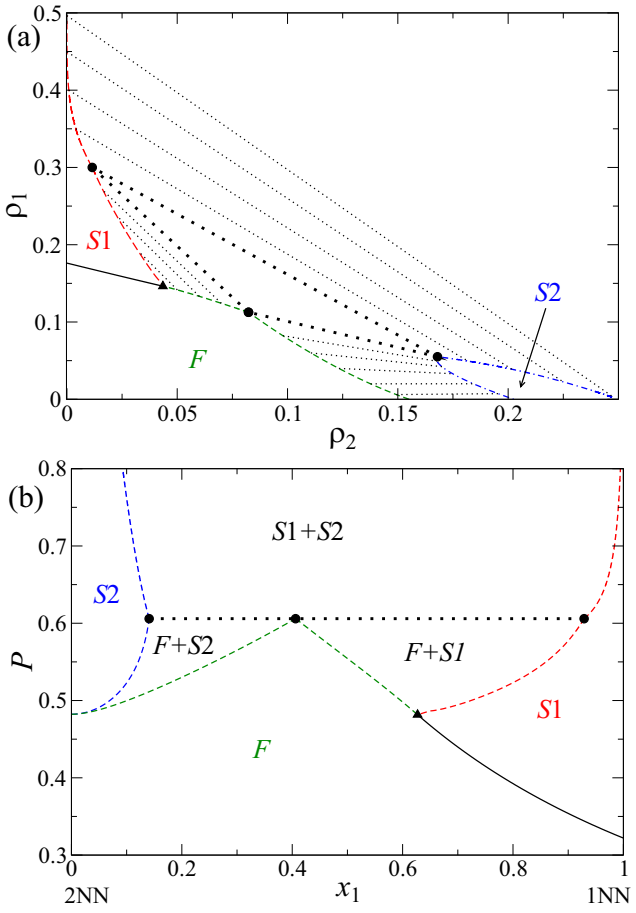

FIG. 5. Phase diagrams for the 1NN-2NN mixture in (a) density (ρ_1, ρ_2) and (b) pressure-composition (P, x_1) space. In both panels the solid and dashed lines denotes the continuous and discontinuous transitions, respectively. The tricritical point is indicated by the triangle, while the circles represent the triple point, which are connect by thicker dotted lines. The thin dotted lines in (a) are tie lines.

stable and both phases are separated by the critical line. This line ends at the tricritical point, located at $(P_{\rm TC}, x_{1,\rm TC}) = (0.4816, 0.6270)$, above which a F-$S1$ coexistence appears. For higher pressures, the F-$S2$ and $S1$-$S2$ coexistences also show up. For instance, the F-$S2$ one starts at $(P, x_1) = (0.4822, 0)$. The triple point, which separates the three regions where each kind of coexistence is the stable one, is located at $P_{\rm TP} = 0.6059$, where $x_1^{(S2)} = 0.1408$, $x_1^{(F)} = 0.4061$ and $x_1^{(S1)} = 0.9286$. For large pressures the $S1$ line tends to $x_1 = 1$, while the $S2$ one goes to $x_1 = 0$, as expected. From the asymptotic behaviors discussed above for the RRs, coexistence line and densities, it is simple to demonstrate that P diverges as $P^{(S1)} \sim -\ln(1 - x_1)$ and $P^{(S2)} \sim -\ln(x_1)$. These behaviors are the same found in the previous section for the 0NN-1NN mixture and for the 0NN-2NN model in Ref. [24], indicating that such logarithmic divergences are universal in these systems.

Interestingly, in contrast with the other mixtures of kNN particles studied so far, the isobaric curves of the total density of particles (ρ_T) are always monotonic decreasing functions of z_1 or z_2. Namely, no density anomaly exists in the 1NN-2NN mixture. This is certainly related to the fact that now the fluid phase is limited to a region of small activities and, so, of small densities. This contrasts with the 0NN-1NN mixture (discussed above and in previous studies related to square lattice [47–49]), as well as with the 0NN-2NN system [24], where the fluid phase extends to $z_0 \to \infty$ and, then, $\rho_0^{(F)}, \rho_T^{(F)} \to 1$. Once the anomaly appears for relatively large densities of the small particles, this strongly suggests that it is absent in the 1NN-2NN case because it is preempted by the F-$S1$ transitions.

V. CONCLUSIONS

We have investigated two binary mixtures of (hard) kNN particles, which exclude up to their kth nearest neighbors and are discretized approximations for hard-spheres on the cubic lattice. More specifically, we have obtained the grand-canonical solution, on a Husimi lattice built with cubes, of the model with point particles (0NN) and 1NN ones; and for the mixture 1NN-2NN. The 0NN-1NN system displays the same thermodynamic behavior already observed for it on the square [46–48] and on the Bethe lattice [49], with a disordered fluid (F) and a solid ($S1$) phase where 1NN particles tend to preferentially occupy one of two sublattices. Such phases are separated by a critical line and a first-order transition line, both meeting at a tricritical point. As demonstrated in Ref. [48], the critical line and the tricritical point found for this mixture on the square lattice belong to the critical and tricritical Ising universality classes in 2D, respectively. Moreover, 3D Ising exponents were obtained by Heringa and Blöte [19] for the pure 1NN model on the cubic lattice. These results suggest that the entire critical line, as well as the tricritical point might be also in the 3D Ising universality classes. Furthermore, in the Bethe lattice with coordination $q = 6$, which is also a mean-field approximation for the cubic lattice, the tricritical point is located at $(z_{0,\rm TC}, z_{1,\rm TC}) = (0.5333, 0.9957)$ [49], which is smaller than the values found here: $(z_{0,\rm TC}, z_{1,\rm TC}) = (0.5958, 1.1277)$. Since the Husimi lattice solution is an improved approach when compared with the Bethe lattice one, this strongly suggests that $(z_{0,\rm TC}, z_{1,\rm TC})$ in the cubic lattice shall be a bit larger than the values found here. Numerical investigations of this mixture on the cubic lattice are necessary to confirm these things.

For the 1NN-2NN mixture, a disordered fluid (F) and the ordered $S1$ phases are still present in the phase diagram and, once again, they are separated by a critical and a coexistence line, which meet at a tricritical point. Nonetheless, there exists also a second solid ($S2$) phase, which is featured by the ordering of 2NN particles into one of four sublattices. Such phase is separated from the F and $S1$ phases by first-order transition lines. Therefore, beyond the fluid-solid (F-$S1$) demixing also observed in the 0NN-1NN mixture, in the 1NN-2NN case there exist also another fluid-solid (F-$S2$) demixing, as well as a solid-solid ($S1$-$S2$) phase separation. In this case, the three phases coexist at a triple point.

It is interesting to remark that the cubic Husimi lattice solution of the 0NN-2NN mixture presents a fluid-fluid demixing [24], which is absent in the mixtures analyzed here. We have indeed scanned the parameter space looking for additional phases, even metastable ones, but it seems that only the three

(F, $S1$ and $S2$) phases discussed above exist in our approach. These results - together with the ones for the 0NN-1NN model on the square lattice, where no fluid-fluid demixing was observed [46–48] - indicate that the condition for observation of fluid-fluid transitions in such systems might be kNN-k'NN with $k' \geqslant k+2$ or, maybe, it is limited to 0NN-kNN mixtures, with $k \geqslant 2$. This is also an important issue to be addressed in future works.

Finally, let us remark that a density anomaly is present in the 0NN-1NN mixture, but it is absent in the 1NN-2NN one. Since this anomaly, which might be important for understanding more complex fluids, have already been observed in previous studies of the 0NN-1NN mixture [48,49] and also in the 0NN-2NN model [24], its absence in the 1NN-2NN system suggests that the presence of point (0NN) particles in the mixtures is imperative for its existence. In fact, in 0NN-kNN mixtures, only the fluid phase is expected to be stable in the phase diagram for small enough activities (z_k) of the larger kNN particles, so that it shall exist for z_0 ranging from 0 to ∞. This was indeed observed in all mixtures of this type investigated so far. For mixtures of the type kNN-k'NN, with $0 < k < k'$, the fluid phase is expected to be stable only in a limited region of parameter space (for small z_k and $z_{k'}$), since it shall present transitions (at least) for the two solid phases associated with the ordering of both kNN and k'NN particles, as indeed observed here in the 1NN-2NN model. In this scenario, it may be the case that the density of small particles ρ_k does not become so large within the fluid phase to allow the onset of the anomalous behavior, which certainly explain its absence in 1NN-2NN. For other mixtures of this type, however, there is no guarantee that this shall happen. So, once again, more studies of these kNN mixtures are important to unveil what are the conditions for the appearance of such entropy-driven anomaly. We notice that the symmetries of the ordered phases of kNN systems with $k > 2$ cannot be captured by a Husimi lattice built with cubes, so that other methods, such as Monte Carlo simulations, shall be employed to answer the important questions raised here.

ACKNOWLEDGMENTS

This work is partially supported by CNPq, CAPES, and Fundação de Amparo à Pesquisa do Estado de Minas Gerais (Brazilian agencies).

APPENDIX: ADDITIONAL DETAILS ON THE SOLUTIONS OF THE MODELS ON THE HUSIMI LATTICE

1. Recursion relations for the 0NN-1NN mixture

The recursion relations (RRs) for the partial partition functions (ppf's) of the 0NN-1NN mixture, defined and obtained as explained in Sec. II, when the root site is in the sublattice A, are given by

$$\begin{aligned} a'_{\varnothing} &= a_{\varnothing}^3 b_{\varnothing}^4 \{3z_1^2A_1^2 + z_1^3A_1^3 + z_0^3A_0^3(1+z_0B_0)^4 + 3z_0^2A_0^2(1+z_0B_0)[z_1A_1 + (1+z_0B_0)^3] + 3z_1A_1(1+z_0B_0+z_1B_1) \\ &\quad + (1+z_0B_0+z_1B_1)^4 + 3z_0A_0\big[z_1^2A_1^2 + 2z_1A_1(1+z_0B_0) + (1+z_0B_0)^3(1+z_0B_0+z_1B_1)\big]\}, \qquad \text{(A1a)} \\ a'_0 &= a_{\varnothing}^3 b_{\varnothing}^4 \{3z_1^2A_1^2 + z_1^3A_1^3 + 3z_1A_1(1+z_0B_0) + z_0^3A_0^3(1+z_0B_0)^4 + 3z_0^2A_0^2(1+z_0B_0)[z_1A_1 + (1+z_0B_0)^3] \\ &\quad + 3z_0A_0\big[z_1^2A_1^2 + 2z_1A_1(1+z_0B_0) + (1+z_0B_0)^4\big] + (1+z_0B_0)^3(1+z_0B_0+z_1B_1)\}, \qquad \text{(A1b)} \\ a'_1 &= a_{\varnothing}^3 b_{\varnothing}^4 \big[1 + 3z_1A_1 + 3z_1^2A_1^2 + z_1^3A_1^3 + z_0B_0 + z_0^3A_0^3(1+z_0B_0) + 3z_0^2A_0^2(1+z_1A_1+z_0B_0) \\ &\quad + 3z_0A_0\big(1 + 2z_1A_1 + z_1^2A_1^2 + z_0B_0\big) + z_1B_1\big], \qquad \text{(A1c)} \end{aligned}$$

where the capital letters A_j and B_j denote the ratios $A_j = a_j/a_{\varnothing}$ and $B_j = b_j/b_{\varnothing}$, for $j = 0, 1$. The RRs for the sublattice B are given by a simple permutation between a (A) and b (B) in the expressions above. Moreover, the RRs for the ratios are obtained by dividing the equations A1, namely, $A'_j = a'_j/a'_{\varnothing}$ and $B'_j = b'_j/b'_{\varnothing}$, with $j = 0, 1$.

2. Solution of the 1NN-2NN mixture

For the 1NN-2NN mixture, the RRs for the ppf's, when the root site is in sublattice A_1, are given by

$$\begin{aligned} a'_{1,\varnothing} &= b_{1,\varnothing}c_{1,\varnothing}d_{1,\varnothing}a_{2,\varnothing}b_{2,\varnothing}c_{2,\varnothing}d_{2,\varnothing}[1 + z_1(C_{1,1} + B_{2,1} + A_{2,1} + D_{1,1} + C_{2,1} + B_{1,1} + z_1\{A_{2,1}C_{2,1} + D_{1,1}B_{1,1} \\ &\quad + B_{2,1}[A_{2,1} + C_{2,1} + B_{1,1} + z_1A_{2,1}C_{2,1}] + C_{1,1}[D_{1,1} + C_{2,1} + B_{1,1} + z_1D_{1,1}B_{1,1}]\} \\ &\quad + D_{2,1}\{1 + z_1[A_{2,1} + D_{1,1} + C_{2,1} + z_1A_{2,1}C_{2,1} + B_{2,1}(1+z_1A_{2,1})(1+z_1C_{2,1})]\}) \\ &\quad + z_2(D_{2,2} + C_{1,2} + B_{2,2} + A_{2,2} + D_{1,2} + C_{2,2} + B_{1,2}) + z_1z_2(D_{1,1}D_{2,2} + D_{2,1}D_{1,2} \\ &\quad + C_{1,1}C_{2,2} + C_{2,1}C_{1,2} + B_{1,1}B_{2,2} + B_{2,1}B_{1,2}) + z_2^2(D_{1,2}D_{2,2} + C_{1,2}C_{2,2} + B_{1,2}B_{2,2})] \qquad \text{(A2a)} \\ a'_{1,1} &= b_{1,\varnothing}c_{1,\varnothing}d_{1,\varnothing}a_{2,\varnothing}b_{2,\varnothing}c_{2,\varnothing}d_{2,\varnothing}\big[1 + z_1(A_{2,1} + D_{1,1} + B_{1,1} + z_1D_{1,1}B_{1,1}) + z_2A_{2,2} \\ &\quad + z_1C_{1,1}(1+z_1D_{1,1})(1+z_1B_{1,1})\big] \qquad \text{(A2b)} \\ a'_{1,2} &= b_{1,\varnothing}c_{1,\varnothing}d_{1,\varnothing}a_{2,\varnothing}b_{2,\varnothing}c_{2,\varnothing}d_{2,\varnothing}(1 + z_1A_{2,1} + z_2A_{2,2}), \qquad \text{(A2c)} \end{aligned}$$

where $A_{i,j}$, $B_{i,j}$, $C_{i,j}$, and $D_{i,j}$, with $i = 1, 2$ and $j = 1, 2$, are the ratios defined by

$$A_{i,j} = \frac{a_{i,j}}{a_{i,\varnothing}}, \quad B_{i,j} = \frac{b_{i,j}}{b_{i,\varnothing}}, \quad C_{i,j} = \frac{c_{i,j}}{c_{i,\varnothing}}, \quad D_{i,j} = \frac{d_{i,j}}{d_{i,\varnothing}}.$$

The RRs for such ratios are defined similarly, by dividing the expressions A2 with index $j \neq \varnothing$ by the ones with $j = \varnothing$, for a given sublattice. From cyclic permutations of the sublattice labels: $A_1 \to B_2$, $B_2 \to C_1$, $C_1 \to D_2$, $D_2 \to A_1$, together with $C_2 \to D_1$, $D_1 \to A_2$, $A_2 \to B_1$, $B_1 \to C_2$, in this order [see Fig. 1(e)], we can obtain the RRs for the ppf's and ratios for the sublattices D_2, C_1 and B_2. Then, the RRs for the sublattices A_2, B_1, C_2 and D_1 can be obtained from the ones for A_1, B_2, C_1 and D_2, respectively, by exchanging all the sublattice indexes i ($1 \leftrightarrow 2$).

The partition function of the 1NN-2NN mixture reads

$$Y = a_{1,\varnothing}a'_{1,\varnothing} + z_1 a_{1,1}a'_{1,1} + z_2 a_{1,2}a'_{1,2} = a_{1,\varnothing}b_{1,\varnothing}c_{1,\varnothing}d_{1,\varnothing}a_{2,\varnothing}b_{2,\varnothing}c_{2,\varnothing}d_{2,\varnothing}y, \tag{A3}$$

where y depends only on the ratios at the fixed point and on the activities (z_1, z_2). From the expanded expression for Y, we can calculate the densities of small and large particles in a given sublattice, at the central cube, using definitions analogous to those in Eq. (2).

The bulk free energy (per site) for the 1NN-2NN mixture is given by

$$\phi_b = -\frac{1}{8}\ln\left[\frac{A_{1,\varnothing}B_{1,\varnothing}C_{1,\varnothing}D_{1,\varnothing}A_{2,\varnothing}B_{2,\varnothing}C_{2,\varnothing}D_{2,\varnothing}}{y^6}\right], \tag{A4}$$

where

$$A_{1,\varnothing} \equiv \frac{a'_{1,\varnothing}}{b_{1,\varnothing}c_{1,\varnothing}d_{1,\varnothing}a_{2,\varnothing}b_{2,\varnothing}c_{2,\varnothing}d_{2,\varnothing}}, \tag{A5}$$

and the other ones can be obtained from this expression by using the same scheme of permutations described above for determining the ratios for other sublattices.

[1] *Granular Matter: An Interdisciplinary Approach*, edited by A. Mehta (Springer-Verlag, New York, 1994).
[2] W. W. Wood and J. D. Jacobson, J. Chem. Phys. **27**, 1207 (1957).
[3] B. J. Alder and T. E. Wainwright, J. Chem. Phys. **27**, 1208 (1957).
[4] W. G. Hoover and F. H. Ree, J. Chem. Phys. **49**, 3609 (1968).
[5] M. D. Eldridge, P. A. Madden, and D. Frenkel, Mol. Phys. **79**, 105 (1993).
[6] B. Widom and J. S. Rowlinson, J. Chem. Phys. **52**, 1670 (1970).
[7] T. W. Melnyk and B. L. Sawford, Mol. Phys. **29**, 891 (1975).
[8] A. A. Louis, R. Finken, and J. P. Hansen, Phys. Rev. E **61**, R1028(R) (2000).
[9] A. Santos, M. López de Haro, and S. B. Yuste, J. Chem. Phys. **132**, 204506 (2010).
[10] M. Dijkstra, Phys. Rev. E **58**, 7523 (1998).
[11] T. Biben and J. P. Hansen, Phys. Rev. Lett. **66**, 2215 (1991).
[12] H. N. W. Lekkerkeker and A. Stroobants, Phys. A **195**, 387 (1993).
[13] J. L. Lebowitz and J. S. Rowlinson, J. Chem. Phys. **41**, 133 (1964).
[14] L. Lafuente and J. A. Cuesta, Phys. Rev. Lett. **89**, 145701 (2002).
[15] L. Lafuente and J. A. Cuesta, J. Chem. Phys. **119**, 10832 (2003).
[16] R. J. Baxter, J. Phys. A **13**, L61 (1980).
[17] R. J. Baxter, *Exactly Solved Models in Statistical Mechanics* (Academic Press, London, 1989).
[18] W. Guo and H. W. J. Blöte, Phys. Rev. E **66**, 046140 (2002).
[19] J. R. Heringa and H. W. J. Blöte, Physica A **232**, 369 (1996).
[20] A. Yamagata, Physica A **215**, 511 (1994).
[21] X. Feng, H. W. J. Blöte, and B. Nienhuis, Phys. Rev. E **83**, 061153 (2011).
[22] H. C. Marques Fernandes, J. J. Arenzon, and Y. Levin, J. Chem. Phys. **126**, 114508 (2007).
[23] A. Z. Panagiotopoulos, J. Chem. Phys. **123**, 104504 (2005), in this work the reported values of $\beta\mu$ are related to activities through $z_i\sigma^3 = e^{\beta\mu}$, where $\sigma = \lambda/a$, so that $z_1 = e^{\beta\mu}/2^{3/2}$ and $z_2 = e^{\beta\mu}/3^{3/2}$.
[24] N. T. Rodrigues and T. J. Oliveira, J. Chem. Phys. **151**, 024504 (2019).
[25] T. Nath and R. Rajesh, Phys. Rev. E **90**, 012120 (2014).
[26] N. Vigneshwar, D. Mandal, K. Damle, D. Dhar, and R. Rajesh, Phys. Rev. E **99**, 052129 (2019).
[27] P. Kasteleyn, Physica **27**, 1209 (1961); H. N. V. Temperley and M. E. Fisher, Philos. Mag. **6**, 1061 (1961); D. A. Huse, W. Krauth, R. Moessner, and S. L. Sondhi, Phys. Rev. Lett. **91**, 167004 (2003); R. Dickman, J. Chem. Phys. **136**, 174105 (2012).
[28] J. Kundu and R. Rajesh, Phys. Rev. E **89**, 052124 (2014); **91**, 012105 (2015); T. Nath, J. Kundu, and R. Rajesh, J. Stat. Phys. **160**, 1173 (2015); P. Gurin, S. Varga, M. González-Pinto, Y. Martínez-Ratón, and E. Velasco, J. Chem. Phys. **146**, 134503 (2017).
[29] A. Ghosh and D. Dhar, Europhys. Lett. **78**, 20003 (2007); J. Kundu, R. Rajesh, D. Dhar, and J. F. Stilck, Phys. Rev. E **87**, 032103 (2013); A. Gschwind, M. Klopotek, Y. Ai, and M. Oettel, *ibid.* **96**, 012104 (2017); N. Vigneshwar, D. Dhar, and R. Rajesh, J. Stat. Mech. (2017) 113304.
[30] A. Verberkmoes and B. Nienhuis, Phys. Rev. Lett. **83**, 3986 (1999).

[31] D. Mandal, T. Nath, and R. Rajesh, Phys. Rev. E **97**, 032131 (2018).
[32] M. Schmidt, J. Phys.: Condens. Matter **16**, L351 (2004).
[33] J. M. Brader and R. L. C. Vink, J. Phys.: Condens. Matter **19**, 036101 (2007).
[34] D. Frenkel and A. A. Louis, Phys. Rev. Lett. **68**, 3363 (1992).
[35] M. Dijkstra and D. Frenkel, Phys. Rev. Lett. **72**, 298 (1994).
[36] M. Dijkstra, D. Frenkel, and J. Hansen, J. Chem. Phys. **101**, 3179 (1994).
[37] R. Dickman and G. Stell, J. Chem. Phys. **102**, 8674 (1995).
[38] R. van Roij, B. Mulder, and M. Dijkstra, Physica A **261**, 374 (1998).
[39] H. H. Wensink, G. J. Vroege, and H. N. W. Lekkerkerker, J. Chem. Phys. **115**, 7319 (2001).
[40] S. Dubois and A. Perera, J. Chem. Phys. **116**, 6354 (2002).
[41] S. Varga, A. Galindo, and G. Jackson, J. Chem. Phys. **117**, 7207 (2002).
[42] M. Schmidt and A. R. Denton, Phys. Rev. E **65**, 021508 (2002).
[43] Y. Martínez-Ratón, E. Velasco, and L. Mederos, Phys. Rev. E **72**, 031703 (2005).
[44] D. de las Heras, Y. Martínez-Ratón, and E. Velasco, Phys. Rev. E **76**, 031704 (2007).
[45] J. Kundu, J. F. Stilck, and R. Rajesh, Europhys. Lett. **112**, 66002 (2016).
[46] D. Poland, J. Chem. Phys. **80**, 2767 (1984).
[47] D.-J. Liu and J. W. Evans, J. Chem. Phys. **114**, 10977 (2001).
[48] T. J. Oliveira and J. F. Stilck, Phys. Rev. E **92**, 032101 (2015).
[49] T. J. Oliveira and J. F. Stilck, J. Chem. Phys. **135**, 184502 (2011).
[50] J. S. van Duijneveldt and H. N. W. Lekkerkerker, Phys. Rev. Lett. **71**, 4264 (1993).
[51] J. S. van Duijneveldt and H. N. W. Lekkerkerker, J. Stat. Phys. **78**, 103 (1995).
[52] A. Verberkmoes and B. Nienhuis, Phys. Rev. E **60**, 2501 (1999).
[53] P. Bartlett and R. H. Ottewill, J. Chem. Phys. **93**, 1299 (1990); A. Imhof and J. K. G. Dhont, Phys. Rev. Lett. **75**, 1662 (1995); J. Baumgartl, R. P. A. Dullens, M. Dijkstra, R. Roth, and C. Bechinger, *ibid.* **98**, 198303 (2007); A. Statt, R. Pinchaipat, F. Turci, R. Evans, and C. P. Royall, J. Chem. Phys. **144**, 144506 (2016); A. L. Thorneywork, D. G. A. L. Aarts, J. Horbach, and R. P. A. Dullens, Phys. Rev. E **95**, 012614 (2017).
[54] K. Husimi, J. Chem. Phys. **18**, 682 (1950).
[55] C. Buzano, E. De Stefanis, and M. Pretti, J. Chem. Phys. **129**, 024506 (2008).
[56] T. J. Oliveira, J. F. Stilck, and M. A. A. Barbosa, Phys. Rev. E **82**, 051131 (2010).
[57] P. D. Gujrati, Phys. Rev. Lett. **74**, 809 (1995).
[58] D. S. Gaunt, J. Chem. Phys. **46**, 3237 (1967).

Fluid-fluid demixing and density anomaly in a ternary mixture of hard spheres

Nathann T. Rodrigues [*] and Tiago J. Oliveira [†]
Departamento de Física, Universidade Federal de Viçosa, 36570-900, Viçosa, MG, Brazil

(Received 27 March 2020; accepted 14 May 2020; published 1 June 2020)

We report the grand-canonical solution of a ternary mixture of discrete hard spheres defined on a Husimi lattice built with cubes, which provides a mean-field approximation for this system on the cubic lattice. The mixture is composed of pointlike particles (0NN) and particles which exclude up to their first (1NN) and second neighbors (2NN), with activities z_0, z_1, and z_2, respectively. Our solution reveals a very rich thermodynamic behavior, with two solid phases associated with the ordering of 1NN ($S1$) or 2NN particles ($S2$), and two fluid phases, one being regular (RF) and the other characterized by a dominance of 0NN particles ($F0$ phase). However, in most part of the phase diagram these fluid (F) phases are indistinguishable. Discontinuous transitions are observed between all the four phases, yielding several coexistence surfaces in the system, among which a fluid-fluid and a solid-solid demixing surface. The former one is limited by a line of critical points and a line of triple points (where the phases RF-$F0$-$S2$ coexist), both meeting at a special point, after which the fluid-fluid coexistence becomes metastable. Another line of triple points is found, connecting the F-$S1$, F-$S2$, and $S1$-$S2$ coexistence surfaces. A critical F-$S1$ surface is also observed meeting the F-$S1$ coexistence one at a line of tricritical points. Furthermore, a thermodynamic anomaly characterized by minima in isobaric curves of the total density of particles is found, yielding three surfaces of minimal density in the activity space, depending on which activity is kept fixed during its calculation.

DOI: 10.1103/PhysRevE.101.062102

I. INTRODUCTION

In two recent works [1,2], we have investigated three athermal binary mixtures of hard spheres placed on the cubic lattice, where they are approximated by kNN particles, i.e., particles which exclude up their kth neighbors. The mixtures considered were composed by pairs of the three smallest "spheres" (0NN-1NN, 0NN-2NN, and 1NN-2NN) and grand-canonical phase diagrams for these systems were obtained through their solution on a Husimi lattice built with cubes [1,2] [see Fig. 1(a)]. Such mean-field solutions display very rich entropy-driven thermodynamic behaviors. In a brief, in the 0NN-1NN case, a fluid (F) and a solid ($S1$) phase (associated with the ordering of 1NN particles) were found, separated by a continuous and a discontinuous transition line, both meeting at a tricritical point [1]. The same phases and behavior were observed in the 1NN-2NN mixture, but now another solid ($S2$) phase (associated with the ordering of 2NN particles) is present in the system and it is separated from the F and $S1$ phases by coexistence lines, which meet the F-$S1$ one at a triple point [1]. For the 0NN-2NN mixture, an even more interesting scenario was found, with two fluid phases, one regular (RF) and another characterized by a dominance of 0NN particles ($F0$), beyond the $S2$ phase. Its phase diagram displays a fluid-fluid demixing transition, characterized by a RF-$F0$ coexistence line, which ends in a critical point and also meet a RF-$S2$ and a $F0$-$S2$ coexistence line in a triple point [2]. Another interesting feature observed in the 0NN-1NN and 0NN-2NN mixtures is a thermodynamic anomaly characterized by minima in isobaric curves of the total density of particles. These different behaviors in the binary systems—especially the absence of the density anomaly in the 1NN-2NN case and the existence of the fluid-fluid demixing only the 0NN-2NN mixture—lead us to inquiry how these things are connected in the more general and interesting case of the 0NN-1NN-2NN ternary mixture. In this paper we address this by tackling the challenging problem of building up the three-dimensional (3D) phase diagram for this ternary model, once again by solving it on a cubic Husimi lattice.

We remark that ternary mixtures are central in a vast number of systems. To name a few, we may cite ternary quasicrystals [3], several chemical reactions involving three species (e.g., $2H_2 + O_2 \leftrightharpoons 2H_2O$), mixtures of cholesterol and lipids which play a key role in cell membranes [4,5], water-oil-surfactant mixtures [6,7], and so on. Moreover, colloids and granular matter in general are usually modeled as hard spheres [8]. In fact, (thermal) models of ternary mixtures have recently been used to investigate, e.g., critical Casimir forces among colloidal particles dispersed in a binary solvent [9,10] and the percolation of patchy colloids [11,12]. Regarding the athermal case, ternary mixtures of hard spheres have been theoretically investigated using different approximation methods [13–16] and in several works such approaches were compared with both simulations [17–23] and experiments [24–29].

Despite these works considering the hard spheres in the continuous space, as long as we know, ternary mixtures of them on the lattice (i.e., of kNN particles) have never been investigated so far. Actually, even binary mixtures of kNN particles on the cubic (or any other three-dimensional) lattice have never be studied before our recent works discussed

[*] nathan.rodrigues@ufv.br
[†] tiago@ufv.br

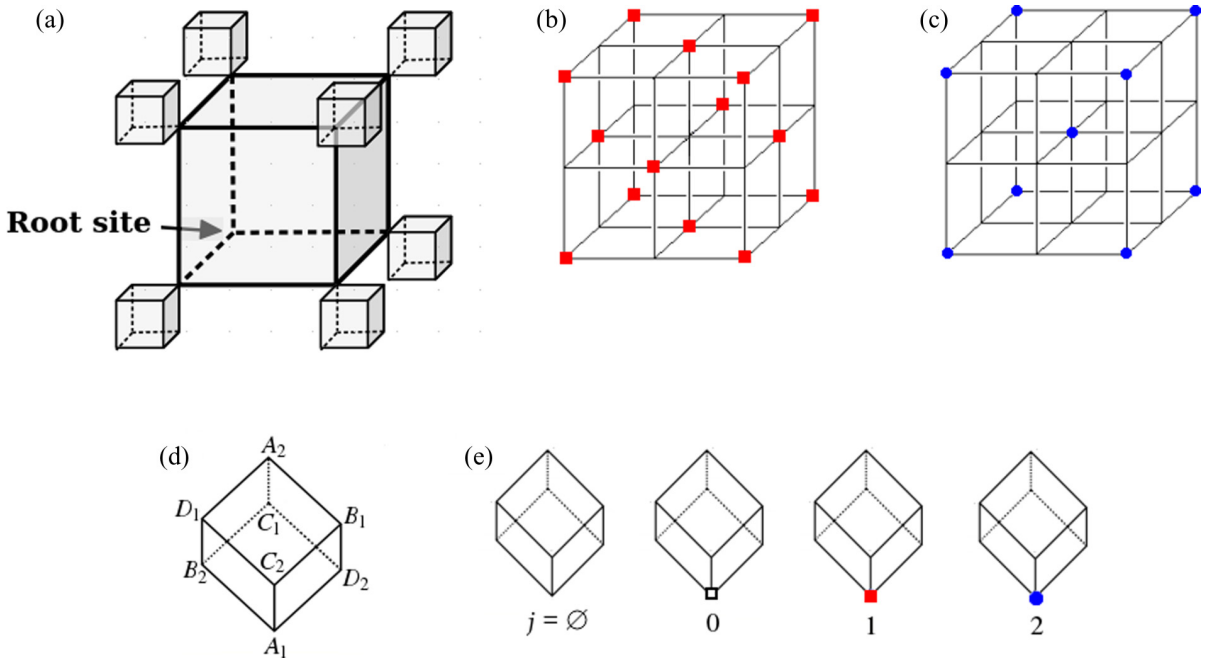

FIG. 1. (a) Illustration of part of a Husimi lattice built with cubes. The ground states of the solid $S1$ and $S2$ phases, in the cubic lattice, are displayed in (b) and (c), respectively. (d) Definition of the sublattice structure in an elementary cube of the Husimi lattice. (e) Representation of the possible states (j) for the root sites. They can be empty ($j = \varnothing$) or occupied by a 0NN ($j = 0$, open square), an 1NN ($j = 1$, full square), or a 2NN ($j = 2$, circle) particle.

above, based on the cubic Husimi lattice solution [1,2]. On the other hand, the 0NN-1NN mixture has been considered by several authors on the triangular [30–32] and square lattice [33–35], beyond a mean-field solution on the Bethe lattice [36]. A central topic in these studies is the possibility of a fluid-fluid demixing transition in kNN-binary mixtures. We remark that in nonadditive mixtures, as is the case in kNN ones, the demixed phases fill the space more effectively than the mixed one, so that a demixing is expected; and it has indeed been observed in several systems [37–47]. In the kNN systems, while van Duijneveldt and Lekkerkerker [31] claimed to have found a fluid-fluid demixing in the 0NN-1NN mixture on the triangular lattice, strong evidence against this have been presented by other authors [30,32], who observed only fluid-solid transitions in this model, similarly to what is found for this mixture on the square [33–35] and hierarchical lattices [1,36].

Therefore, it seems that among all kNN-binary mixtures investigated so far the 0NN-2NN case on the cubic Husimi lattice is the single one presenting a stable fluid-fluid demixing [2]. Hence, it is quite interesting to analyze what happens with this transition when 1NN particles are introduced in this system. As will be demonstrated below, the RF-$F0$ coexistence still exists for small densities of 1NN particles, giving rise to a fluid-fluid demixing surface in the 3D phase diagram of the 0NN-1NN-2NN mixture. Such phase diagram is also featured by several other coexistence surfaces, including a solid-solid demixing one, a critical F-$S1$ surface and lines of critical, tricritical, and triple points, giving rise to a very rich thermodynamic behavior.

The rest of the paper is organized as follows. In Sec. II the model is defined and solved on the cubic Husimi lattice in terms of recursion relations, which are presented in the Appendix. Its thermodynamic behavior is discussed in Sec. III. Our final discussions and concluding remarks are presented in Sec. IV.

II. MODEL DEFINITION AND SOLUTION ON THE HUSIMI LATTICE

The model considered here consists of a ternary mixture of hard spheres, with diameter λ, defined on—and centered at the vertices of—a cubic lattice. By assuming the lattice spacing being a, the smallest (0NN) particles corresponds to spheres of diameter $\lambda = a$, so that they occupy a single lattice site and effectively do not interact with each other. The intermediate (1NN) and largest (2NN) particles are spheres of diameters $\lambda = \sqrt{2}a$ and $\lambda = \sqrt{3}a$, respectively, which thus exclude up to their nearest- and next-nearest neighbors of being occupied by other particles. Let us remark that in our previous works on binary mixtures [1,2], we have wrongly stated that the 1NN and 2NN particles would correspond to *cubes* of lateral sizes $\lambda = \sqrt{2}a$ and $\lambda = \sqrt{3}a$, respectively, instead of *spheres*. An activity z_k is associated with each kNN particle (with $k = 0, 1, 2$) in our grand-canonical study of the model. It is worthy recalling that while the pure 0NN model can be exactly solved and it does not present any phase transition, the pure 1NN and 2NN models on the cubic lattice are known to undergo a continuous [48–51] and a discontinuous [51] phase transition, respectively, from disordered fluid to ordered solid phases.

The translational symmetry breaking of these solid phases display sublattice ordering, as illustrated in Figs. 1(b) and 1(c). In the ground state (the full occupancy limit) the solid

phase for the pure 1NN system (the $S1$ phase) is characterized by particles occupying one of two sublattices: either sublattices with index 1 or 2 in Fig. 1(d). On the other hand, the solid related to the pure 2NN system (the $S2$ phase) is featured by particles occupying one among four sublattices [A_i, B_i, C_i, or D_i, with $i = 1, 2$, in Fig. 1(d)], so that its ground state is fourfold degenerated. Thereby, to correctly capture the symmetries of both solid phases in the 0NN-1NN-2NN mixture, we have to deal with eight sublattices, as defined in Fig. 1(d).

Following our recent studies on the corresponding binary mixtures [1,2], here we will investigate the ternary 0NN-1NN-2NN case by defining the model on a Husimi lattice built with cubes [see Fig. 1(a)]. It is important to remark that the Husimi lattice consists of an infinite Cayley tree where each vertice is replaced by a polygon or a polyhedron. So, since the dimension of such lattice is infinity, the critical transition behavior is lead by mean-field exponents. Despite this, solutions on the Husimi lattice carry some degree of correlation of the system on the relevant lattice (the cubic lattice here), usually giving better results than other mean-field methods [52]. In fact, in some lattice gas systems, the Husimi solution even presents some quantitative agreement with simulation results on regular lattices [53,54].

To solve the ternary mixture on the Husimi lattice, we define a root site on an elementary cube [as shown in Fig. 1(a)] and partial partition functions (ppf's) according to its state. For each sublattice, the root site (and any other lattice site as well) can be empty ($j = \varnothing$), occupied by a 0NN ($j = 0$), by an 1NN ($j = 1$), or by a 2NN particle ($j = 2$), totaling 4 states [see Fig. 1(e)]. Hence, since we have eight sublattices, there are 32 ppf's for this system. One cube defines the 0-generation of the hierarchical lattice; so by attaching the root sites of seven cubes to the vertices of such cube, with exception of its root site, one obtains a subtree with 1-generation. Then, by attaching seven of such subtrees to the vertices of a new cube with exception of its root site, a 2-generation subtree is built. By repeating this process, we can create a $(M + 1)$-generation subtree from seven ones with M generations. Then, by summing over all possibilities of creating such subtree, by appropriately taking into account the particle exclusions, with its root site kept fixed in the state s and sublattice g, one obtains a recursion relation for the ppf g'_s as function of all ppf's in the previous generation g_j, with $g = a_1, a_2, \ldots, d_1, d_2$ and $s, j = \varnothing, 0, 1, 2$. Some details on such recursion relations (RRs) are presented in the Appendix.

Since we are interested in infinite subtrees, and the RRs usually diverges in this thermodynamic limit, we will work with ratios of them, defined as

$$G_j = \frac{g_j}{g_\varnothing}, \tag{1}$$

where $G_j = A_{1,j}, A_{2,j}, \ldots, D_{1,j}, D_{2,j}$, and $j = 0, 1, 2$. Thereby, from the 32 RRs for the ppf's one obtains 24 RRs for the ratios. The thermodynamic phases of the system are given by the stable and positive fixed points of these RRs. To analyze the stability of a given phase, we calculate the Jacobian matrix and its leading eigenvalue, Λ, at the associated fixed point. The phase is stable in the regions of the parameter space (z_0, z_1, z_2), where $\Lambda < 1$, while $\Lambda = 1$ defines its spinodal.

Similarly to the ppf's, we can obtain the partition function, Y, of the model on the tree by summing over all possibilities of attaching the root sites of eight subtrees to a central cube. It can be written in a compact form in terms of the ppf's, e.g., as

$$\begin{aligned} Y &= a_{1,\varnothing}a'_{1,\varnothing} + z_0 a_{1,0}a'_{1,0} + z_1 a_{1,1}a'_{1,1} + z_2 a_{1,2}a'_{1,2} \\ &= a_{1,\varnothing}b_{1,\varnothing}c_{1,\varnothing}d_{1,\varnothing}a_{2,\varnothing}b_{2,\varnothing}c_{2,\varnothing}d_{2,\varnothing}y, \end{aligned} \tag{2}$$

where y is a function of the ratios [Eq. (1)] and the activities z_0, z_1, and z_2. Then, the density of kNN particles in the sublattice A_1 at the central cube is given by

$$\rho_k^{(A_1)} = \frac{A_{1,k}}{8Y}\frac{\partial Y}{\partial A_{1,k}}, \tag{3}$$

with $k = 0, 1, 2$. A similar equation holds for the other sublattices, by replacing A_1 with $A_2, B_1, \ldots$, or D_2. Once we have the density of a kNN particle in all sublattices, its total density is $\rho_k = \rho_k^{(A_1)} + \rho_k^{(A_2)} + \cdots + \rho_k^{(D_1)} + \rho_k^{(D_2)}$. From the partition function we can also calculate the bulk free energy per site. Following the ansatz proposed by Gujrati [52], and discussed in detail for a Husimi lattice build with cubes in Ref. [2], for the ternary mixture one has

$$\phi_b = -\frac{1}{8}\ln\left[\frac{A_{1,\varnothing}B_{1,\varnothing}C_{1,\varnothing}D_{1,\varnothing}A_{2,\varnothing}B_{2,\varnothing}C_{2,\varnothing}D_{2,\varnothing}}{y^6}\right], \tag{4}$$

where

$$A_{1,\varnothing} \equiv \frac{a'_{1,\varnothing}}{b_{1,\varnothing}c_{1,\varnothing}d_{1,\varnothing}a_{2,\varnothing}b_{2,\varnothing}c_{2,\varnothing}d_{2,\varnothing}}, \tag{5}$$

and the other ratios can be obtained by the sublattice permutation scheme described in the Appendix. The bulk free energy is handy to determine where a first-order transition takes place. In a region where two or more phases have $\Lambda < 1$, the equality of their bulk free energies determines the point, line, or surface of coexistence among these phases.

III. THERMODYNAMIC BEHAVIOR OF THE MODEL

A. Summary of results for the binary mixtures

Once the binary mixtures 0NN-1NN ($z_2 = 0$), 0NN-2NN ($z_1 = 0$), and 1NN-2NN ($z_0 = 0$) are the boundary planes of the (z_0, z_1, z_2) space for the ternary case, it is interesting to start the presentation of results by discussing in detail the thermodynamic behavior of such planes [1,2].

For the 0NN-1NN mixture—the plane $(z_0, z_1, 0)$—we have found two thermodynamic stable phases [1]: a disordered fluid (F) phase, where the RRs for the ratios assume a homogeneous solution $A_{1,j} = B_{1,j} = \cdots = C_{2,j} = D_{2,j}$ with $j = 0, 1, 2$, and the solid $S1$ phase, associated with the ordering of the 1NN particles, where the RRs take the form $A_{i,j} = B_{i,j} = C_{i,j} = D_{i,j} = r_{i,j}$, with $i = 1, 2$ and $j = 0, 1, 2$, and $r_{1,j} > r_{2,j}$ for $j = 0, 1$, while $r_{1,2} < r_{2,2}$, when the sublattices with index 1 are the ones more occupied. Namely, in this phase one has $\rho_j^{(A_1)} = \cdots = \rho_j^{(D_1)} > \rho_j^{(A_2)} = \cdots = \rho_j^{(D_2)}$, for $j = 0, 1$ and the opposite for $j = 2$. (Note that these fixed points and densities are for these phases in the ternary case; and obviously $\rho_2^{(X)} = 0$, $\forall$ sublattice X, in the 0NN-1NN

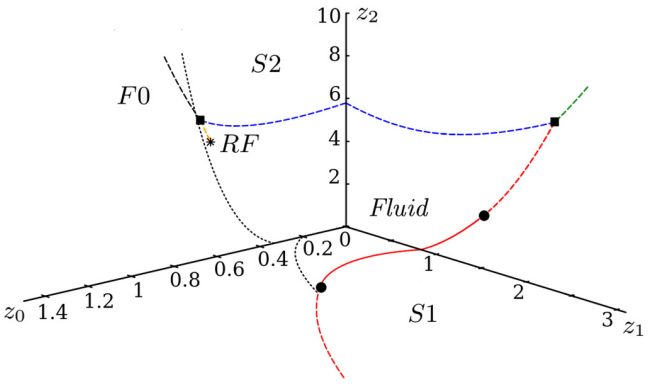

FIG. 2. Phase diagrams for the binary mixtures in the (z_0, z_1, z_2) space. The solid and dashed lines are continuous and discontinuous transition lines between the indicated phases they are separating. The squares are triple points, the circles are tricritical points and the star is a critical point. The dotted lines are the LMDs.

mixture). For small z_0 there is a continuous F-$S1$ transition, while for large z_0 such transition becomes discontinuous. The critical and the coexistence F-$S1$ lines meet at a tricritical point, located at $(z_0, z_1, z_2)_{\rm TC} = (0.5958, 1.1277, 0)$ [see Fig. 2]. Interestingly, this mixture presents a thermodynamic anomaly, characterized by minima in isobaric curves of the total density of particles as function of one activity (z_0 or z_1). A line of minimum density (LMD) exists within the fluid phase, starting at $z_0 \approx 0.20$ for $z_1 \to 0$ and ending close to the tricritical point in a region where the F phase is metastable (see Fig. 2).

A similar anomaly has also been observed in the 0NN-2NN mixture—the plane $(z_0, 0, z_2)$. In this case, the LMD starts at $z_0 \approx 0.333$ for $z_2 \to 0$ and, as in the 0NN-1NN case, it ends inside the region where the fluid phase is metastable [2] (see Fig. 2). Actually, beyond the RF phase (whose RRs have the symmetry just mentioned for the F phase), the 0NN-2NN mixture displays another stable disordered fluid phase characterized by a dominance of 0NN particles, reason for which it was baptized as the $F0$ phase in Ref. [2]. The RRs are also featured by $A_{1,j} = B_{1,j} = \ldots = C_{2,j} = D_{2,j} = r_j$ in the $F0$ case, but with $r_1 \approx 1$, $r_2 \approx 0$, and $r_3 \approx 0$, while in RF case the values of r_j strongly depend on the activities. These very same symmetries apply for the particle densities: While in RF phase ρ_0, ρ_1, and ρ_2 considerably vary with z_0, z_1, and z_2, in the stable region of the $F0$ phase one has $\rho_0 \gg \rho_1$ and $\rho_0 \gg \rho_2$. Beyond these two fluid phases, the solid $S2$ phase is also present in the phase diagram, which is associated with the ordering of the 2NN particles and characterized by a fixed point with $A_{1,j} = A_{2,j} > B_{1,j} = C_{1,j} = \cdots = C_{2,j} = D_{2,j}$, for $j = 0, 1, 2$, when the sublattices A_1 and A_2 are the more populated ones. This yields densities $\rho_j^{(A_1)} = \rho_j^{(A_2)} > \rho_j^{(B_1)} = \cdots = \rho_j^{(D_2)}$, for $j = 0, 1, 2$. A stable fluid-fluid demixing is observed in this system, whose discontinuous RF-$F0$ transition line ends at a critical point (CP), located at $(z_0, z_1, z_2)_{\rm CP} = (0.6297, 0, 5.4243)$, so that for $z_2 < z_{2,\rm CP}$ the RF and $F0$ phases cannot be distinguished. Hereafter, whenever this happens we will refer to these phases simply as the fluid (F) phase. The $S2$ phase is the most stable one for large z_2 and it is separated from the two fluid phases by discontinuous transition lines. The three coexistence lines RF-$F0$, RF-$S2$, and $F0$-$S2$ meet at a triple point (TP) located at $(z_0, z_1, z_2)_{\rm TP} = (0.6774, 0, 6.5671)$ [see Fig. 2].

Finally, in the 1NN-2NN mixture—the plane $(0, z_1, z_2)$—we have found the fluid F and the two solid $S1$ and $S2$ phases [1]. Similarly to the 0NN-1NN mixture, continuous and discontinuous F-$S1$ transition lines are observed, which meet at a tricritical point, located at $(z_0, z_1, z_2)_{\rm TC} = (0, 1.5273, 2.5016)$. The solid $S1$ and $S2$ phases are observed in the regions of large z_1 and z_2, respectively, and are separated by a discontinuous transition line. Another coexistence line exists between the F-$S2$ phases, which meet the F-$S1$ and $S1$-$S2$ ones in a triple point, located at $(z_0, z_1, z_2)_{\rm TP} = (0, 2.3102, 7.8746)$ (see Fig. 2). In contrast with the previous binary mixtures, no density anomaly was found in the 1NN-2NN case.

The summary of the behavior for the binary mixtures, displayed in Fig. 2, indicates that the 3D phase diagram for the ternary case is quite complex and interesting. For instance, the presence of the two fluid-$S2$ discontinuous transition lines in the planes $(0, z_1, z_2)$ and $(z_0, 0, z_2)$ strongly suggests the existence of a coexistence fluid-$S2$ surface in the 3D parameter space. Similarly, the F-$S1$ transitions in the planes $(z_0, z_1, 0)$ and $(0, z_1, z_2)$ strongly indicates that a critical and a coexistence F-$S1$ surface exist in the full phase diagram, both meeting at a line of tricritical points (a TC line). Besides these features, everything else is less clear. For example, it is unclear from the binary mixtures what can be expected for the LMD lines found in the planes $(z_0, z_1, 0)$ and $(z_0, 0, z_2)$, since the values of z_0 where they start in each plane do not coincide. So this could indicate either a complex scenario with two (or more) surfaces of minimum density, or that one or both of such surfaces do not exist. In the same token, it is not possible to known at this point whether the fluid-fluid demixing is a particular feature of the case $z_1 = 0$, or if it extends for $z_1 > 0$, giving rise to a RF-$F0$ coexistence surface, as well as to a line of triple points (where the phases RF-$F0$-$S2$ coexist) and a critical line in the 3D phase diagram. In what follows, these points will be addressed in great detail.

B. The fluid-fluid transition

From all thermodynamic properties observed in the binary mixtures discussed above, the fluid-fluid demixing transition in the 0NN-2NN ($z_1 = 0$) system is the most surprising one, in face it is absence in other kNN mixtures studied so far. For this reason, we will start the building up of the 3D phase diagram for the ternary mixture by analyzing the RF-$F0$ transition.

In order to do this, we investigate the phase behavior of slices of the 3D space for fixed values of z_1. Some relevant examples of such slices are shown in Fig. 3. For small z_1, specifically for $z_1 < 0.3177$ [see Fig. 3(a) for the case $z_1 = 0.1$], the same thermodynamic behavior of the case $z_1 = 0$ is found, with the phases RF, $F0$, and $S2$ pairwise separated by discontinuous transition lines which meet at a triple point, while the fluid-fluid demixing transition ends in a critical point. This demonstrates that in the 3D phase diagram there exist coexistence surfaces separating the RF-$F0$, RF-$S2$, and $F0$-$S2$ phases, all of them meeting at a line of triple points (the RF-$F0$-$S2$ TP line). Moreover, there is a line of critical

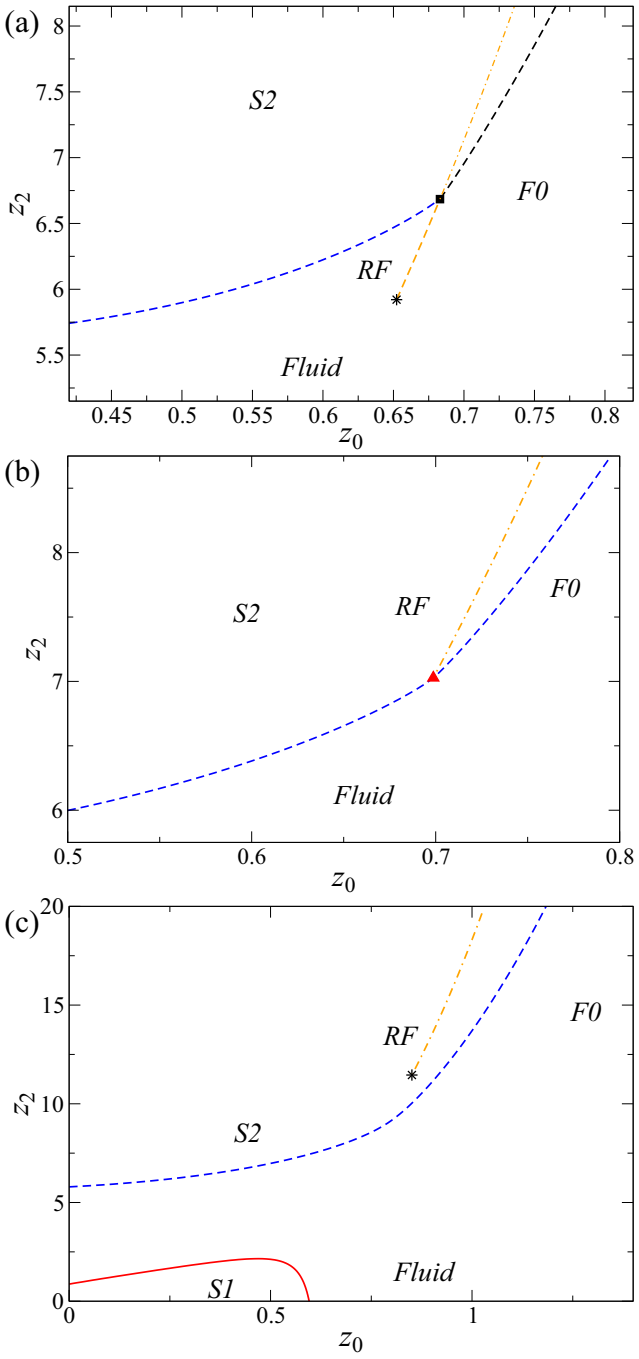

FIG. 3. Phase diagrams for fixed (a) $z_1 = 0.10$, (b) $z_1 = 0.3177$, and (c) $z_1 = 1.10$. In all panels, the dashed lines represent *stable* coexistence lines between the phases they are separating, while the dashed-dotted lines are the *metastable* RF-$F0$ coexistence lines. The solid line in (c) is the F-$S1$ critical line. The square in (a) is the RF-$F0$-$S2$ TP, while the stars are the RF-$F0$ CP and the triangle in (b) represents the special point where the TP line ends.

points (a CP line), where the RF-$F0$ coexistence surface ends. Substantially, this confirms that the fluid-fluid demixing transition is not restricted to the $z_1 = 0$ case, being a feature of the ternary mixture.

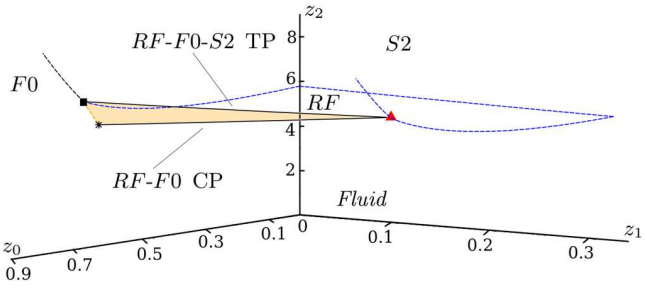

FIG. 4. Part of the 3D phase diagram for the ternary mixture in the activity space, highlighting the region around which the fluid-fluid demixing surface [the shaded (orange) one in the plot] takes place. All the surfaces presented here (separating the phases RF- or F-$S2$, $F0$-$S2$, and RF-$F0$) are coexistence surfaces. The triangle is the special point, where the CP line meets the RF-$F0$-$S2$ TP line. The star and the square represent the CP and the TP point, respectively, in the $(z_0, 0, z_2)$ plane.

Quantitatively, we observe that while the (z_0, z_2) coordinates of the TP line mildly change with z_1, the z_2 one for the CP line presents a strong variation with z_1, leading the stable region of the RF-$F0$ coexistence to decrease as z_1 increases. For instance, the RF-$F0$ coexistence line occurs in an interval $\Delta z_2 \approx 1.14$ for $z_1 = 0$ but only $\Delta z_2 \approx 0.76$ for $z_1 = 0.1$. In fact, by increasing z_1 one observes that the CP line becomes closer to the TP line, and at the special point $(z_0, z_1, z_2)^* = (0.6987, 0.3177, 7.0280)$ both lines meet, so that the *stable* fluid-fluid demixing transition disappears at this point. This gives rise to the phase diagram displayed in Fig. 3(b), for $z_1 = z_1^*$, with the (now completely metastable) RF-$F0$ coexistence line ending at the special point, so that the RF-$S2$ coexistence surface for $z_1 < z_1^*$ now becomes a F-$S2$ coexistence, which meets the $F0$-$S2$ coexistence line at the special point.

For not so large values of $z_1 > z_1^*$, one still finds the RF-$F0$ coexistence ending at the CP line, as shows Fig. 3(c) for $z_1 = 1.1$, but now this line is also metastable, occurring inside the region where the $S2$ phase is the most stable one. Therefore, the more complex scenario observed for small z_1 gives place to a simple F-$S2$ discontinuous transition. Namely, for $z_1 > z_1^*$ the fluid-fluid demixing transition becomes preempted by the fluid-solid transition. Hence, at the special point the CP line becomes metastable and the RF-$F0$-$S2$ TP line ends. A summary of these behaviors in the 3D space is presented in Fig. 4.

Although in general we will not be interested in discussing metastable transitions here, it is interesting to take a close look on this for the fluid-fluid demixing, to verify how further the RF-$F0$ coexistence surface goes as z_1 increases. First, we notice that, regardless the value of z_1, the metastable part of this surface is always limited from above, i.e., it ends when it meets the spinodal of the RF phase, as shown in Figs. 5(a) and 5(b). Second, for large z_1 the $S1$ phase also appears in the phase diagram in the region of small z_0 and z_2, as seen in Fig. 3(c), and the fluid phase let to be stable in such region. This is clearly seen by comparing the phase diagram in Fig. 5(c) with the spinodals of the fluid phases in Fig. 5(b). Curiously, by increasing z_1 the spinodal of the fluid phase

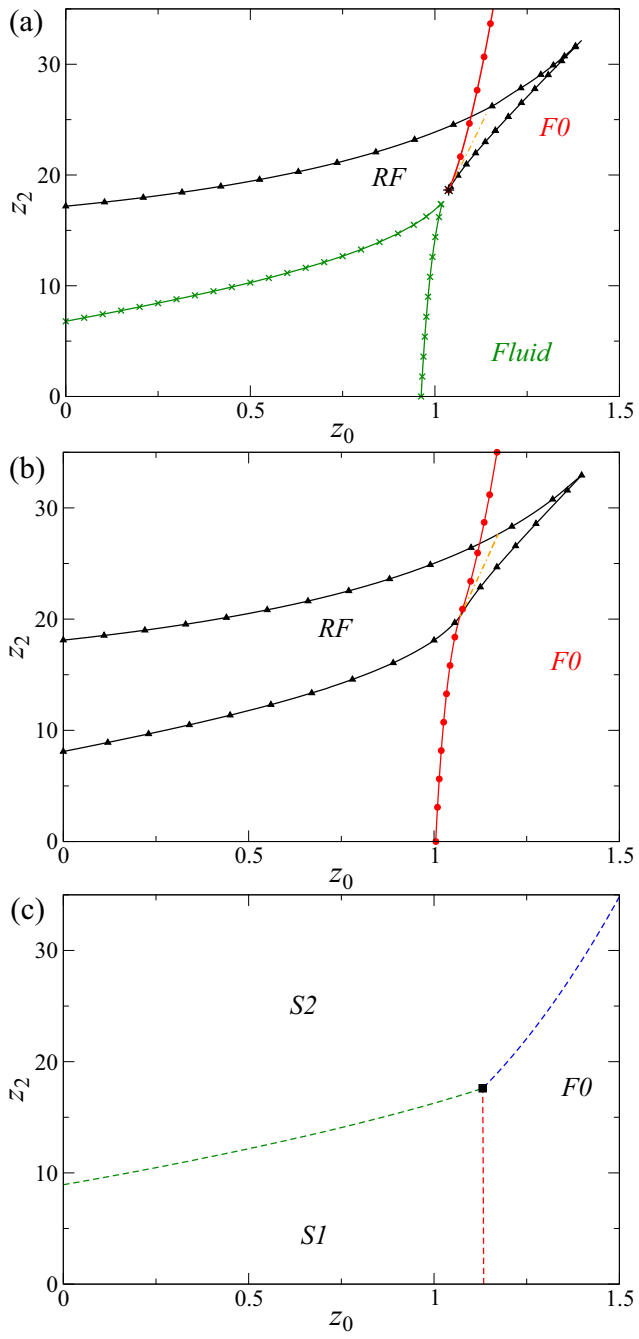

FIG. 5. Spinodals of the disordered fluid phases (solid lines) and the metastable RF-$F0$ coexistence lines (dash-dotted lines) for fixed (a) $z_1 = 2.3$ and (b) $z_1 = 2.5$. The lines with triangles, circles, and crosses are the RF, $F0$, and fluid (where RF and $F0$ phases cannot be distinguished) spinodals, respectively. The star in (a) is the metastable CP. For comparison, the phase diagram for $z_1 = 2.5$ is presented in (c), where the dashed lines represent coexistence lines between the indicated phases they are separating and the square is the TP. The phase diagram for $z_1 = 2.3$ is quite similar to this one.

develops a cusp, which approximates of the (metastable) CP line as z_1 increases, see Fig. 5(a) for $z_1 = 2.3$. Such approximation occurs until $z_1 \approx 2.3731$, after which the cusp meets the RF and $F0$ spinodals (in the point where there was the CP line), changing completely the scenario of such spinodals. In fact, as demonstrated in Fig. 5(b), for $z_1 = 2.5$, the stability region of RF phase becomes now limited to a closed domain of the (z_0, z_2) phase diagram, and the (metastable) RF-$F0$ coexistence line ends at the point where the spinodal of the $F0$ phase crosses the one for the RF phase. Therefore, the CP line ends at $z_1 \approx 2.3731$, while the fluid-fluid demixing still exists for larger values of z_1. However, by increasing z_1, one observes that the domain of the RF stability shrinks, yielding a decreasing in the in RF-$F0$ coexistence line, which finally disappears at $z_1 = 5.7157$.

C. The phase diagram for the ternary mixture

From the results in the previous subsection, one knows that for $z_1 < z_1^*$ the 3D phase diagram presents three coexistence surfaces (RF-$F0$, RF-$S2$, and $F0$-$S2$), a RF-$F0$-$S2$ TP line and a CP line, which meet (and ends or becomes metastable) at the special point, as depicted in Fig. 4. Moreover, for $z_1 > z_1^*$, but not so large, this behavior gives place to a simple F-$S2$ coexistence surface.

As shows Fig. 3(c), a critical F-$S1$ transition line is found in slices of the phase diagram for z_1 fixed (and large enough), giving rise to a critical F-$S1$ surface in the 3D space, as expected from the behavior of the binary mixtures. Such surface starts at $z_1 = 0.7284$—which turns out to be the point of minimum (in relation to z_1) of the F-$S1$ critical line in the 0NN-1NN mixture [i.e., in the plane $(z_0, z_1, 0)$] [1]—and exists in a limited region of the parameter space. Namely, it gives place to a discontinuous F-$S1$ transition surface for large z_1, as confirmed in Fig. 5(c). These features are better seen in slices of fixed and small z_0, as the one in Fig. 6(a) for $z_0 = 0.2$, where one finds a phase diagram similar to the one for $z_0 = 0$, with a continuous and a discontinuous F-$S1$ transition line meeting at a TC point. This confirms not only the existence of a critical and a coexistence F-$S1$ surface, but also the presence of a TC line where they meet in the 3D space. By analyzing several slices for fixed z_0 or z_2, we have accurately determined the TC line, which connects the two tricritical points found in the planes $(z_0, z_1, 0)$ and $(0, z_1, z_2)$. Interestingly, it presents a complex non-monotonic behavior, attaining a maximum point, with respect to z_1 and z_2, at $(z_0, z_1, z_2)_{\mathrm{TC,max}} = (0.6719, 1.4216, 4.6678)$. This line, as well as the critical and coexistence F-$S1$ surfaces are depicted in Fig. 7, which shows this part of the 3D phase diagram in detail.

The z_0 slices, as those in Figs. 6(a) and 6(b), also confirm the presence of the discontinuous F-$S2$ surface, as well as unveil the existence of a surface of solid-solid ($S1$-$S2$) demixing in the ternary mixture. Moreover, one always observes that the F-$S1$, F-$S2$, and $S1$-$S2$ coexistence surfaces meet in a line of triple points (the F-$S1$-$S2$ TP line), as seen in Figs. 5(c) and 6. This line starts at the triple point of the 1NN-2NN mixture [i.e., in the $(0, z_1, z_2)$ plane] and extends to $z_0, z_1, z_2 \to \infty$; its behavior is also shown in Fig. 7. It is important to notice that, since the TC line (and then the critical F-$S1$ surface) ends at a finite value of z_0, for large values of this activity everything we find in this part of the 3D phase diagram are the F-$S1$, F-$S2$, and $S1$-$S2$ coexistence surfaces meeting at the TP line [see Fig. 6(b)].

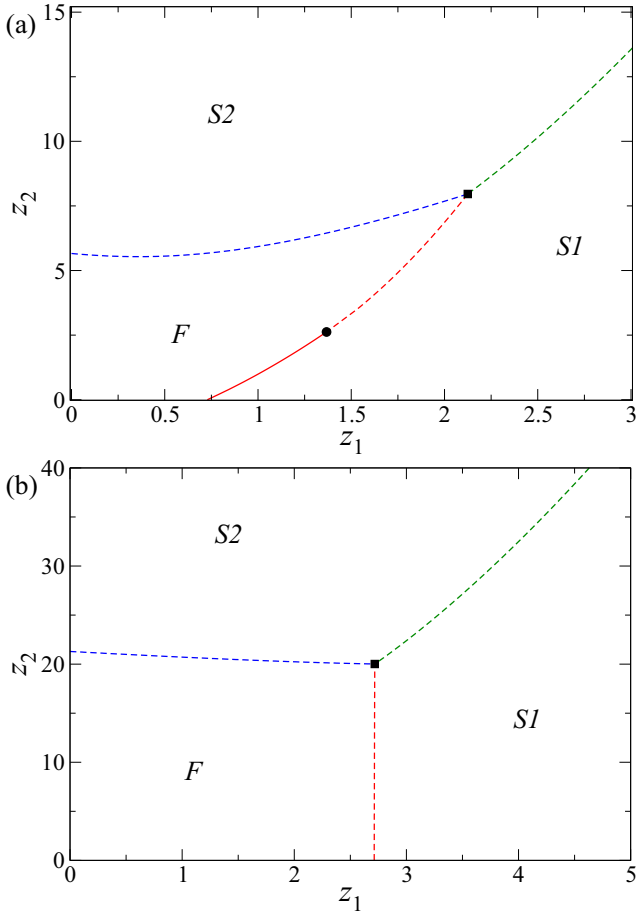

FIG. 6. Phase diagrams for fixed (a) $z_0 = 0.20$ and (b) $z_0 = 1.20$. The solid and dashed lines represent critical and coexistence lines, respectively, between the indicated phases they are separating. The black squares and the circle denote the TP and the TC point, respectively.

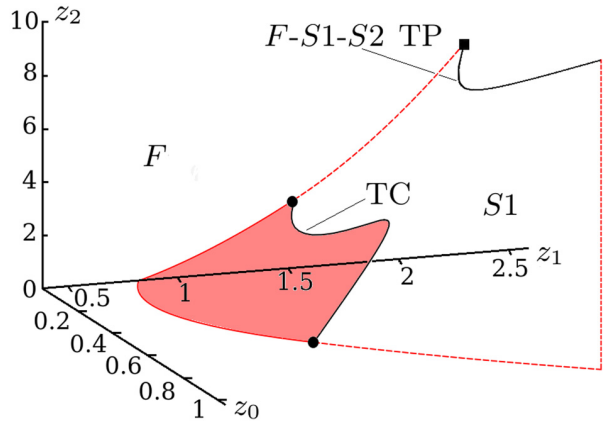

FIG. 7. Part of the 3D phase diagram for the ternary mixture in the activity space, highlighting the region where the critical F-$S1$ surface [the shaded (red) one in the plot] takes place. The the dashed lines indicate the F-$S1$ coexistence surface, which meets the critical surface at the TC line and is limited from above by the F-$S1$-$S2$ TP line. The circles and the square mark the location of the TC line and TP line, respectively, in the boundary planes.

The existence of the F-$S1$-$S2$ TP line in the limit of $z_0, z_1, z_2 \to \infty$ can be justified by the existence of a $F0$-$S1$, a F-$S2$, and a $S1$-$S2$ coexistence line in the binary mixtures, all of them extending to infinity [1,2]. Since the RRs assume simple forms in such limit, it is straightforward to determine the behavior of the TP line there. For instance, the fixed point for the RRs in the fluid phase has the form $A_{i,0} = B_{i,0} = C_{i,0} = D_{i,0} = 1$ and $A_{i,j} = B_{i,j} = C_{i,j} = D_{i,j} = 0$ for $i = 1, 2$ and $j = 1, 2$. For the $S1$ phase one finds $A_{1,j} = B_{1,j} = C_{1,j} = D_{1,j} = 1$ for $j = 0, 1$, while all others RRs vanish, when the sublattices indexed by 1 are the more populated ones. In the $S2$ phase, if the sublattices A_1 and A_2 are the ones more populated, one has $A_{i,j} = 1$ and $B_{i,j} = C_{i,j} = D_{i,j} = 0$, for $i = 1, 2$ and $j = 0, 1, 2$. Using these solutions, it is simple to calculate the free energies in this limit, being $\phi^{(F)} = (1 + z_0)^8$, $\phi^{(S1)} = (1 + z_0 + z_1)^4$, and $\phi^{(S2)} = (1 + z_0 + z_1 + z_2)^2$. By making $\phi^{(F)} = \phi^{(S1)} = \phi^{(S2)}$ and solving in terms of z_0, one finds

$$z_1 = z_0^2 + z_0 \tag{6}$$

and

$$z_2 = z_0^4 + 4z_0^3 + 5z_0^2 + 2z_0. \tag{7}$$

Therefore, as $z_0 \to \infty$ this TP line behaves has $z_1 \approx z_0^2$ and $z_2 \approx z_0^4$. This result can be understood as follows: At full occupancy an 1NN particle effectively occupies the volume of two 0NN ones, while a 2NN particle occupies the volume of four 0NN ones, in agreement with the exponents above. The calculated free energies also allow us to determine the behavior of the F-$S1$, F-$S2$, and $S1$-$S2$ coexistence surfaces in the limit of $z_0, z_1, z_2 \to \infty$, where one finds $z_1 \approx z_0^2$ and $z_2 \approx z_0^4$ for the F-$S1$ and F-$S2$ cases, respectively. Therefore, in slices of the 3D phase diagram for very large and fixed z_0, these surfaces shall appear as straight lines at constant z_1 and z_2, respectively. The $S1$-$S2$ coexistence surface, on the other hand, behaves as $z_2 \approx (z_0 + z_1)^2$, being a quadratic function of z_1 (z_0) for fixed z_0 (z_1). In fact, these results are somewhat confirmed in Fig. 6(b) for $z_0 = 1.2$, where we see that the F-$S1$ and F-$S2$ lines occur at almost constant values (specially the former one), while the $S1$-$S2$ line is not so straight, indicating the existence of a nonlinear dependence between z_2 and z_1. Results (not shown) for slices for much larger values of z_0 indeed confirm the correctness of the predicted surfaces.

Figure 8 presents the complete 3D phase diagram in the space of activities, summarizing all the features discussed so far. In face of its complexity—it has a fluid-fluid, a solid-solid, and several fluid-solid coexistence surfaces, with three of them (F-$S1$, F-$S2$, and $S1$-$S2$) extending to $z_0, z_1, z_2 \to \infty$, beyond a critical fluid-solid surface, a CP line, a TC line, and two TP lines—it is a bit hard drawing this phase diagram in an intelligible way. Notwithstanding, it is important to make clear how the partial diagrams depicted in Figs. 4 and 7 connect, what the sizes of the transition surfaces are (at least the ones which exist in limited domains), and so on.

At this point, it is important to stress that we have carefully looked for new phases in the general case, but only the four phases already present in the binary mixtures were found.

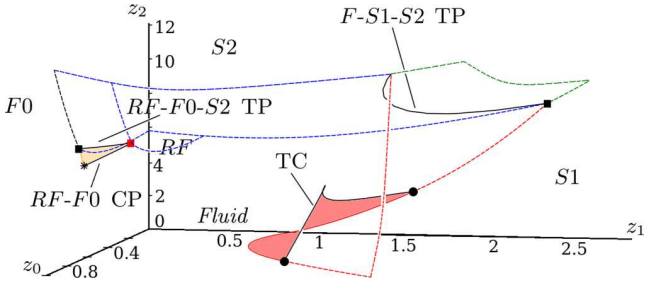

FIG. 8. Phase diagram for the ternary mixture in the activity space, indicating all phases and transition surfaces and lines, following the same scheme of symbols and colors from the previous figures.

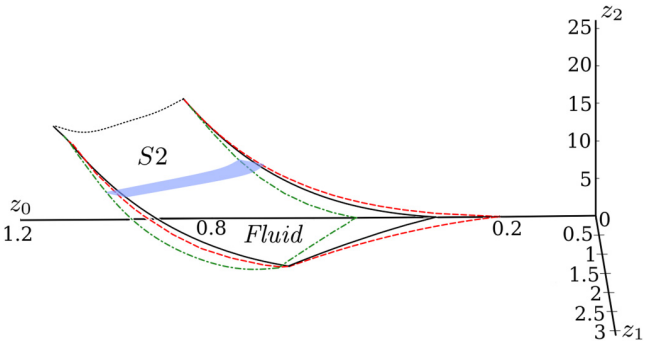

FIG. 9. Surfaces of minimum density in the activity space. The dash-dotted (green), continuous (black) and dashed (red) lines are the z_0-, z_1-, and z_2-SMD, respectively. The dotted (black) line is the LMD where all three SMDs seems to end. The shaded (blue) surface is part of the F-$S2$ coexistence surface, above which the SMDs become metastable.

D. The surfaces of minimum density

As discussed in Sec. III A, two lines of minimum density (LMDs) were found in the binary mixtures *inside the fluid phase*, one in the 0NN-1NN ($z_2 = 0$) and other in the 0NN-2NN ($z_1 = 0$) case. In the former system, the LMD starts at $z_0 \approx 0.333$ when $z_1 \to 0$, while in the last one it starts at $z_0 \approx 0.20$ when $z_2 \to 0$, and in both cases they end at the spinodal of the fluid phase, inside regions where the corresponding solid phases are more stable than the fluid [1,2]. The difference between these starting points suggests a complex scenario for the ternary mixture with at least two surfaces of minimum density (SMDs). Before discussing them, however, it is important to remark that such starting points were calculated through a limiting process. For example, for the 0NN-1NN mixture, we located the (z_0, z_1) coordinate where the total density—defined as $\rho_T = \rho_0 + 2\rho_1 + 4\rho_2$—presents a minimum for a given pressure, P,[1] i.e., along an isobaric curve of $\rho_T \times z_0$ (or z_1) (see, e.g., Fig. 5 in Ref. [2]). Then, by varying P we can build up the LMD curve and determine it as close as we want of the z_0 axis by making $z_1 \to 0$. Exactly on the z_0 axis, however, one has $\rho_T = z_0/(1 + z_0)$, so that no anomaly exists there.

Now, if we take slices of fixed $z_2 > 0$, then one still finds LMDs in the way just described, forming a SMD in the 3D space. Such z_2-SMD (since it is obtained for fixed values of z_2) starts at the LMD in the plane $(z_0, z_1, 0)$ and varies smoothly in the space, ending at the spinodal of the fluid phase, deep inside the region where the fluid is metastable. Although this surface does not exist exactly in the plane $(z_0, 0, z_2)$, using the limiting process we can obtain it as close as we want of this plane, so that there exists a LMD for $z_1 \to 0$ limiting this surface (see Fig. 9). Proceeding in the same way, but now considering slices of fixed z_1, a second SMD (the z_1-SMD) is obtained, which starts in the LMD on the plane $(z_0, 0, z_2)$ and also ends at the spinodal of the fluid phase in the metastable region. In this case, the SMD does not exist exactly in the plane $(z_0, z_1, 0)$, but it can be determined in the limit of $z_2 \to 0$. This z_1-SMD is also shown in Fig. 9. The existence of these two SMDs indicates, for sake of completeness, the existence of a third one for fixed z_0. As shown in Fig. 9, such z_0-SMD indeed exists in the 3D space and, albeit it cannot be observed exactly in the planes $(z_0, z_1, 0)$ and $(z_0, 0, z_2)$, it can be obtained in the limits $z_2 \to 0$ and $z_1 \to 0$, respectively. In such limits, the starting point of the z_0-SMD is at $z_0 \approx 0.50$ and, similarly to the other SMDs, it also ends in the spinodal of the fluid phase. As observed in Fig. 9, the three SMDs become quite close for large z_2 and they seem to be limited from above by a single line. However, it is quite hard to assure this numerically and it may be the case that they end at different (but very close) lines, or become a single surface before this.

[1]In our grand-canonical formalism $P = -\phi/a^3$.

IV. CONCLUSIONS

We have determined the thermodynamic behavior of a ternary mixture of hard spheres, defined on the cubic lattice, composed by pointlike particles (0NN) and particles which exclude up to their first (1NN) and second (2NN) neighbors. We treat this model by solving it on a Husimi lattice built with cubes, where four phases were found in the phase diagram, being two fluid and two solid ones, separated by several coexistence surfaces and a critical surface, which end or meet in lines of critical, tricritical, and triple points. One of the disordered phases is a regular fluid (RF), in the sense that the particle densities (ρ_0, ρ_1 and ρ_2) strongly depends on the activities, while in the second disordered fluid ($F0$) phase one always has $\rho_0 \gg \rho_1$ and $\rho_0 \gg \rho_2$. The solid $S1$ ($S2$) phase is featured by a sublattice ordering of 1NN (2NN) particles. We notice that columnar and smectic phases, observed for hard cubes on the cubic lattice [55,56], are absent in our solution. Although this can be due to the hierarchical structure of the Husimi lattice, we remark that these phases have never been found in previous studies of the pure 1NN and 2NN models on the cubic lattice [48–51], strongly suggesting that they should indeed not appear in their mixture.

A fluid-fluid (RF-$F0$) demixing surface is observed in the system, which is limited from below [in the (z_0, z_1, z_2) space] by a line of critical points (CP), whose coordinate $z_{2,c}$ increases fast with $z_{1,c}$, while the CP line and the whole RF-$F0$ coexistence surface exist in a narrow range of z_0. This shows that, by increasing ρ_1, a large ρ_2 is need to yield the demixing,

confirming that the fluid-fluid transition is not a feature restricted to the 0NN-2NN mixture, but the presence of the 1NN particles turns its appearance more difficult. In fact, although the demixing surface extends for a large portion of the phase diagram, it is stable only in a small area, when compared with the other transition surfaces. Such stable part is limited from above by the RF-$F0$-$S2$ triple point line, which ends when it meets the CP line at a special point [located at $(z_0, z_1, z_2)^* = (0.6987, 0.3177, 7.0280)$]. Therefore, the demixing surface becomes completely metastable (i.e., preempted by the F-$S2$ transition) already for $z_1 > z_1^*$, corresponding to a very small density of 1NN particles: $\rho_1 > \rho_1^* = 0.014$. This scenario lets clear why a fluid-fluid demixing has not been observed in the 0NN-1NN and 1NN-2NN binary mixtures. A possible explanation for this fact is that, although these are nonadditive mixtures, the particle sizes are not so dissimilar as in the 0NN-2NN case to yield a demixing. Further investigations of kNN mixtures with larger k's are necessary to confirm this.

We have also observed an anomaly in isobaric curves of the total density of particles (versus z_i, with $i = 0, 1, 2$), inside the fluid phase, which increase after passing to a minimum. Three surfaces of minimum density (SMDs) were found in the 3D parameter space, each one defined for one of the activities kept fixed. These SMDs start at different lines when we approximate the planes $(z_0, 0, z_2)$ and $(z_0, z_1, 0)$ by making $z_1 \to 0$ and $z_2 \to 0$, respectively, and ends at the spinodal surface of the fluid phase. For very large z_2, deep inside the metastable fluid region, these three surfaces either become quite close or collapse into a single surface. Although it is hard to decide this numerically, it is simple to figure out that this occurs because in this region one has $\rho_2 \gg \rho_0$ and $\rho_2 \gg \rho_1$, so that $\rho_T \approx 4\rho_2$ independently of the activity being fixed. We remark that density anomalies are typically found in complex polymorphic fluids, whose modeling is usually very elaborated (as is the case, e.g., in lattice gases with directional interactions) [57]. Therefore, the existence of this kind of anomaly in the simple athermal system analyzed here indicates that mixtures of hard spheres (and hard disks as well [35]) might be useful as a starting point to understand anomalies in more complex fluids.

ACKNOWLEDGMENTS

We acknowledge support from CNPq, CAPES, and FAPEMIG (Brazilian agencies).

APPENDIX: RECURSION RELATIONS FOR THE TERNARY MIXTURE

The RRs for the partial partition functions (ppf's) of the 0NN-1NN-2NN mixture were obtained using the method described in Sec. II. For the root site in the sublattice A_1, they are given by

$$
\begin{aligned}
a'_{1,\varnothing} = {} & b_{1,\varnothing}c_{1,\varnothing}d_{1,\varnothing}a_{2,\varnothing}b_{2,\varnothing}c_{2,\varnothing}d_{2,\varnothing}\big\{(1+z_0B_{1,0})(1+z_0C_{1,0})(1+z_0D_{1,0})(1+z_0A_{2,0})(1+z_0B_{2,0})(1+z_0C_{2,0}) \\
& \times(1+z_0D_{2,0}) + z_1(B_{1,1}+C_{1,1}+D_{1,1}+A_{2,1}+B_{2,1}+C_{2,1}+D_{2,1}) \\
& + z_1^2[B_{1,1}(D_{1,1}+A_{2,1}+B_{2,1}+C_{2,1}) + C_{1,1}(B_{2,1}+C_{2,1}+D_{2,1}) + D_{1,1}(A_{2,1}+C_{2,1}+D_{2,1}) + A_{2,1}C_{2,1} + B_{2,1}D_{2,1}] \\
& + z_1^3[B_{1,1}D_{1,1}(A_{2,1}+C_{2,1}) + B_{1,1}A_{2,1}C_{2,1} + C_{1,1}B_{2,1}D_{2,1} + D_{1,1}A_{2,1}C_{2,1}] \\
& + z_1^4B_{1,1}D_{1,1}A_{2,1}C_{2,1} + z_0z_1[B_{1,1}(D_{1,0}+A_{2,0}+B_{2,0}+C_{2,0}) + C_{1,1}(B_{2,0}+C_{2,0}+D_{2,0}) \\
& + D_{1,1}(B_{1,0}+A_{2,0}+C_{2,0}+D_{2,0}) + A_{2,1}(B_{1,0}+D_{1,0}+C_{2,0}) + B_{2,1}(B_{1,0}+C_{1,0}+D_{2,0}) \\
& + C_{2,1}(B_{1,0}+C_{1,0}+D_{1,0}+A_{2,0}) + D_{2,1}(C_{1,0}+D_{1,0}+B_{2,0})] \\
& + z_0^2z_1[B_{1,1}D_{1,0}(A_{2,0}+B_{2,0}+C_{2,0}) + B_{1,1}A_{2,0}(B_{2,0}+C_{2,0}) + B_{1,1}B_{2,0}C_{2,0} + C_{1,1}B_{2,0}(C_{2,0}+D_{2,0}) \\
& + C_{1,1}C_{2,0}D_{2,0} + D_{1,1}B_{1,0}(A_{2,0}+C_{2,0}+D_{2,0}) + D_{1,1}A_{2,0}(C_{2,0}+D_{2,0}) + D_{1,1}C_{2,0}D_{2,0} \\
& + A_{2,1}B_{1,0}(D_{1,0}+C_{2,0}) + A_{2,1}D_{1,0}C_{2,0} + B_{2,1}B_{1,0}(C_{1,0}+D_{2,0}) + B_{2,1}C_{1,0}D_{2,0} \\
& + C_{2,1}B_{1,0}(C_{1,0}+D_{1,0}+A_{2,0}) + C_{2,1}C_{1,0}(D_{1,0}+A_{2,0}) + C_{2,1}D_{1,0}A_{2,0} + D_{2,1}C_{1,0}(D_{1,0}+B_{2,0}) + D_{2,1}D_{1,0}B_{2,0}] \\
& + z_0^3z_1[B_{1,1}D_{1,0}A_{2,0}(B_{2,0}+C_{2,0}) + B_{1,1}D_{1,0}B_{2,0}C_{2,0} + B_{1,1}A_{2,0}B_{2,0}C_{2,0} + C_{1,1}B_{2,0}C_{2,0}D_{2,0} \\
& + D_{1,1}B_{1,0}A_{2,0}(C_{2,0}+D_{2,0}) + D_{1,1}B_{1,0}C_{2,0}D_{2,0} + D_{1,1}A_{2,0}C_{2,0}D_{2,0} + A_{2,1}B_{1,0}D_{1,0}C_{2,0} + B_{2,1}B_{1,0}C_{1,0}D_{2,0} \\
& + C_{2,1}B_{1,0}C_{1,0}(D_{1,0}+A_{2,0}) + C_{2,1}B_{1,0}D_{1,0}A_{2,0} + C_{2,1}C_{1,0}D_{1,0}A_{2,0} + D_{2,1}C_{1,0}D_{1,0}B_{2,0}] \\
& + z_0^4z_1(B_{1,1}D_{1,0}A_{2,0}B_{2,0}C_{2,0} + D_{1,1}B_{1,0}A_{2,0}C_{2,0}D_{2,0} + C_{2,1}B_{1,0}C_{1,0}D_{1,0}A_{2,0}) \\
& + z_0z_1^2[B_{1,1}D_{1,1}(A_{2,0}+C_{2,0}) + B_{1,1}A_{2,1}(D_{1,0}+C_{2,0}) + B_{1,1}C_{2,1}(D_{1,0}+A_{2,0}) + C_{1,1}B_{2,1}D_{2,0} + C_{1,1}D_{2,1}B_{2,0} \\
& + D_{1,1}A_{2,1}(B_{1,0}+C_{2,0}) + D_{1,1}C_{2,1}(B_{1,0}+A_{2,0}) + A_{2,1}C_{2,1}(B_{1,0}+D_{1,0}) + B_{2,1}D_{2,1}C_{1,0}] \\
& + z_0^2z_1^2(B_{1,1}D_{1,1}A_{2,0}C_{2,0} + B_{1,1}A_{2,1}D_{1,0}C_{2,0} + B_{1,1}C_{2,1}D_{1,0}A_{2,0} + D_{1,1}A_{2,1}B_{1,0}C_{2,0} \\
& + D_{1,1}C_{2,1}B_{1,0}A_{2,0} + A_{2,1}C_{2,1}B_{1,0}D_{1,0}) + z_0z_1^3(B_{1,1}D_{1,1}A_{2,1}C_{2,0} + B_{1,1}D_{1,1}C_{2,1}A_{2,0} + D_{1,1}A_{2,1}C_{2,1}B_{1,0} \\
& + B_{1,1}A_{2,1}C_{2,1}D_{1,0}) + z_2(B_{1,2}+C_{1,2}+D_{1,2}+A_{2,2}+B_{2,2}+C_{2,2}+D_{2,2}) \\
& + z_2^2(B_{1,2}B_{2,2}+C_{1,2}C_{2,2}+D_{1,2}D_{2,2}) + z_0z_2(B_{1,2}B_{2,0}+C_{1,2}C_{2,0}+D_{1,2}D_{2,0}+B_{2,2}B_{1,0}+C_{2,2}C_{1,0}+D_{2,2}D_{1,0}) \\
& + z_1z_2(B_{1,2}B_{2,1}+C_{1,2}C_{2,1}+D_{1,2}D_{2,1}+B_{2,2}B_{1,1}+C_{2,2}C_{1,1}+D_{2,2}D_{1,1})\big\}
\end{aligned}
\tag{A1a}
$$

$$
\begin{aligned}
a'_{1,0} = {} & b_{1,\varnothing}c_{1,\varnothing}d_{1,\varnothing}a_{2,\varnothing}b_{2,\varnothing}c_{2,\varnothing}d_{2,\varnothing}\big\{(1+z_0B_{1,0})(1+z_0C_{1,0})(1+z_0D_{1,0})(1+z_0A_{2,0})(1+z_0B_{2,0})(1+z_0C_{2,0}) \\
& \times(1+z_0D_{2,0}) + z_1(C_{1,1}+A_{2,1}+B_{2,1}+D_{2,1}) + z_1^2(C_{1,1}B_{2,1}+C_{1,1}D_{2,1}+B_{2,1}D_{2,1}) + z_1^3C_{1,1}B_{2,1}D_{2,1} \\
& + z_0z_1[C_{1,1}(B_{2,0}+C_{2,0}+D_{2,0}) + A_{2,1}(B_{1,0}+D_{1,0}+C_{2,0}) + B_{2,1}(B_{1,0}+C_{1,0}+D_{2,0}) + D_{2,1}(C_{1,0}+D_{1,0}+B_{2,0})] \\
& + z_0^2z_1[C_{1,1}B_{2,0}(C_{2,0}+D_{2,0}) + C_{1,1}C_{2,0}D_{2,0} + A_{2,1}B_{1,0}(D_{1,0}+C_{2,0}) + A_{2,1}D_{1,0}C_{2,0} \\
& + B_{2,1}B_{1,0}(C_{1,0}+D_{2,0}) + B_{2,1}C_{1,0}D_{2,0} + D_{2,1}C_{1,0}(D_{1,0}+B_{2,0}) + D_{2,1}D_{1,0}B_{2,0}] \\
& + z_0^3z_1(C_{1,1}B_{2,0}C_{2,0}D_{2,0} + A_{2,1}B_{1,0}D_{1,0}C_{2,0} + B_{2,1}B_{1,0}C_{1,0}D_{2,0} + D_{2,1}C_{1,0}D_{1,0}B_{2,0}) \\
& + z_0z_1^2(C_{1,1}B_{2,1}D_{2,0} + C_{1,1}D_{2,1}B_{2,0} + B_{2,1}D_{2,1}C_{1,0}) + z_2A_{2,2}\big\}
\end{aligned} \tag{A1b}
$$

$$
\begin{aligned}
a'_{1,1} = {} & b_{1,\varnothing}c_{1,\varnothing}d_{1,\varnothing}a_{2,\varnothing}b_{2,\varnothing}c_{2,\varnothing}d_{2,\varnothing}\big\{1 + z_0(C_{1,0}+A_{2,0}+B_{2,0}+D_{2,0}) + z_0^2[C_{1,0}(A_{2,0}+B_{2,0}+D_{2,0}) \\
& + A_{2,0}(B_{2,0}+D_{2,0}) + B_{2,0}D_{2,0}] + z_0^3[C_{1,0}A_{2,0}(B_{2,0}+D_{2,0}) + C_{1,0}B_{2,0}D_{2,0} + A_{2,0}B_{2,0}D_{2,0}] \\
& + z_0^4C_{1,0}A_{2,0}B_{2,0}D_{2,0} + z_1(C_{1,1}+A_{2,1}+B_{2,1}+D_{2,1}) + z_1^2(C_{1,1}(B_{2,1}+D_{2,1}) + B_{2,1}D_{2,1}) \\
& + z_1^3C_{1,1}B_{2,1}D_{2,1} + z_0z_1[C_{1,1}(B_{2,0}+D_{2,0}) + B_{2,1}(C_{1,0}+D_{2,0}) + D_{2,1}(C_{1,0}+B_{2,0})] \\
& + z_0^2z_1(C_{1,1}B_{2,0}D_{2,0} + B_{2,1}C_{1,0}D_{2,0} + D_{2,1}C_{1,0}B_{2,0}) \\
& + z_0z_1^2(C_{1,1}B_{2,1}D_{2,0} + C_{1,1}D_{2,1}B_{2,0} + B_{2,1}D_{2,1}C_{1,0}) + z_2A_{2,2}\big\}
\end{aligned} \tag{A1c}
$$

$$
a'_{1,2} = b_{1,\varnothing}c_{1,\varnothing}d_{1,\varnothing}a_{2,\varnothing}b_{2,\varnothing}c_{2,\varnothing}d_{2,\varnothing}(1 + z_0A_{2,0} + z_1A_{2,1} + z_2A_{2,2}), \tag{A1d}
$$

where $A_{i,j}$, $B_{i,j}$, $C_{i,j}$, and $D_{i,j}$, with $i = 1, 2$ and $j = 0, 1, 2$, are the ratios defined in Eq. (1). The RRs for the other sublattices can be obtained from cyclic permutations of the sublattice labels: $A_1 \to B_2$, $B_2 \to C_1$, $C_1 \to D_2$, $D_2 \to A_1$, together with $C_2 \to D_1$, $D_1 \to A_2$, $A_2 \to B_1$, $B_1 \to C_2$. Following this order, we can find the RRs for the sublattices D_2, C_1, and B_2. Those for sublattices A_2, B_1, C_2, and D_1 can be obtained from the ones for A_1, B_2, C_1, and D_2, respectively, by exchanging all the sublattice indexes i ($1 \leftrightarrow 2$). Once we have the RRs for the ppf's at hand, the ones for their ratios are obtained by simply dividing the corresponding equations, e.g., by dividing Eqs. (A1b), (A1c), and (A1d) by (A1a).

[1] N. T. Rodrigues and T. J. Oliveira, Phys. Rev. E **100**, 032112 (2019).
[2] N. T. Rodrigues and T. J. Oliveira, J. Chem. Phys. **151**, 024504 (2019).
[3] *Quasicrystals: Structure and Physical Properties*, edited by H.-R. Trebin (Wiley, New York, 2006).
[4] R. Elliott, I. Szleifer, and M. Schick, Phys. Rev. Lett. **96**, 098101 (2006).
[5] D. Wüstner and K. Solanko, Biochim. Biophys. Acta **1848**, 1908 (2015).
[6] S. Abbott, *Surfactant Science: Principles & Practice* (Destech, Lancaster, Pennsylvania, 2017).
[7] W. F. C. Sager, Microemulsion templating, in *Nanostructured Soft Matter: Experiment, Theory, Simulation and Perspectives*, edited by A. V. Zvelindovsky (Springer, Berlin, 2007), pp. 3–44.
[8] *Granular Matter: An Interdisciplinary Approach*, edited by A. Mehta (Springer-Verlag, New York, 1994).
[9] N. Tasios and M. Dijkstra, J. Chem. Phys. **146**, 134903 (2017).
[10] A. Maciolek and S. Dietrich, Rev. Mod. Phys. **90**, 045001 (2018).
[11] F. Seiferling, D. de las Heras, and M. M. Telo da Gama, J. Chem. Phys. **145**, 074903 (2016).
[12] P. I. C. Teixeira and J. M. Tavares, Curr. Opin. Colloid Interface Sci. **30**, 16 (2017).
[13] D. Gazzillo, Mol. Phys. **84**, 303 (1995).
[14] K. Fotouh and K. Shukla, Chem. Eng. Sci. **51**, 4923 (1996).
[15] E. Paschinger, A. Reiner, and G. Kahl, Mol. Phys. **94**, 743 (1998).
[16] A. König and N. W. Ashcroft, Phys. Rev. E **63**, 041203 (2001).
[17] H. M. Schaink, Physica A **210**, 113 (1994).
[18] S. B. Yuste, A. Santos, and M. López de Haro, J. Chem. Phys. **108**, 3683 (1998).
[19] A. Santos, S. B. Yuste, and M. López de Haro, J. Chem. Phys. **117**, 5785 (2002).
[20] A. Malijevský, A. Malijevský, S. B. Yuste, A. Santos, and M. López de Haro, Phys. Rev. E **66**, 061203 (2002).
[21] A. Malijevský, S. Labík, and A. Malijevský, Phys. Chem. Chem. Phys. **6**, 1742 (2004).
[22] C. N. Patra and S. K. Ghosh, J. Chem. Phys. **118**, 3668 (2003).
[23] Y.-X. Yu, J. Chem. Phys. **121**, 1535 (2004).
[24] K. Hoshino, J. Phys. F: Met. Phys. **13**, 1981 (1983).
[25] K. Fotouh and K. Shukla, Chem. Eng. Sci. **51**, 4933 (1996).
[26] S. Matsunaga, S. Tamaki, and S. Takeda, Phys. Chem. Liq. **37**, 395 (1999).
[27] A. Baylaucq, M. Moha-ouchane, and C. Boned, Phys. Chem. Liq. **38**, 353 (2000).
[28] B. J. Anderson, V. Gopalakrishnan, S. Ramakrishnan, and C. F. Zukoski, Phys. Rev. E **73**, 031407 (2006).
[29] L. Y. Yi, K. J. Dong, R. P. Zou, and A. B. Yu, Ind. Eng. Chem. Res. **50**, 8773 (2011); Powder Technol. **224**, 129 (2012); R. P. Zou, X. Bian, D. Pinson, R. Y. Yang, A. B. Yu, and P. Zulli, Part. Part. Syst. Charact. **20**, 335 (2003).
[30] D. Frenkel and A. A. Louis, Phys. Rev. Lett. **68**, 3363 (1992).

[31] J. S. van Duijneveldt and H. N. W. Lekkerkerker, Phys. Rev. Lett. **71**, 4264 (1993); J. Stat. Phys. **78**, 103 (1995).
[32] A. Verberkmoes and B. Nienhuis, Phys. Rev. E **60**, 2501 (1999).
[33] D. Poland, J. Chem. Phys. **80**, 2767 (1984).
[34] D.-J. Liu and J. W. Evans, J. Chem. Phys. **114**, 10977 (2001).
[35] T. J. Oliveira and J. F. Stilck, Phys. Rev. E **92**, 032101 (2015).
[36] T. J. Oliveira and J. F. Stilck, J. Chem. Phys. **135**, 184502 (2011).
[37] R. Dickman and G. Stell, J. Chem. Phys. **102**, 8674 (1995).
[38] M. Dijkstra, Phys. Rev. E **58**, 7523 (1998).
[39] M. Schmidt, J. Phys.: Condens. Matter **16**, L351 (2004).
[40] J. M. Brader and R. L. C. Vink, J. Phys.: Condens. Matter **19**, 036101 (2007).
[41] R. van Roij, B. Mulder, and M. Dijkstra, Physica A **261**, 374 (1998).
[42] H. H. Wensink, G. J. Vroege, and H. N. W. Lekkerkerker, J. Chem. Phys. **115**, 7319 (2001).
[43] S. Dubois and A. Perera, J. Chem. Phys. **116**, 6354 (2002).
[44] S. Varga, A. Galindo, and G. Jackson, J. Chem. Phys. **117**, 7207 (2002).
[45] M. Schmidt and A. R. Denton, Phys. Rev. E **65**, 021508 (2002).
[46] Y. Martínez-Ratón, E. Velasco, and L. Mederos, Phys. Rev. E **72**, 031703 (2005).
[47] D. de las Heras, Y. Martínez-Ratón, and E. Velasco, Phys. Rev. E **76**, 031704 (2007).
[48] D. S. Gaunt, J. Chem. Phys. **46**, 3237 (1967).
[49] A. Yamagata, Physica A **215**, 511 (1994).
[50] J. R. Heringa and H. W. J. Blöte, Physica A **232**, 369 (1996).
[51] A. Z. Panagiotopoulos, J. Chem. Phys. **123**, 104504 (2005).
[52] P. D. Gujrati, Phys. Rev. Lett. **74**, 809 (1995).
[53] C. Buzano, E. De Stefanis, and M. Pretti, J. Chem. Phys. **129**, 024506 (2008).
[54] T. J. Oliveira, J. F. Stilck, and Marco Aurélio A. Barbosa, Phys. Rev. E **82**, 051131 (2010).
[55] L. Lafuente and J. A. Cuesta, J. Chem. Phys. **119**, 10832 (2003).
[56] N. Vigneshwar, D. Mandal, K. Damle, D. Dhar, and R. Rajesh, Phys. Rev. E **99**, 052129 (2019).
[57] *Liquid Polymorphism*, Advances in Chemical Physics Vol. 152, edited by H. E. Stanley (Wiley, New York, 2013).

Chapter 4

Hard-squares on the square lattice

Here we present the preprint version of the pure 2NN lattice gas model. In the paper we approach the well know 1NN and the challenging 2NN model using high-level Husimi lattice solutions and the theory of coherent anomaly to characterize the critical behavior.

Husimi lattice solutions and the coherent-anomaly-method analysis for hard-square lattice gases

Nathann T. Rodrigues* and Tiago J. Oliveira†
Departamento de Física, Universidade Federal de Viçosa, 36570-900, Viçosa, MG, Brazil
(Dated: October 21, 2020)

Although lattice gases composed by kNN particles, forbidding up to their kth nearest neighbors of being occupied, have been widely investigated in literature, the location and the universality class of the fluid-columnar transition in the 2NN model on the square lattice is still a subject of debate. Here, we present grand-canonical solutions of this model on Husimi lattices built with diagonal square lattices of effective lateral size $\sqrt{2L(L+1)}$, for $L \leqslant 7$. The systematic sequence of mean-field solutions confirms the existence of a continuous transition in this system and extrapolations of the critical chemical potential $\mu_{2,c}(L)$ and density $\rho_{2,c}(L)$ to the thermodynamic limit ($L \to \infty$) yield precise estimates for these quantities on the *square* lattice, which agree with some less accurate results from Monte Carlo simulations. To confirm the reliability of this approach, we employ it also for the 1NN model, where a quite good agreement with the best known values for the critical parameters $\mu_{1,c}(\infty)$ and $\rho_{1,c}(\infty)$ — for the fluid-solid transition in this model on the square lattice — was found in extrapolations of data for $L \leqslant 6$. Despite the good agreement found in the critical parameters, the application of the coherent anomaly method (CAM) yields unreliable values for the critical exponents β and γ for both models. This confirms that the use of the CAM for calculating the non-classical exponents in such models is problematic, at least for the set of L's we were able to deal with here.

I. INTRODUCTION

Entropy-driven phase transitions have received a lot of attention for their role in the packing of dense fluids [1], in granular systems [2, 3], in adsorption of molecules onto a surface [4] and so on. In fact, a large number of studies have considered hard-disks, hard-spheres and other hard-objects, through analytical treatments and numerical simulations, in the continuous space (see, e.g., Refs. [5, 6] and references therein). In another front, lattice gases (LGs) composed by hard-particles have been also widely investigated through different methods for a number of particle shapes, such as triangles [7], dimers [8], rectangles [9], pentagons [10], tetrominoes [11], rods [12], Y-shaped [13], cubes [14], etc. on different lattices.

Among these hard-LGs, certainly the most studied ones are those of kNN particles, which forbid up to their kth nearest neighbor (NN) sites of being occupied by other particles, since they are discrete approximations for hard-spheres and hard-disks and find applications in several areas [15]. While the $k = 0$ case is boring, since the point particles present only a trivial thermodynamic behavior, for $k \geqslant 1$ this simple athermal LGs can present single or multiple transitions from disordered to ordered phases. For instance, on the simple cubic lattice, the 1NN model displays a continuous order-disorder transition [16–19] in the 3D Ising universality class [18], while in the 2NN case this transition seems to be discontinuous [19, 20], as well as for some larger values of k [19]. Results for the body-centered- and face-centered-cubic lattices can be found, e.g., in [21, 22] and references therein. On the honeycomb lattice, the 1NN model is long known to present a continuous fluid-solid transition belonging to the 2D Ising class [23, 24], whereas only very recently systems for larger k's were analyzed on this lattice [25], revealing that the 2NN case presents three stable phases: columnar, solid-like and fluid, with a first-order transition separating the first two ones [25]. On the triangular lattice, the 1NN case is the Baxter's hard-hexagon model [26, 27], the single kNN one for which an exact solution is available, showing that it displays a continuous fluid-solid transition in the class of the 3-state Potts model. The 2NN model [28–31] and more recently larger k's [32, 33] have been also investigated on the triangular lattice, where the continuous fluid-solid transition in the 2NN case seems to be in the 4-state Potts class [30, 31].

Despite all these works, most of the studies on kNN models have been performed on the square lattice, which is also the case of interest here. Since its introduction approximately 70 years ago [34], the 1NN hard-square model has been considered in a vast number of works [21, 35–53] and it is well-known to undergo a continuous fluid-solid transition in the 2D Ising class. Particularly in the transfer-matrix study by Guo and Blöte [50], this was firmly established and the critical chemical potential and density were accurately estimated as $\mu_c = 1.33401510027774(1)$ and $\rho_c = 0.3677429990410(3)$. More recent works have focused on extended hard-core exclusions [15, 51, 54] — for instance, $k \leqslant 820302$ was analyzed in Ref. [54] — and some of them revealed the existence of multiple phase transitions in these systems for large k's [15, 54].

The 2×2 hard-square model (i.e., the 2NN case) has also received much attention in the literature [6, 39, 42, 51, 55–66] and it is known to present a disordered fluid and an ordered columnar phase for low and high particle

* nathan.rodrigues@ufv.br
† tiago@ufv.br

densities, respectively. However, the nature, the location and even the existence of a transition between such phases have been a subject of constant debate. In fact, this is a taught model, for which different approximation methods usually return quite different outcomes for μ_c, ρ_c and the order of the transition (see e.g. the tables in Refs. [51, 54] for summaries of the existing results). While the recentest studies on this model agree in that the transition is continuous, its universality class is a bit controversial. For instance, it was suggested in Ref. [51] that it is the class of the 2D Ising model, similarly to the 1NN case, while exponents close, but deviating from the Ising ones were subsequently reported in [62, 63, 65]. Particularly in Ref. [65], convincing evidence that this system presents Ashkin-Teller criticality was reported, as previously hinted in [63].

In view of this discussion — and considering that it is being mainly based on Monte Carlo simulations, once finite-size analysis successfully applied to the 1NN model [50] has proved to be inconclusive in the 2NN case [63] — it is important to further investigate the 2×2 hard-square model considering other approaches. Here, we address this through semi-analytical grand-canonical solutions on Husimi lattices whose basic building blocks are diagonal square lattices with $2L(L+1)$ sites. Continuous fluid-columnar transitions are found at all levels of approximation analyzed (up to $L = 7$), yielding a series of even better mean-field results for the critical point [$\mu_c(L)$ and $\rho_c(L)$]. Extrapolations of these numerically exact parameters to $L \to \infty$ return values close, but more accurate than the best known estimates for them (from extensive Monte Carlo simulations on the square lattice). To check the reliability of this procedure, we employ it also for the 1NN model, where again results in good agreement with those in literature are obtained for the critical parameters. To investigate the *non-classical* critical exponents of these systems *on the square lattice*, we use the coherent anomaly method (CAM) [67]. We remark that this method has been applied in the study of the criticality in a diversity of classical and quantum systems, as well as nonequilibrium ones [68, 69]. However, for the best of our knowledge, for LG systems there exits a single study applying CAM in soft (Lennard-Jones type) LGs [70], where the method has failed in providing the expected critical exponents. So, our work may serve also as a check of the effectiveness of this method for hard-LGs. Unfortunately, for the low levels we are able to deal with here, the estimated exponents for both 1NN and 2NN models do not allow us to draw any conclusion about their universality classes.

The outline of this paper is as follows. In Sec. II we define the kNN models and devise the method for solving them on square Husimi lattices of different levels. Results for the critical parameters for the 1NN and 2NN models are presented, respectively, in Secs. III and IV. In Sec. V the coherent anomaly method is briefly discussed and applied to both models. Section VI summarizes our final discussions and conclusions.

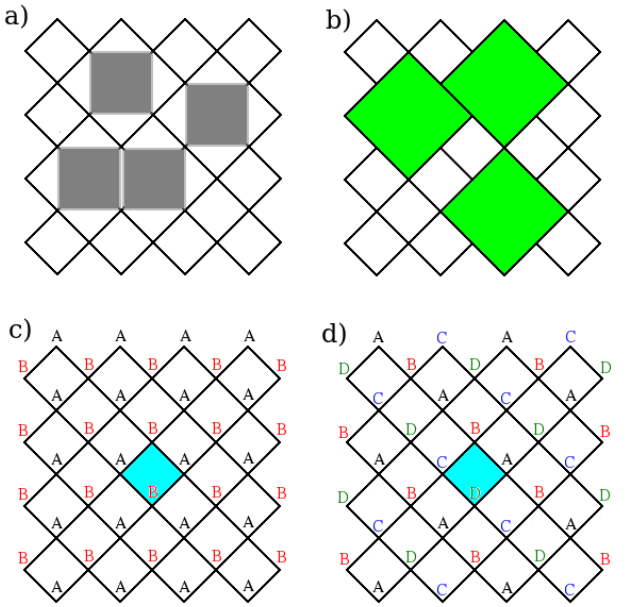

FIG. 1. Illustration of a) 1NN and b) 2NN particles on the diagonal square lattice with $L = 4$. The definitions of sublattices for studying the 1NN and 2NN models are respectively presented in (c) and (d).

II. MODELS AND METHODS

A. Models

A given kNN model is composed by hard-core particles, placed on (and centered at) the vertices of a given lattice, which exclude up to their first k next nearest neighbors of being occupied by other particles. In our grand-canonical treatment of these systems, an activity $z_k = e^{\mu_k}$, where $\mu_k = \tilde{\mu}_k/k_BT$ is the reduced chemical potential, will be associated with each kNN particle. For the sake of simplicity, hereafter we will refer to μ_k simply as "the chemical potential". On the square lattice, the 1NN particles correspond to hard squares of lateral size $\lambda = \sqrt{2}a$ tilted by 45° in relation to the lattice, where a is the lattice spacing [see Fig. 1(a)]. In the full occupancy limit, when $\mu_1 \to \infty$ and the density is $\rho_{1,max} = 1/2$, only one of two sublattices [A or B, as defined in Fig. 1(c)] are occupied, so that the system presents long-range order in this solid phase. By decreasing μ_1 a melting transition is observed for a disordered fluid phase, where both sublattices are equally populated (i.e., $\rho_1^{(A)} = \rho_1^{(B)}$). Thereby, an appropriate definition of the order parameter for this transition is [51]

$$Q_1 = \frac{1}{\rho_{1,max}} |\rho_1^{(A)} - \rho_1^{(B)}|, \tag{1}$$

since $Q_1 = 0$ ($Q_1 > 0$) in the fluid (solid) phase, being $Q_1 = 1$ in the ground state. The way to calculate the densities will be devised in the Appendix.

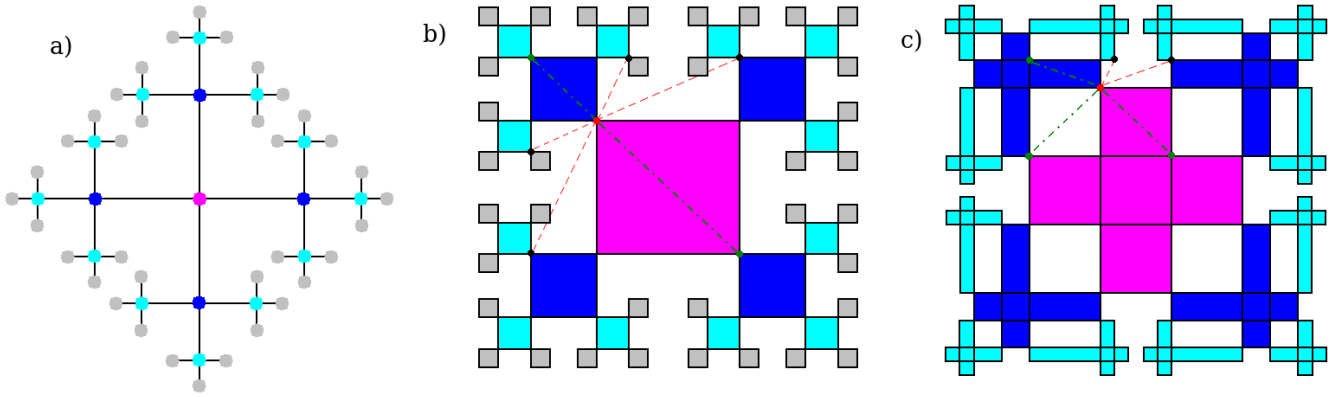

FIG. 2. a) Bethe lattice with coordination $q = 4$. Square Husimi lattices of b) first- ($L = 1$) and c) second-level ($L = 2$). Lattices with three [two] generations are shown in (a) and (b) [(c)], once we are considering the central (magenta) building blocks as the starting point. Different colors are associated with each generation. The dashed red lines in (b) and (c) indicate the NNNs *external to the plaquettes* of the red sites they are emanating, while the dash-dotted green lines connect the red sites with their *internal* NNNs.

The 2NN particles correspond to hard squares of lateral size $\lambda = 2a$ occupying four elementary plaquettes of the square lattice, as shows Fig. 1(b). In the limit of $\mu_2 \to \infty$, where $\rho_2 = \rho_{2,max} = 1/4$, this system presents a long-range columnar order, rather than a solid phase, due to a sliding instability, and four sublattices [$A, \ldots, D$, see Fig. 1(d)] are needed to characterize this fourfold degenerate ground state. By decreasing μ_2, a transition is expected from the columnar phase to a disordered fluid phase, where $\rho_2^{(A)} = \rho_2^{(B)} = \rho_2^{(C)} = \rho_2^{(D)}$. The fourfold symmetry breaking in such transition can be captured by the order parameter [51]

$$Q_2 = \frac{1}{\rho_{2,max}}(|\rho_2^{(A)} - \rho_2^{(C)}| + |\rho_2^{(B)} - \rho_2^{(D)}|), \qquad (2)$$

once $Q_2 = 0$ in the fluid phase and $Q_2 > 0$ in the solid one.

B. Husimi lattice solutions

A *Bethe lattice* (BL) is the core of an infinite Cayley tree: a hierarchical structure, without loops, which can be built by successively adding $q - 1$ edges to each boundary site of the previous generation ($M - 1$), starting with a "central" site and adding q edges to it to form the first generation of the tree. In this way, all sites in the interior of the tree have coordination q, while those at the boundary have a single neighbor [see Fig. 2(a)]. Since loops are absent in the BL, solutions of models on it can be seen as the zeroth-level mean-field approximation for a given model on a regular lattice (where loops are present). This can be improved by replacing the sites and edges of the BL by clusters, yielding the so-called *Husimi lattices* (HLs) [71]. In the ordinary (first-level) HL approximation for the square lattice, a square cactus is built by connecting elementary squares by a single vertex, as shown in Fig. 2(b). Similar treelike lattices can be built with triangles, cubes and so on. Recent examples of systems investigated on these Husimi cacti include frustrated magnets [72], polymers [73] and lattice gases [74]. In particular, quite recently binary [75] and ternary [76] mixtures of kNN particles were analyzed by us on a HL built with cubes.

In order to obtain reliable solutions for a given model on these treelike structures, it is obviously imperative that the symmetries of all of its phases have to be reproduced on such lattices. However, this is not always possible when dealing with the lowest levels. For example, the definition of the 2NN model on the BL is somewhat arbitrary, due to the definition of second neighbors in this lattice. In fact, by doing this considering the chemical distance, a discontinuous order-disorder transitions is obtained for this model [77]. Actually, even in the ordinary square HL of Fig. 2(b), it seems not possible to appropriately account for the correlations of the columnar phase. In such situations, we are compelled to consider high level HLs, where the elementary square plaquette is replaced by a cluster of plaquettes forming a small square lattice. Here, we will adopt the scheme introduced by Monroe [79], using diagonal square lattices as building blocks, which share L sites between two consecutive generations of the tree in each of its four sides. Figure 3 shows these building blocks for levels $L \leqslant 4$. The HL for $L = 2$ is depicted in Fig. 2(c), where some plaquettes had to be deformed to allow the drawing of a tree with more than one generation in the plane.

It is important to remark here that even in HLs the definition of second and high order neighbors is problematic. Let us concentrate first on the $L = 1$ case of Fig. 2(b), where each site clearly has only two next-nearest neighbors (NNNs) internal to the plaquettes, while this number should be four in the square lattice. If one considers also the NNNs external to the plaquettes, each site has four of such neighbors, as indicated by the dashed

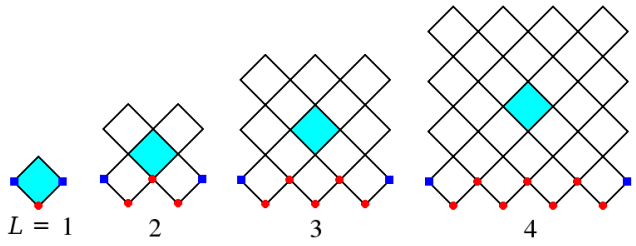

FIG. 3. Building blocks of square Husimi lattices of level $L \leqslant 4$. The generalization for higher L's is obvious. The sites composing the root zigzag lines for the solution of the 1NN model are indicated by the red dots, while for solving the 2NN model the sites indicated by the blue squares are also included in the root lines. The colored plaquettes are the central ones.

lines in Fig. 2(b), so that the total number of NNNs now becomes six. As demonstrated in Ref. [78], in thermal systems with NNN interactions associated with a Boltzmann weight ω, one way to conciliate this with the square lattice is by giving weights ω for each of the two internal NNNs and $\sqrt{\omega}$ for each of the four external ones. Since this does not apply for the athermal 2NN model, we have to either underestimate or overestimate the number of NNN sites. This problem lessens for higher L's, where most of sites have four NNNs internal to the plaquettes. The exceptions are the eight sites at the corners of the building blocks shown in Fig. 3, which have only three internal NNNs, as seen in Fig. 2(c). So, we can solve the 2NN model underestimating (U) the neighborhood of these corner sites, by excluding only their three internal NNNs. Another possibility is to extend the exclusion also to the two external NNNs of the corner sites [see Fig. 2(c)], overestimating (O) this. As will be demonstrated in the following, approach U yields unreliable results for small L's, although both solutions (O and U) are expected to become equivalent for $L \to \infty$.

The solutions of the models on the square HLs are discussed in detail in the Appendix. We anticipate here that such solutions are obtained in terms of recursion relations (RRs) for ratios of partial partition functions (ppf's), $R_{\sigma,S}$, where σ accounts for the particles' states and S for the sublattice configuration in the root zigzag line of rooted building blocks [see Fig. 3]. The real and positive fixed points of these RRs define the thermodynamic phases of the model on the HL. The free energies *per site* (ϕ_1 and ϕ_2 for the 1NN and 2NN models, respectively) will be calculated in the central building blocks of the HLs. In our grand-canonical formalism, they are related to the pressure as $P_k = -\phi_k/a^2$, where a^2 is volume of each site. The particle densities will be calculated in the four sites of the central plaquettes in the building blocks, as shown in Figs. 1 and 3, where one can calculate $\rho^{(S)}$ for all sublattices S appropriated for each model. As pointed out by Monroe [79], this central plaquette is the one for which the better results are expected for the densities, since it is the farthest one from the boundary of the HL.

III. CRITICAL PARAMETERS FOR THE 1NN MODEL

Let us start analyzing the 1NN model, which is solved here on square HLs of levels $1 \leqslant L \leqslant 6$. In all levels, two types of fixed points are found for the recursions relations (RRs) for the ratios of ppf's defined in the appendix. One has a fixed point associated with the disordered fluid (F) phase, characterized by a homogeneous solution of the RRs, with $R_{\sigma,A} = R_{\sigma,B}$ for $\sigma = 1, 2, ..., N_L - 1$, where N_L is the total number of ppf's for a given L and sublattice (A or B). There are two other equivalent fixed points associated with the ordered solid (S) phase, where one of the sublattices is more populated. For example, $R_{\sigma,A} > R_{\sigma,B}$ when sublattice A is the one more occupied.

The stability analysis, for all levels, reveals that the F (S) phase is stable for small (large) z_1 and that the spinodals of both phases take place at the same value of z_1. This characterizes a continuous F-S phase transition, as expected for the 1NN model. This is confirmed also by the behavior [not shown] of the densities (ρ_1), free energies (ϕ_1) and order parameters (Q_1). The values found for the critical parameters $\mu_{1,c} = \ln(z_{1,c})$, $\rho_{1,c}$ and $\phi_{1,c}$ for different L's are summarized in Tab. I.

With the data for the critical chemical potential $\mu_{1,c}(L)$ at hand, we can use different methods for extrapolating them to $L \to \infty$, which will correspond the thermodynamic limit and shall provide an estimate of $\mu_{1,c}$ for the model on the square lattice. As usual, we will assume the finite-size scaling form

$$\mu_{1,c}(L) = \mu_{1,c}(\infty) + a_1 L^{-\Delta_1} + a_2 L^{-\Delta_2} + ..., \quad (3)$$

where one expects that $0 < \Delta_1 < \Delta_2 < \cdots$. As a first approximation, we can truncate this series at the second term, by assuming that $a_i = 0$ for $i \geqslant 2$. This lets us with three unknowns [$\mu_{1,c}(\infty)^{(1)}$, a_1 and Δ_1] that can be easily estimated from three-point extrapolations. The values of $\mu_{1,c}(\infty)^{(1)}$ and Δ_1 from such extrapolations for the sets of L's $(1,2,3)$, $(2,3,4)$, $(3,4,5)$ and $(4,5,6)$ are depicted in Tab. II. They can be reduced to two values with another three-point extrapolation and so on. Using this

L	$\mu_{1,c}$	$\rho_{1,c}$	$\phi_{1,c}$
1	0.68252587	0.269594	−0.57156
2	0.92990791	0.308815	−0.86793
3	1.03574380	0.319238	−1.02970
4	1.09621330	0.327915	−1.13145
5	1.13559460	0.333132	−1.20130
6	1.16338910	0.336462	−1.25230

TABLE I. Critical chemical potentials $\mu_{1,c}$, particle densities $\rho_{1,c}$ and free energies $\phi_{1,c}$ for the 1NN model on square HLs of different levels L.

Set of L's	$\mu_{1,c}(\infty)^{(1)}$	Δ_1	$\rho_{1,c}(\infty)^{(1)}$	$\phi_{1,c}(\infty)^{(1)}$
$(1,2,3)$	1.44933	0.561955	0.33950	−4.12490
$(2,3,4)$	1.40530	0.621107	0.37088	−2.10232
$(3,4,5)$	1.37521	0.681918	0.36760	−1.82332
$(4,5,6)$	1.36141	0.720412	0.36769	−1.73235

TABLE II. Three-point extrapolations for the critical parameters $\mu_{1,c}(\infty)^{(1)}$ and $\rho_c(\infty)^{(1)}$ for the sets of L's $(1,2,3)$, $(2,3,4)$, $(3,4,5)$ and $(4,5,6)$ and the respective values of Δ_1 for the extrapolations of $\mu_{1,c}(\infty)^{(1)}$.

procedure we have found $\mu_c(\infty) = 1.33740$ which differs approximately 0.2% of the value $\mu_c(\infty) \approx 1.3340151002$ reported in [50]. To verify the reliability of this extrapolation method we have applied the scheme to the data of the critical temperature of the 2D Ising model presented in [79], where the Ising model is solved in HLs up to $L = 5$. The sequence of three-point extrapolation gives $T_c = 2.263298$ a value differing 0.2% from the Onsager value.

We can improve the extrapolation scheme by considering the third term of Eq. 3. First we can try to find the value of Δ_1 and perform a four-point extrapolation. However, from the data of Δ_1 shown in Tab. II, it is unclear it extrapolated value. From a three-point extrapolation on the Δ_1 of the sets $(2,3,4)$, $(3,4,5)$ and $(4,5,6)$, we have found $\Delta_1 = 0.9194$. Using this value on the four-point extrapolation we have found $\mu_{1,c}(\infty) = 1.37516$, which makes no improvement in the value found with sequences of three-point extrapolations. With Δ_1 unknown we can perform a five-point extrapolation. In [79] this extrapolation gives the best results with the critical temperature differing only 0.003% from the Onsager value. Unfortunately, we have not found any physical solution for $\mu_c(\infty)$ (or any of the other critical parameters) with the five-point extrapolation which can indicates that the L's considered here are not high enough to have a simple correction to scale as presented in Eq. 3.

By assuming that the finite-size correction in the critical density $\rho_{1,c}(L)$ have a behavior similar to that of Eq. 3, we employ the tree-point extrapolation for the data up to $L = 6$. The extrapolated values of the sets $(1,2,3)$, $(2,3,4)$, $(3,4,5)$ and $(4,5,6)$ are shown in Tab. II. The four extrapolated points obtained fluctuate, making it impossible to utilize another three-point extrapolation. Then, we consider the value of $\rho_c(\infty)$ of the highest set of L's, $(3,4,6)$, which gives $\rho_c(\infty) = 0.36769$. This value differs only 0.01% of the one reported in [50] of $\rho_c(\infty) \approx 0.367744$.

Similar to the others quantities, we also assume a finite-size correction of the form of Eq. 3 for the free energy $\phi_{1,c}$. By making the three-point extrapolation of the values of $\phi_{c,1}$ shown in Tab. I we have found the extrapolated values, $\phi_{1,c}(\infty)^{(1)}$, presented in Tab. II. With another three-point extrapolation in the values of $\phi_{1,c}(\infty)^{(1)}$ for the sets $(2,3,4)$, $(3,4,5)$ and $(4,5,6)$, we have found $\phi_{1,c}(\infty) = -1.62911$ a value, in module, approximately twice bigger than the value of $\phi_{1,c}(\infty) = 0.791602643166112(1)$ reported in [50].

IV. CRITICAL PARAMETERS FOR THE 2NN MODEL

Now, we investigate the 2NN model for HLs of level up to $L = 7$ ($L = 8$) in the approximation O (U), which overestimates (underestimates) the number of NNN sites for some sites. The densities and free energies were calculated only in the O case, for $L \leqslant 6$. Similarly to the 1NN model, here, in both approximations, the RRs assume a homogeneous solution, related to the fluid (F) phase, characterized by $R_{\sigma,A} = R_{\sigma,B} = R_{\sigma,C} = R_{\sigma,D}$, with $\sigma = 1, 2, 3, ..., N-1$, which is stable for small z_2. For large z_2, in both O and U approaches, we find four equivalent fixed points associated with the columnar nature of the ordered phase of the 2NN model. Although these fixed points are not so simple as in the fluid phase or in the solid phase of the 1NN model, by inspection of the values of $R_{\sigma,S}$ for all σ's and sublattices S, it is possible to verify, for example, that there are two possibilities for the sublattice A be more occupied: one in which the sublattice B is also more occupied; and other with the sublattice D, instead of B, being also more occupied. Each of these fixed points are associated with columns being formed in one of the two directions of the square lattice.

In all levels, the stability analysis reveals that exists a critical point separating the fluid and the columnar phases. This strongly indicates that the fluid-columnar transition in the square lattice is continuous, in agreement with most of the works on these hard-squares, as already discussed in the Introduction. Moreover, this demonstrates that the first-order transition observed by Robledo and Varea [77] for the 2NN model on the Bethe lattice is indeed a consequence of the failure of this lattice in capturing the correlations of the columnar phase.

In Fig. 4 we compare the value of μ_c found in the approximation O and U. The underestimation of the number of NNN sites highly affect the critical value for low L's, as in the case of $L = 2$ and 3 shown in Fig. 4, reducing the accuracy of any extrapolation analysis. Both approximations displays an almost linear behavior when plotted against $L^{-0.75}$ indicating that $\Delta_1 \approx 3/4$. However, a much smoother behavior is observed for the approximation O. Beyond this, in order to both approximations converge a non-monotonic behavior shall appears on the U approximation. Then, from now on we will only shown the critical parameters and analysis for the overestimate approximation. The critical parameters $\mu_{2,c}$, $\rho_{2,c}$ and the critical free energy $\phi_{2,c}$ are shown in Tab. III.

As in the 1NN we start by the three-point extrapolation. In Tab. IV the extrapolation values for the sets of L's $(2,3,4)$, $(3,4,5)$, $(4,5,6)$ and $(5,6,7)$ is shown.

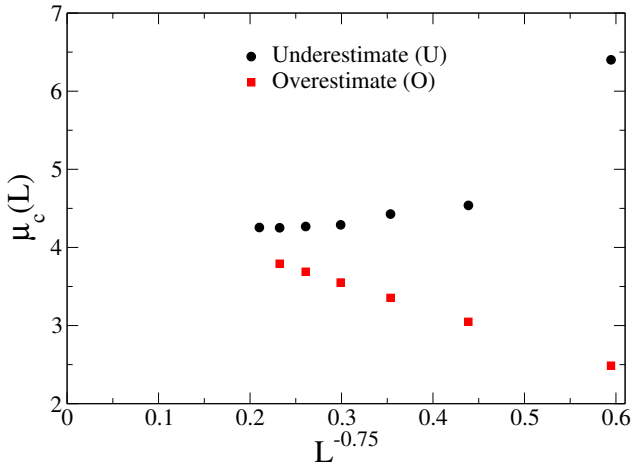

FIG. 4. The black circles are the values of $\mu_{2,c}$ of the underestimate approximation, while the red squares the data of the overestimation case. Both cases are plotted against $L^{-\Delta_1}$ with $\Delta_1 = 0.75$.

L	$\mu_{2,c}$	$\rho_{2,c}$	$\phi_{2,c}$
2	2.4867416	0.2004193	0.519643
3	3.0481278	0.2090740	0.457326
4	3.3545774	0.2133478	0.393478
5	3.5505669	0.2157784	0.340409
6	3.6884884	0.2172566	0.300490
7	3.7913584	–	0.267941

TABLE III. Critical chemical potentials $\mu_{2,c}$, particle densities $\rho_{2,c}$ and free energies $\phi_{2,c}$ for the 2NN model in HLs of different level L.

The values of $\mu_{2,c}(\infty)^{(1)}$ fluctuate for the different sets making impossible to reduce the data with another three-point extrapolation. From the highest set of L's we have found $\mu_{2,c}(\infty) = 4.63792$ a value close to the one reported in [63] of $\mu_{2,c}(\infty) = 4.584(2)$ and of the value $\mu_c(\infty) \approx 4.576$ reported in [51]. As shown in Fig. 4 the values of $\mu_{2,c}(L)$ have a behavior close to linear when plotted against $L^{-\Delta_1}$ with $\Delta_1 = 0.75$, in fact, in all sets of three-point extrapolation the value obtained for the exponent Δ_1 is close to 3/4. By fixing this value and considering the third term of the Eq. 3, we perform a four-point extrapolation which gives $\mu_c = 4.57104$, an value that differs 0.2% from [63] and 0.1% from [51].

For the critical density, as in the 1NN case, we employ the three-point extrapolation. With the three-point we have observed $\rho_{2,c}(\infty)$ for the sets $(2,3,4)$, $(3,4,5)$ and $(4,5,6)$ close to each other, considering the highest L's the we have found $\rho_{2,c}(\infty) = 0.2221$ a value slight lower than the one of $\rho_c(\infty) \approx 0.233$ found in [51, 66]. Lastly the critical free energy, as shown in Tab. IV the three-point extrapolation gives values in a wide range between $-0.6959 < \phi_{2,c}(\infty) < 0.63410$, with any clear tendency for a further extrapolation we are not able to determine a reliable value for $\phi_{2,c}(\infty)$.

Set of L's	$\mu_{2,c}(\infty)^{(1)}$	Δ_1	$\rho_{2,c}(\infty)^{(1)}$	$\phi_{2,c}(\infty)^{(1)}$
$(2,3,4)$	4.62538	0.750954	0.2256	0.63410
$(3,4,5)$	4.62265	0.752407	0.2266	1.24463
$(4,5,6)$	4.65061	0.734765	0.2221	−0.2172
$(5,6,7)$	4.63792	0.743947	–	−0.6959

TABLE IV. 2NN model three-point extrapolations of $\mu_{2,c}$, ρ_c, $\phi_{2,c}$ and the exponent Δ_1 extracted from the $\mu_{2,c}$ extrapolations.

V. COHERENT ANOMALY METHOD

In this section, we will analyze the *non-classical* critical exponents of both 1NN and 2NN models through the coherent anomaly method (CAM). Let us start remarking that, independently of its level L (finite), the dimension of the HLs is always infinity. Hence, in all levels, the critical exponents assume their classical values. Of particular interest here will be the order parameters Q_1 and Q_2, defined in Eqs. 1 and 2, respectively, and the susceptibilities associated with their fluctuations χ defined in Eq. 10. Close to the critical point these quantities are expected to behave as

$$Q_i(L) = \bar{Q}_i(L)\mu_i^*(L)^{\beta_{cl}} \tag{4}$$

and

$$\chi_i(L) = \bar{\chi}_i(L)\mu_i^*(L)^{\gamma_{cl}}, \tag{5}$$

where $i = 1$ for the 1NN model and $i = 2$ for 2NN one. The rescaled chemical potential μ_i^* will be defined as

$$\mu_i^*(L) = \frac{|\mu_{i,c}(\infty) - \mu_{i,c}(L)|}{\mu_{i,c}(\infty)}. \tag{6}$$

In Eqs. 4 and 5, $\bar{Q}_i$ and $\bar{\chi}_i$ are non-universal amplitudes, while $\beta_{cl} = 1/2$ and $\gamma_{cl} = 1$ are the classical exponents. According to the CAM theory, the non-universal amplitudes of a sequence of systematically improved mean-field approximations, as is the case of our HL solutions, encode information on the non-classical values of the critical exponents, being related to them as [67]

$$\bar{Q}_i(L) \sim \mu_i^*(L)^{\beta-1/2}, \quad \bar{\chi}_i(L) \sim \mu_i^*(L)^{1-\gamma}. \tag{7}$$

Therefore, the exponents β and γ and the chemical potential $\mu_{i,c}(\infty)$ can be obtained from the scaling of $\bar{Q}_i$ and $\bar{\chi}_i$, all of them calculated for different L's. The calculation of such quantities requires much more computational resources than the critical parameters, because of this we have calculated $\bar{Q}$ for $L \leqslant 6$ in the 1NN and 2NN models. In particular, as we will show, the calculation of χ is quite cumbersome, and as we have not observed the

expected values for the well know non-classical exponents β and γ on the 1NN model we have calculated only β for the much challenging 2NN model.

As already mentioned we have calculated the densities in the central sites of the plaquettes of level L. However, to calculate the susceptibility is more convenient to consider the density of the entire plaquette. Then, for the 1NN model, we have calculated two forms of the order-parameter, one considering the density of the central sites, $Q_1^{(C)}$, calculated for the level up to $L = 6$, and another considering the density of the central plaquette, $Q_1^{(S)}$, calculated up to $L = 5$. In Tab. V the amplitudes associated with these order-parameters are shown. To calculate the susceptibilities we introduce the field-like variable $\bar{z}$ conjugated to the order-parameter by defining

$$z = \frac{z_A + z_B}{2} \tag{8}$$

and

$$\bar{z} = \frac{z_A - z_B}{2}, \tag{9}$$

where z_A and z_B is the activities associated with the sublattices A and B, respectively. With the definition above we can rewrite the ratios for the partial partition functions in terms of z and $\bar{z}$ and then calculate the order-parameter in terms of these quantities. The susceptibility then obtained by the following derivative of the order-parameter

$$\chi_1 = \left(\frac{\partial Q_1}{\partial \bar{z}} \right)_{z,\bar{z}=0} \tag{10}$$

In order to obtain χ_1 we need to obtain the derivatives of RRs in terms of $\bar{z}$. As it is not possible to find an exact solution for the RRs in terms of the activity, these derivatives should be calculated implicit. However, this process leads to a linear system of implicit derivatives to be solved. As the L increase the linear system begins to be more difficult to obtain and solve. So, we have determined χ_1 by numerically calculating the derivative of Eq. 10 in the limit of $\bar{z} \to 0$. Our tests with $L = 1$ and $L = 2$ showed that this method is reliable once we can numerically solve the RRs with high precision for any $\bar{z}$ and z. The amplitudes of $\bar{\chi}_1$ obtained thorough this method are displayed in Tab. V

We start the application of the CAM theory by determining the exponent β. The Eq. 4 have three unknown quantities so we can use the three-point extrapolation method to obtain β and $\mu_c^{(1)}(\infty)$, in Tab. VI the values found are displayed. Using the values of $\bar{Q}_1^{(C)}$ for the set $(1, 2, 3)$ we have not found physical solutions for β and μ. For the set $(2, 3, 4)$ we have found $\beta = 0.124$ which differs 0.8% of $\beta = 1/8$ expected for the 2D Ising class. A good agreement is also observed for the chemical potential, we have found $\mu_c^{(1)}(\infty) = 1.3259$ for $(2, 3, 4)$, differing 0.6% of the value reported in [50]. However this good agreement is found only for this set of L's. When considering the set $(3, 4, 5)$, we have found $\beta = 0.098$, which differs 21% of the 2D Ising value, and $\mu_c^{(1)}(\infty) = 1.34361$ deviating 0.7% of [50]. The deviation from the Ising value increases even more for the set of largest L's, i.e. $(4, 5, 6)$, where we have found $\beta = 0.031$ and $\mu_c^{(1)}(\infty) = 1.38125$.

L	$\bar{Q}_1^{(C)}$	$\bar{Q}_1^{(S)}$	$\bar{\chi}_1$	$\bar{Q}_2^{(C)}$
1	1.1904	1.1904	0.80195	–
2	2.9762	1.4868	3.9336	2.7426
3	3.3453	1.6862	6.2789	3.0762
4	3.6525	1.8466	11.224	3.3267
5	3.9160	2.0163	22.107	3.5410
6	4.1426	–	–	3.7192

TABLE V. Amplitudes of the order-parameter for the 1NN model considering central sites ($\bar{Q}_1^{(C)}$) and central plaquete densities ($\bar{Q}_1^{(S)}$) for different levels L. Amplitudes for the susceptibility ($\bar{\chi}_1$) for the 1NN model and of the order-parameter $\bar{Q}_2^{(C)}$ for the 2NN model are also shown for different L's.

L's	$\mu_c^{(1)}(\infty)$	β $(Q_1^{(C)})$	β $(Q_1^{(S)})$	γ
$(1, 2, 3)$	–	–		
$(2, 3, 4)$	1.3259	0.124		
$(3, 4, 5)$	1.3461	0.098		
$(4, 5, 6)$	1.3812	0.031		
$(1, 2, 3)$	–		–	
$(2, 3, 4)$	1.3769		0.034	
$(3, 4, 5)$	1.1854		0.330	
$(1, 2, 3)$	–			–
$(2, 3, 4)$	1.1396			1.665
$(3, 4, 5)$	1.1802			2.071

TABLE VI. Estimates of the non-classical exponents β and γ and the critical chemical potential using the CAM theory for the 1NN model for different set of L's.

When considering the amplitudes $\bar{Q}_1^{(S)}$ similar deviations are found. For the lowest set of L's a non-physical solution of $\beta < 0$ is observed, while for $(2, 3, 4)$ the value of $\beta = 0.034$ with $\mu_c^{(1)}(\infty) = 1.3769$ is found. For the set largest L's, $(3, 4, 5)$, a much higher value is found, we have observed $\beta = 0.330$ with $\mu_c^{(1)}(\infty) = 1.1854$, showing that the utilization of the exponent β does not allow the confirmation of the universality class for 1NN model. In fact, as reported in [79] the deviation found for the the β exponent with the CAM theory in the 2D Ising model on the square lattice was of 11.2%, a much close value is found for the γ exponent deviating only 1.6% [79].

Similar to the exponent β, we have used the classical amplitudes obtained for χ (see Tab. V) and Eq. 5 with a three-point extrapolation to determine the non-classical value of γ. The lowest set of L's does not present any physical solution, while for L's $(2, 3, 4)$ we have found $\gamma = 1.665$ a value that differs 4.8% of the expected value of $\gamma = 7/4$. A much higher disagree-

ment is observed for the set of largest L's, i.e. $(3,4,5)$, we have found $\gamma = 2.071$ differing 18% of the expected value. We have also observed large deviations on the value of $\mu_c^{(1)}(\infty)$ determined by $\bar{\chi}$. For $(2,3,4)$ we have found $\mu_c^{(1)}(\infty) = 1.1396$ while for $(3,4,5)$ the value $\mu_c^{(1)}(\infty) = 1.1802$, differing 14.5% and 11.5% of the value reported in [50], respectively.

The large deviation observed in γ and β for the 1NN model shows that we may need large values of L to proper use the CAM theory in kNN LG models. As we are not able to conclude nothing about the universality class of the much well behaved 1NN model we can expected at least a similar situation for the 2NN one. In fact, using the displayed values of $\bar{Q}_2^{(C)}$ on Tab. V, we have found for $(2,3,4)$ $\beta = 0.0633$ and $\mu_{2,c}(\infty) = 4.91517$, while for $(3,4,5)$ and $(4,5,6)$ we have found $\beta = 0.1798$ with $\mu_{2,c}(\infty) = 4.46095$ and $\beta = -0.0025$ with $\mu_{2,c}(\infty) = 5.03236$, respectively. As we can see the value of β vary between a non-physical value for the largest L's to a large value of 0.179, which, as in the 1NN, makes impossible to make conclusions about the universality class for the 2NN model.

VI. FINAL DISCUSSIONS AND CONCLUSIONS

We have solved the hard square models, of 1NN or 2NN particles, on a sequence of high level Husimi lattices having small square lattices (of effective size L) as building blocks. The thermodynamic behavior of the 1NN (2NN) model was obtained for $L \leqslant 6$ ($L \leqslant 7$) by the computational determination of recursive relations for partial partition functions and by the linear stability analysis of their fixed points (thermodynamic phases).

For the 1NN model two phases have been found: a fluid and a solid one. For all orders considered, the phases are always separated by a critical fluid-solid transition. By using three-point extrapolations for the sequence of values obtained for the critical chemical potential and particle density, we have found results very close to the more accurate ones reported in literature [50]. In particular, the critical density differs only 0.01% from the value reported in [50], showing that the systematic approximations with higher-level Husimi lattices can, in fact, give quantitatively correct results for these system in lattice being approximated (the square lattice here).

In the 2NN case, the expected fluid and columnar phases were also observed in our solutions. In all levels analyzed, a critical fluid-columnar phase transition was found in this system. By extrapolating the data obtained for the different levels, we have found $\mu_{2,c} = 4.57104$ and $\rho_{2,c} = 0.2221$. The critical chemical potential found is in good agreement with the estimates reported in [51, 63] differing less than 0.3% of them, but it is slightly different from the more recent value reported in [66]. The value of the critical density found here is a little bit smaller than the value $\rho_{2,c} \approx 0.233$ reported in [51, 66].

To determine the non-classical critical exponents, we have used the coherent anomaly method (CAM). Despite the high accuracy of the critical parameters $\mu_{i,c}$ and $\rho_{i,c}$ calculated here, we were unable to obtain reliable values for the non-classical exponents. In particular, the 1NN model is well-know to belong to the 2D Ising class, but the application of the CAM for it returned values of β and γ ranging between $0.031 < \beta < 0.330$ and $1.665 < \gamma < 2.071$.

The deviations observed in β and γ for the 1NN model shows that, at least for the levels considered here, the application of the CAM theory is unable to proper determine the value of non-classical exponents thorough a systematic approach with Husimi lattices for kNN hard-LGs. A similar conclusion is also given in the only work (as far as we know) that applies CAM to LGs systems. In [70] a Monte Carlo version of the CAM is applied to 2D Lennard-Jones LG systems on the square lattice. Considering cluster sizes with up to 373 particles they found significant divergences of the exponent associated to the correlation length ν and the susceptibility exponent γ with respect to the 2D Ising class.

When utilizing the same systematic approach with HL for the ferromagnetic Ising model on the square lattice Monroe [79] had found the critical temperature differing only 0.003% of the Onsager value. However, the utilization of CAM output much less accurate estimation, with β and γ differing 11.2% and 1.6%. One possible explanation for the difficulty in the utilization of CAM is the simply scaling form for the classical amplitudes (see Eq. 7). As showed in [81] logarithm corrections are present in the CAM scaling relation for the Weiss- and Beth-type mean-field approximations. As far as we know, the study of correction to scaling for the CAM in mean-field approximations like HL has not been considered yet. Moreover, the sub-lattice ordering in kNN LGs effectively reduces the size of the system as only a fraction of the lattice can be occupied leading the need of higher levels of HL. Unfortunately, due to the exponential grown in computational resources needed to solve higher-levels HL ($L > 7$) we are unable to improve our results or explore the possible corrections present in the CAM scaling. To address these problems more efficient methods to obtain and solve the recursive relations for the ppf's must be developed to increase the level of approximation.

ACKNOWLEDGMENTS

We acknowledge support from CNPq, CAPES and FAPEMIG (Brazilian agencies) and the use of the Computing Cluster of the Universidade Federal de Viçosa.

L	N_L (1NN)	Conf. 1NN
2	10	1704
3	26	1146118
4	68	3985772648
5	178	70897617428720
6	466	6438412592897497526
7	1220	–
L	N_L (2NN)	Conf. 2NN
2	36	8312
3	76	950636
4	164	357340560
5	352	435265986532
6	756	258990287426480
7	1624	3729631034070503744

TABLE VII. The number N of ppf's and the total number of configurations for the 1NN (top) and 2NN (bottom) models, for the Lth level HL.

Appendix A: Solution of the kNN models on the square Husimi lattices

To solve the kNN models on a L-level square Husimi lattice, we define partial partition functions (ppf's) associated with the possible states of a root zigzag line [see Fig. 3] of a rooted building block (BB). For solving the 1NN model, these root line can be defined with $2L-1$ sites, whereas to include exclusion among external NNN sites in the 2NN case they must have $2L+1$ sites. Let us focus on the former case, since the extension to the latter one is quite obvious. In the 1NN model with $L=2$, for example, there are $N_2=5$ configurations of particles for the root line: all sites empty ($\sigma=0$), one site occupied (there are 3 possibilities here, $\sigma=1,2,3$) and two sites occupied ($\sigma=4$). Since these sites can have two different sublattice configurations (the sequences ABA or BAB), there is a total of 10 possible states for the root line of the 1NN model with $L=2$. For the sake of simplicity, we will use only the sublattice of the leftmost site of the root line to identify the sublattice configuration, namely, we will use "A" to refer to ABA and "B" to BAB. Thereby, in this case one has 10 ppf's: $G_{\sigma,S}$, with $\sigma=0,\ldots,4$ and $S=A,B$. For comparison, for the 2NN model with $L=2$ one has $N_2=9$ and four sublattice configurations, totaling 36 states and ppf's: $G_{\sigma,S}$, with $\sigma=0,\ldots,8$ and $S=A,\ldots,D$. In our solutions, we will always define the configuration $\sigma=0$ as the one with the root line empty. In Tab. VII the number N_L of particle configurations in the root line is presented for different levels, for both 1NN and 2NN models.

A recursion relation for the ppf $G_{\sigma,S}$ can be obtained by keeping the rooted BB with the root line in the state (σ,S) and considering the operation of attaching three subtrees (three branches) to it, one at each of its sides, with exception of the root line. Note that, if each of these subtrees has M generations, this process yields a new subtree with $M+1$ generations. By summing over all possible ways of attaching the three subtrees in the rooted BB — i.e., by considering all the possible configurations for their root lines, respecting the particle exclusions and sublattice order —, one obtains the ppf $G'_{\sigma,S}$ in generation $M+1$ as a polynomial function in terms of the ppf's $(G_{i,J})$ of M-generations.

Being more explicit, in the 1NN model, if the root line is in sublattice configuration A, then, one has to connect a subtree in configuration A on the top of the BB and subtrees in configuration B in its lateral sides [see Fig. 1(c)]. This means that the recursion relations for the ppf's $G'_{\sigma,A}$ will be given by a sum of terms of the form $G_{\alpha,B}G_{\beta,A}G_{\gamma,B}$, with $\alpha,\beta,\gamma=0,\ldots,N-1$. Thereby, at first, the polynomial for a given ppf might have N^3 of such terms. However, there exits several combinations of $G_{\alpha,B}G_{\beta,A}G_{\gamma,B}$ which are forbidden, due to the particle exclusions, leading to a smaller number of allowed terms. Anyhow, we can sum over all N^3 configurations and introduce a variable $\delta_{\sigma,\alpha,\beta,\gamma}$, such that $\delta_{\sigma,\alpha,\beta,\gamma}=0$ for the forbidden configurations and $\delta_{\sigma,\alpha,\beta,\gamma}=1$ otherwise. In this way, the ppf's for the 1NN model in sublattice configuration A can be written as

$$G'_{\sigma,A}=\sum_{\{\alpha,\beta,\gamma\}}\delta_{\sigma,\alpha,\beta,\gamma}z^{\frac{1}{2}n^{(S)}_{\sigma,\alpha,\beta,\gamma}}f_{\sigma,\alpha,\beta,\gamma}(z)G_{\alpha,B}G_{\beta,A}G_{\gamma,B}. \tag{A1}$$

The ppf's for the sublattice configuration B are given by the same expression with A and B exchanged. In both cases, one has

$$f_{\sigma,\alpha,\beta,\gamma}(z)=\sum_{i=1}^{K_{\sigma,\alpha,\beta,\gamma}}m_{i;\sigma,\alpha,\beta,\gamma}z^{n_i^{(B)}}, \tag{A2}$$

which is a polynomial accounting for the bulk configurations in the rooted BB. Note that for $L\geqslant 2$ this BB can be divided into two regions: the surface, composed by the $4L$ sites that will be shared between consecutive generations; and the bulk, defined by the remaining sites, which belongs exclusively to the BB. Once we have fixed the state, (σ,A) for example, of the root line and the configuration $\{\alpha,\beta,\gamma\}$ of the three incoming subtrees, the number $n^{(S)}_{\sigma,\alpha,\beta,\gamma}$ of particles at surface is determined. This number is multiplied by half in Eq. A1 because these particles are shared by two generations of the tree. Note that the state of the root line fixes also the configuration of some few bulk sites of the rooted BB, but, for a given surface state, there may still exists several ways of placing particles in the other bulk sites and one has to sum over all these configurations, what is done in Eq. A2. In this expression, $m_{i;\sigma,\alpha,\beta,\gamma}$ is the number of ways of placing $n_i^{(B)}$ particles in the bulk sites (with exception of those belonging to the root line), while $K_{\sigma,\alpha,\beta,\gamma}$ is the maximal number of particles possible there. It is obvious that such quantities will depend on the level L, but this is omitted for the sake of simplicity. Moreover, in the case $L=1$, where there is no bulk sites, one has $f_{\sigma,\alpha,\beta,\gamma}=1$.

The ppf's for the 2NN model will be given by expressions analogous to A1. The difference is only in the sublattice configurations. For example, for even L, as is the case in Fig. 1(d), one has that if the root line is in sublattice configurations A, subtrees in configurations B and D will be attached in the lateral sides, while in the top side the subtree shall be in configuration A. Hence, we must have $G_{\alpha,B}G_{\beta,A}G_{\gamma,C}$ in place of $G_{\alpha,B}G_{\beta,A}G_{\gamma,B}$ in Eq. A1. When L is odd, one has to make $G_{\alpha,B}G_{\beta,A}G_{\gamma,B} \to G_{\alpha,B}G_{\beta,C}G_{\gamma,D}$ in Eq. A1, since in this case the subtree attaching to the top of the BB shall be in configuration C. Once we have the recursion relations for the ppf's in sublattice A, the ones for the other sublattices can be obtained by cyclic permutations of their indexes: $A \to B$, $B \to C$, $C \to D$ and $D \to A$.

The determination of the recursion relations for the ppf's is done computationally by calculating $\delta_{\sigma,\alpha,\beta,\gamma}$, the multiplicity $m_{i;\sigma,\alpha,\beta,\gamma}$, the number of surface particles $n^{(S)}_{\sigma,\alpha,\beta,\gamma}$ and the total number of particles in the bulk $K_{\sigma,\alpha,\beta,\gamma}$ for each surface configuration. For small L this exact enumeration process can be easily done, but as L increases it becomes very demanding, limiting the maximal feasible L to small values. To let clear the complexity of this method, the sum of all allowed terms in all the ppf's for a given L, $K_T = \sum_{\{\sigma,\alpha,\beta,\gamma\}} \delta_{\sigma,\alpha,\beta,\gamma} K_{\sigma,\alpha,\beta,\gamma}$, is shown in Tab. VII for both models. Note that this number of terms, becomes of order $\sim 10^{18}$ already for $L = 6$ ($L = 7$) for the 1NN (2NN) model. To efficiently enumerate these large number of terms, we use a recursive method, where the information for the already made counting for $L-1$ is used to determine the recursion relations for the ppf's of Lth order. A caveat of the method is that, to save time, all informations of all recursion relations for the case $L-1$ have to be stored in the RAM memory, to allow rapid access. For instance, in the 2NN case, these informations for $L = 8$ require at least 256GB of RAM memory. The main problem, however, is that to be efficient one must have these informations also in the HD, what produces 5.2 terabytes of data for $L = 8$.

After concluding the enumeration process and, thus, determining all ppf's for a given L, we start the study of the thermodynamic properties of the models for this level. The first step is the determination of the fixed points, each fixed point is associated with a thermodynamic phase. As shown in Eq. A1 the ppf's are composed by a sum of positive terms which in the thermodynamic limit diverge. To overcome the divergence the ratio of ppf's $R_{\sigma,S} = \frac{G_{\sigma,S}}{G_{0,S}}$ is defined. The Eq. A1 can be easily write in terms of $R_{\sigma,S}$ and by iterating the recursive relations the fixed points are numerically found. The stability of the fixed points is then determined by the maximum eigenvalue, Λ, of the Jacobian matrix of the recursive relations ratios for the ppf's. In the region whereof the activity space z where $\Lambda < 1$ the phase is stable, the stability limit, the spinodal, of the phase is determined by $\Lambda = 1$. As the counting process to the ppf's the determination of the fixed points and its stability becomes very costing for L large. For $L = 8$ the program needs to handle 3488 equations each one being in the order of 10^{21} terms.

Similar to the ppf's the partition function can be obtained by attaching four sub-trees to a central square of Lth-level. As the ppf's are parts of the partition function we can write the partition function Y in the generic form for a Lth-level HL

$$Y = \sum_{i=0}^{N}\sum_{j=0}^{N} \delta_{ij} G_{j,S} G'_{i,A} = \left(\prod_k G_{0,k}\right) y, \qquad \text{(A3)}$$

where δ_{ij} is zero if the 1NN (2NN) particles overlap at the root line and equal to one otherwise, y is function of the ratios $R_{\sigma,S}$ and of the activity z and $k = A, B$ for 1NN and $k = A, B, C, D$ for the 2NN model. The sublattice S in Eq. A3 is always A for the 1NN model and the 2NN depends on L, being A if L is odd and C in the case of L even. With the partition function, the density of particles, ρ_T, at the central square of Lth-level can be calculated as follows

$$\rho_T = \frac{z}{VY}\frac{\partial Y}{\partial z}, \qquad \text{(A4)}$$

where V is the volume of the central square defined by $V = 2(L^2+L)$. We can also calculate the bulk free energy per site. Using the ansatz proposed by Gujrati [80] the free energy for a Lth-order HL can be written as

$$\phi_b = -\frac{1}{V}\ln\left(\frac{\prod_i \Omega_{0,i}}{y^2}\right), \qquad \text{(A5)}$$

where $\Omega_{0,i}$ is given by

$$\Omega_{0,i} = \frac{G'_{0,i}}{\prod_j G_{0,j}}, \qquad \text{(A6)}$$

with $i, j = A, B$ for the 1NN model and $i, j = A, B, C, D$ for the 2NN.

[1] B. Simon, *The Statistical Mechanics of Lattice Gases*, Princeton University Press, New Jersey (1993).
[2] F. Ritort and P. Sollich, Adv. Phys. **52**, 219 (2003).
[3] *Granular Matter: An Interdisciplinary Approach*, edited by A. Mehta (Springer-Verlag, New York, 1994).
[4] J. W. Evans, Rev. Mod. Phys. **65**, 1281 (1993).
[5] D. Frenkel, Physica A **263**, 26 (1999).
[6] L. Lafuente and J. A. Cuesta, J. Chem. Phys. **119**, 10832 (2003).
[7] A. Verberkmoes and B. Nienhuis, Phys. Rev. Lett. **83**,

3986 (1999).
[8] P. Kasteleyn, Physica **27**, 1209 (1961); H. N. V. Temperley and M. E. Fisher, Philos. Mag. **6**, 1061 (1961); D. A. Huse, W. Krauth, R. Moessner, and S. L. Sondhi, Phys. Rev. Lett. **91**, 167004 (2003); R. Dickman, J. Chem. Phys. **136**, 174105 (2012).
[9] J. Kundu and R. Rajesh, Phys. Rev. E **89**, 052124 (2014); J. Kundu and R. Rajesh, Phys. Rev. E **91**, 012105 (2015); T. Nath, J. Kundu, and R. Rajesh, J. Stat. Phys. **160**, 1173 (2015); P. Gurin, S. Varga, M. González-Pinto, Y. Martínez-Ratón, and E. Velasco, J. Chem. Phys. **146**, 134503 (2017).
[10] T. Schilling, S. Pronk, B. Mulder, and D. Frenkel, Phys. Rev. E **71**, 036138 (2005).
[11] B. C. Barnes, D. W. Siderius, and L. D. Gelb, Langmuir **25**, 6702 (2009).
[12] A. Ghosh and D. Dhar, Europhys. Lett. **78**, 20003 (2007); J. Kundu, R. Rajesh, D. Dhar, and J. F. Stilck, Phys. Rev. E **87**, 032103 (2013); A. Gschwind, M. Klopotek, Y. Ai, and M. Oettel, Phys. Rev. E **96**, 012104 (2017); N. Vigneshwar, D. Dhar, and R. Rajesh, J. Stat. Mech. (2017) 113304.
[13] D. Mandal, T. Nath, and R. Rajesh, Phys. Rev. E **97**, 032131 (2018).
[14] N. Vigneshwar, D. Mandal, K. Damle, D. Dhar, and R.Rajesh, arXiv: 1902.06408.
[15] T. Nath and R. Rajesh, Phys. Rev. E **90**, 012120 (2014).
[16] D. S. Gaunt, J. Chem. Phys. 46, 3237 (1967).
[17] A. Yamagata, Physica A 215, 511 (1994).
[18] J. R. Heringa and H. W. J. Blöte, Physica A 232, 369 (1996).
[19] A. Z. Panagiotopoulos, J. Chem. Phys. **123**, 104504 (2005).
[20] J. Orban, Chem. Phys. Lett. **3**, 702 (1969).
[21] L. Lafuente and J. A. Cuesta, Phys. Rev. E **68**, 066120 (2003).
[22] B. R. Riemenschneider and D. A. Huckaby, J. Chem. Phys. **58**, 3940 (1973).
[23] L. K. Runnels, L. L. Combs, and J. P. Salvant, J. Chem. Phys. **47**, 4015 (1967).
[24] J.-M. Debierre and L. Turban, Phys. Lett. A **97**, 235 (1983).
[25] F. C. Thewes and H. C. M. Fernandes, arXiv:2002.04603v1
[26] R. J. Baxter, J. Phys. A **13**, L61 (1980).
[27] R. J. Baxter, *Exactly Solved Models in Statistical Mechanics*, Academic Press, London (1989).
[28] J. Orban and A. Bellemans, Chem. Phys. Lett. **1**, 205 (1967); J. Chem. Phys. 49, 363 (1968).
[29] L. K. Runnels, J. R. Craig, and H. R. Stereiffer, J. Chem. Phys. 54, 2004 (1971).
[30] N. C. Bartelt and T. L. Einstein, Phys. Rev. B **30**, 5339 (1984).
[31] W. Zhang and Y. Deng, Phys. Rev. E **78**, 031103 (2008).
[32] S. S. Akimenko, V. A. Gorbunov, A. V. Myshlyavtsev, and P. V. Stishenko, Phys. Rev. E **100**, 022108 (2019).
[33] S. Darjani, J. Koplik, S. Banerjee, and V. Pauchard, J. Chem. Phys. **151**, 104702 (2019).
[34] C. Domb, Nuovo Cimento **9**, 9 (1958); D. M. Burley, Proc. Phys. Soc. **75**, 262 (1960); D. Burley, Proc. Phys. Soc. **77**, 451 (1961).
[35] D. S. Gaunt and M. E. Fisher, J. Chem. Phys. **43**, 2840 (1965).
[36] L. K. Runnels, Phys. Rev. Lett. **15**, 581 (1965).
[37] L. K. Runnels and L. L. Combs, J. Chem. Phys. **45**, 2482 (1966).
[38] F. H. Ree and D. A. Chesnut, J. Chem. Phys. **45**, 3983 (1966).
[39] A. Bellemans and R. K. Nigam, J. Chem. Phys. **46**, 2922 (1967).
[40] R. M. Nisbet and I. E. Farquhar, Physica **76**, 259 (1974).
[41] R. J. Baxter, I. G. Enting and S. K. Tsang, J. Stat. Phys. **22**, 465 (1980).
[42] K. Binder and D. P. Landau, Phys. Rev. B **21**, 1941 (1980).
[43] Z. Ràcz, Phys. Rev. B **21**, 4012 (1980).
[44] H. Meirovitch, J. Stat. Phys. **30**, 681 (1983).
[45] P. A. Pearce and K. A. Seaton, J. Stat. Phys. **53**, 1061 (1988).
[46] C.-K. Hu and K.-S. Mak, Phys. Rev. B **39**, 2948(R) (1989).
[47] C.-K. Hu and C. N. Chen, Phys. Rev. B **43**, 6184 (1991).
[48] A. Baram and M. Fixman, J. Chem. Phys. **101**, 3172 (1994).
[49] D.-J. Liu and J. W. Evans, Phys. Rev. B **62**, 2134 (2000).
[50] W. Guo and H. W. J. Blöte, Phys. Rev. E **66**, 046140 (2002).
[51] H. C. Marques Fernandes, J. J. Arenzon and Y. Levin, J. Chem. Phys. **126**, 114508 (2007).
[52] Y.-B. Chan, J. Phys. A: Math. Theor. **45**, 085001 (2012).
[53] I. Jensen, J. Phys. A: Math. Theor. **45**, 508001 (2012).
[54] T. Nath and R. Rajesh, J. Stat. Phys. **2016**, 073203 (2016).
[55] A. Bellemans and R. K. Nigam, Phys. Rev. Lett. **16**, 1038 (1966).
[56] F. H. Ree and D. A. Chesnut, Phys. Rev. Lett. **18**, 5 (1967).
[57] R. M. Nisbet and I. E. Farquhar, Physica **73**, 351 (1974).
[58] W. Kinzel and M. Schick, Phys. Rev. B **24**, 324 (1981).
[59] P. A. Slotte, J. Phys. C: Solid State Phys. **16**, 2935 (1983).
[60] J. Amar, K. Kaski and J. D. Gunton, Phys. Rev. B **29**, 1462 (1984).
[61] M. Schmidt, L. Lafuente and J. A. Cuesta, J. Phys.: Condens. Matter **15**, 4695 (2003).
[62] M. E. Zhitomirsky and H. Tsunetsugu, Phys. Rev. B **75**, 224416 (2007).
[63] X. Feng, H. W. J. Blöte and B. Nienhuis, Phys. Rev. E **83**, 061153 (2011).
[64] K. Ramola and D. Dhar, Phys. Rev. E **86**, 031135 (2012).
[65] K. Ramola, K. Damle and D. Dhar, Phys. Rev. Lett. **114**, 190601 (2015).
[66] T. Nath, D. Dhar and R. Rajesh, Europhys. Lett. **114**, 10003 (2016).
[67] M. Suzuki, J. Phys. Soc. Jpn. **55**, 4205 (1986); M. Suzuki, M. Katori and X. Hu, J. Phys. Soc. Jpn. **56**, 3092 (1987); M. Katori and M. Suzuki, J. Phys. Soc. Jpn. **56**, 3113 (1987).
[68] M. Suzuki and M. Kolesik. Coherent Anomaly Method and its Applications. In: *Theory and Applications of the Cluster Variation and Path Probability Methods*, edited by J. L. Morán-L'opez and J. M. Sanchez, Springer, Boston, 1996, p. 113-124.
[69] M. Suzuki. *Coherent Anomaly Method: Mean Field, Fluctuations and Systematics*, World Scientific, Singapore, 1995.
[70] A. Patrykiejew and P. Borowski, Phys. Rev. B **42**, 4670 (1990).

[71] K. Husimi, J. Chem. Phys. **18**, 682 (1950).
[72] H. J. Liao, Z. Y. Xie, J. Chen, X. J. Han, H. D. Xie, B. Normand, and T. Xiang, Phys. Rev. B **93**, 075154 (2016); R. Huang and Y. Jiang, Results in Physics **11**, 777 (2018).
[73] M. Pretti, Phys. Rev. E **93**, 032110 (2016); T. J. Oliveira and J. F. Stilck, Phys. Rev. E **93**, 012502 (2016); T. J. Oliveira, W. G. Dantas, T. Prellberg, and J. F. Stilck, J. Phys. A: Math. Theor. **51**, 054001 (2018).
[74] A. P. Furlan, T. J. Oliveira, J. F. Stilck, and Ronald Dickman, Phys. Rev. E **100**, 022109 (2019).
[75] N. T. Rodrigues and T. J. Oliveira, J. Chem. Phys. 151, 024504 (2019); Phys. Rev. E **100**, 032112 (2019).
[76] N. T. Rodrigues and T. J. Oliveira, arXiv ??? (2020);
[77] A. Robledo and C. Varea, J. Stat. Phys. 63, 1163 (1991).
[78] T. J. Oliveira, J. Phys. A: Math. Theor. **49**, 155001 (2016).
[79] J. L. Monroe, Phys. Rev. E **64**, 016126 (2001).
[80] P. D. Gujrati, Phys. Rev. Lett. **74**, 809 (1995).
[81] N. Ito and M. Suzuki, Phys. Rev. B **43**, 3483 (1991).

Chapter 5

Ongoing Work

At the moment, beyond the finishing of the preprint presented on Chap. 4, we are working on another problem related to polymer adsorption. As pointed out in Chap. 1, most of the existing works on this consider the surface as being flat. However, the scenario of a perfectly flat surface is far from reality. Namely, most of the surfaces have some kind of defect, which might have a significant effect on the adsorption behavior of a polymer there. One example of this is the case of rough surfaces [83, 84], which has recently been studied by means of Monte Carlo simulations [85], presenting a complex kinetic and thermodynamic behavior. Of course, this is only relevant when the monomer is smaller than (or at least of the same scale of) the defects, otherwise, the surface can be very well approximated as flat.

With the mentioned scale in mind, we have been working on the adsorption problem on vicinal stepped surfaces, which are commonly observed in crystal and are formed by a sequence of terraces separated by steps as shown in Fig. 5.1. On this type of surface, the polymer can either adsorb on a terrace, which is similar to adsorption on flat surfaces, or on one step (see Fig. 5.1). On the step edges the monomers has effectively more contacts with the surface sites, then, as in the modeling of crystal growth, it is natural to assume different interaction energies for step edge and for terrace contacts. We remark that adsorption of monomers on the step edge can enhance the polymerization process [86], and the characterization of the adsorption transition in these surfaces can be an important part of the process. Moreover, deposition of materials on vicinal surfaces is topic of much interest [87, 88], with appealing applications as the production of nanowires [89–91].

Despite the polymer adsorption on vicinal surfaces be a relevant problem in polymer physics, as far as we know, the global properties of the adsorption transition in this scenario have never been explored yet. To tackle this problem, we consider self-avoiding walks (SAW) on the cubic lattice with a vicinal surface at its bottom. The model has two types of surface interactions: an energy $-\epsilon_t$ for contacts with terraces and an energy $-\epsilon_s$ for the step edge contacts. The partition function of this vicinal adsorption model is given by

$$Z_n(\omega_t, \omega_s) = \sum_{m_t, m_s} c_n(m_t, m_s)\omega_t^{m_t}\omega_s^{m_s}, \tag{5.1}$$

where $\omega_i = e^{\beta\epsilon_i}$ with $i = \{t, s\}$ and $\beta = 1/k_bT$. The sum is evaluated over all possible number of terrace contacts, m_t, and step edge contacts, m_s, for a SAW with n steps and with $c_n(m_t, m_s)$ being the density of states. To characterize the adsorption transition, we need to find an order parameter. An ideal candidate is the surface energy, which is the order parameter for the flat-surface adsorption. So, by extending this concept for two different energies: one associated with the terrace, $u_n^{(t)}$, and another with the step, $u_n^{(s)}$, each one being the order parameter for either the terrace or step edge adsorption. These

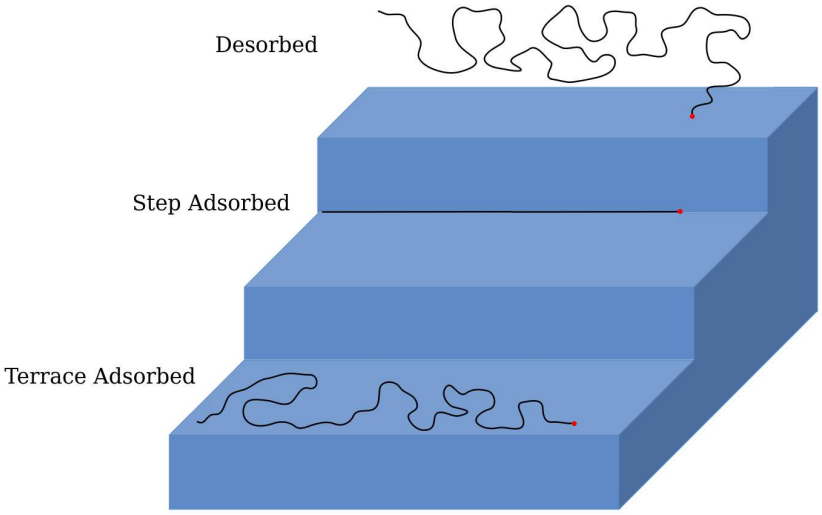

Figure 5.1: Representation of a vicinal surface with the typical polymer phases in a good solvent regime. On the top terrace a desorbed configuration is sketched, followed by an step adsorbed in the first step and a terrace adsorbed configuration on the bottom.

energies are defined by

$$u_n^{(t)} = \frac{< m_t >}{n} \text{ and } u_n^{(s)} = \frac{< m_s >}{n} \tag{5.2}$$

In the same spirit, it is reasonable to assume that close to the adsorption point these order parameters behave as

$$u_n^{(i)} \sim n^{\phi^{(i)}-1} f(\tau n^{1/\delta^{(i)}}), \tag{5.3}$$

with $i = \{t, s\}$, $f(x)$ is a scale function and τ the rescaled temperature. The exponents $\phi^{(t)}$ and $1/\delta^{(t)}$ characterize the terrace adsorption, while $\phi^{(s)}$ and $1/\delta^{(s)}$ the step edge adsorption. The aim of this work is to characterize both adsorption transitions. To do so, we follow the same procedures employed in Chap. 2. Namely, first we perform the two-parameter version of the flatPERM [96] for polymer chains of short lengths, 128 steps, and build the fluctuation map. Then, with the fluctuation map, we can identify the phases present and the possible order of the transitions among them. To characterize the exponents we will perform the one-parameter flatPERM with 1024 steps and possible the PERM with walks going up to 10000 steps.

At the moment of the writing of this thesis this this work is in an initial state. Since no similar work as been done before, we start by considering two effectively infinite terraces with only a single step at surface with the SAW tethered on it. By running 10^9 samples of the two-parameter flatPERM for chains with 128 steps, we build up the fluctuation map shown in Fig. 5.2. By analyzing the distribution of step edges and terrace contacts we have identified the phases present in the model. For small of ω_s and ω_t, we have observed, as expected, the non-adsorbed coil phase, characterized by an small number of terrace and step edge contacts. Increasing ω_s with ω_t small, a step edged adsorbed phase (large number of step edge contacts) is found and for large ω_t the terrace adsorbed phase (large number of terrace contacts) takes place.

By analyzing the peak behavior of the contacts distribution we have identify three regions of possible phase transitions. For small values of ω_t, a two peaked distribution behavior is observed indicating a possible first-order transition from the coil to the step adsorbed phase while for low ω_s a single peak is observed, which indicates a, possible,

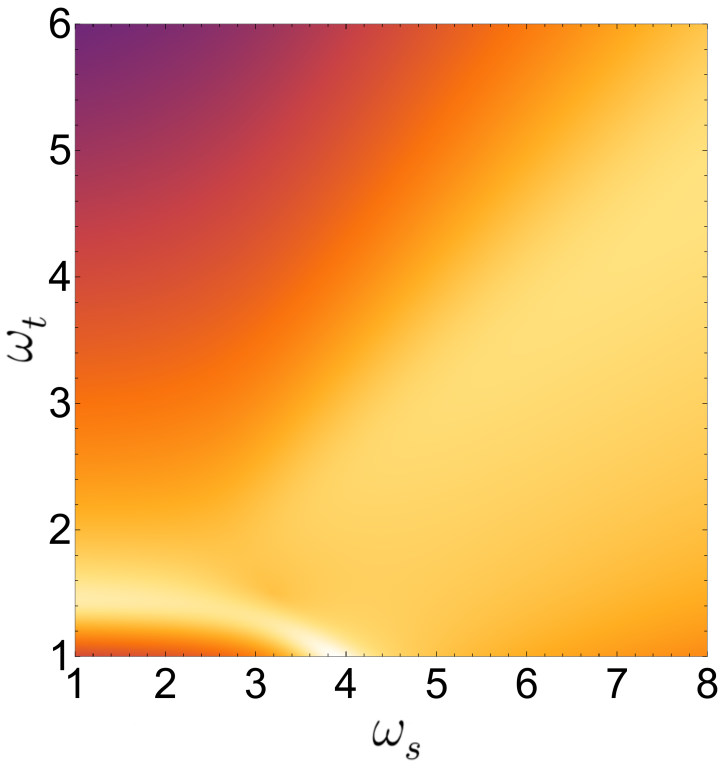

Figure 5.2: Fluctuation map for SAW with 128 steps. The brighter colors indicate the regions of large fluctuations.

critical desorbed-terrace adsorbed transition. A critical transition is also observed for large values of ω_s and ω_t between the step and terrace adsorbed phases. With the possibility of two critical lines and one discontinuous, we infer that the discontinuous line should end in a critical point connecting the lines.

Although no simulation for long chains has been done so far, the nature of each phase present on the diagram allows us to fairly speculate about the exponents of each transition line. As the desorbed-step adsorbed transition seems to be marked by a two-peak distribution behavior, characteristic of a first-order transition, the exponents should assume the theoretical values of $\phi^{(s)} = 1/\delta^{(s)} = 1$ for discontinuous transitions. For the terrace adsorption, the transition is expected to be identical to the flat-surface adsorption on the cubic lattice for SAW. In fact, for short lengths, the transition seems to be close to $\omega_t \approx 1.4$, which is not so far from the expected one $\omega_t \approx 1.33$ [92]. Therefore, the exponents should be close to the values $\phi^{(s)} = 1/\delta^{(s)} \approx 0.48$ [93] expected for the three-dimensional adsorption. Finally, the transition between the step and terrace adsorbed phases involves one phase quasi-two-dimensional and other quasi-one-dimensional. If one faces the terrace adsorbed as a desorbed coil phase on two-dimensional space, then the step phase can be seen as the adsorbed phase onto a line in the 2D space. Using this analogy, we can infer that the step-terrace adsorption is similar to the coil-adsorbed phase transition for SAW on a square lattice. If this is correct, the exponents shall assume the value $\phi^{(t)} = \phi^{(s)} = 1/\delta^{(t)} = 1/\delta^{(s)} = 0.5$.

Besides the characterization of the transitions and the build of the phase diagram, we shall also explore aspects of the problem. For example, what is the effect of the number of steps? For now, we have only considered a single step at the surface, which consists in the case where the distance between steps is much larger than the polymer size, for distances comparable to the polymer size can more adsorbed phases appears?. Another generalization that we have the intention of exploring is the solvent condition, which

leads to questions like, how the globule phase adsorbs in the presence of steps? We can also explore the scenario where a semi-flexible polymer is considered, with the addition of stiffness a crystalline phase can be formed [94], which can also lead to a crystalline adsorbed phase. In all cases, a much richer thermodynamic behavior can be expected to increase the complexity of the work.

Chapter 6

Final Conclusion and perspectives

We have studied several statistical models for polymers and fluids. By using efficient and sophisticated stochastic grown methods for polymers (flatPERM [96] and PERM [95]) we have explored the adsorption and the polymer collapse by modeling it as interacting self-avoiding trails in two dimensions, on the square and triangular lattice. The fluid systems were modeled as lattice gas models of hard particles on the square and cubic lattices. The lattice gases studied are composed of particles that exclude up to their kth nearest-neighbors (kNN). On the square lattice, we considered the pure lattice gas systems of 1NN and 2NN particles, we manage to solve them using a semi-analytical approach with high-order Husimi lattices built with squares lattices as building blocks approximating the square lattice. Beyond these pure systems, four different mixtures were studied on the cubic lattice, three binary ones composed by pair of the particles 0NN, 1NN and 2NN and the ternary mixture composed by the same particles. We solve all these mixtures on a Husimi lattice built with cubes.

On the collapse and the adsorption of SAT on the square lattice we have explored the universality of the adsorption exponents ϕ^s and $1/\delta^s$. Three different boundary scenarios were considered: the monomer-surface (MS), where the surface energy is determined by the number of monomers in contact with the surface; the bond-surface (BS), where the energy is determined by the number of bonds at surface, both in a horizontal surface; and the case of a diagonal surface (DS) with the energy associated with surface monomers. By carefully determining the exponents with long SATs, we observed that in all scenarios the exponents are in the adsorption universality class in two dimensions with $\phi^s = 1/\delta^s = 1/2$ for the normal adsorption. However, a deviation on the values of the exponents between the scenarios was observed for the special point where the trail at the collapse point adsorbs. The large difference is observed between the DS case and the MS one. As pointed out in the paper we believe that the discrepancy is due to strong corrections to scaling at the collapse point. However, with the analysis done we can not entirely discard the possibility of the diagonal and the horizontal surface cases being in a different universality class. As a future work to address this question, we will consider a slightly different model for the horizontal surface adsorption. On the DS case, every time a monomer 'touch' the surface the next one is always out of the surface, forming, at the fully adsorbed phase, a stepped chain with only half of the monomers being adsorbed. On the horizontal surface, the same situation does not happen and in the fully adsorbed state all monomers are adsorbed. The idea to address the question of universality is to make the horizontal surface SAT more equal to the DS, so that each time a monomer makes two sequential contacts with the surface the next one is forced to be away from the surface. Another idea is to change the inclination of the surface, considering inclinations between the horizontal and the diagonal case. With these approaches, we can test if either the

diagonal and the horizontal surface are in the same class or not.

On the triangular lattice, the adsorption and collapse of the SAT present an extra challenge. Since in the triangular lattice each site can be occupied by up to three monomers, the is an extra interaction energy related to the triply visited sites, besides the one for doubly visited sites. Along with the surface interaction, the model presents three parameters of interaction, leading to a 3D phase diagram. With the use of the flatPERM to build several 2D slices of the phase diagram, we were able unveil the full picture of the thermodynamic behavior. A very complex phase diagram with four phases: coil, globule, crystal and adsorbed. With the analysis for short lengths, we identify a special multicritical point where three multicritical lines and one line of critical-end-points meets. As the assumption of the location of the special point is based on samples of trails with up to 128 steps a further improvement on the location of the point and also the determination of the critical exponents values with longer trails can be of interest. As a further project, we also have the intention of exploring the SAT collapse and adsorption on the cubic lattice. As on the triangular lattice, on the cubic one a 3D phase diagram is expected to be built with the additional difficulty that more phases, as the surface attached globule (SAG) one will be present.

For the pure 1NN and 2NN lattice gases models, we have solved them on improved Husimi lattices up to sixth-level for the 1NN and seventh-level for the 2NN. For the 1NN hard squares, in all levels we have observed a critical fluid-solid transition and, by extrapolating the data, we have found values for the critical chemical potential and density close to the more precise values reported in the literature. Similarly, in the 2NN case, we have observed in all levels a critical fluid-columnar phase transition and extrapolation return critical parameters close to the values reported in the literature. With the coherent anomaly method (CAM) we have obtained the non-classical value of the exponent β and γ, but unfortunately our analysis does not allow conclude nothing about the universality class of the models considered.

Three different binary mixtures of kNN particles have also been studied. In all cases, a rich thermodynamic behavior is observed with critical, triple and tricritical points, critical and discontinuous lines separating two fluid and two solid phases. In particular, the binary mixture 0NN-2NN presents a fluid-fluid transition leading to a very interesting phase diagram with two fluid phases and solid one. As all the thermodynamic behavior was determined by a mean-field approach (solutions on a Husimi lattice built with cubes), the next step is to simulate the binary mixtures on the cubic lattice. Usually, the results of solutions on Husimi lattices are qualitatively correct and, then, by using our findings here as a guide and with an appropriated Monte Carlo method, we intend to verify if all the properties found on the Husimi lattice holds on the cubic one. Besides the binary mixtures, we also solved the ternary 0NN-1NN-2NN mixture using the Husimi lattice build with cubes. An even richer phase diagram is observed in the ternary mixture with several surfaces of transition, critical, triple and tricritical lines as well three different surfaces of anomalies, showing that despite the simplicity of these athermal systems a variety of complex behaviors can emerge from the entropy-driven process.

Along with the conclusion of the work for the hard squares on the square lattice, we are also working in the vicinal adsorption problem for polymers. Despite the work being in its initial phase, by modeling the polymer as a self-avoiding walks on a single stepped surface using the flatPERM method we have found interesting results with two adsorbed phases and the desorbed one. The full characterization of the phase transitions is the next step, as well as the exploration of how the number of steps affects the thermodynamic behavior. Lastly, we have the intention of introducing bulk interactions along the chain to induce the collapse transition or even the crystallization transition.

Appendix A

Monte Carlo methods

The PERM [95] and flatPERM [96] are stochastic growth algorithms based on the classical Rosenbluth-Rosenbluth (RR) [97] method being both very efficient to produce samples of large sizes for a polymer chains modeled by self-avoiding walks and related models. Briefly, the RR method can be described for the SAW by the following steps: the walk is initiated at the vertex v_0 of a hypercubic of dimension d, the second vertex then is randomly chosen from the $2d$ nearest-neighbors. Then, the following vertices are randomly chosen from the σ free nearest-neighbors. In the case of $\sigma = 0$, i.e., when there is no free vertex, the walk is trapped and it is entirely rejected and a new one is started from v_0. Otherwise the new vertex is accepted and a monomer is placed at this position. This grown process is repeated until the desired maximum length of the walk be attained.

The chosen of the new vertex from the free neighbors introduce a bias in the grown process and the RR does not produce an ensemble of equiprobable walks. Each walk, s_i, generated by the RR has a statistical weight, $W_n(s_i)$, and the probability of a certain walk being sampled is given by

$$P_n(s_i) \propto \frac{1}{W_n(s_i)} \tag{A.1}$$

The statistical weight is calculated along the grown process by the product of the number of free neighbors σ at each step, for a walk s with n steps $W_n(s)$ is given by

$$W_n(s) = \prod_{j=1}^{n-1} \sigma_j \tag{A.2}$$

Initially the walk has $W_0 = 1$ and, once a new vertex is accepted, the weight is updated by doing $W_n(s_i) \to W_n(s_i) * \sigma_{i-1}$. An estimate for the partition function, Z_n, for a set of N walks with n steps is obtained by averaging summing over the weights of all walks in the set generated by the RR

$$\langle Z_n \rangle_N = \frac{1}{N} \sum_{i=1}^{N} W_n(s_i). \tag{A.3}$$

Then, naturally, estimate the value of any observable O, one calculates

$$\langle O \rangle_N = \frac{\sum_{i=1}^{N} W_n(s_i) O(s_i)}{\sum_{i=1}^{N} W_n(s_i)}. \tag{A.4}$$

For $N \to \infty$ the estimate of a quantity is expected to converge its the average value. The RR method has two major flaws, the first one is the difficult to obtain long chains, since eventually the walks becomes rapped. Despite the RR method be an improvement

over the Simple Sample method [1], where the next step is always chosen between the $2d$ neighbors, the attrition of the walk (trapped conformations) is still a problem. In fact, on the square lattice the trapped configurations dominates when the length of the walk exceeds 150 steps which makes the number of sampled walks for long lengths vanishes, as shown in Fig. A.1.

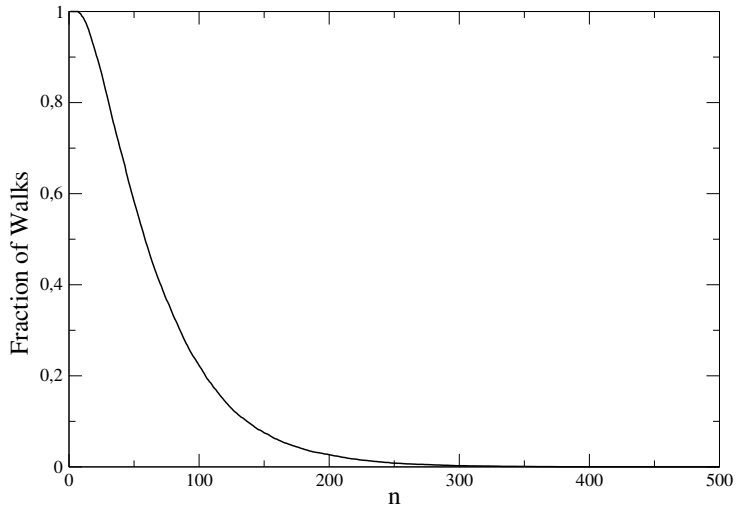

Figure A.1: Fraction of surviving self-avoiding walks as function of the number of steps on the square lattice.

Beyond the attrition problem, the RR method has also an issue of weight dispersion. Eventually, few walks with a large statistical weight starts to dominates the set of sampled walks reducing the effective size of the sample and affecting the quality of the results. In order to solve this problems we need to implement strategies to overcome the attrition and to reduce the weight dispersion. Peter Grassberg [95] propose to solve these problems by introducing the procedures of pruning and enrichment in the RR giving rise to the Pruned-enriched Rosenbluth Method (PERM). The method was latter improved by Prellberg et al. [96] with the flatPERM. As both methods are central for the works presented in Chap. 2, we will discuss them in more details with a scheme for an algorithm for the flatPERM being presented at end of this Appendix.

In the PERM algorithm, walks with large weights are enriched (copies of the walks are made) and their individual weight is reduced, walks with low weights, on other hand, are pruned. These two procedures reduce the dispersion weight and the enrichment increase the number of longer walks. To introduce this procedures in the RR we define a cut-off threshold, $\mathcal{T}$, and a lower threshold t. If at length n a walk s has $W_n(s) > \mathcal{T}_n$, then a copy of the walk s is made and the weight of the original walk and the copy is $W_n(s)/2$, after that the original walk and the copy are grown independently. In the case of $W_n(s) < t_n$ then, with a certain probability $1/q$, the walk is pruned by stopping its growth and making $W_n(s) = 0$. If the walk is not pruned, then, the RR grown process continues with the walks weight being increased by a factor of q (usually $q = 2$ is used).

The estimative of any quantity is calculated in the same way as in the RR, the difference is that for N started walks, usually, due to the prune and enrichment process, we end up with a larger sample of walks. As shown in Fig. A.2 on the PERM, roughly, a constant number of walks is sampled for each length n until the maximum length of 5000

[1] For a complete review about Monte Carlo methods for self-avoiding walks see [98].

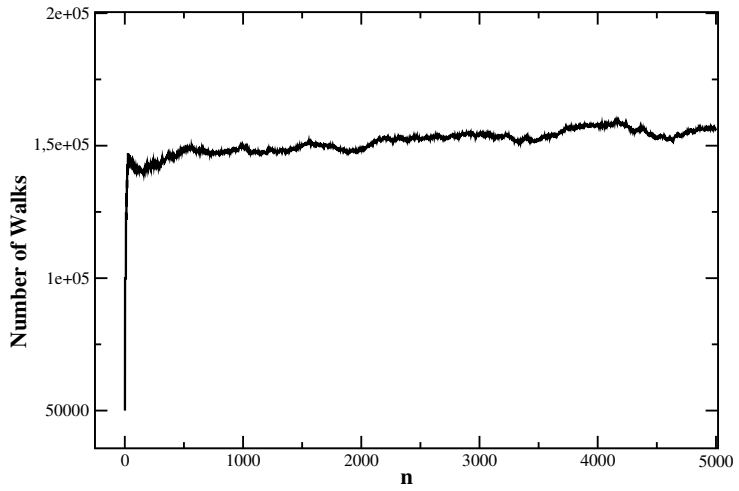

Figure A.2: Surviving SAWs as function of the monomer number in the square lattice. Differently of the RR method we have a large number of walks reaching the maximum chain size.

steps on the square lattice. The thresholds $\mathcal{T}$ and t can be calculated during the grown process by the expressions

$$t_n = c\,\langle Z_n\rangle_N \quad , \quad \mathcal{T}_n = C\,\langle Z_n\rangle_N\,, \tag{A.5}$$

where c and C are parameters of the simulation and they are in general chosen in a way that $C/c \approx 10$ [95]. As one can see, the implementation of the PERM depends on the value of some parameters but, usually, the value of c and C chosen affects only the final size of the sample, and a "wrong" choose of these parameters will require the initiation of more walks. Beyond these parameters, the thresholds also depend of a previous estimate of the partition function. There is two ways to overcome this issue. The first one is by initially running the RR method for walks of short lengths and then using the estimatives of the partition function as an input to PERM. Another way, more convenient, is to initiate $t = 0$ and $\mathcal{T}$ as a large value, then during the simulation as the $< Z_n >$ is obtained the thresholds are updated. Initially, the values of the threshold will be very wrong and a large number of walks can be enriched for small lengths (as shown in Fig. A.2), however, as the simulations goes on the estimative of Z_n is improved and the number of pruned and enriched walks stabilize becoming roughly constant for each step.

Despite the PERM method be very efficient to sample large walks, it can be improved. To see how, let us first consider a more general case where some form of interaction between sites of the walk are allowed. For example, let I be the number of non-consecutive nearest-neighbors (NN) (see Fig. A.3), for each pair an energy ϵ is associated. Defining $c_{n,I}$ as the number of configuration of n-steps with the total of I NN interactions. The partition function in of this more general model is given by

$$Z_n(\beta) = \sum_I c_{n,I} e^{\pm|\beta|I}, \tag{A.6}$$

with $|\beta| = |\epsilon|/(k_B T)$, where k_B is the Boltzmann's constant and T the temperature, the signal of the exponential depends on whether the interaction is attractive or repulsive. The approach with the PERM is similar to the one already described with the only change being on the statistical weight of a walk s with n steps, now the Boltzmann weight is introduced and we have

$$W_n(s) = \prod_{j=1}^{n-1} \sigma_j e^{\pm|\beta|\delta_j}, \tag{A.7}$$

where δ_j is equal to the number of interactions of the vertex j. In this more general case, the PERM gives the estimative of Z_n for a given temperature (or strength of interaction) β, and several runs of the method for different values of β are required to explore the thermodynamic behavior of the model. How we can avoid this cumbersome process? In fact, with few modifications on the PERM routine we can turn the method more "cleaner", without any parameter to prune and enrich, and instead access directly the density of states $c_n(I)$, allowing the determination of the thermodynamic properties for any temperature. This microcanonical implementation of the PERM is know as the flatPERM [96].

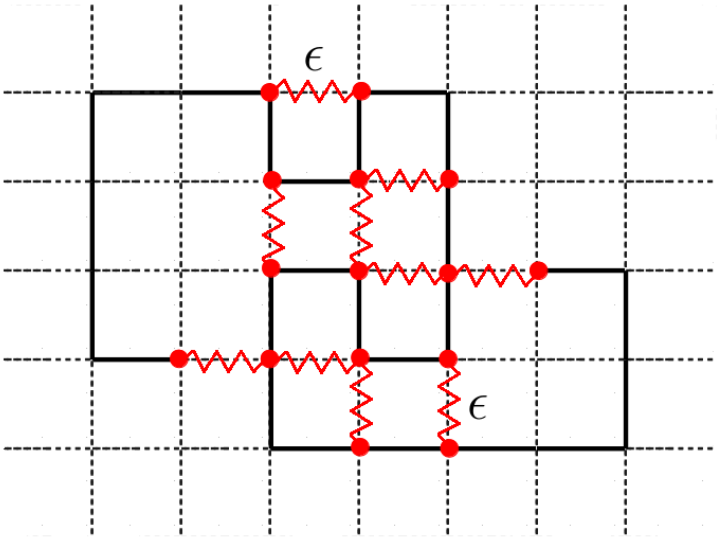

Figure A.3: A nearest-neighbor interacting self-avoiding walk on the square lattice with $n = 25$ steps and $I = 10$ interaction contacts.

As shown above, in then PERM algorithm walks are pruned and enriched in a way that an uniform sampling in the size of the walk is obtained (see Fig. A.2). In the flatPERM, we achieve an uniform sampling in the size and in the energy state by changing the way that the walks are pruned and enriched. Instead of considering thresholds for the weight the pruning/enrichment process is guided by the estimative of the density of states, $c^{est}_{n,I}$, given by

$$c^{est}_{n,I} =< W_n >= \frac{1}{\mathcal{S}_{n,I}} \sum_{i=1}^{\mathcal{S}_{n,I}} W_n(s_i), \tag{A.8}$$

where $\mathcal{S}_{n,I}$ is the number of walks s_i sampled with n steps and I interactions and $W_n(s_i)$ is given by Eq. A.2. If a n-step walk has a weight W_n then we calculate the ratio r

$$r = \frac{W_n}{< W_n >} \tag{A.9}$$

If $r > 1$ then the walk has a larger weight than the target one and has a probability p, that depends of r, to be enriched. Otherwise, if $r < 1$, with a probability $1-p$ the walk is pruned. Initially with a poor estimation of $c_{n,I}$ the method will blindly prune and enrich. However, as the number of walks increases the estimative improves and the method start to prune and enrich around the right number of configurations for each bin of energy I. The flatPERM can be easily generalized for models with more parameters of interaction

by simply changing the Eq. A.8

$$c^{est}_{n,I_1,I_2,....,I_N} =< W_n >= \frac{1}{\mathcal{S}_{n,I_1,I_2,...,I_N}} \sum_{i=1}^{\mathcal{S}_{n,I_1,I_2,...,I_N}} W_n(s_i), \tag{A.10}$$

where $I_1, I_2, ...I_N$ are the total number of interactions being each one associated to an energy ϵ_k and $\mathcal{S}_{n,I_1,I_2,...,I_N}$ is the number of sampled walks with n steps and $I_1, I_2, ..., I_N$ interactions.

As the number of types of interaction increases the flatPERM takes longer to converge and estimate the density of states. In many cases this time limitation impose a needed to decrease the size of the walk. For example, for a interacting self-avoiding walk model with two types of attractive interactions the flatPERM converge the density of states, in a feasible time, only for short lengths (~ 100 steps). Despite this limitation in the size, as shown in Chap. 2, the complete density of states allows a finite-size (usually qualitatively correct) picture of the thermodynamic behavior of the model. If our example model has a partition function given by

$$Z_n(\omega_1, \omega_2) = \sum_{I_1,I_2} c_{n,I_1,I_2} \omega_1^{I_1} \omega_2^{I_2}, \tag{A.11}$$

where $\omega_1 = e^{\beta\epsilon_1}$ and $\omega_2 = e^{\beta\epsilon_2}$ are the Boltzmann weights. Then, the total density of states with the two parameters free is determined, for short lengths, by (two-parameter version) the flatPERM. By fixing the value of one of the parameters, we have only one free parameter which reduces the dimension of the density of states allowing the (one-parameter version) flatPERM to samples much longer walks, typically thousands of steps. If all parameters of the model are fixed then the (zero-parameter version) flatPERM will produce an uniform sampling in the size. In other worlds the zero-parameter flatPERM version is the PERM and walks with millions of steps can be sampled with the benefit of not needing any simulation parameter. Next we present an sketch of an algorithm for the implementation of the flatPERM. We draw the algorithm in an optimized way with the recursive subroutine idea from the Grassberg PERM [95] and ideas of an optimal way to choose between prune/enrichment from Prellberg [99].

Algorithm 1 flatPERM

Initiate the weight $W_0 \leftarrow 1$ and the total number of walks $\mathcal{S} \leftarrow 0$
Initiate the density of states $c_{n,I_1,...I_N} \leftarrow 0$
Sample $\leftarrow 0$

while Sample < MaxSamples **do** {Main loop}
  Initiate a walk at vertex v_0
  $\mathcal{S}_{0,0,...0} \leftarrow \mathcal{S}_{0,0,...0} + 1$
  $c_{0,0,...0} \leftarrow c_{0,0,...0} + W_0$
  Call Step
end while

Recursive Subroutine Step
  Determine the number σ of free neighbors
  if $(\sigma = 0)$ **then**
    Trapped configuration **return**
  end if
  Draw one of the free neighbors uniformly at random
  Step to the new site
  $n \leftarrow n + 1$, $W_n \leftarrow W_{n-1} * \sigma$
  Determine the total of interactions $I_1, ...I_N$
  $\mathcal{S}_{n,I_1,...I_N} \leftarrow \mathcal{S}_{n,I_1,...I_N} + 1$
  $c_{n,I_1,...I_N} \leftarrow c_{n,I_1,...I_N} + W_n$
  if $(n < n_{\max})$ **then**
    $< W_n >= c_{n,I_1,...I_N}/\mathcal{S}_{0,0,...0}$
    $r \leftarrow W_n / < W_n >$
    $W_n \leftarrow < W_n >$
    $p \leftarrow r \bmod 1$
    Draw a random number $a \in [0, 1]$
    if $(a < p)$ **then** {Determines if the walk is going to be pruned or enriched}
      $k \leftarrow \text{Int}[r] + 1$ {k is the number of copies made}
    else
      $k \leftarrow \text{Int}[r]$ {If $k = 0$ the walk is naturally pruned}
    end if
    Call Step k times
  else if $(n = n_{\max})$ **then** {Shrink the walk to the previous Step call}
    Delete the last vertex of the walk
    $n \leftarrow n - 1$
    return
  end if

  if $(n > 0)$ **then**
    Delete the last vertex of the walk
    $n \leftarrow n - 1$
    return
  else
    Sample $\leftarrow$ Sample +1
    return {Return to the main loop, the first call of Step}
  end if
End Subroutine

Appendix B

Mean-Field methods

The mean-filed approximations considered here are solutions of the models on the hierarchical lattices of Bethe and Husimi. The Bethe lattice consist in the core of an infinity Cayley tree while the Husimi lattice is the core of the infinity Cayley build with blocks such as squares, triangles, cubes, etc. In such structures, any two elements (points in the Bethe and blocks in the Husimi) are connected by only one path. A symmetric Cayley tree with coordination q can be built in a recursive fashion from the starting vertex. The initial vertex composes the zero-generation, where q new vertex is connected forming the first generation or shell. At each one new vertex of the first generation, we add $q-1$ new vertices, forming the second generation, and so on. Hence, the n-generation is obtained from the connection of $q-1$ vertices to each one of the $n-1$ generation. In Fig. B.1 a Cayley tree of coordination $q=3$ is shown up to the fourth generation.

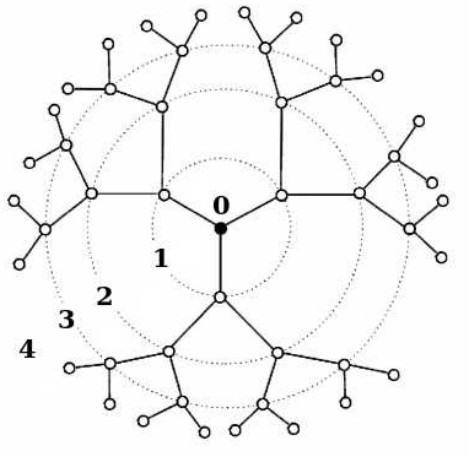

Figure B.1: Example of a Cayley Tree with coordination $q=3$ and four generations.

One important feature of the Cayley trees is the lattice dimensions. The dimensionality can be evaluated using the limit

$$d = \lim_{n\to\infty} \frac{\ln C_n}{\ln n}, \tag{B.1}$$

where C_n is the total number of vertices in the lattice. For a tree with coordination q and n generations C_n can be written as

$$C_n = \frac{q(q-1)^n - 2}{q-2}. \tag{B.2}$$

Then, by replacing Eq. B.2 in Eq. B.1 we obtain, for $q > 2$: $d \to \infty$, leading to the conclusion that solutions in hierarchical lattices, like Cayley tree, are mean-filed approximation to a problem on regular lattices.

Another important issue is the boundary effect present in the Cayley trees. In regular lattices, the ratio between the number of sites at the boundary and the ones from interior goes to zero in the thermodynamic limit. Meaning that in this limit there are no effects due to the boundary sites. However, such vanishing is not true for Cayley trees. In fact, the number of sites in a tree with n-generation and coordination q is given by

$$C_s = q(q-1)^{n-1} \tag{B.3}$$

then, the ratio C_s/C_n in the thermodynamic limit ($n \to \infty$) is given by

$$\frac{C_s}{C_n} = \frac{q-2}{q-1}. \tag{B.4}$$

Namely, a Cayley tree with $q = 3$, have 50% and with $q = 4$ 66%, of its sites at the boundary. With this dominant fraction of boundary sites, solutions in the Cayley tree can contain unphysical effects produced by the different coordination number of the boundary sites. For this reason, when approaching problems in regular lattices the hierarchical lattices considered are the Bethe or the Husimi lattice. As these lattices are the core of infinity Cayley trees they does not carry the boundary effects.

While the Bethe lattices is build with singles points in each generation, as in the Cayley tree shown in Fig. B.1, the Husimi lattice is build with more complex structures such as polygons and polyhedrons as shown in Fig. B.2.

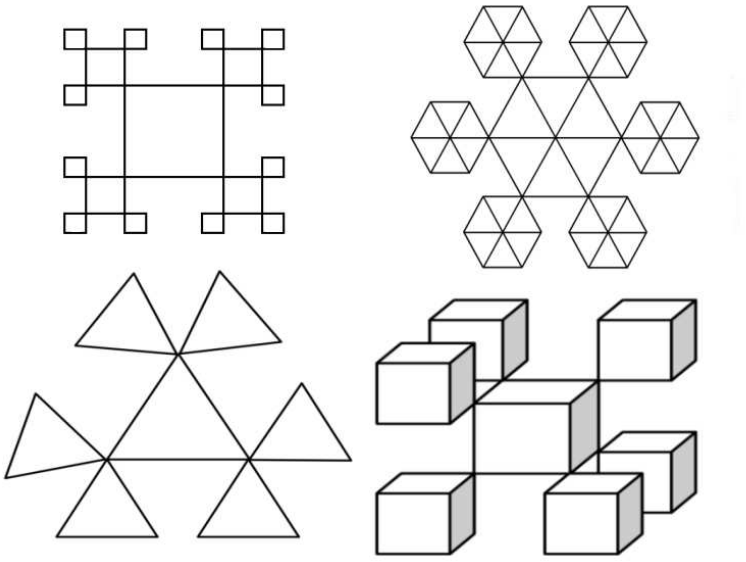

Figure B.2: Examples of Husimi lattices. In the left corner, we have a Husimi lattice build up with squares (an approximation to the square lattice). On the right and the bottom left two approximations to the triangular lattice are shown. Last, on the bottom right, a Husimi lattice build with cubes are shown.

Due to the hierarchical nature of those lattices, a large number of physical systems with short-range interactions can be analytically (or semi-analytically) solved on them. Moreover, as shown in [100], despite the solutions in those lattices being mean-field ones, they give a better approximation than the usual mean-field methods. Usually, in the

conventional mean-field methods, the geometry of lattice is kept, but the correlations between sites are not taken into account. On Bethe and Husimi lattices the approach is different, the geometry is deformed to be approximated by the structure of the Cayley tree, but some of the original correlation is retained making the solutions in those lattices more reliable than the conventional mean-field methods.

To illustrate how we can solve short-range problems in hierarchical lattices we will solve ferromagnetic Ising model on the square lattice approximated by the Bethe and Husimi lattices.

B.1 Ising model on Bethe lattice

Let's consider the ferromagnetic ($J > 0$) Ising model in the absence of an external field, for which the Hamiltonian is given by

$$\mathcal{H} = -J \sum_{<ij>} \sigma_i \sigma_j, \tag{B.5}$$

where $\sigma_i = \pm 1$ and the sum is evaluated over the pairs of nearest-neighbors i and j. The partition function of the model is defined by

$$Z = \sum_{\{\sigma\}} e^{-\beta \mathcal{H}} \tag{B.6}$$

Defining $w = e^{\beta J}$, we can identify two types of terms in Eq. B.6: either w or $1/w$. To obtain an approximation for the square lattice, we need to consider a Bethe lattice with coordination $q = 4$ (see Fig. B.3).

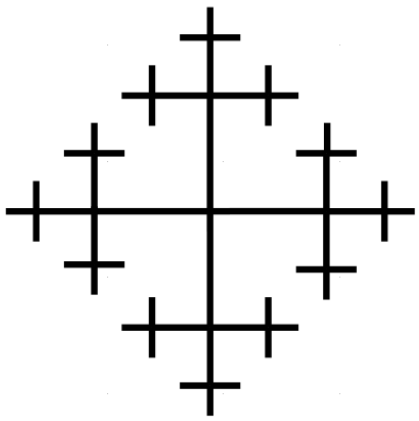

Figure B.3: Three generations of a Bethe lattice with $q = 4$, an approximation for the square lattice.

We begin the solution of the Ising model on this lattice by defining all the possible configuration for a root site of nth-generation which will be the 'root' for the next $n+1$-generation. As in the Ising model one has $\sigma = \pm 1$, then, as shown in Fig. B.4, only two configurations can happen in the root site. We define g_1 as the contribution associated with $\sigma = 1$ (spin-up) and g_2 with $\sigma = -1$ (spin down).

By adding $q-1$ subtrees of generation $n-1$ to the root site, a subtree of n-generation is formed. Doing this process for g_1 and g_2 considering all the possible configurations for the $q-1$ new sites, we obtain recursive relations on the form

$$g_i^{(n+1)} = f(g_1^{(n)}, g_2^{(n)}). \tag{B.7}$$

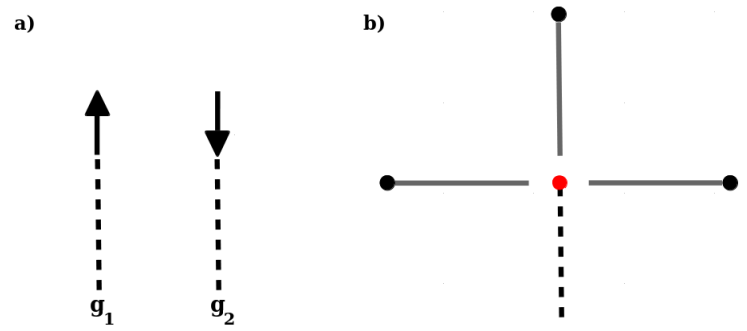

Figure B.4: (a) The configurations for the root site, g_1 spin up and g_2 spin down. (b) The building of the $n+1$ generation, three sub-trees of generation $n-1$ (black circles) are added to the root site (red circle).

We can obtain the partition function in a similar fashion. For a given central vertex of type g_1 or g_2, we add q sub-trees leading to a partition function of the form: $Z^{(n+1)} = h(g_1^{(n)}, g_2^{(n)})$. As g_1 and g_2 are a partial contribution in the partition function we, usually, refer to this quantities as the partial partition functions (ppfs).

For the Ising model, the recursion relations for the ppfs can be easily obtained. Let's start with a root site g_1, then, we connect 3 new sites and evaluate the sum over all allowed configurations of the new sites. For example, if the three new sites have a configuration with all spins up ($\sigma = 1$) we have an associated term of $w^3 g_1^3$ and in the case of two spins up and one down we have a term $3wg_1^2 g_2$, where the factor 3 is the multiplicity of this configuration. Following this process, we obtain the recursion relations for g_1 and g_2

$$g_1^{'} = w^3 g_1^3 + 3wg_1^2 g_2 + 3\frac{1}{w} g_1 g_2^2 + \frac{1}{w^3} g_2^3 = \left(wg_1 + \frac{1}{w} g_2\right)^3, \tag{B.8}$$

$$g_2^{'} = \left(wg_2 + \frac{1}{w} g_1\right)^3, \tag{B.9}$$

where, in order to facilitate the notation, we have changed $g_i^{(n+1)}$ and $g_i^{(n)}$ to $g_i^{'}$ e g_i. Real and positive solutions of the recursion relations for the ppfs, the fixed points given by $g_i^{'} = g_i$ (thermodynamic limit), are related with the thermodynamic phases present in the model. However, as shown in Eqs. B.8 and B.9, the recursion relations are composed by a sum of positive terms which can diverge in the thermodynamic limit. To avoid the divergent behavior, define a convergent ratio $R = g_1/g_2$ and then we can write the ratios for the ppfs

$$R^{'} = \left(\frac{w^2 R + 1}{R + w^2}\right)^3 \tag{B.10}$$

By making $R^{'} = R$ we find the fixed points

$$R^* = \left\{1, \frac{1}{2}(-a + \sqrt{-4 + a^2}), \frac{1}{2}(-a - \sqrt{-4 + a^2})\right\}, \tag{B.11}$$

where $a = 3w^2 - w^6$. For $R^* = 1$ we have $g_1 = g_2$, meaning that there is an equal contribution of spins up and down in the system. In other words, this fixed point is associated with the disordered phase of the Ising model. The other fixed points are related to the two possible ordered phases. These solutions become complex for high

temperatures, $w \to 0$, and by analyzing these solutions for low temperatures, $w \to \infty$, we find

$$R_-^* = \frac{1}{2}(-a - \sqrt{-4+a^2}) \to 0 \quad \text{and} \quad R_+^* = \frac{1}{2}(-a + \sqrt{-4+a^2}) \to \infty \tag{B.12}$$

For R_-^* at low temperatures limit we have $g_1/g_2 \to 0$, characterizing a state where the spins pointing down dominate. Such a state is obviously one of the two possible ground states, in this case with all spins with $\sigma = -1$. Naturally, for the other one, we have $g_1/g_2 \to \infty$, characterizing the phase with all spins up.

Once all the physical fixed points are found, we move on to the characterization of the thermodynamic behavior of the phases present. We start by making a linear stability analysis of the fixed points, by finding the eigenvalues of the Jacobian matrix, $\mathcal{J}$, defined generally for a system with n recursion relations R_i by

$$\mathcal{J} = \begin{bmatrix} \frac{\partial R_1'}{\partial R_1} & \cdots & \frac{\partial R_1'}{\partial R_n} \\ \vdots & \ddots & \vdots \\ \frac{\partial R_n'}{\partial R_1} & \cdots & \frac{\partial R_n'}{\partial R_n} \end{bmatrix}. \tag{B.13}$$

We evaluate the Jacobian in the fixed points and by finding the leading eigenvalue, λ_{max}, we can determine the stability of a fixed point. If $\lambda_{max} < 1$ the fixed point is stable and for $\lambda_{max} > 1$ the fixed point is said to be unstable. The stability limit of a fixed point, i.e., of a thermodynamic phase of the system, is defined by the set of parameters, in the case of the Ising model w, where $\lambda_{max} = 1$. If a system has two phases, namely I being stable for low t and II stable for large t, then, as shown in Fig. B.5 with t being the system parameter, the limit stability of each phase can behave in two ways

1) The stability limits of each phase happens for different values of t in a way such in some regions both phases are stable. In this case, a coexistence region is created and a first-order transition separates the phases.

2) The stability limits of both phases are at the same value of t. This scenario happens whenever a critical phase transition exists between the phases I and II.

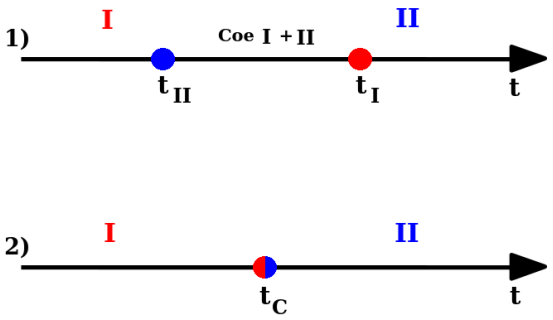

Figure B.5: 1) Stability limits of phases I and II located at different values of t, creating a coexistence region. 2) Critical behavior defined by a single stability point.

For the Ising model the stability analysis can be easily done, we have a single ratio for the ppfs and then only one eigenvalue given by

$$\lambda = \frac{3(1+Rw^2)^2(w^4-1)}{(R+w^2)^4} \tag{B.14}$$

Evaluating λ for the fixed points of the ordered and the disordered phases we find that both phases have the same stability limit and then, as expected, we have a critical order-disorder phase transition in the ferromagnetic Ising model in the Bethe lattice with coordination $q = 4$. The observed critical point, $w = \sqrt{2} \rightarrow \frac{k_B T_c}{J} = 2.885$, is the same result found in the Bethe approximation [101]. Curiously, the name Bethe lattice does not derive from Hans Bethe but from the fact that the Bethe approximation is exact in such lattice for the Ising model.

We conclude the thermodynamic analysis by calculating the partition function of the model. As done for the ppfs, the partition function is obtained by the counting of all possible configurations for 4 new sites being added to a central vertex

$$Z^{'} = g_2^4 \left[\left(wR + \frac{1}{w} \right)^4 + \left(\frac{R}{w} + w \right)^4 \right] = g_2^4 z, \tag{B.15}$$

where z is the convergent part of the partition function. With the partition function calculated we can obtain several other quantities like the bulk free energy, ϕ_b, which is given by [100]

$$\phi_b = -\frac{1}{2} \log \left[\frac{Z^{'}}{Z^{q-1}} \right] \tag{B.16}$$

By using Eqs. B.15 and B.9 we can write

$$\phi_b = -\log \left[\frac{(w + R/w)^6}{z} \right] \tag{B.17}$$

Once calculated the free energy we can identify the coexistence point of two phases (I e II) by making $\phi_{bI} = \phi_{bII}$. In a critical transition, such a point must coincide with the stability limit of the phases. In fact, using the fixed points previously calculated and equaling the free energies, we obtain $w = \sqrt{2}$ as the coexistence point between the disordered and the ordered phases, as expected.

B.2 Ising on the Husimi lattice

We can improve the approximation to the square lattice by building a Bethe lattice with squares (see Fig.B.2), such lattice is known as a Husimi lattice. The process of solving the Ising model in the Husimi lattice is very similar to the one for the Bethe lattice. As shown in Fig. B.6, we start by determining the ppf connecting three sub-trees to the square of generation n forming the new generation.

As the lattice is built with more complex structures then points the recursive relations for the ppfs obtained are more complex due to a large number of configurations for a given root site. Following a similar procedure to count the configuration we obtain the ppfs for the Ising model on the Husimi lattice build with squares

$$g_1^{'} = w^4 g_1^3 + 3 g_1^2 g_2 + (2 + 1/w^4) g_1 g_2^2 + g_2^3 \tag{B.18}$$

$$g_2^{'} = w^4 g_2^3 + 3 g_2^2 g_1 + (2 + 1/w^4) g_2 g_1^2 + g_1^3 \tag{B.19}$$

The recursion relation for the convergent ratio, $R = g_1/g_2$, is then given by

$$R^{'} = \frac{w^4 R^3 + 3R^2 + (2 + 1/w^4)R + 1}{w^4 + 3R + (2 + 1/w^4)R^2 + R^3} \tag{B.20}$$

By looking for fixed points, we find the same thermodynamic phases as those already found in the Bethe lattice, with the main difference, that large expressions are

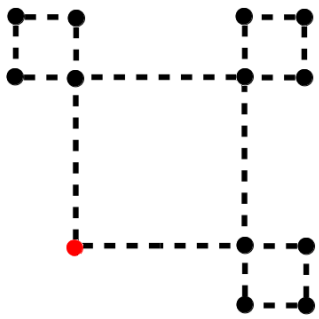

Figure B.6: The red circle represents the root site of the square where the new squares are connected (black circles).

obtained for such fixed points. With the analysis of linear stability, as in the Bethe lattice, we have found that the ordered and disordered phases have same limit of stability. The critical order-disorder transition is observed at $\frac{k_b T_c}{J} \approx 2.770797$. This value a little bit closer to the exact value for the Ising model on the square lattice $\frac{k_b T_c}{J} \approx 2.269$ [102] than the one from the Bethe lattice. This shows that the approach with a hierarchical lattice can be improved by considering structures more close to the regular lattice being approximated. In fact, as we are going to show in the next section, the approximation can be improved even further by systematically increasing the building structures of lattice creating high-level Husimi lattices.

B.3 High level Husimi lattices

We will define the level L of a Husimi lattice as the number of sites shared by two generations (see Fig. B.7). The Husimi lattices are now build with plaquettes, which in the case of an square lattice being approximated, composed by several squares. As we increase the level the number of possible configurations for the root line increases which leads to a large number of ppfs to handle. As an example, for the Ising model in the $L = 1$ Husimi lattice, as showed, we have 2 ppfs while for $L = 7$ it will be 8192 ppfs.

As large the level the closer the results are expected to be of the regular lattice which is being approximated. The use of Husimi lattices of a high level was introduced by Monroe [103] in 2001. In his work, he solved the Ising model up to a fifth-level Husimi lattice. By doing an extrapolation of five points in his data the author found the value of $T_c \approx 2.269127$ for the critical point with a difference of only 0.003% to the exact value by Onsager.

As shown in the previous sections to solve any model in the Husimi lattice we need to obtain the recursion relations for the ppfs, however, in the case of Husimi lattice of high level the solving process can not be done by hand, then we need an efficient computational method to count all the possible configurations for a given level. As shown in the Chap. 4, where we use this method to solve the problem of the lattice gas of 2NN particles on the square lattice, we employ a recursive method to obtain the ppfs of level L by using the previously counted configurations for the Husimi lattice of level $L - 1$.

To illustrate the method, lets consider the Ising model in a Husimi lattice of level

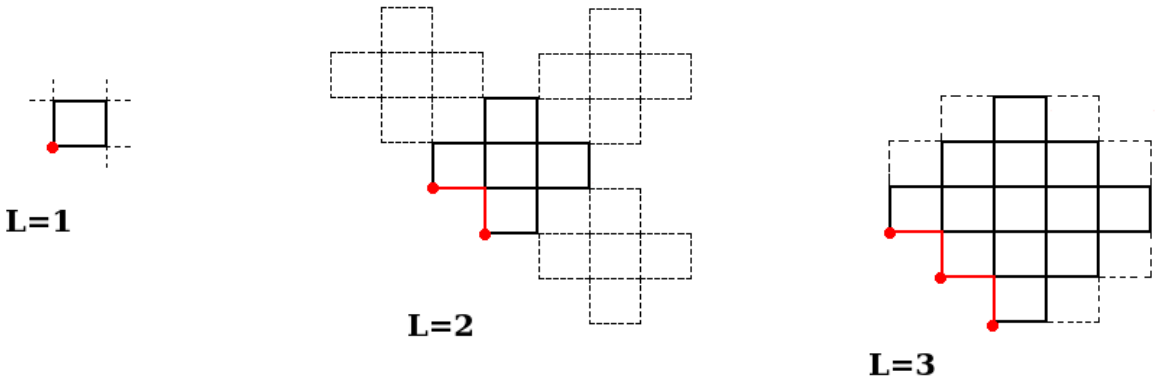

Figure B.7: Husimi lattices of different levels for the approximation of the square lattice. The red lines represent the root lines in each level. The dashed lines showed where the three sub-tree connects to form the new generation, and example of how the sub-tree connects to form a new generation is sketched for $L = 2$.

L. Any ppf, g_σ, will have the general form

$$g'_\sigma = \sum_{i=1}^{N} m_i \omega^{n_{+,i}-n_{-,i}} g_{x_i} g_{y_i} g_{z_i}, \tag{B.21}$$

where sum is evaluated over the N configurations of the plaquette of L level, m_i is the multiplicity of the ith-configuration, g_{x_i}, g_{y_i} and g_{z_i} are terms associated with the three sub-trees connected to form a new generation and $n_{+,i}$ is the number of pairs of spins that produce the contribution ω while $n_{-,i}$ is the number of pairs which produces $1/\omega$. So, considering g_1 as the ppfs for all spins up in the root line, a configuration i where all n spins of the Lth-level plaquette are pointed up we will have $m_i = 1$ and $g_{x_i} = g_{y_i} = g_{z_i} = g_1$ generating a term $\omega^n g_1^3$ for the considered ppf. In the configuration with all spins up the multiplicity is trivial to be determined, but, in general, this quantity is hard to be determined by hand and a computational counting process is needed. So the main goal of the method to obtain the ppfs is to determine the m_i, $n_{+,i}$ and $n_{-,i}$ for each contribution $g_{x_i} g_{y_i} g_{z_i}$.

The recursive counting method employed here consist on the fact that the $L-1$th-level plaquette is part of Lth-level one (see Fig. B.8). So, once the count of the level $L-1$ is done all the information obtained can be used to perform the count for the level L lattice. There is several ways to implement this kind of procedure. Here, we will present in general terms the procedure that we follow. First, as shown in Fig. B.8, we identify all of the $L-1$-level sites inside of the L-level and the exclusive sites of the Lth-level plaquette. We then fix the root line to the configuration of the desired ppf. For a fixed configuration of the exclusive sites of L we vary all the possible configurations of the boundary of $L-1$. If the configuration is allowed then, we update the list of configurations of L with the information of the exclusives sites and the already know information of the $L-1$-level configuration.

A main downside of our method is that in order to obtain the ppfs for the level L all the information of the level $L-1$ need to be stored. For low levels this is not a problem, but as the number of configurations increases exponentially we reach a point where the

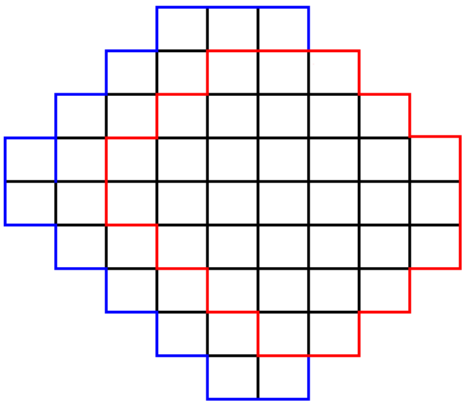

Figure B.8: Blue line denote the sites that are exclusive of the fifth-level lattice while the red line is the boundary of a fourth-level lattice.

storage of the information requires too much computational resource. As an example, to solve the lattice gas composed by 2NN particles on a 9th-level Husimi lattice we need at least $256GB$ of RAM and hundreds of terabytes to storage the output information.

Independently of the level of the Husimi lattice the dimension of the hierarchical tree is infinity. Then we only obtain mean-field results for the critical exponents. For example, the magnetization, m, of a lattice of level N follows the scaling law

$$m_N(T) = A|\tau|^{1/2}, \qquad \tau = \frac{T - T_c(N)}{T_c(N)}, \tag{B.22}$$

where A is a non-universal amplitude and $1/2$ is the classical value of the critical exponent β. Despite m being related to the classical exponent, Susuki [104] demonstrated that the systematic variations of the amplitudes as functions of the level N, called coherent anomaly, are related to the non-trivial critical exponents. The coherent anomaly method (CAM) described by Susuki shows that the classical amplitudes, obtained through mean-filed methods, have a scaling behavior of the form

$$A(N) = \bar{m}_s(N) \approx (T_c(N) - T_c(\infty))^{\beta - 1/2} \tag{B.23}$$

$$\bar{\chi}(N) \approx (T_c(N) - T_c(\infty))^{\gamma - 1}, \tag{B.24}$$

where $\bar{\chi}(N)$ is the amplitude associated with the classical susceptibility. The critical exponents γ and β are the non-classical and $T_c(\infty)$ is the critical temperature of the regular lattice that is being approximated. This method can be employed in the Husimi lattices of a high level. In his work Monroe applied the method and obtained γ with a value 1.2% different from the exact one, a large deviation was observed for β with 11.2% of difference with relation to the expected value for the Ising model on the square lattice. The larger deviation found for the exponents when compared with the value of found for the critical temperature shown the needed to solve the model for a higher-level Husimi lattice. However, as already mentioned an immense computational cost is needed to obtain the ppfs and to solve the model. As shown in Chap 4, where we employ the CAM to obtain the critical exponents for the 1NN and the 2NN model, the solution of the 2NN model in a Husimi lattice of 8th-level requires computational resources to handle 3484 ppfs each one with an average of 10^{21} terms, which making the computational implementation of the method very challenging.

Bibliography

[1] P. C. Hiemenz and R. Rajagopalan; "Principles of Colloid and Surface Chemistry, Revised and Expanded"; 3rd edition, CRC Press, 1997.

[2] E. B. Priestley, P. J. Wojtowicz and P. Sheng; "Introduction to Liquid Crystals"; Springer, Boston, MA, 1974.

[3] P.G de Gennes; "Scaling Concepts in Polymer Physics"; Ithaca, NY: Cornell University Press; (1979).

[4] M. E. Cates; "Complex Fluids: The Physics of Emulsions"; arXiv:1209.2290 (2012).

[5] W. Poon, T. Mcleish and A. Donald; "Soft condensed matter: Where physics meets biology"; Physics Education, **37**, 25-33 (2002).

[6] M. Kardar; "Statistical Physics of Field"; Cambridge University Press (2007).

[7] E. Eisenriegler; "Polymers Near Surfaces"; World Scientific (1993).

[8] H.J. Butt, K. Graf and M. Kappl; "Adsorption"; Physics and Chemistry of Interfaces (2 ed.). Federal Republic of Germany: Wiley-VCH. pp. 187–217 (2006)

[9] A. A. Mohsenipour and R. Pal; "A Review of Polymer–Surfactant Interactions"; pp 639-684 (2015).

[10] A. G. García, M. M. B. Nagelkerke, R. Tuinier and M. Vis; "Polymer-mediated colloidal stability: on the transition between adsorption and depletion"; Advances in Colloid and Interface Science, **275**, 102077 (2020).

[11] T. J. Oliveira and J. F. Stilck; "Transfer-matrix study of a hard-square lattice gas with two kinds of particles and density anomaly"; Phys. Rev. E **92**, 032101, (2015).

[12] P.J Flory; "The Configuration of Real Polymer Chains"; J.Chem.Phys. **17**, 3 (1949).

[13] A. Karatrantos, N. Clarke and M. Kröger; "Modeling of Polymer Structure and Conformations in Polymer Nanocomposites from Atomistic to Mesoscale: A Review"; Polymer Reviews, **56**, 385-428, (2016).

[14] D. I. Bower; "An Introduction to Polymer Physics"; Cambridge University Press, 2002.

[15] P.G de Gennes; "Exponents for the excluded volume problem as derived by the Wilson method"; Phys. Lett. **38A**, 339 (1972).

[16] B. Nienhuis; "Phase transitions and crítical phenomena", vol 11, Academic Press (1987).

[17] S.F. Edwards; "The statistical mechanics of polymers with excluded volume"; Proc. Phy. Soc. **85**, 613 (1985).

[18] N. Clisby; "Accurate estimate of the critical exponent ν for self-avoiding walks via a fast implementation of the pivot algorithm"; Phys. Rev. Lett 104, **5**, 55702 (2010).

[19] N. Clisby; "Scale-free Monte Carlo method for calculating the critical exponent γ of self-avoiding walks"; J. Phy. A, **50**, 264003 (2017).

[20] T. Prellberg; "Scaling of Self-Avoiding Walks and Self-Avoiding Trails in Three Dimensions"; J. Phys. A **34**, L599-L602 (2001).

[21] C. Vanderzande; "Lattice Models of Polymers"; Cambridge University Press (1998).

[22] A. L. Owczarek, T. Prellberg and R. Brak; "New scaling form for the collapsed polymer phase"; Phys. Rev. Lett. **70** 951–53 (1993). B. Duplantier; "Exact scaling form for the collapsed 2D polymer phase" Phys. Rev. Lett. **71** 4274-4274 (1993). A. L. Owczarek, T. Prellberg, and R. Brak; "Reply to 'Exact Scaling Form for the Collapsed 2D Polymer Phase' by B. Duplantier"; Phys. Rev. Lett. **71**, 4275 (1993).

[23] B. Duplatier and H. Saleur; "Exact tricritical exponents for polymers at the FTHETA point in two dimensions"; Phys.Rev.Lett *59*, 539 (1987).

[24] I. S. Chang and H. Meirovitch;"Collapse transition of self-avoiding walks on a square lattice in bulk and near a linear wall: the universality classes of the Θ and Θ' points"; Phys. Rev. E **48** 3656–60 (1993).

[25] H. Meirovitch, and H. A. Lim; "The collapse transition of self-avoiding walks on a square lattice: A computer simulation study"; J. Chem. Phys. **91**, 2544 (1989).

[26] H. Meirovitch, and H. A. Lim; "Computer simulation study of the θ-point in three dimensions. I. Self-avoiding walks on a simple cubic lattice"; J. Chem. Phys. **92**, 5144 (1990).

[27] M. C. Tesi, E. J. J. van Rensburg, E. Orlandini, and S. G. Whittington; "Monte carlo study of the interacting self-avoiding walk model in three dimensions"; J. Stat. Phys. **82**, 155 (1996).

[28] P.G de Gennes; "Collapse of a polymer chain in poor solvents"; J. Phys. Lett. **36**, L55 (1975).

[29] P.G de Gennes; "Collapse of a flexible polymer chain II"; J. Phys. Lett. **39**, L299 (1978).

[30] H. W. J. Blöte and B. Nienhuis; "Critical behaviour and conformal anomaly of the O(n) model on the square lattice"; J. Phys. A **22**, 1415 (1989).

[31] S. O. Warnaar, M. T. Batchelor, and B. Nienhuis; "Critical properties of the Izergin-Korepin and solvable O(n) models and their related quantum spin chains" ; J. Phys. A **25**, 3077 (1992).

[32] N. T. Rodrigues and T. J. Oliveira; "Monte Carlo simulations of polymers with nearest- and next nearest-neighbor interactions on square and cubic lattices"; J. Phys. A **47**, 405002 (2014).

[33] D. P. Foster; "Universality of collapsing two-dimensional self-avoiding trails" J. Phys. A **42**, 372002 (2009).

[34] A. L. Owczarek and T. Prellberg; "The collapse point of interacting trails in two dimensions from kinetic growth simulations"; J. Stat. Phys. **79**,951 (1995); "Collapse transition of self-avoiding trails on the square lattice"; Physica A **373**,433(2007).

[35] C. J. Bradly, A. L. Owczarek and T. Prellberg, "Universality of crossover scaling for the adsorption transition of lattice polymers"; Phys. Rev. E **97** 022503 (2018).

[36] P. Grassberger; "Simulations of grafted polymers in a good solvent"; J. Phys. A: Math. Gen. **38** ,323 (2005).

[37] M. T. Batchelor and C. M. Yung; "Exact Results for the Adsorption of a Flexible Self-Avoiding Polymer Chain in Two Dimensions"; Phys. Rev. Lett. **74**, 2026 (1995).

[38] A. L. Owczarek, A. Rechnitzer, J. Krawczyk, and T. Prellberg; "On the location of the surface-attached globule phase in collapsing polymers" J. Phys. A **40**, 13257-13267 (2007).

[39] J. Krawczyk, A. L. Owczarek, T. Prellberg, and A. Rechnitzer; "Layering transitions for adsorbing polymers in poor solvents"; Europhys. Lett. **70**, 726-732 (2005).

[40] J. A. Plascak, P. H. L. Martins, and M. Bachmann; "Solvent-dependent critical properties of polymer adsorption"; Phys. Rev. E **95**, 050501 (2017).

[41] C. J. Bradly, A. L. Owczarek and T. Prellberg, "Adsorption of neighbor-avoiding walks on the simple cubic lattice"; Phys. Rev. E **98**, 062141 (2018).

[42] C. J. Bradly, A. L. Owczarek and T. Prellberg, "Phase transitions in solvent dependent polymer adsorption in three dimensions", Phys. Rev. E **99**, 062113 (2019).

[43] N. T. Rodrigues, T. Prellberg and A. L. Owczarek; "Adsorption of interacting self-avoiding trails in two dimensions"; Phys. Rev. E. **100**, 022121 (2019).

[44] N. T. Rodrigues, T. J. Oliveira, T. Prellberg and A. L. Owczarek; "Adsorption of two-dimensional polymers with two- and three-body self-interactions"; Phys. Rev. E, **100**, 062504 (2019).

[45] N. T. Rodrigues and T. J. Oliveira; "Three stable phases and thermodynamic anomaly in a binary mixture of hard particles"; J. Chem. Phys. **151**, 024504 (2019)

[46] N. T. Rodrigues and T. J. Oliveira; "Thermodynamic behavior of binary mixtures of hard spheres: Semianalytical solutions on a Husimi lattice built with cubes"; Phys. Rev. E, **100**, 032112 (2019).

[47] N. T. Rodrigues and T. J. Oliveira; "Fluid-fluid demixing and density anomaly in a ternary mixture of hard spheres"; Phys. Rev. E, **101**, 062102 (2020).

[48] M Rovere, D W Heermann and K Binder; "The gas-liquid transition of the two-dimensional Lennard-Jones fluid"; J. Phys.: Condens. Matter, **2** 7009 (1990).

[49] X. C. Zeng and David W. Oxtoby; "Gas–liquid nucleation in Lennard-Jones fluids"; J. Chem. Phys. **94**, 4472 (1991).

[50] W. B. Streett; "Monte Carlo studies of the fluid-solid phase transition in the Lennard-Jones system"; J. Chem. Phys. **61**, 1960 (1974).

[51] JP. Hansen and L. Verlet; "Phase Transitions of the Lennard-Jones System"; Phys. Rev. **184**, 151 (1969).

[52] A. Mulero; "Theory and Simulation of Hard-Sphere Fluids and Related Systems"; Springer, Berlin, Heidelberg (2008).

[53] H. C. Andersen, J. D. Weeks, and D. Chandler;"Relationship between the Hard-Sphere Fluid and Fluids with Realistic Repulsive Forces"; Phys. Rev. A **4**, 1597 (1971).

[54] G. Bryant, S. R. Williams, L. Qian, I. K. Snook, E. Perez, and F. Pincet; "How hard is a colloidal "hard-sphere" interaction?"; Phys. Rev. E **66**, 060501(R) (2002).

[55] M.S.Wertheimt; "Exact Solution of the Percus-Yevick Integral Equation for Hard Spheres"; Phys. Rev. Leet. **10**, 321 (1963).

[56] M.S.Wertheimt; "Analytic Solution of the Percus-Yevick Equation"; J. math. Phys. **5** 643 (1964).

[57] E. Thiele; J. chem. Phys, **39**, 474 (1963).

[58] L. S. Ornstein and F. Zernike; "Accidental deviations of density and opalescence at the critical point of a single substance";Royal Netherlands Academy of Arts and Sciences (KNAW). Proceedings. 17: 793–806. (1914).

[59] A. A. Khan and A. A. Broyles; "Interatomic Potentials and X-Ray-Diffraction Intensities for Liquid Xenon"; J. Chern. Phys. **43**, 43 (1965).

[60] G. J. Throop and R. J. Bearman; "The pair correlation function and thermodynamic properties for the Lennard-Jones 6–12 potential and the Percus-Yevick equation"; Physica **32**, 1298 (1966).

[61] D. Levesque, "Etude des equations de percus et yevick, d'hyperchaine et de born et green dans le cas des fluides classiques"; Physica **32** 1985 (1966).

[62] R. O. Watts; "Percus-Yevick Equation Applied to a Lennard-Jones Fluid"; J. Chern. Phys. **48**, 50 (1968).

[63] R. J. Baxter; "Percus-Yevick Equation for Hard Spheres with Surface Adhesion"; J. Chern. Phys. **49**, 2770 (1968).

[64] P. Hutchinson; "The phase transition of the hard sphere fluid"; Molecular Physics, **13** 495 (1967).

[65] "Fluid-Solid Transition in a Hard-Core System"; Phys. Rev. Lett. **96**,025701 (2006).

[66] R. J. Baxter; "Hard hexagons: exact solution"; J. Phys. A **13**, L61 (1980).

[67] R. J. Baxter, "Exactly Solved Models in Statistical Mechanics"; Academic Press, London, (1989).

[68] D. Frenkel; "Entropy-driven phase transitions"; Physica A **263** 26-38 (1999).

[69] W. G. Henk and W. J. Blote; "Finite-size analysis of the hard-square lattice gas"; Phys. Rev. E, **66**, 046140 (2002).

[70] H. C. Marques Fernandes, J. J. Arenzon and Y. Levin; "Monte Carlo simulations of two-dimensional hard core lattice gases"; J. Chem. Phys. **126**, 114508 (2007).

[71] X. Feng, H. W. J. Blote and B. Nienhuis; "Lattice gas with nearest- and next-to-nearest-neighbor exclusion"; Phys. Rev. E **83**, 061153 (2011).

[72] T. Nath, D. Dhar and R. Rajesh; "Stability of columnar order in assemblies of hard rectangles or squares"; Europhys. Lett. **114**, 10003 (2016).

[73] A. Robledo and C. Varea; "The hard-sphere order-disorder transition in the bethe continuum"; J. Stat. Phys. **63** , 1163 (1991).

[74] R. Nisbet and I. Farquhar; "Hard-core lattice gases with residual degrees of freedom at close packing"; Physica **73** , 351 (1974).

[75] S. B Zimmerman and A. P. Minton; "Macromolecular crowding: biochemical, biophysical, and physiological consequences."; Ann. Rev. Biomol. Struct., **22** (1993).

[76] Herzfeld; "Entropically Driven Order in Crowded Solutions: From Liquid Crystals to Cell Biology"; Acc. Chem. Res., **29**, 31 (1996).

[77] D. Poland; "The coexistence curve for a mixture of hard-particle lattice gases"; J. Chem. Phys. **80**, 2767 (1984).

[78] D.-J. Liu and J. W. Evans; "Phase transitions in mixed adsorbed layers: Effect of repulsion between “hard squares” and “point particles” "; J. Chem. Phys. **114**, 10977 (2001).

[79] T. J. Oliveira and J. F. Stilck; "Solution on the Bethe lattice of a hard core athermal gas with two kinds of particles"; J. Chem. Phys. **135**, 184502 (2011).

[80] J. S. van Duijneveldt and H. N. W. Lekkerkerker; "Three-phase equilibrium in a binary hard-core lattice model"; Phys. Rev. Lett. **71**, 4264 (1993).

[81] A. Verberkmoes and B. Nienhuis; "Evidence against a three-phase point in a binary hard-core lattice model"; Phys. Rev. E **60**, 2501 (1999).

[82] T. J. Oliveira, J. F. Stilck and M. A. A. Barbosa; "Solution of an associating lattice-gas model with density anomaly on a Husimi lattice"; Phys. Rev. E **82**, 051131 (2010).

[83] D. Hone, H. Ji and P. A. Pincus;"Polymer adsorption on rough surfaces. 1. Ideal long chain"; Macromolecules, **20**, 2543-2549 (1987).

[84] H. Ji and D. Hone;"Polymer adsorption on rough surfaces. 2. Good solvent conditions"; Macromolecules, **21**, 2600-2605 (1988).

[85] A. Venkatakrishnan and V. K. Kuppa; "Polymer adsorption on rough surfaces"; Current Opinion in Chemical Engineering **19**, 170-177 (2018).

[86] A. Saywell, J. Schwarz, S. Hecht, and L. Grill; "Polymerization on Stepped Surfaces: Alignment of Polymers and Identification of Catalytic Sites"; Angew. Chem. Int. Ed. **51**, 5096 –5100 (2012).

[87] P. M. Petroff, A. C. Gossard, and W. Wiegmann;"Structure of AlAs-GaAs interfaces grown on (100) vicinal surfaces by molecular beam epitaxy"; Appl. Phys. Lett. **45**, 620 (1984).

[88] V. Marsico, M. Blanc, K. Kuhnke, and K. Kern; "Discrete Row Growth at Vicinal Surfaces"; Phys. Rev. Lett. **78**, 94 (1997).

[89] P. Gambardella, M. Blanc, H. Brune, K. Kuhnke, and K. Kern; "One-dimensional metal chains on Pt vicinal surfaces"; Phys. Rev. B **61**, 2254 (2000).

[90] N. Néel, J. Kröger, and R. Berndt; "Fullerene nanowires on a vicinal gold surface"; Appl. Phys. Lett. 88, 163101 (2006).

[91] C. Bilel, S. Blel and A. B. H.Hamouda; "Formation of Fe nanowires on Cu(100) vicinal surfaces" Results in Phys. **15**, 102638 (2019).

[92] Meng-Bo Luo; "The critical adsorption point of self-avoiding walks: A finite-size scaling approach"; J. Chem. Phys. **128**, 044912 (2008).

[93] C. J. Bradly, A. L. Owczarek and T. Prellberg; "Adsorption of neighbor-avoiding walks on the simple cubic lattice"; Phys. Rev. E. **98**, 062141 (2018).

[94] J. Krawczyk, A. L. Owczarek and T.Prellberg; "A semi-flexible attracting-segment model of three-dimensional polymer collapse"; Physica A **431** 74–83 (2015)

[95] P. Grassberg; "Pruned-enriched Rosenbluth method: Simulations of θ polymers of chain length up to 1 000 000"; Phys. Rev. E. **56**, 3682 (1997).

[96] T. Prellberg and J. Krawczyk; "Flat Histogram Version of the Pruned and Enriched Rosenbluth Method"; Phys.Rev.Lett. **92**, 120602 (2004).

[97] M. N. Rosenbluth and A. W. Rosenbluth; "Monte Carlo Calculation of the Average Extension of Molecular Chains"; J.Chem.Phys. **23**, 2 (1955).

[98] E. J. J. van Rensburg; "Monte Carlo methods for the self-avoiding walk"; J. Phys. A: Math. Theor, **42** 323001 (2009).

[99] T. Prellberg; "From Rosenbluth Sampling to PERM - rare event sampling with stochastic growth algorithms"; arXiv:1205.3734 (2012).

[100] P. D. Gujarati; "Bethe or Bethe-like Lattice Calculations Are More Reliable Than Conventional Mean-Field Calculations"; Phys. Rev. Lett **74**, 809 (1995).

[101] Hans A. Bethe; "Statistical theory of superlattices"; Proc. Roy. Soc. London A, 150:552-558 (1935).

[102] L. Onsager; "Crystal Statistics. I. A Two-Dimensional Model with and Order-Disorder Transition"; Phys. Rev. **65**, 117 (1944).

[103] J. L. Monroe; "Systematic approximation method for the crítical properties of lattice spin systems"; Phys. Rev. E, V**64**, 016126, (2001).

[104] M. Suzuki, M. Katori and X. Hu; "Coherent Anomaly Method in Critical Phenomena. I."; J. Phys. Society of Japan, V**53**,N 9, pp 3092-3112, (1987).